Ultrasound supported electrodeposition of metals and preparation of metal/ceramic composites, colloidal nanoparticles and oxide materials

Doctoral Thesis

(Dissertation)

to be awarded the degree of

Doctor Ingenieur (Dr.-Ing.)

submitted by

Dipl. Ing. Slađana Martens

from

Zaječar, Serbia

approved by the

Faculty of Natural and Materials Sciences

Clausthal University of Technology

Date of oral examination

24. 08. 2011

Chairperson of the Board of Examiners
Prof. Dr. A. Wolter

Chief Reviewer
Dr. rer. nat. habil. Oliver Schneider

Reviewer
Prof. Dr. Christos Argirusis
Prof. Dr. Wolfgang Maus - Friedrichs

Acknowledgments

My special acknowledgment is given to Dr. Schneider, for the great supervising this work. I am thankful for the help with theoretical as well as with practical problems and for the many fruitful discussions. Many thanks for the patience and understanding.

I would like to thank Prof. Argirusis for the opportunity to come to Clausthal and work on new and interesting things, for support and help to find good directions in work.

To Prof. Maus-Fridrichs I am grateful for accepting my work for the revision and giving constructive comments and ideas.

I would like to thank to the group of Prof. Borchardt and other colleagues and friends in the Institute of Metallurgy for the good working atmosphere, help and support during this work. It would not be possible to accomplish this work without help of the technicians, especially Ms. Lenk, Mr. Werman and Mr Herrmann, so many thanks to them too.

A very special acknowledgment is given to my husband Lars, my daughter Lea and my parents, especially my mum Ljiljana for the support, encouragement, patience and love.

Finally I would like to thank to my good friends in Germany and Serbia.

To my mum

Table of contents

Standard Abbreviations:

CV	Cyclic Voltammetry
DLS	Dynamic Light Scattering
EDX	Energy Dispersive X-ray Spectroscopy
EDTA	Ethylenediaminetetraacetic Acid Disodium Salt
EQCM	Electrochemical Quartz Crystal Microbalance
EPMA	Electron Probe Microanalysis
EPR	Electron Paramagnetic Resonance
LSV	Linear Sweep Voltammetry
KVG	Quartz Crystal Technology
NHE	Normal hydrogen electrode
PVA	Polyvinyl Alcohol
PVP	Polyvinyl Pyrrolidone
PEMFC	Proton exchange membrane fuel cells
OCP	Open Circuit Potential
QCM	Quartz Crystal Microbalance
RDE	Rotating Disc Electrode
RE	Reference Electrode
SDS	Sodium Dodecyl Sulfonate
SEM	Scanning Electron Microscopy
SOFC	Solid oxide fuel cells
TEM	Transmission Electron Microscopy
vol%	volumetric percent
WE	Working Electrode
wt%	weight percent
XPS	X-Ray Photoelectron Spectroscopy
XRD	X-Ray Diffraction

List of Symbols

A	area of the electrode
A	area of the horn tip
a	chemical activity
a_O	chemical activity of oxidized species
a_R	chemical activity of reduced species
c	sound velocity
c	concentration
c_R	concentration of reduced species in front of electrode
c_R^*	bulk concentration of reduced species
c_O	concentration of oxidized species in front of electrode
c_O^*	bulk concentration of oxidized species
d	electrode-horn separation (sonoelectrochemistry)
D	diffusion coefficient
E	electrode potential
E^0	standard electrode potential
f	frequency of ultrasound
f	frequency of quartz resonator
f_0	resonance frequency of bare quartz
f_R	general resonance frequency of quartz
Δf	resonance frequency change
F	Faraday constant, 96487 C/mol
I	current
I_a	ultrasound intensity
j	current density
j_0	exchange current density
j_a	anodic current density
j_{cath}	cathodic current density
j_{corr}	corrosion current density
j_M	current density calculated from mass change
j_l, j_{lim}	mass transport limiting current density
j_k	current density in absence of any mass transport limitation
J	charge flux (Fick's law)
M	molar mass
m	mass
Δm	mass change
O	oxidized species

P_W	ultrasonic power
P_a	pressure variation induced by ultrasound
P_{tot}	pressure in liquid in a moment of bubble collapse
P_{bub}	pressure in bubble in its maximal size
P_A	pressure amplitude
Q	charge density
ΔQ	change in charge density
R	gas constant, 8.314 $Jmol^{-1}K^{-1}$
R	reduced species
r	electrode radius
Re(Z)	real part of electrical impedance
T	period of sound wave
T_0	ambient temperature
T_{max}	maximal temperature after bubble collapse
t	time
v	scan rate
w	damping of quartz
x	distance
x	displacement of a medium particle
x_0	maximal displacement
Y	electrical admittance
z	number of electrons
Z	electrical impedance
Z_Q	mechanical impedance of quartz
α	charge transfer coefficient
δ	diffusion layer thickness
ε	current efficiency
ε_{app}	apparent current efficiency
η	viscosity
η_D	overpotential
μ_q	shear modulus of quartz
ν	stoichiometric coefficient
ν	kinematic viscosity
ρ	density of liquid
ρ_q	density of quartz
χ	standard deviation
ω	rotation rate for RDE experiments

Abstract

Ultrasound as an additional source of energy was used to support the chemical and electrochemical preparation of different types of materials, especially materials with potential application in fuel cells. First a fundamental study on sonoelectrochemistry is presented, which was performed in water and different copper electrolytes. In this study the applicability of the EQCM technique in an ultrasound field was demonstrated. The influence of ultrasound on the resonance spectra, the frequency and the damping of the quartz as well as on the noise of the admittance curve was studied in water through variation of the ultrasonic intensity and the distance between the electrode and the ultrasonic horn. Deposition and dissolution processes, in Cu-based electrolytes, were followed during cyclic voltammetry and the influence of ultrasound on the current efficiency was studied. The morphology of potentiostatically deposited Cu layers under the impact of ultrasound was characterized. In order to understand better what is the major influence of ultrasound on the electrochemical reactions a rotating disc electrode study was performed as well. Acoustic streaming, caused by ultrasound, was found to enhance the mass transport significantly and surface cavitation led to the development of corrosion and erosion. Further, ultrasound in combination with EQCM was used for the electrodeposition of metal/ceramic composites. Ni/CeO_2 and Co/CeO_2 composites were synthesized from Watts and sulfamate based electrolytes containing dispersed ceria using ultrasonic irradiation for the deagglomeration of oxide particles and their better distribution in the metal matrix. The composition of the obtained composites was characterized and the influence of the ultrasound on the particle incorporation was investigated. Moreover, using the planar circular end of the ultrasonic horn-tip itself as the electrode, during short electric pulses, metal nanoparticles were deposited. The electric pulses were followed by successive ultrasound pulses, by which the formed particles were removed from the electrode and their further growth in the next electric pulse was prevented. Under the action of surfactants added to the solution, the agglomeration of the particles produced was prevented and nanoparticles were successfully stabilized. Finally, the sonochemical preparation of molybdenum oxides by decomposition of molybdenum hexacarbonyl was performed in two different solvents, decane and hexadecane, with oleic acid as the stabilizer. Sonication lasted up to ten minutes and stable colloidal solutions were obtained. The particles were spherical or tubular in shape and most of them showed an amorphous structure.

Zusammenfassung

Ultraschall ist als zusätzliche Energiequelle verwendet worden, um die chemische und elektrochemische Herstellung von verschiedenartigen Materialien zu unterstützen, insbesondere für Materialien, die eine potenzielle Anwendung in Brennstoffzellen finden. Zunächst wird eine grundlegende Studie über Sonoelektrochemie vorgestellt, die in Wasser als Medium und in verschiedenen Kupferelektrolyten durchgeführt wurde. In dieser wurde die Anwendbarkeit der EQCM-Technik in Gegenwart von Ultraschall erprobt. Der Einfluss des Ultraschalls auf das Resonanzspektrum, die Frequenz und die Dämpfung des Quarzes als auch auf das Rauschen der Admittanz-Kurve ist durch Variation der Ultraschallintensität und des Abstands zwischen Elektrode und Sonotrode in Wasser untersucht worden. Anschließend Untersuchungen mittels zyklischer Voltammetrie zu Abscheidungs- und Auflösungsprozessen in Cu-basierten Elektrolyten vorgestellt, wodurch u.a. der Einfluss des Ultraschalls auf die tatsächliche Stromausbeute ermittelt wurde. Der Einfluss des Ultraschalls auf die Morphologie der potentiostatisch abgeschiedenen Kupferschichten wird diskutiert. Um besser zu verstehen, was der Haupteinfluss von Ultraschall auf die elektrochemischen Reaktionen ist, ist zum Vergleich eine Studie mit einer rotierenden Scheiben-Elektrode durchgeführt worden. Es wurde festgestellt, dass das durch den Ultraschall hervorgerufene akustische Strömen deutlich den Stofftransport verbessert und die Oberflächen-Kavitationen zu der Entwicklung von Korrosion und Erosion führen. Weiterhin wurde Ultraschall in Kombination mit EQCM für die galvanische Abscheidung von Metall-Keramik-Kompositen verwendet. Ni/CeO_2- und Co/CeO_2-Verbindungen wurden aus Watts-Elektrolyten und sulfamatbasierten Elektrolyten, die dispergiertes Ceroxid enthielten, synthetisiert. Ultraschall wurde für die Desagglomeration der Oxidpartikel und ihre bessere Verteilung in der Metallmatrix benutzt. Die Zusammensetzung der entstandenen Verbindungen wurde bestimmt und der Einfluss von Ultraschall auf die Einlagerung der Partikel wurde untersucht. Schließlich wird die sonoelektrochemische Herstellung von Nanopartikeln diskutiert. Dazu wurde das flache kreisförmige Ende der Sonotrode selbst als Elektrode verwendet. Durch kurze elektrische Impulse wurden Metallnanopartikel abgeschieden. Den elektrischen Impulsen folgten Ultraschallimpulse, bei denen die gebildeten Partikel von der Elektrode mechanisch abgelöst wurden und somit ihr weiteres Wachstum bei den nächsten elektrischen Impulsen verhindert wurde. Unter der Einwirkung von Tensiden, welcher der Lösung hinzugefügt wurden, ist die Agglomeration der produzierten Partikeln verhindert worden und die Nanopartikel wurden erfolgreich stabilisiert. Zum Abschluss wird die sonochemische Herstellung von Molybdänoxiden durch die Zersetzung von Molybdänhexacarbonyl in zwei verschiedenen Lösungsmitteln, Decan und Hexadecan, und mit Ölsäure als Stabilisator erläutert. Die Beschallung dauerte bis zu 10 Minuten und es wurden stabile kolloidale Lösungen erhalten. Die Partikel waren kugel- oder röhrenförmig und die meisten von ihnen zeigten eine amorphe Struktur.

Aim of the work

Due to the importance of nanomaterials and the constant demand for developing new synthetic routes comprising low cost materials and improved, environmentally friendly techniques, the present study as one small contribution to the expanding field was carried out.

Materials with particle sizes from a few nanometers to less than 100 nanometers, in at least one dimension, are recognized as nanomaterials [1, 2]. Nanotubes, nanowires and nanocrystals are some of the known particular nanostructures whose collections can give arrays, assemblies and superlattices of these nanostructures. The physical and chemical properties of nanomaterials usually greatly differ from the bulk materials of the same composition and it is possible by reducing the particle size of the old and recognized materials to obtain new properties [3]. They exhibit unique structure, energetics, response, dynamics and chemistry. Appropriately tailored characteristics and response of the nanostructures could be the base for future advanced devices and technologies [4]. Over the past decade, the synthesis of nano-sized materials has become the focus of intensive research. A variety of synthetic methods are nowadays available, as well as the tools for the characterization and manipulation. Increased interest in nanoparticles arises from their numerous applications in diverse fields such as the production of catalysts [5, 6], semi-conductors [7], magnetic devices [8], supermagnets [9] and photo-electronic devices [10]. Properties of nanoparticles and their size strongly depend on the used preparation methods and the applied experimental conditions. Up to now, a variety of methods has been used for the synthesis of nano-materials, among them chemical vapor deposition [11, 12] sol-gel processes [13], hydrothermal reactions [14, 15], thermal decomposition [16, 17], physical evaporation [18], laser ablation [19, 20] and thermal evaporation [20].

T.J. Mason [21] distinguished a few main advantages which the use of power ultrasound in synthesis of nanomaterials gives. Under ultrasound irradiation it is possible to obtain nanomaterials in amorphous state which is important in catalysis, magnetism, coatings, etc. Generally, reaction times are much shorter. For the synthesis of mesoporous materials, instead days needed for the sol-gel preparation, several hours are sufficient when the sonochemical method is employed. Further, when nanomaterials are inserted in the mesoporous materials, their pores are not blocked. For the synthesis of some materials such as inorganic fullerenes, there is no need for high temperatures as with other methods. A. Gedanken [22] underlined some more advantages of sonochemistry as the tool in nanomaterials production. One of them is the deposition of nanoparticles on ceramic and polymeric surfaces. Metals, metal oxides and semiconductors have been deposited on ceramic surfaces [23, 24]. The sonochemical method is reported to be superior to all other techniques in the formation of proteinaceous micro- and nanospheres [25-27]. In general, sonochemically produced materials are nanosized, amorphous or crystalline in the structure, depending on the nature of the precursors, and they can also vary in the morphology. Nanospheres, nanotubes, nanowires, nanorods, nested

fullerenes, hollow spheres are just some of the shapes which sonochemically obtained materials can have.

In recent years, the sonoelectrochemical technique has been widely used, a combination of the technique of electrodeposition [28, 29], known to be generally cheaper than other conventional techniques for nanoparticles synthesis, and ultrasound irradiation. Furthermore, a relatively new cost-effective production technology has been developed for nanopowders where the ultrasound probe is used itself as the cathode (then known as the sonotrode), onto which by short electrical pulses metal nanoparticles are deposited and afterwards removed from the electrode by successive ultrasonic pulses [30]. The presence of an appropriate surfactant could further prevent agglomeration of the produced particles and thus the loss of the precious surface area of the nanoparticles.

The present study was carried out with the aim to apply the method for the electroplating of metals, alloys and composites, a particularly important technique which may show a significant potential for the synthesis of electrocatalysts for the proton exchange membrane fuel cells (PEMFC) as well as modified materials for solid oxide fuel cells (SOFC) and the molten carbon fuel cell (MCFC) [31]. It is possible to deposit films or particles of metals, alloys and composites employing this technique and the amount of produced electrocatalyst could be monitored as well. Further, the codeposition of metals and ceramic particles has been applied extensively to modify metal properties like hardness, corrosion resistance, and high temperature oxidation resistance. The electrochemical quartz crystal microbalance technique (EQCM) was shown to be of great importance in the study of the deposition processes and several reviews on the technique are available [32, 33]. Additional information about mass changes during electrochemical experiments complement the purely electric parameters and enables the determination of current efficiencies and a better understanding of the overall process mechanism. EQCM has been widely used under silent conditions [34-36]. However, the EQCM technique had not been used before in an ultrasound field. The main idea for this study was therefore to check for the possibility to apply the EQCM technique in a strong ultrasonic field. If successful, the limits of use of the EQCM technique coupled with ultrasound irradiation were to be explored for the study of sonoelectrochemical reactions [37] and the fundamentals of the methods combination were to be investigated using as model systems Cu-chloride and Cu-sulfate-based electrolytes [38]. Further, if the method combination would be found convenient, this combination should be applied for the synthesis of materials with practical applications such as composites like Ni/CeO_2 and Co/CeO_2 [39, 40]. Since nanoparticles can be obtained applying pulsed electrodeposition [41] and their shape, size and size distribution can be tailored by optimization of the experimental conditions, the combination with pulsed ultrasound irradiation could be beneficial. Therefore, against the background of possible applications in fuel cells sonochemical and sonoelectrochemical methods should be employed for preparation of nano-scaled materials.

Chapter 1-Background

1.1 Ultrasound

Acoustic waves, with frequencies higher than the level on which the human ear can respond, are called ultrasound. Since the limit of the hearing of one young, healthy adult is approximately 20 kHz, this value serves as the lower limit of the ultrasound frequency [42, 43]. Ultrasound, being a travelling wave, is a mechanical wave and thus needs a medium, with elastic properties, through which it is transmitted causing vibrational motions of the medium molecules. In liquids and gases particular motions are in the direction of the wave inducing longitudinal waves. In solids, possessing shear elasticity, particular motions can be also perpendicular to the direction of the waves and transverse waves can be induced, thus sound transmits as both, longitudinal and transverse waves.
The displacement x of a medium particle, at any time t, from its rest position can be described as a function of the passing ultrasound wave frequency:

$$x = x_0 \sin 2\pi f t \tag{1.1}$$

where x_0 is the maximal displacement, the amplitude and f is the sound frequency.

The longitudinal motion of the medium particles produces regions where the particles are compressed and a high pressure is developed and they are called compression regions. On the other hand low pressure regions, so called rarefaction regions are developed too and in them the particles are further spread apart than in a silent medium [44]. A repeating pattern of high pressure and low pressure regions moving through the medium determines sound as a pressure wave (Fig. 1.1). The frequency of the wave is the number of compressions or rarefactions which pass a given point per unit of time. In other words it is also the number of complete back-and-forth vibrations of a particle of the medium per unit of time [45]. A commonly used unit for frequency is Hertz (abbreviated Hz), where1 Hertz = 1 vibration/second. The wavelength of the sound wave, λ, is the length of one complete wave cycle, whereas the amplitude is the maximum displacement of the medium particle from its rest position.

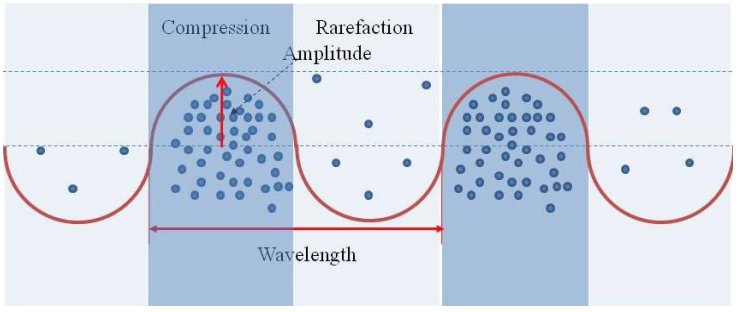

Figure 1.1 Sound shown as a pressure wave, with noted areas of compression and rarefaction, amplitude and wavelength.

The induced pressure variation P_a, at any time t, can be also described as a function of the sound frequency f [45]:

$$P_a = P_A \sin 2\pi f t \quad (1.2)$$

where P_A is the pressure amplitude.

The displacement and pressure are out of phase, when particles are farther separated than normal and a bigger displacement is formed, the pressure is decreased, corresponding to rarefaction.
The intensity of the sound I_a is a measure of the sound wave energy and is proportional to the square of the pressure amplitude [45]:

$$I_a = \frac{P_A^2}{\rho c} \quad (1.3)$$

where ρ is the liquid density and c the sound velocity.

Under the influence of the sound wave the molecules of the medium vibrate, experiencing viscous interactions and degrading part of the acoustic energy into heat.
The period of the sound wave T, can be defined as the time for a particle of a medium to make one complete vibrational cycle or it is the time of one compression and one rarefaction cycle. The period is measured in units of time such as seconds in a repeating event, so the period is the reciprocal of the frequency, $T=1/f$.

1.1.1 Application of ultrasound

Dependent on the frequency range ultrasound found a wide range of applications in a variety of fields. In medicine, high frequency ultrasound found application in diagnostics as a non invasive technique [46]. The high frequency ultrasound waves transmit and as a response the reflection from the soft tissue structures is detected. The most often it is used in obstetrics to follow the pregnancy [47] but it is also frequently used in gynecology/urology, in abdominal, vascular system, brain, prostate, breasts, musculoskeletal and eyes. Ultrasound at lower frequencies and higher power is used in therapeutic medicine where interactions of ultrasound with biological tissues may be caused by either a thermal or a mechanical mechanism. Basically, anywhere where there is a need to promote blood circulation and reduce swelling and edema, ultrasound can help. Lately, ultrasound is also known to be used for cancer treatment [48]. In dentistry ultrasound is used for drilling and cleaning of teeth, in biology and biochemistry for homogenisation and cell disruption. There are many known applications of ultrasound in industry and engineering [49]. At first, ultrasound is widely used in processes of cleaning and degreasing of surfaces. It is used to help in cutting, drilling, grinding, metal casting as well as in welding of plastics and metals. Applications in mixing and emulsification, extraction,

impregnation, filtration, crystallization are also very well established. Ultrasonic energy is also used for environmental applications, to remove contaminants from air and to break down toxic compounds in water and soil [50].

Finally, ultrasound with lower frequencies and high power can be used in the field of chemistry to cause or enhance chemical reactivity. Power ultrasound can be used as a form of energy in chemical systems [51, 52].

1.2 Ultrasound in chemistry - Sonochemistry

The field of chemistry where ultrasound is applied as an energy source to provoke chemical activity is called sonochemistry. The range of conventional power ultrasound is 20-100 kHz with an extended range for use in sonochemistry up to 2 MHz. Ultrasound is different from all other sources of energy in terms of duration, pressure and energy per molecule. Sonochemistry gives a range of energy, combination of time and pressure not available from any other source of energy.

Since the frequency of the ultrasound is higher than 20 kHz and consequently the wave length between 10-10^{-3}cm, it can be concluded that chemical activity cannot be the result of a direct interaction between the ultrasound and molecular species. The physical phenomenon responsible for the chemical activity caused by the ultrasound is known as acoustic cavitation [53].

1.2.1 Acoustic cavitation

Acoustic cavitation is developed during transition of the ultrasound through a liquid medium [54]. Cavitation occurs through three steps, forming of micro bubbles, growth and finally their violent collapse. Since sound is a pressure wave, it causes alternating compression and rarefaction cycles within a medium. During the rarefaction cycle, particles in a medium are farther away one from another. If the negative pressure exceeds the tensile strength of the liquid, the average distance between molecules reaches the critical molecular distance necessary to keep the liquid intact, the liquid will tear apart and a micro bubble can be formed. If just one bubble is formed this phenomenon is known as a single bubble cavitation and when a bubble cloud is formed we speak of multi bubble cavitation (mostly present in sonochemical reactions). The presence of so called weak spots in the liquid, such as gas molecules can facilitate this process and lower the negative pressure necessary for cavitation to be initialized. Particulate matter with possible trapped gas nuclei in the crevices and recesses may also help. Once formed, bubbles can grow in size in a way depending on the type of cavitation. One distinguishes stable and transient cavitation [55]. “Stable cavitation” refers to the formation of stable bubbles, existing over several acoustic cycles and their growth during rarefaction is equal to their shrinkage during compression cycle. Therefore they oscillate around a mean radius in a sound field before collapsing or they do nott collapse at all. On the contrary, “transient cavities”

exist only during a few acoustic cycles and grow via a process known as rectifying diffusion [56, 57]. Each time the bubble is growing during the rarefaction cycle stronger than it is shrinking during the compression cycle due to the unequal diffusion of gases and vapour from the bulk liquid into the bubble. In the case of multi bubble cavitation, it is also possible for bubbles to grow by coalescence [58]. After reaching a critical size, several times larger than its initial size, the cavity cannot grow any longer and collapses violently [59]. The reached critical size of the bubble is related to the nature of the liquid medium and the frequency of the applied ultrasound. The overgrown bubble can no longer absorb energy and stand pressure and liquid strikes in [60, 61]. The process of acoustic cavitation is shown schematically in Figure 1.2.

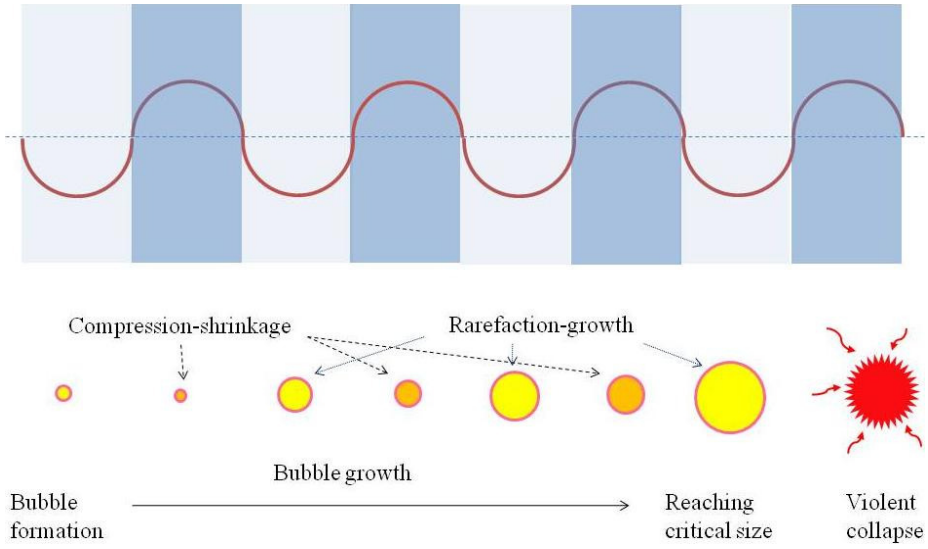

Figure 1.2 Acoustic cavitation development (made according to Ref. 45).

Two known theories explain chemical effects due to cavitation: the hot spot theory and the electrical theory. According to the generally more accepted hot spot theory, the diffuse energy of the sound is concentrated in the chemically useful energy due to the caused localized "hot spots" upon bubble collapse, with temperatures up to 5000 °C, pressures up to 1000 atm, lifetime less than μs and heating and cooling rates more than 10^{10} °C/s [62]. This high temperature and pressure are enough to induce dissociation of water molecules (so-called sonolysis of water) into primary hydrogen ($H^{\cdot}$) and hydroxyl ($OH^{\cdot}$) radicals and production of H_2O_2 [63]. The extreme conditions developed upon bubble collapse are responsible for advantages in the chemical activity caused by the ultrasound. According to the electrical theory, on the surface of a cavitational bubble an electrical charge is formed, giving rise to huge electrical field gradients across the bubble and causing bond breakage upon bubble collapse [64]. Furthermore, the bubble collapse has a mechanical impact on the liquid medium via released pressure as shock waves and intense shear forces formed in a bulk liquid [21]. If cavitation occurs in a liquid near to a surface, due to the asymmetric collapse liquid microjets can be also formed leading to surface damage.

1.2.2 Active areas during sonication

Electron paramagnetic resonance (EPR) and spin trapping studies done on the volatile and non-volatile solutes showed existence of three sonochemically active areas in a sonicated liquid [65,66]:

- The bubble interior, containing permanent gas and vaporised reaction mixture, where the most extreme conditions are created with temperatures up to 5000 °C, pressures up to 1000 atm, and heating and cooling rates of more than 10^{10} °C/s. Here gas phase reactions take place. If the reaction takes place in this area (the case where volatile solutes are employed) amorphous nanoparticles will be obtained [67, 68].
- The surrounding of the bubble, actually the interfacial area between the bubble and the bulk solution, with an average thickness of 200 nm. In comparison with the bubble interior, conditions are less extreme with temperatures up to 1900 °C, but still enough to initiate sonochemical reactions. In this area, less volatile or non volatile compounds such as salts react and products can be either amorphous or crystalline [69]. When surfactants are present, they also participate in reactions taking place in this area.
- The bulk solution, where liquid reactions take place and involve radicals which escaped the implosion (around 10 %) [70]. Still, in this area, the mechanical effect, as the consequence of the intense shear forces and shock waves formed upon violent bubble collapse, is more pronounced. Furthermore, if there is a solid surface like particles in a liquid due to the asymmetric bubble collapse liquid microjets toward the surface are also formed which can break the particles in pieces and/or activate their surface. It is possible to keep the temperature in this area to normal values, for example with a cooling water jacket around the sonication vessel for adjusting of the desired constant temperature.

The estimations of the reached temperatures in the bubble interior as well as in the interfacial gas-liquid area were found experimentally using comparative rate thermometry [69], a technique developed for use in shock tube chemistry [71]. Similar values were obtained by theoretical calculations using hydrodynamic models for cavitational collapse [72].
Recent works in Ken Suslick´s group give evidence of existence of a plasma core in the cavitation bubbles. This means even higher temperatures of up to 20000 K (depending on the gas involved) [73, 74].

1.2.3 Parameters influencing cavitation

The ultrasound frequencies used in sonochemical reactions are in the range from 20 kHz up to 2 MHz. The critical size of the cavitational bubble is influeneced by the ultrasound frequency. If ultrasound waves have lower frequencies, the rarefaction cycle lasts longer and sufficient negative pressure can be developed for cavitation to be easily initiated. The formed bubbles have longer lifetime and can reach a bigger critical size. The compression cycle is also long enough for the bubbles to collapse extremely violent, generating an enormous temperature and pressure. In contrary, when the frequency is very high, it can happen that on the one hand the rarefaction cycle is not long enough, reducing intensity or duration of the negative pressure and making it difficult for cavitation to start and on the other hand compression cycle occurs faster and the lifetime of bubbles is shorter and the reached critical size is smaller. Although high frequency causes less violent cavitational collapse there can be more cavitational events and thus more free radicals produced, which can escape to the bulk liquid causing there chemical reactions. Depending on what is essential for a certain process, either intense temperature and pressure (enhanced by lower frequencies) or the rate of single electron transfer (enhanced by higher frequency) there is an optimal value of the frequency for each process. It is found for oxidation reactions that a higher frequency may lead to the higher reaction rates [49]. For example, the rate of sonochemical oxidation of iodide in the presence of air was found to be more than 30 times higher at 900 kHz than at 20 kHz [75]. Further, the degradation of carbon tetrachloride was enhanced using 500 kHz instead of 20 kHz ultrasonic waves [76]. In some reactions, like dissociation of carbon disulfide there was no such effect observed when ultrasound frequency was enhanced [77]. When the reaction is taking place in a gas phase, for example decomposition of volatile transition metal carbonyls, 20 kHz ultrasound frequency is normally used [78].

The ultrasound intensity I_a is the dissipated acoustic power in the system per area of the ultrasound waves source (normally tip of the horn), $I_a = P_w/A$, with unit Wcm^{-2}. In many works it was found that with increase in acoustic power, the reaction rate increases up to a certain value and then starts to decrease [79]. A possible explanation could be that at increased power, a dense bubble cloud is formed near to the ultrasound probe blocking energy to be transmitted to a fluid [80]. It was also found for the optimal value of the power to be dependent on the ultrasound frequency [81].

The nature of the solvent influences cavitation through the surface tension, viscosity and the vapor pressure. Since for cavities to be formed it is necessary that the negative pressure exceeds the tensile strength and overcomes cohesive forces between molecules of the liquid, a lower values of surface tension and viscosity and a higher value of vapor pressure facilitate cavitation initiation. On the other hand, the intensity of the cavitational collapse (reached temperatures and pressures as well as intensity

of developed shear forces and shock waves) is found to be influenced inversely [49]. It has been reported for cavitation to be the most intensive in solvents with a higher viscosity [82]. Further, it was found for solvents with very high vapor pressure to reduce cavitation effect [83].

The presence and the nature of the dissolved gases have a great impact on cavitation. Gas molecules can serve as nuclei for cavitational sites and thus facilitate cavitation to be initiated. On the other side, more gas content could lead to less violent collapse and lower intensity of the shock waves as well as to lower temperatures developed. Since it is assumed that cavitational collapse occurs adiabatically, more energy can be converted upon cavitation collapse by monoatomic gases due to the larger polytropic constant (ratio of the specific heats) as explained by Equation 1.4.

$$T_{max} = T_0 \left\{ \frac{P_{tot}(\gamma-1)}{P_{bub}} \right\} \quad (1.4)$$

where T_{max} is maximal developed temperature upon cavitational collapse, T_0 is the ambient temperature, γ is the polytropic constant of the present gas, P_{tot} is the pressure in the liquid in the moment of the collapse and P_{bub} is the pressure in the bubble at its maximal size.

Still, there is always a certain, small amount of heat which is transferred to a bulk liquid during collapse causing reduced temperature developed upon collapse. When the gas present has a higher thermal conductivity more heat can be lost. Further, the solubility of the gas has also a certain role. When the gas is extremely soluble it can lead to dissolving of the bubble before the collapse, reducing the number of cavitational events and thus the overall effect of the cavitation. On the opposite, bubbles from insoluble gases can grow very large and lead to a floating of bubbles at the surface and eventually their collapse there without causing real cavitational effect. M. H. Entezari and co-workers [77] reported the higher rate of the carbon disulfide dissociation under He than under Ar (both monoatomic) due to the larger solubility of He and thus more nucleation sites and easier cavitation development.

The temperature of the liquid medium has also an opposite effect on the cavitation threshold and cavitation intensity. A temperature increase, leads to easier cavitation initiation due to increased vapor pressure but has a negative impact on an overall cavitation effect as the formed bubbles contain more vapor. It was observed that lower temperatures lead to more effective cavitational events [49]. Still, there were some indications that an optimal temperature value exists for each process. S. V. Ley and C. M. R. Low [84] reported an increase in the reaction kinetics upon an increase in the temperature till the point where the effect of the reducing vapor content in the bubble starts to dominate the system. With a further temperature increase the rate of the reaction decreases.

An ambient pressure increase would lead to a vapor pressure decrease and thus more difficult cavitation threshold but also more effective cavitational collapse. J. Berlan et al [85] suggested the existence of an optimal value for each given system.

With an appropriate choice of the conditions, sonochemical reactions can follow desired reaction pathways and lead to the desired final materials. For example, in the fields where materials with large specific surface areas are required, the preparation of amorphous materials with nano-sized particles would be a goal of the study [3, 53]. Since high cooling rates (more than 10^{10} °C/s) are reached during sonication when the reaction takes place in the bubble interior there is not enough time for the organizing and crystallizing of a product and amorphous materials are produced. Such materials are very important in many fields of science, for example in catalysis where they are found to be more active than crystalline particles of the same size due to their high surface area. The high surface area of the amorphous product increases both, the chemical as well as the catalytic activity [86]. Beside the absence of the crystalline order, the amorphous materials own unique electronic, magnetic and corrosion resistant properties.

Since reactions of volatile precursors under ultrasound occur inside of the collapsing bubble and high cooling rates are reached, products are always amorphous. Reactions of non-volatile precursors such as salts occur in the surroundings of the bubbles and the products can be amorphous but also crystalline.

The choice of non-volatile solvents (eg. decan, decalin, hexadecan) gives a higher probability that only vaporised solutes will be in the bubble and it follows that P_{bub} is in fact the vapour pressure of the solute. According to Equation 1.4 it can be concluded that a lower vapour pressure leads to higher bubble temperatures and consequently to higher reaction rates. One can conclude that reactions, including volatile precursors under ultrasound should be run at lower temperatures in order to avoid an increase in vapour pressure and thus more vapour in the bubble leading to reduction of the cavitation effect. A part of the energy generated during collapse would be used for the purpose of the vapour condensation and would be actually lost for sonochemical reaction.

Varying the precursor concentration the desired size of particles can be obtained. With the intention to obtain smaller particles, the solution should be more diluted. A very important fact is that the particle size and the size distribution of the sonochemical product can be controlled by the monitoring of the sonochemical reactions conditions [87-89].

1.2.4 Reaction types

The liquid medium has a great impact on the development of the acoustic cavitation and thus on the character of a sonochemical reaction. Based on the properties of the liquid medium, sonochemical reactions can be generally divided in two main areas: homogeneous and heterogeneous [45].

Homogeneous reactions

In a homogeneous liquid phase, the cavitation bubbles remain spherical during growth till the collapse. At first, when the liquid is not pre-degassed, bubbles will contain trapped gas or air, the origin of the nucleation sites. Further, depending on the properties of reactants and solvent (at first place volatility) bubbles will contain their vapours. During the collapse of the bubble its interior will be subjected to the extreme conditions of temperature and pressure and this will lead to molecular fragmentations and formation of active radicals. If the liquid phase is water there will be $H^{\cdot}$ and $OH^{\cdot}$ radicals as well as H_2O_2 generated. There will be three regions formed: the interior of the bubble with the most extreme conditions, the interface between bubble and surrounding bulk liquid phase with intermediate conditions and the bulk liquid where intensive shear forces, shock waves and liquid jets are created.

Heterogeneous reactions

Heterogeneous reactions can be further divided into three main types with respect to the acoustic cavitation development.

In a liquid, near to a solid surface, the cavitational bubbles will not remain spherical due to a resistance provided by the nearby surface. As liquid from the opposite side of the bubble rushes in, powerful liquid jets targeting the surface are formed. In this way the potential energy of the expanded bubbles is converted into kinetic energy of a liquid jet. The effect, similar to high pressure jetting, is the reason that ultrasound can be used for the purpose of cleaning. This effect can also activate solid catalysts and increase mass and heat transfer to the surface by disruption of the boundary layers.

In a liquid, which contains suspended particles, cavitation can produce dramatic effects on these particles. Surface imperfections or trapped gas can act as nuclei for cavitation bubble formation on the particle surface and the subsequent collapse can then lead to shock waves which break the particle apart. A cavitation bubble collapse in the liquid phase in the vicinity of a particle can force it into a rapid motion. Under these circumstances a general dispersive effect is accompanied by inter-particle collisions which can lead to an erosion effect, surface cleaning, wetting of the particles and particle size reduction.

In a biphasic liquid system the cavitational collapse near the interface can disrupt the interface and overcome attractive forces in liquids which hold large droplets together. The droplets burst into smaller ones which are dispersed increasing in this way the active surface contact area and chemical reactions can be accelerated.

1.2.5 Sonoluminescence

An accompanying phenomenon to the acoustic cavitation is sonoluminescence, the occurrence of very short light flashes during cavitational bubble collapse [90]. During the rarefaction cycle of the ultrasound propagation, gases dissolved in a liquid such as oxygen, nitrogen and argon, etc. can enter the bubble. Under the extremely high temperatures developed upon bubble collapse the gas becomes partly ionized and the recombination of electrons and ions leads to the emission of light [91]. These are actually short flashes of light which last about 100 ps. This phenomenon can be partially understood by the conservation of energy where potential energy of bubbles is converted to heat and light [91]. For example, nitrogen molecules dissociate into nitrogen radicals and then react to form gases such as NH and NO. These highly soluble gases re-dissolve in the surrounding water after bubble collapse. As the bubble expansion begins again, the next reaction cycle starts. Calculations of the energy budget of sonoluminescence show that the amount of energy going into endothermic chemical reactions inside the bubble is two orders of magnitude higher than that going into light emission [62].

1.3. Sonochemistry in materials science

In most sonochemical reactions with inorganic products nanomaterials are produced. The assumption is that in every collapsing bubble several nucleation sites are formed and their growth is limited due to the fast collapse. Depending on the area where reaction takes place, amorphous or crystalline products are obtained. They can differ in size, shape and structure but they are always nano-sized [3].

With the great potential, sonochemistry is recognised as a new technique for obtaining amorphous nanostructured materials with large surface area. These materials find application in all fields where this material's characteristic is essential. In catalysis of some reactions, amorphous nano-materials, probably due to their enhanced surface area, showed better catalytic activity in comparison with the same nano-materials with crystalline structure. For example, amorphous iron powder in the Fischer-Tropsch process (hydrogenation of CO) was ten times and in the hydrogenolysis and dehydrogenation of saturated hydrocarbons more than thirty times more reactive than crystalline iron [92].

One of the frequently used synthetic routes for producing amorphous nanomaterials is the sonication of volatile transition metal carbonyls in low-volatile solvents such as alkanes (Fig. 1.4) [3, 62, 93]. Decomposition of the volatile precursor takes place inside of the collapsing bubble and the generated metal atoms agglomerate forming in that way nanostructured materials. Just with a change of the reaction medium different types of nanomaterials can be obtained. If a surface active agent is present in solution nanoparticles can be caught before they agglomerate and stable metal colloids are the final result. Also in the presence of a support nanoparticles are immobilized and in that way serve as very active heterogeneous catalysts. In the presence of oxygen nano-scaled metal oxides can be produced. Similar holds when a sulphur source is present in the reaction mixture leading to nano-scaled metal sulphides.

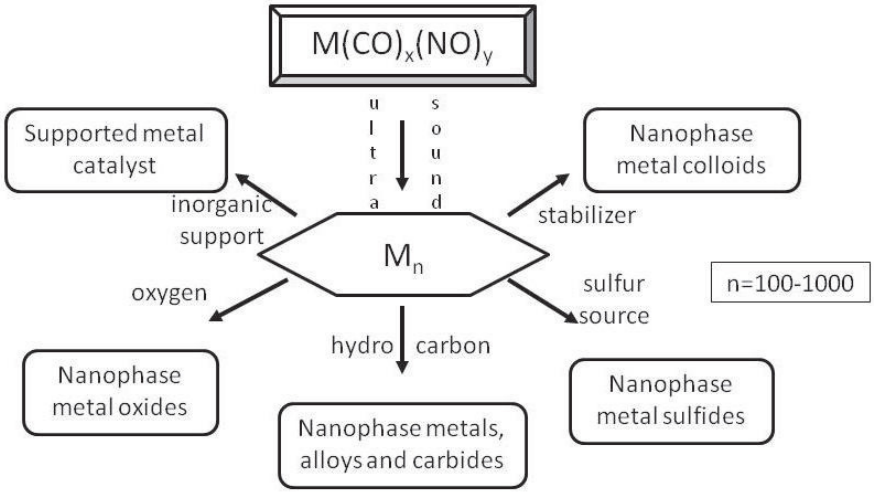

Figure 1.4 General scheme of the nanostructured inorganic materials synthesis [62].

1.3.1 Preparation of amorphous products – metals, alloys and metal oxides

It is possible to obtain amorphous metals by cold quenching of bulk metals. When this method is extended to metal oxides, the required cooling rates cannot be easily reached and therefore addition of glass former is necessary [94, 95]. These additives can be avoided when the sonochemical technique is applied and in addition nano-sized materials are obtained [3].

Metals

The sonochemical production of several transition metals is very well established in literature. Sonication of neat or volatile transition metal carbonyls solutions (e.g. $Fe(CO)_5$, $Ni(CO)_4$, $Co(CO)_3NO$, $Mo(CO)_6$ …) in low vapor pressure solvents under inert atmosphere leads to highly porous aggregates of nanometer-size clusters of amorphous metals [96, 97].

In one of the first works, X. Cao and co-authors [87] studied the dependence of the metal particle size on the precursor concentration during sonication of different concentrations of $Fe(CO)_5$ in decane as the solvent. They proved the ability to control the particle size of the product and concluded that a lower precursor concentration yields smaller particles. In a work published one year later, with addition of polymeric ligands to the initial solution, and in otherwise the same procedure, a stable nanophase metal colloid of Fe was obtained [98]. In this manner, work was extended to other transition metals and amorphous nano-sized nickel was produced both by sonication of pure $Ni(CO)_4$ and of a 2M solution in decane [99]. It showed much better catalytic activity than commercial palladium on activated carbon for the H_2O_2 decomposition reaction. By sonication of $Fe(CO)_5$ and $Mo(CO)_6$ in hexadecane, metallic Fe and molybdenum carbide Mo_2C were produced, with a mean particle size of ~ 10 nm and ~3 nm, respectively [100]. The influence of temperature on decomposition kinetics change was studied in this work as well and a higher temperature generally led to higher reaction yields. Decomposition of $Co(CO)_3NO$ solution in decane in the presence of oleic acid as the stabilizing agent under ultrasound irradiation, yielded a magnetic colloidal solution of 5-10 nm sized spherical particles [101]. With time different states of aggregation were observed leading from the initially spherical to elliptical cobalt nanoparticles.

Several years later, in similar work, W.J. Erasmus et al. obtained 5 nm sized cobalt particles by decomposition of $Co(CO)_3(NO)$ in n-decane under ultrasound irradiation [102]. With addition of silica or oleic acid, they reduced the particle size to 3 and 2 nm, respectively. They also claimed that parameters as sonication time, precursor concentration, ultrasound intensity and temperature do not have an influence on the particle size. By a combination of the sonochemical method and the polyol process (consists of the reduction of metallic compounds such as oxides, hydroxides and salts in liquid alcoholic medium), tin nanorods were produced [103], an interesting anode material for Li

rechargeable battery electrodes [104]. Sonication of $SnCl_2$ in ethylene glycol gave crystallized metallic tin rods with 50-100 nm in diameter and up to 3 μm in length.

Alloys

Ultrasound irradiation of solutions which contain precursors of more than one metal leads to the production of nanostructured amorphous metal alloys. Following a similar pattern of synthesis as for metals, a variety of metal alloys was obtained. R. Bellissent et al. produced binary amorphous $Fe_{1-x}Co_x$ by sonication of $Fe(CO)_5$ and $Co(CO)_3NO$ in dry decane and suggested ferromagnetic behavior of the obtained alloy [105]. They also proved that by changing the ratio of precursor concentrations the alloy composition can be controlled and adjusted to the one required by the future application of the resulting material. Different compositions of Fe-Ni alloys were prepared by ultrasonic irradiation of a solution of $Fe(CO)_5$ and $Ni(CO)_4$ in decalin [106]. $Fe_{20}Ni_{80}$, $Fe_{40}Ni_{60}$ and $Fe_{60}Ni_{40}$ were some of the obtained compositions. During the study, it was noticed that the sonochemical efficiency for the decomposition is less for $Fe(CO)_5$ than for $Ni(CO)_4$. Thus an initial excess of $Fe(CO)_5$ was taken in order to obtain the final desired alloy composition. These alloys were found to be very efficient catalysts for the oxidation of cyclohexane, one of the least efficient industrial processes [107].

Metal oxides

In the case of sonochemical reactions in the presence of air, metal oxides are obtained. Amorphous metal oxides find a number of very important applications due to their specific magnetic and electronic properties. Produced with amorphous structure and consequently high surface area they are widely used in catalysis. Following similar procedures with decomposition of metal carbonyls as described above just in the presence of air instead of inert atmosphere a variety of oxides were produced. Sonication of neat $Fe(CO)_5$ or its solution in decaline gave amorphous Fe_2O_3 [108]. In order to optimize the sonochemical process, M. Sivakumar and A. Gedanken analyzed more in detail the sonication of $Fe(CO)_5$ in decaline [109]. They studied the influence of two parameters, the precursor concentration and the power density, and realized that those play an important role for the yield of the amorphous Fe_2O_3 product. Finding optimal values for these parameters led to even 100 % precursor decomposition. Further, nanostructured $CoFe_2O_4$ particles were obtained by heat treatment of Co and Fe oxides obtained by the sonochemical decomposition of the corresponding carbonyls in decalin [110]. By the sonochemical decomposition of $W(CO)_6$ in diphenylmethane (DPhM) in the presence of an argon-oxygen gaseous mixture amorphous tungsten oxide was prepared [111]. After heating of the as prepared material, a mixture of monoclinic and orthorhombic WO_2 crystals, with snowflake-like dendritic particles, was obtained. Annealing of the as-prepared material at 1000 ºC under Ar gave a WO_2-WO_3 mixture consisting of nanorods (~50 nm in diameter) and their agglomerates. When the

material was heated in air for 3 hours triclinic WO_3 crystals were formed (~50-70 nm size). N. A. Dhas and co-authors obtained amorphous Mn_2O_3 and Cr_2O_3 by the sonication of $KMnO_4$, and $(NH_4)_2Cr_2O_7$ respectively, in aqueous solution at room temperature with a corresponding particle size of 50 and 200 nm [112].

1.3.2 Synthesis of mesoporous materials and insertion of nanomaterials into them

Ultrasound irradiation enables producing of mesoporous materials. Employing sonochemistry as a technique in much shorter time a large surface area is obtained and in a time similar to the ones necessary in more conventional methods much more stable products [113] are formed, probably due to the thicker walls of the sonochemical products [114]. Sonochemical synthesis of mesoporous silica [115], titania [116] and YSZ [117] have been reported in literature. A common scheme for obtaining porous metal oxides is shown in Figure 1.5.

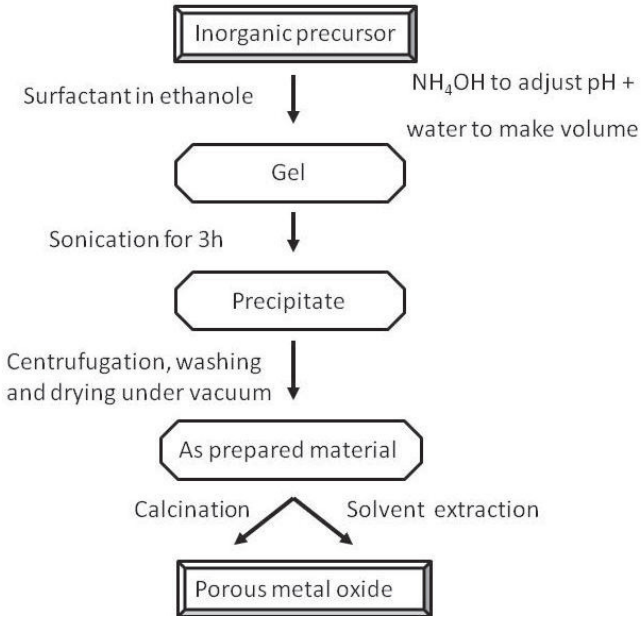

Figure 1.5 General scheme of the porous metal oxides synthesis [113].

According to the presented scheme (Fig 1.5), with an appropriate choice of precursors, surfactants, and pH of the medium, mesoporous Fe [118] and Sn [119] oxides with large surface area were synthesized. Mesoporous oxides of Ni and Co were at first produced from the corresponding alkoxides [120] and afterwards from the corresponding simple inorganic precursors [121] for the application as a catalyst in the oxidation of hydrocarbons.

In addition, ultrasound was applied for insertion of synthesized amorphous nanomaterials into the pores of mesoporous materials. There are two possible ways for insertion, either precursors of the catalyst and mesoporous material are mixed together and during sonication the catalyst is embedded in the mesoporous body or in previously prepared pores, catalyst material is subsequently incorporated.

Detailed examinations showed that with this method pores are not blocked but just smooth layers are formed in inner mesoporous walls [122]. Mo and Co-Mo oxides were deposited into the MCM-41 type of silica as well as into the pores of Al-MCM-41 silica [123]. Furthermore, Fe_2O_3 was successfully anchored into the mesoporous titania [124] and WS_2 and MoS_2 slabs inserted inside SBA-15 silica [125, 126]. I. Grigoriants et al. used the sonochemical method for insertion of tin nanoparticles into mesoporous carbon to be used as a building block for the anode in rechargeable Li batteries [127].

1.3.3 Synthesis of noble metal nanoparticles

Metallic nanoparticles, showing specific physicochemical properties and among them catalytic activity, optic, magnetic and electronic properties [128], constantly attract a lot of attention in recent years. Noble metal particles due to their high catalytic activity are particularly interesting [129, 130]. Under ultrasound irradiation from appropriate solutions of noble metal salts with presence of proper stabilizers fine and stable nanoparticles can be obtained. Due to the great importance of the noble metal nanoparticles, a lot of effort for synthesizing these materials was reported in recent period. Some of the first works were published at the end of 1980's and beginning of 1990's. K. Okitsu and co-authors reported the synthesis of noble metal nanoparticles, such as Ag, Au, Pt, Pd, and Rh with a fairly narrow particle size distribution [131]. They studied optimal experimental conditions for each metal and proposed three main reaction pathways: reduction by H atoms, reduction by secondary reducing radicals formed by hydrogen abstraction from organic additives with $OH^{\cdot}$ radicals and H atoms, and reduction by radicals formed from the pyrolysis of the additives at the interfacial region between cavitation bubbles and the bulk solution. The same group of authors studied synthesis of Au nanoparticles in more details comparing results obtained in different reaction pathways, in different atmospheres and also the influence of different additives [132]. They obtained an average particle size of 10 nm and with certain additives Au particles were stable for several months in the colloidal state. The synthesis of Pt nanoparticles by sonochemical reduction of Pt(II) ions was explored by Mizukoshi et al. [133]. They obtained, in the presence of sodium dodecyl sulfate (SDS) as additive, a stable colloid of homogeneously spherical and relatively monodispersed particles with an average diameter of 2.6 nm. Later on, the production of Pt nanoparticles with a diameter of 1 and 3 nm by reduction of Pt(IV) ions was also reported and in addition the influence of different additives was studied [134]. R. A. Salkar and co-authors synthesized amorphous Ag nanoparticles with ~ 20 nm size by the sonochemical reduction of an aqueous silver nitrate solution in an argon–hydrogen atmosphere [135]. Several years later, J. Park et al. reported the synthesis of Au nanoparticles with multiple shapes and sizes and claimed the possibility to control these two characteristics by adjusting an optimal ratio of noble metal precursor and surfactant concentration as well as the ultrasonic power [136].

Beside the interest in synthesis of noble metal nanoparticles, a pathway for producing bimetallic noble nanoparticles attracted also a lot of attention. Two main pathways were reported, a simultaneous and a

successive one. In the simultaneous pathway, precursors of both noble metals are mixed and introduced to the ultrasound irradiation. In the successive pathway, first a precursor of one noble metal is irradiated and then the precursor of the second noble metal is successively added. Depending on the chosen pathway, different structures of bimetallic noble nanomaterials were obtained. C. Kan et al. compared the effectiveness of proposed pathways in producing core-shell structures of Au/Pd bimetallic nanoparticles in ethylene glycol and proved that the successive method is more efficient for producing an Au-core/Pd-shell structure [137]. In the same year H. Takatani et al. studied the synthesis of Au/Pd and Au/Pt by the simultaneous method in the presence of different additives [138]. In addition, the influence of the precursor concentration, the additive concentration and the irradiation time were studied. By changing the experimental conditions the particle size varied between ~7 and ~11.7 nm.

1.3.4 Immobilization of sonochemically synthesized noble metal nanoparticles on different types of substrates

The microstructure of metallic nanomaterial catalysts with oxide supports are of great interest for a variety of applications in heterogeneous catalysis. Due to high price and limited availability of precious metals which are known as best catalytic materials a lot of research work is done to develop materials with lower content of expensive material but with satisfying properties. It has been shown that with the sonochemical technique immobilization of noble metal nanoparticles on different types of substrates can be done and their properties, especially catalytic ones, are well examined and established [139, 140]. Y. Mizukoshi and co-authors did a lot of work in the field of synthesizing noble metal nanoparticles and their immobilization on different substrates using the sonochemical method [141]. They investigated the mechanism of Au nanoparticles immobilization on the surface of γ-Fe_2O_3 in order to control their morphology and evaluate their adsorption selectivity for several kinds of amino acids [142]. By changing the type of noble metal precursor and the amount of co-existing alumina, they reported the possible control of the Pd particle size immobilized on alumina by ultrasound irradiation [143]. With prolonged sonication, Pt, Au and Pd nanoparticles, sonochemically prepared, were immobilized onto TiO_2. Prepared catalysts were used as the photocatalysts in H_2 production from ethanol. The activity of the prepared catalysts was dependent on the dimensions of supported nanoparticles and they were in general more efficient than catalysts synthesized by conventional methods [144]. After extended work where metallic amorphous nanoparticles such as Ag, Au, Pd and Pt were coated on various substrates as silica spheres, carbon spherules, titania and alumina [145-148], V. Pol et al. synthesized nanocrystalline Ag, Au, Pd and Pt via ultrasound irradiation and deposited them on polystyrene spheres [149]. Pt nanoparticles were greatly dispersed and embedded into CeO_2 nanopowders by an ultrasound assisted reduction process and used as catalysts for the ethyl acetate combustion, reaching complete conversion at low temperature. It was

further concluded that the performance of the synthesized catalyst was dependent on the dispersion of Pt in the ceria support and due to the homogeneous incorporation of 2-4 nm Pt particles these catalysts demonstrated much better activity than those ones obtained by the traditional incipient wetness impregnation method [150].

1.3.5 Synthesis of different transition metal compounds

As already explained (Fig. 1.4), it is possible, with a simple variation of the additives present in the initial precursor solution, to obtain different metal compounds dependent on the final desired application of a certain material. Showing similarity in activity with Pt group metals, Mo and W carbides were studied as possible heterogeneous catalysts [151-153]. Sonochemically prepared Mo_2C and WC were often compared, in selectivity they demonstrate for dehydrogenation of alkanes, to Ru and Pt [93]. MoS_2 is the best known as the standard automotive lubricant [93] and is also the predominant hydrodesulfurization catalyst heavily used by the petroleum industry to remove sulfur from fossil fuels before combustion [154]. Sonochemical synthesis of amorphous MoS_2 from a solution of molybdenum hexacarbonyl and sulfur in 1,2,3,5-tetramethylbenzene with unusual morphology was reported [155]. It was also demonstrated that the sonochemically prepared MoS_2 catalyzes the hydrodesulfurization (HDS) of thiophene with activities roughly five-fold better than conventional MoS_2 and comparable to those observed with RuS_2, one of the best commercial catalysts. S. Nikitenko et al. [156] obtained amorphous WS_2 by ultrasound assisted decomposition of $W(CO)_6$ in diphenylmethane (DPhM) and in the presence of sulfur. From the amorphous material after heating at 800 ºC in Ar inert atmosphere nanorods and their agglomerates of WS_2 were obtained. They were 3-10 nm in thickness and 1-5 mm in length. Further, J. Lu and co-authors used ultrasonic irradiation to synthesize in a safe way transition metals (Fe, Co and Ni) monoarsenides, from the reaction of transition metal chlorides, arsenic (which is the least toxic arsenic feedstock) and zinc in ethanol [157]. They could, due to their unusual physical properties, be used as semiconductors.

Some of the important areas where the sonochemical method can be used have been presented. In some of them this technique dominates above all other known methods. It is very important to emphasize that sonochemical reactions and consequently the obtained products as well as their structure and properties can be controlled depending on their future application.

The main characteristic of materials obtained under sonication is that they are mainly nano-sized and with appropriately chosen precursors amorphous. This leads to materials with large surface area and improved catalytic properties. It has been proven that some of sonochemically obtained catalysts are much more efficient comparing with those prepared with other techniques. In this way lowering of the content of expensive materials such as noble metals is possible without loosing of catalytic efficiency.

1.4 Ultrasound in electrochemistry-Sonoelectrochemistry

Electrochemistry is a field of physical chemistry studying chemical properties, reactions and equilibrium states in ionic conductors (electrolytes) and at the interface between electrolytes and electronic conductors (electrodes). In an electrode process conversion between electrical and chemical energy occurs and the main carriers are charged species, electrons or ions. The flow of these charged species, electrons in an electrode or ions in an electrolyte, produces electric current *I*, given as a function of charge *Q* and time *t* [158]:

$$I = \frac{dQ}{dt} \tag{1.4.1}$$

The electrode processes take place at the interface between electrolyte and electrode where the double layer is formed and due to an unbalance in electric charge a potential difference is established. These potential differences are further correlated with thermodynamics and kinetics of electrode reactions. Basically, manipulation of potential differences at the interface allows an external control of an electrode reaction. According to Faraday's law, the mass of the substance *m* altered in one electrode process can be quantitatively presented as:

$$m = \frac{Q}{F}\frac{M}{z} \tag{1.4.2}$$

where *F* is the Faraday constant (96485 $Cmol^{-1}$), *M* is the molar mass and *z* is the number of the transferred electrons.

In an electrochemical experiment on typically uses the three electrode setup consisting of the working electrode WE, the electrode of interest, where the electrode process occurs, the reference electrode RE with a constant potential and the counter electrode CE, whose electrochemical properties do not influence the working electrode. The potential is measured between WE and RE and the current between WE and CE. Since the potential of the RE is constant, any change in a cell potential is due to the changes in the WE potential.
A redox reaction occurring at the working electrode can be generally written as:

$$\sum \nu_{iO}\, O + ze^{-} \rightleftharpoons \sum \nu_{iR} R \tag{1.4.3}$$

where O is the oxidant, R is the reductant and ν_{iO} and ν_{iR} are the stoichiometric coefficients.

A correlation between the activities (concentrations) of the electroactive species and the electrode potential in equilibrium is given by the Nernst equation [159]:

$$E = E^0 + \frac{RT}{zF} ln \frac{\prod a_O{}^{\nu_O}}{\prod a_R{}^{\nu_R}} \quad (1.4.4)$$

where E^0 is the standard electrode potential, R is the gas constant, T is the temperature, a_O and a_R are the activities of the oxidant O and reductant R and ν_O and ν_R the stoichiometric coefficients.

Neglecting activity coefficients, the Nernst equation is expressed as:

$$E = E^0 + \frac{RT}{zF} ln \frac{\prod c_O{}^{\nu_O}}{\prod c_R{}^{\nu_R}} \quad (1.4.5)$$

where c_O and c_R are concentrations of the oxidant (O) and reductant (R) at the electrode surface, respectively.

The potential of the electrode is connected with energy of electrons. Driving the electrode to a more negative potential leads to the raising of electron energy and flowing of the current from the electrode to the electrolyte – a so called cathodic current. In contrary, a more positive potential leads to the current flow from the electrolyte to the electrode and therefore to an anodic current. The critical potentials where these processes occur are connected with standard electrode potentials E^0 [159].
In dynamic equilibrium state, the rate of the reduction reaction is equal to the rate of the anodic reaction. The net current is 0 and the potential is the equilibrium potential given by the Nernst equation. When the potential is different from the equilibrium one, the rates of the reduction and oxidation reactions are not the same and there is a net current flowing. Several possible steps lead to an electrode reaction:

1. Electroactive species have to be brought to the electrode-mass transfer process
2. Charge transfer at the electrode/electrolyte interface
3. Homogeneous or heterogeneous chemical reaction following the charge transfer
4. Surface reactions-adsorption, desorption…

There are three forms of mass transfer: migration (movement of the charged body under electrical field influence), diffusion (movement of a species due to a concentration gradient, or, more accurately, a gradient in chemical potential) and convection (can be natural-caused by density gradient and forced).
The rate of the electrode reaction is determined by the rates of processes included. The magnitude of the current is generally limited by the slowest process-rate determining step.
One simple electrode reaction consists of mass transfer of the electroactive species to the electrode, charge transfer at the electrode/electrolyte interface and mass transfer of the formed species to the bulk solution.

When the transfer of the charge carriers through the electrical double layer is the only factor influencing reaction rates, the net current flow is given in a function of the potential by the Butler-Volmer equation:

$$j = j_a + j_c = j_0 \left[\frac{c_R}{c_R^*} exp\left(\frac{\alpha z F \eta_D}{RT}\right) - \frac{c_O}{c_O^*} exp\left(-\frac{(1-\alpha) z F \eta_D}{RT}\right) \right] \quad (1.4.6)$$

where j is the current density (current per area of the electrode) given as the sum of the anodic and cathodic current densities j_a and j_c, j_0 is the exchange current density (measure of the anodic and cathodic partial reaction rates in equilibrium), c^* concentrations of the reductant R and oxidant O in bulk solution, α is the transfer coefficient or barrier symmetry factor and η_D=*E(i)-E(i=0)* is the activation overpotential.

For high overpotentials one part of the Butler-Volmer equation can be neglected (depending on which overpotential is high-anodic or cathodic) and the equation can be simplified and a logarithmic dependency between current and overpotential is obtained and given as Tafel equation:

$$\eta_D = a + b \log j \quad (1.4.7)$$

where $a = log j_0 \cdot RT/\alpha F$ and $b = RT/\alpha F$.

When the charge transfer reaction is fast, a concentration gradient is formed and mass transfer starts to play an important role. With adding the supporting electrolyte in concentrations much higher than the concentration of the electroactive species, one can usually neglect migration as a mode of mass transfe r and the net current is given via law of diffusion as:

$$j = zFJ = -zFD \left(\frac{\partial c(x,t)}{\partial x}\right)_{x=0} \quad (1.4.8)$$

where J is the charge flux given by the Fick's first law of diffusion: $J = -D \left(\frac{\partial c(x,t)}{\partial x}\right)_{x=0}$, D is the diffusion coefficient and x is the distance from the electrode.

At moderate overpotentials, a relation between the electrode potential and the concentration of the electroactive species is given by the Butler-Volmer equation for a small exchange current density and by the Nernst equation for a large exchange current density.
At high overpotentials due to the very fast charge transfer kinetics, the concentration of the electroactive species at the electrode can be assumed to be 0 and current is given as follows:

$$j = -zFD \frac{c^*}{\delta} \quad (1.4.9)$$

where δ is the diffusion layer thickness.

Furthermore, in the cases when the dependence of the diffusion layer thickness on the time has to be taken in account and there is no natural convection, the current for the diffusion limiting conditions for a planar electrode is expressed by the Cottrel equation:

$$j(t) = \frac{zFAD^{1/2}c^*}{\pi^{1/2}t^{1/2}} \qquad (1.4.10)$$

For the study of one electrochemical system one usually starts with cyclic voltammetry (CV). This electrochemical method allows observing the basic characteristics of a studied system giving first informations about the mechanism of the electrode reactions and kinetic parameters in a relatively short period of time. The method is based on the variation of the working electrode potential with a fixed rate (scan rate) between an upper and a lower potential limit. The starting potential is usually chosen with respect to an open circuit potential, where no net reaction takes place, thus no current flows. The recorded cyclic voltammogram shows the current response of the system as a function of the electrode potential. The potential of the electrode and the electrode kinetics determine the shape of the cyclic voltammogram. When the potential is sufficiently below the equilibrium one for a certain reaction, current starts to flow and it increases with change in potential. With time electroactive species at the electrode are consumed and it comes to their depletion near to the electrode and the current starts to decrease due to the lower concentration gradient. The layer where the concentration gradient in the vicinity of the electrode changes is called the diffusion or Nernst layer and it is growing with the time at stationary electrodes without forced convection. In praxis, it is found for the diffusion layer to have an upper limit due to the natural convection developed at the electrode stimulated by the developed density gradient.

For the study of the reaction mechanism of the redox reactions where mass transfer has a significant influence, one of the hydrodynamic techniques commonly used in electrochemistry is the rotating disc electrode (RDE) setup. Due to the forced convection generated by the rotation of the working electrode and the laminar flow of species toward the electrode, the mass transfer is faster and has less influence on the electron transfer kinetics. The diffusion layer thickness is constant with time and dependent on the rate of the electrode rotation. The current increases in the beginning when lowering the potential (for a reduction reaction) but steady state conditions are reached relatively fast and the current reaches a maximal value and becomes constant not depending on potential any more. This maximal value for the current is known as the limiting current and is dependent on the rotation rate.

The correlation between the limiting current and the rotation rate is given by the Levich equation for the totally mass-transfer limited conditions. The limiting current or Levich current is proportional to c_0 and $\omega^{1/2}$ and described as follows:

$$j_{l,c} = 0.62zFD^{2/3}\nu^{-1/6}\omega^{1/2}c_O^* \qquad (1.4.11)$$

where *v is* the kinematic viscosity, ω is the angular rotation rate ($\omega = 2\pi f$), and c_0 the bulk concentration of the electroactive species.

From a so-called Levich study (a series of rotating disc voltammograms for different rotation rates) one can plot the measured j_l versus $\omega^{1/2}$ and obtain the Levich plot. One could expect a straight line when limiting behavior is reached for all applied ω and from the slope the calculate diffusion coefficient.
The diffusion layer thickness δ could be calculated as well:

$$\delta = 1.61\omega^{-1/2}\nu^{1/6}D^{1/3} \qquad (1.4.12)$$

When there is a mixed kinetic and mass transport control at the RDE, the Koutecký-Levich equation can be used and it is given as:

$$\frac{1}{j} = \frac{1}{j_k} + \frac{1}{j_{l,c}} = \frac{1}{j_k} + \frac{1}{0.62nFAD_0^{2/3}\omega^{1/2}\nu^{-1/6}C_0^*} \qquad (1.4.13)$$

where j_k would be the current in the absence of any mass transport effects, when the concentration at the electrode would be equal to the bulk concentration and the current would flow under the kinetic limitation. Similar as with the Levich plot, a plot *1/j* versus $1/\omega^{1/2}$ gives the Koutecký-Levich plot, which also allows determination of the kinetic parameters.

Electrochemical methods can be employed for the synthesis of a broad spectrum of materials. By varying the conditions during electroplating of metals, alloys and metal ceramic composites, it is possible to control the microstructure dependent on the future application. When ceramic particles are present in the metal electrolyte, the co-deposition of metal-ceramic composites can be done. Further, synthesis of materials applied in electrochemical devices, such as electrolytes and electrodes for fuel cells and batteries, is possible.
Due to the number of complex phenomena caused by power ultrasound introduced in a liquid media such as active radical species generation, turbulent flow [160], bubble oscilation and cavitation [161], microjets and shock waves generation and especially effects caused at the solid–liquid interface due to the asymmetric bubble collapse[162], ultrasound found the place in electrochemistry as well. Specific areas of application include electroplating [163, 164], the deposition of polymer films [165, 166] and electrosynthesis [167, 168]. In turn, electrochemical experiments with microelectrodes are exploited for the study of the acoustic cavitation and other phenomena occuring in an ultrasound field [169, 170]. Besides a possible insertion of the electrochemical cell in an ultrasonic bath [171-173], ultrasound can be more directly introduced to a cell using a so-called horn probe. The electrochemical cell can be divided in a part where the electrochemical setup is placed and is separated from the horn by a glass separator [174] or a polymer coating [175]. Still, the largest effect is gained when the horn

probe is directly immersed in the solution where an electrochemical reaction is taking place. Aside from the so-called "side on geometry" [176], usually the "face on" geometry, where the ultrasonic probe is face to face to the working electrode, is used. Distances between horn and electrode vary in a range of 1-80 mm, found to be the best for the purpose of the deposition of different materials, metals, alloys, and composite coatings.

Similar to equation 1.4.11, a correlation between limiting current j_{lim} and ultrasound intensity I_a has been reported and verified in literature [170, 177, 178]:

$$j_l = Kd^{-1/2}A^{1/2}D^{2/3}cI_a^{1/2} \quad (1.4.14)$$

where K is a constant depending on v, A is the tip (planar circular are on the bottom of the horn) area and I_a the ultrasonic intensity.

Local mass transport at the electrode is often recognized as the critical parameter for the electrochemical deposition of metals and alloys. Depletion of the electroactive species and growing of the diffusion layer thickness can lead to enhanced side reactions and possible deposition of metal hydroxides [179]. During propagation of the ultrasound waves through a viscous liquid, due to the formed sound pressure field and repeated cavitational bubble collapse, turbulent convection is formed. Momentum being absorbed by the liquid media and manifested as turbulent flow in the direction of the sound field is described as acoustic streaming [180, 181] and is reported to cause local flow rates of more than 10 m/s [182]. In electrochemical systems, ultrasound causes enhanced mass transport regime and it is presumed that the diffusion layer at the electrode is thinned. Mass transport to an electrode in the presence of the ultrasound can be described by equation 1.4.14 [181]. Ultrasound, causing a decrease of the diffusion layer thickness formed near the electrode and diminishing of the electroactive species depletion provides the possibility to control electrochemical deposition mechanism at the electrode [179]. This has more significance in the low concentrated solutions which run easier into diffusion limitation regime. In the presence of the ultrasound it is found that obtained deposits have changed and mainly improved properties [173,182].

Furthermore, ultrasound is responsible for surface cleaning and thus electrode surface activation but also for roughening end erosion of the electrode [173,183], caused by acoustic cavitation close to the electrode surface and then also microjets in the vicinity and/or at the electrode surface. Presence of the ultrasound and caused phenomena are responsible for the change in local temperatures, which can further influence processes of nucleation and growth and speed up electrode reactions. In more concentrated solutions, with charge transfer control, ultrasound influence is reported to be less pronounced [182]. For the studied systems, no obvious direct influence of the ultrasound on the simple electron transfer was reported and that the rather dominant effect of ultrasound is enhanced mass transport [184].

More advanced in the sonoelectrochemical setup is the use of the horn tip, normally a planar circular surface at the bottom, as an electrode after it has been electrically insulated from the rest of the horn (sonotrode) [185]. This setup is frequently employed in many research works [186]. In addition, the applied pulsed mode permits production of nanomaterials [187]. The principle of the method lies in the interplay between short successive electrical and ultrasonic pulses. First an electric pulse is applied causing the formation of many small nuclei on the horn tip, the growth of which can be controlled by the pulse length, and then an ultrasonic pulse, which bursts the formed deposit into the solution. With the addition of appropriate surfactant to the solution it is possible to obtain a stable colloidal suspension of nanosized particles [188].

1.4.1 EQCM

The quartz crystal microbalance (QCM) is a well-known technique which has been used for a long time to monitor thin film deposition in gas or vacuum [189, 190].With the extended use of QCM in liquid systems the number of applications significantly increased [191-193]. A quartz crystal is an acoustic based sensor device capable of detection mass changes in ng range by monitoring changes in oscillation frequency [194].The method is based on the piezoelectric behavior of the quartz crystal.

Piezoelectricity is the ability of certain crystals to respond to an applied mechanical stress by generating an electrical potential difference across the crystal with a quantity proportional to the applied mechanical stress. This phenomenon was discovered in 1880 by Jacques and Pierre Curie. Soon after the initial discovery the converse piezoelectric effect was experimentally proved. When a voltage is applied across piezoelectric crystals their mechanical deformation is caused and this effect is employed in the QCM technique [195]. Typical piezoelectric crystals are quartz, lithium niobate [196], langasite [197] and gallium orthophosphate [198]. A precondition for the piezoelectricity is that the space groups in the crystals show no inversion symmetry. Due to the crystal symmetry an applied potential of one polarity will induce strain and shear motions of the crystal in one direction and of the opposite polarity in the opposite direction. The magnitude of the strain in the crystal is proportional to the applied potential and its direction is determined by the polarity. The application of an AC voltage induces in the case of a properly cut quartz transverse acoustic waves (shear waves). These shear waves can be reflected at the crystal surface back into the quartz [199]. A quartz crystal disc is sandwiched between two electrodes, usually gold electrodes and for a given thickness d_q (quartz with electrodes) a standing wave can be created for a specific frequency, the resonance frequency f_0.

The condition for the formation of a standing wave is that the thickness of the quartz including the electrodes equals half of the wavelength. The resonance frequency then depends on the shear modulus μ_q and the density ρ_q of the resonator, and is given by equation 1.4.15.

$$f_0 = \frac{v_{tr}}{2d_q} = \frac{\mu_q^{1/2}/\rho_q^{1/2}}{2d_q} \quad (1.4.15)$$

where v_{tr} is the transverse velocity of the sound in AT-cut quartz (3.34×10^{-4} m/s).

The QCM is widely used in electrochemical systems for the study of electrochemical interfaces and it is then called EQCM (electrochemical quartz crystal microbalance) [37-40]. In electrochemical experiments one of the electrodes on the quartz is used as the working electrode, whereas the electrode on the other side needs to be isolated from the electrolyte. By applying an alternating potential, oscillation of the quartz at the applied frequency is generated. An oscillator circuit is often used to cause mechanical oscillations of the quartz at its resonance frequency f_0 and a frequency counter for measuring f_0. The resonance frequency of the quartz is sensitive to mass changes of the quartz and its electrodes [32]. During an electrochemical experiment the change in the mass per unit area (Δm) can be calculated from the observed change in the resonance frequency (Δf) of the quartz. An important equation which connects these two parameters is known as Sauerbrey equation:

$$\Delta f = -\frac{2f_0^2}{Z_Q}\Delta m = -\frac{2f_0^2}{\sqrt{\mu_q\rho_q}}\Delta m \quad (1.4.16)$$

where Δf is the frequency change, f_0 is the resonance frequency of the quartz before the measurement, Δm is the mass change and Z_Q is the mechanical impedance of the quartz ($8.849\cdot10^5$ $gcm^{-2}s^{-1}$) determined by the density and shear modulus of the quartz.

This equation shows that an increase in mass leads to a decrease in the frequency and that these values are directly proportional. The Sauerbrey equation enables quantitative determination of mass changes during EQCM measurements [200]. The Sauerbrey equation is derived under certain assumptions and has some limitations. It is valid only for acoustically thin, rigid films, and assumes no slip conditions, i.e that particle displacement and shear stress are continuous across the interface to the deposited layer. Since the mechanical properties of the quartz resonator can be expressed in electrical equivalents, characterization can be done by network analysis. By the measurement of the electrical admittance (impedance) between the gold electrodes in a small frequency range around the resonance frequency the characteristics of the quartz as well as the interaction between the quartz and the contacting medium can be evaluated. The shape of the real part of the admittance (Re(Y)) as a function of the frequency f is a Lorentz type curve (Fig. 1.6) and is characterized by the position of the peak maximum, its resonance frequency f_r, and the full width of the peak at half maximum, which is a measure for energy losses of the quartz crystal due to viscoelastic behavior or roughness called damping, w [201, 202]. If one deposits a layer, and roughness does not contribute significantly to the frequency shift (pure mass response) then peak height and damping will stay the same, and the entire curve is simply shifted to lower frequencies. If the damping increases, it can be detected by broadening of the curve, and if Δw is more than 10% of Δf then the application of Sauerbrey equation

is no longer accurate [203]. Then one characterizes the resonance behavior of the quartz more accurately by definition of a complex frequency shift [204].

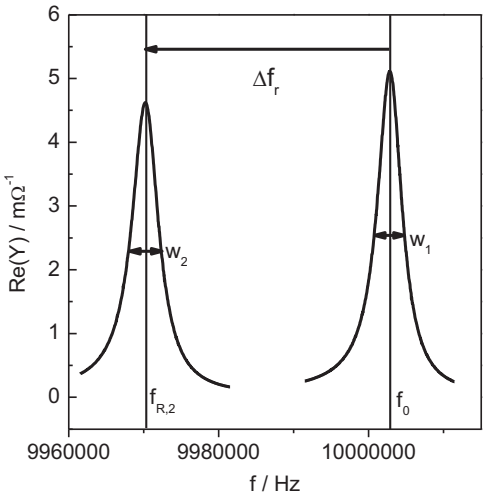

Figure 1.6 Real part of the quartz resonator admittance in the vicinity of the resonance frequency f_0 before any deposition (right curve) and after deposition (left curve), with marked damping w (width of the peak at a half peak height).

EQCM gives the advantage to obtain mechanistic information about film deposition and dissolution, surface morphology changes, and mass changes in thin films caused by redox or other chemical processes in addition to electrochemical data [32, 201]. When one assumes that simple metal electrodeposition without side reactions is taking place on the electrode, thus that the current efficiency is 100%, the ratio of mass density (mass per area) and charge density can be calculated from Faraday's law:

$$\frac{\Delta m}{\Delta Q} = -\frac{M}{zF} \tag{1.4.17}$$

where Δm is the measured mass change and ΔQ the charge flux, M is the molar mass.

On the other hand, EQCM data provide both the mass change and the total charge flux obtained in the electrochemical measurement, thus also their ratio. When the value of this ratio, obtained from the experimental data, is compared to the calculated ratio, the current efficiency can be calculated.
From these mass/charge ratios it is possible also to conclude about the nature of the species deposited, ion exchange processes (e.g. in polymers), and mechanisms of electrochemical reactions. Further at known molar mass the number of transferred electrons per deposited metal atom can be determined.
Due to the dependence of the measured parameters on the potential and time, integral values can be replaced with differential values and in that way the obtained parameters can be determined time or potential dependent [205].

$$\frac{dm}{dQ} = \frac{1}{i}\frac{dm}{dt} = -\frac{M}{zF} \tag{1.4.18}$$

If further the mass charge ratio obtained in experiments is compared to the theoretically calculated one, an (apparent) current efficiency ε can be obtained.

$$\varepsilon = \frac{(dm/dQ)_{exp}}{(dm/dQ)_{th}} \Rightarrow \frac{\varepsilon}{z} = -\frac{F}{M}\left(\frac{dm}{dQ}\right)_{exp} \tag{1.4.19}$$

Finally, from the mass change and assuming 100 % current efficiency, a corresponding electrical current can be calculated as:

$$i_M = -\frac{zF}{M}\frac{dm}{dt} \tag{1.4.20}$$

Going back to the initial assumption about having a single reaction taking place on the electrode, one can already presume that for more complicated cases this analysis would not work anymore without considering individual reactions. Then, each reaction would have a certain contribution to the mass and charge. Further, when the current is crossing zero (dQ=0, change from net reduction to net oxidation or vice versa), a mathematic discontinuity appears in Equation 1.4.19 and ε tends to infinity.

Chapter 2-Experimental

2.1 Experimental setup

In the present study, most experiments were performed using a three electrode setup consisting of a working electrode (WE), a counter electrode (CE) and a reference electrode (RE). The experimental setup for most sonoelectrochemical experiments (fundamental study and synthesis of the composites) is shown schematically in Figure 2.1 and is similar to one used in [173]. A home-made Teflon cell, inserted in a steel cooling jacket, connected with a thermostat, served as electrochemical cell. Additional temperature regulation was provided via a glass cooling coil inserted directly into the cell. Usually the volume of the electrolyte used in experiments was 125 ml. Except for the experiments with nickel, done at 50 ºC, all other experiments were done at room temperature of 25 ºC. The quartz resonators (KVG Quartz Crystal Technology) used are AT cut (obtained by slicing of the quartz rod with an angle of ~ 35º with respect to the crystallographic x axis), 169 μm thick and have a resonance frequency of about 10 MHz. They have keyhole shaped Au electrodes (with a Cr adhesion layer underneath) on each side that are used in establishing alternating potential differences across the quartz [206]. Only in the circular part, in the middle of the quartz, there is an electrode on both sides, and only that part of the quartz is piezoelectrically active. The quartz was placed in the bottom of the cell and one of its Au electrodes was exposed upwards to the electrolyte and served as the working electrode (WE). Fluoropolymer (Simriz™) O-rings with dimensions of 10 x 2 mm were employed for the isolation of the backside of the quartz resonators from the electrolyte. All potentials measured in this study are given with respect to an Ag/AgCl (E_0 = 0.197V vs. NHE) reference electrode (RE) saturated with KCl. The counter electrode (CE) was either a high purity copper sheet (Alfa) for measurements in Cu containing electrolytes without deaeration, or a Pt-plated Ti wire (Intrepid Industries) for measurements in Ar atmosphere and for measurements in Cu-free electrolytes.

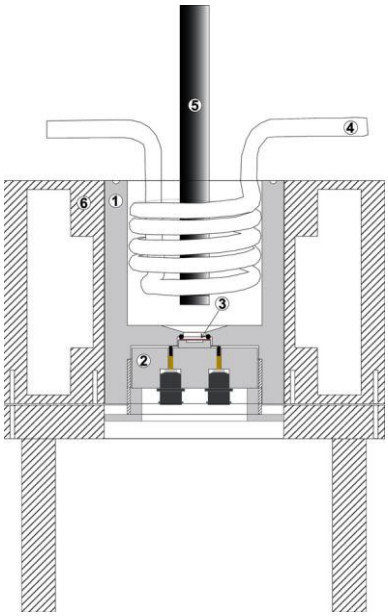

Figure 2.1 Electrochemical quartz crystal microbalance setup for sonoelectrochemical experiments: (1) homemade Teflon cell, (2) contact unit, made from teflon body, and two BNC connectors with soldered Pt foil to provide contact to electrodes on quartz, (3) 10 MHz EQCM quartz and sealing O-ring. Working electrode contact from backside through use of conductive silver paint, (4) glass cooling coil, (5) lower end of ultrasonic horn with tip facing quartz (6) stainless steel cooling jacket serving at the same time as holder for the EQCM cell [38].

A picture of the used sonoelectrochemical setup is shown in Figure 2.2 with an enlarged part where the position of the horn, RE and CE electrode can be closely seen. The reference electrode was placed in a way that there was no shielding from the working electrode through the ultrasonic horn and the counter electrode was placed in a way not to be between the horn and WE.

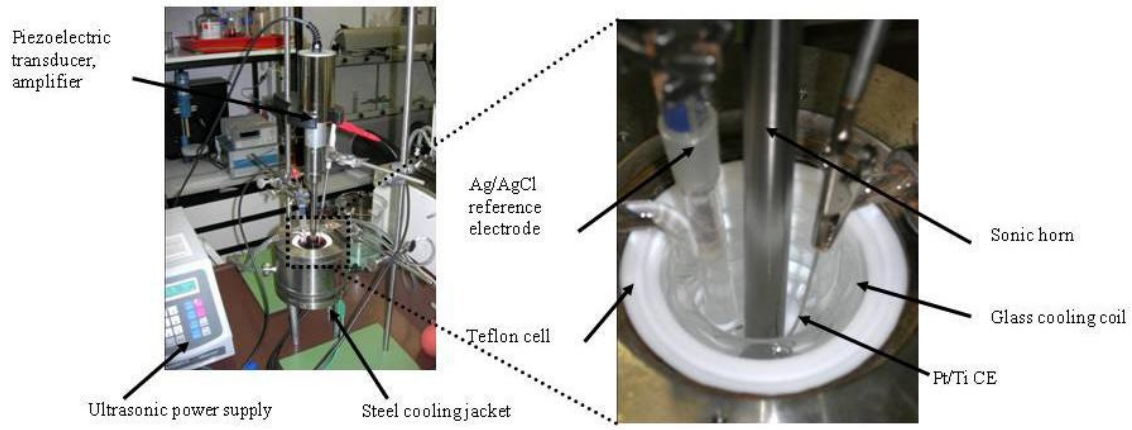

Figure 2.2 Photo of the sonoelectrochemical setup with cobalt solution (left) together with an enlarged part of the setup in Teflon cell without solution (right).

An ultrasonic horn probe, Ti-6Al-4V alloy (full wavelength probe, 20 kHz) with a planar exchangeable tip (area 1.2 cm^2 or 1.09 cm^2) was placed above the WE in the face-on geometry. The distance between horn and WE was varying between 8, 10, 15 and 22 mm. A part of the experiments was performed in inert gas atmosphere with the entire setup placed in an Ar-filled glove bag. Some of

the experiments, under silent conditions, were done in the Teflon cell closed with a Teflon lid, with openings for reference and counter electrode as well as for argon inlet and outlet and without cooling coil and ultrasonic horn. The cell was continuously purged with Ar before, during and in between experiments. Ar purging was stopped for the duration of the experiment during measurements without ultrasound. The resonance frequency of the quartz f_R and its damping w were determined after the experiments from the spectra by fitting the real part of the admittance to a Lorentz function.

Experiments with a rotating disc electrode setup were done in a five neck glass cell with a water cooling jacket (Pine Research Instrumentation, AFCELL3) under air and under Ar. In these experiments a commercial Pt-disc served as the working electrode, a Pt/Ti-wire as counter electrode and Ag/AgCl as reference electrode. The same cell was also used for the preliminary experiments on the sonoelectrochemical production of colloidal nanoparticles. A planar circular area on the bottom of the ultrasonic horn served as the working electrode and the same reference and counter electrode as in other sonoelectrochemical experiments were used.

A five-neck glass reaction vessel with cooling jacket was used for the sonochemical decomposition of Mo-carbonyl in hexadecane for 3 hours lasting experiment. The sonication probe with a teflon adapter was placed in the central neck. In order to track the temperature change, one of four side-necks was closed with a septum lid through which the temperature sensor was immersed. The sensor was connected to the control unit of the ultrasonic processor and the temperature was directly read from its display. The other side-necks were closed in order to prevent the loss of solvent due to possible evaporation under sonication conditions. In order to provide cooling of the reaction system, the cooling jacket of the vessel was connected to a thermostat adjusted at 22°C. For all other experiments a cylindrical vessel open to air was used. The ultrasonic probe was mounted to be on the half height of the solution (~2 cm from the bottom of the vessel) and there was no temperature regulation of the reaction vessel applied. To prevent the overheating of the transducer, it was wrapped with pipes filled with cooling water.

2.2 Electrochemical techniques used in the study

An open circuit potential measurement (OCP), was normally done for several minutes in the beginning of the electrochemical experiments, in order to check the conditions in the electrolyte.
Linear sweep voltametry (LSV) is one of the potential sweep methods where potential is varied linearly with a time at a constant sweep rate (in a range from a few mV up to about 1000 V/s for conventionally applied electrodes). During LSV measurement the current is recorded and can be presented as a function of time or potential.

Cyclic voltammetry (CV) was done as the starting point for the study of each system (method explained in more details in Chapter 1.4). Recorded cyclic voltammograms provided first informations about the system. The influence of ultrasound on the electrochemical parameters was followed by recording CV's without and with the presence of ultrasound as well as with intensity variation. The influence of ultrasound on the current efficiencies was studied as well.

Electrochemical depositions were done either potentiostatically (at a certain given potential) or galvanostatically (at a certain given current density). At certain given conditions electrodeposition was at first done without ultrasound and thereafter under ultrasound irradiation with different intensities. The morphology of the obtained deposits was examined and they were compared. For the production of nanoparticles pulsed deposition was applied. Metal nuclei were galvanostatically deposited during short electric pulses which were then followed by ultrasonic pulses removing particles from the electrode surface and preventing their growth (more details on the technique are given in Chapter 5.2.1).

Rotating disc electrode (RDE) experiments were done with a variation of the rotation rate between 500 and 3000 rpm (more details on the technique can be found in Chapter 1.4). Influence of the forced convection provided by the rotation of the working electrode was compared with an influence of the acoustic streaming caused by ultrasound waves introduced into the solution.

In EQCM (explained in details in Chapter 1.4.1) measurements the change in the resonance frequency of the quartz resonator was recorded simultaneously to the electrochemical measurements and change in mass was then calculated by Sauerbrey's equation. Additional informations obtained by EQCM were very helpful for the study of the ultrasound influence on electrochemical parameters and especially current efficiencies. Current-less processes such are corrosion and erosion were also easier to follow with data provided by EQCM.

2.3 Solutions used in the study

Preliminary experiments were done in bi-distilled water. Cu plating was performed from sulfate and chloride based electrolytes. 0.01 M $CuSO_4 \times 5H_2O$ (Merck, >99.0 % purity) and 0.1 M $Na_2SO_4 \times 10H_2O$ (Merck, >99.0 % purity), with pH adjusted to ~1 by addition of an appropriate amount of concentrated H_2SO_4, was the electrolyte composition for the sulfate based system. 0.01 M $CuCl_2$ and 0.5 M NaCl (Merck, min 99.5 % purity) with pH adjusted to ~1 by addition of an appropriate amount of concentrated HCl was the composition of the chloride based electrolyte.

For the electrodeposition of Ni/CeO_2 composite, two different electrolyte compositions were used: Watts electrolyte (30 g/l $NiCl_2 \times 6\ H_2O$ (Merck, ≥98 % purity) + 234 g/l $NiSO_4 \times 6\ H_2O$ (Merck, ≥99 % purity)+ 30 g/l H_3BO_3 (Merck, ≥99.5 % purity)+ 3 mg/l sodium dodecylsulfate (SDS) [207]) and a sulfamate bath (100 ml/l of a 50 wt% solution of $Ni(NH_2SO_3)_2$ (Alfa Aesar 50 % w/w aqueous solution)+ 10 g/l $NiCl_2 \times 6H_2O$ (Merck, ≥98 % purity) + 40 g/l H_3BO_3 (Merck, ≥99.5 % purity) [208]).

For the co-deposition in Co system, 0.1 M $CoSO_4 \times 5H_2O$ (Alfa Aesar 98 %) + 0.1 M Na_2SO_4 with pH adjusted to 4 [209] was used.

Sonochemical synthesis of molybdenum oxide was done by decomposition of molybdenum hexacarbonyl $Mo(CO)_6$ (~Alfa Aesar 98% pure) in n-decane (>94% pure) and n-hexadecane (>99% pure) as solvents and in presence of a stabilizer, oleic acid (90% pure), purchased from Aldrich and centrifuged prior to use.

For the pulsed sonoelectrochemical deposition of nanoparticles the following precursors were used: for Au nanoparticles $HAuCl_4 \times 3\ H_2O$ (Sigma Aldrich for analysis), for Ag nanoparticles $AgNO_3$ (Merck for analysis) and for Cu nanoparticles $CuSO_4 \times 5H_2O$ (Merck, >99.0 % purity). Polyvinyl pyrrolidone (PVP K30 Aldrich) was used as the stabilizer.

2.4 Instruments used in the study

Most electrochemical measurements were computer controlled by a Solartron Si1287 electrochemical interface. In parallel to the sonoelectrochemical measurements the electrical admittance spectra of the quartz resonator were measured in the vicinity of its resonance frequency using an Agilent E5100A network analyzer, which had been calibrated before the measurements using a “thru”-calibration (short-circuit) in the entire frequency range applied later on during electrochemistry. For the rotating disc electrode setup a Pine Research Instrumentation controller, AFMSRCE, was employed. In some experiments also an Ivium CompactPlus potentiostat and a Zahner IM5 electrochemical workstation were used.

Ultrasound waves with a 20 kHz fixed frequency were provided by an ultrasonic processor (Sonics VCX 750 or Bandelin Sonopuls HD 3200) connected to electrical power by an isolating transformer. This was necessary in order to prevent the horn to be connected to the ground, which would have shortened it with the working electrode in the electrochemical setup. The power output of the ultrasonic horn was determined using a calorimetric method based on [210]. From the power output the ultrasonic intensity I_a was calculated by dividing the power by the tip area.

2.4.1 Ultrasound equipment

There are two main types of ultrasonic equipment commonly used in a laboratory, ultrasonic baths and ultrasonic liquid processors.

An ultrasonic bath consists of a chamber in which a number of transducers for the ultrasound generation are built. These transducers have a fixed frequency usually in a range of 20-100 kHz. The bath is filled with water or some other appropriate liquid and chemical cells or objects for cleaning are then placed in the bath. Baths are mostly used for the purpose of cleaning and they are quite efficient in this application. Beside the cleaning purpose they are sometimes used for sonochemical reactions

where the reaction vessel is placed in the bath. Still with very low, unequal and fixed intensity they have a lot of limitations in their application for sono(electro)chemical reactions.

Ultrasonic processors, on the other hand, with a much higher intensity are the better choice especially for chemical systems. They consist of three major parts, an ultrasonic power supply or generator, a converter or transducer and an ultrasonic probe or horn [211].

1. The ultrasonic power supply transforms 50/60 Hz electrical power to a high frequency 20 kHz electrical power.
2. Further, this 20 kHz electrical power is by the converter changed into the mechanical vibrations. These converters are based on the piezoelectric effect described above. In ultrasound transducers, zircon-titanate piezoelectric ceramic discs function as piezoelectric materials. An alternating voltage with high frequency is applied to the opposing faces of the discs and they expand and contract with the change in polarity so they vibrate with the same frequency as the applied voltage. This structure is so constructed to resonate at a certain frequency and its length is commonly a half wave length of the resonant frequency.
3. The ultrasonic probes serve to amplify the vibrations generated by the converters. The amplification factor is influenced by the mass ratio between upper and lower part (tip) of the assembly. Depending on the diameter of the tip, the intensity of generated cavitation is different as well as possibly the processed volume of liquid. In the case of a smaller tip the cavitation is more intensive but it is focused in a small area below the tip and the processed volume is small. With a larger tip diameter the cavitation intensity is lower but it can be spread over a larger area and the processed volume is consequently larger. The probes are commercially produced mostly from the high quality titanium alloy Ti-6Al-4V and with lengths (multiple of half of the US wavelength in the alloy) and diameters which are predetermined for certain volumes of liquids. Also some of the probes are produced with ends (tips) which can be replaced with another tip when the old one is damaged, with micro-tips or with boosters and all dependent on the purpose in a certain system. The micro-tips can process small volumes with very high intensity. They can be made as stepped or tapered micro-tips with characteristics appropriate for certain applications. Boosters are additional parts which can be inserted between the converter and the probe in order to increase the amplitude of vibrations at the probe tip and they are recommended for bigger systems or some difficult applications.

In operating with an ultrasonic processor, the ultrasonic probe is directly immersed in the reaction liquid, generating ultrasound waves within the liquid. Adjusting of the reaction vessel geometry as well as positioning of the ultrasonic probe in it is a very important factor in order to adjust the appropriate conditions for the acoustic cavitation induction. It is normally necessary for the probe to be at least one centimeter immersed into the liquid. When a reaction takes place in an open vessel due to the probable evaporation of a liquid it is possible that in one moment the probe vibrates in air. This should not last more than 10 seconds in order to avoid probe damages.

2.4.2 Calibration of the ultrasonic power

For the purpose of the present study, Sonics Vibra Cell (750 W) and Bandelin SONOPULS HD 3200 (200 W) ultrasonic processors were used to produce the ultrasound field. The frequency of the generated ultrasound waves was fixed for both instruments to 20 kHz. Percentage of the probe vibration amplitude (range 20-100 % for Sonics and 10-100 % for Bandelin) is the parameter which was controlled by the instrument. 100 % amplitude corresponds to a maximum vertical displacement of the probe of 124 μm. Output power, delivered to the probe, as the characteristic of the irradiated energy, was then read on the display for the applied amplitude. When ultrasound is introduced into a liquid, under the influence of the possibly developed acoustic cavitation, the irradiated energy is not by default equal to the absorbed one, and only a part of the energy can be really active in the process under study [212]. Thus, it is necessary to determine the truly absorbed ultrasonic power in the liquid and connect it with irradiated power read from the display, and therefore to perform a calibration. Calibration was prepared for the entire available power range of the instruments. The basis of the calibration was a comparative calorimetric method, taken from the literature [210, 213]. Basically, temperature changes produced by the ultrasound and by an electrical heater were compared. By adjustment of the electric power to produce the same temperature change in the same time as the one produced with ultrasound irradiation, the really absorbed acoustic power can be determined without knowing the accurate heat capacity of the system. Furthermore, properties of the reaction vessel and all present objects as well as heat transport to them do not have to be known, since the used setup (the system) is the same during sonication as well as during heating with the electrical heater. A home-made electrical heater was completely immersed into the liquid and stayed together with the ultrasonic horn in the liquid during all measurements.

This system is schematically presented in Figure 2.3.

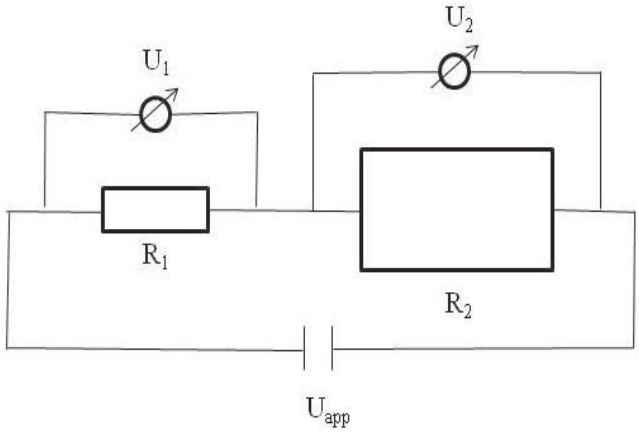

Figure 2.3 A scheme of a circuit consisting of a small resistor R_1 with voltage U_1 across in series with the heating wire with a resistance R_2 with voltage U_2 across and the overall applied voltage $U_{appl}=U_1+U_2$.

R_1 is a small resistor with a specified resistance connected in series with the heating wire. The voltage U_1 was measured across the small resistance and U_2 across the heating wire. The power of the electrical heater was calculated as $P_{el}=U_2 \cdot U_1/R_1$ (in more details in Annex 1). Via the power supply the applied voltage and thus electric power were varied. An Agilent 34970A data acquisition module with a 34901A multiplexer unit was used for measuring voltages.

In order to prevent an unequal temperature distribution in the liquid, it was constantly stirred with a magnetic stirrer during the measurements. Calibration measurements were done in the cell used for the studied processes, to avoid deviations possibly caused by change in dimensions and the shape of the cell. A Pt100 thermoresist served for the temperature measurement. A measuring converter transformed the resistance changes in a way that the temperature range of 0-100 °C corresponded to a voltage output of 0-10 V.

Calorimetric procedure:

1. The ultrasound processor was turned on for a short time t_{US} (normally 8 to 10 s) and the temperature change ΔT_{US} was recorded.

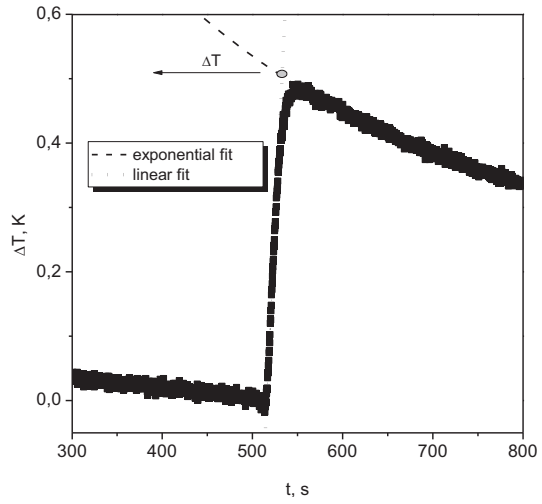

Figure 2.4 Recorded temperature change during ultrasound irradiation with 40 % amplitude of the Bandelin processor. Dot line-linear fit, dash line-exponential fit and intersection of fits gave ΔT.

In Figure 2.4 the typical determination of ΔT_{US} from the plot of temperature change with time is shown (example for 40 % amplitude). A linear part during heating up and an exponential part during cooling down can be distinguished. From the intersection of the linear and exponential fit curves ΔT_{US} was read on the y axis.

2. After cooling of the solution, the electrical heater was turned on for the same time and a similar curve was obtained for the electrical heating as for ultrasound and ΔT_{el} was recorded and determined in the same way as ΔT_{US}.

3. The electric power was varied (by varying applied voltage), and for each applied power ΔT_{el} was recorded and afterwards a plot of the electric (heating) power versus temperature change was made.

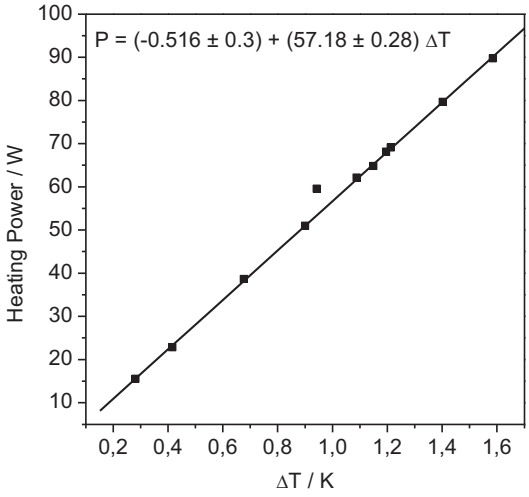

Figure 2.5 The electric (heating) power in the function of the temperature change (with line-linear regression) for the Bandelin processor.

4. From the temperature change measured during ultrasonic irradiation and from the corresponding heating experiments P_{direct} was determined.

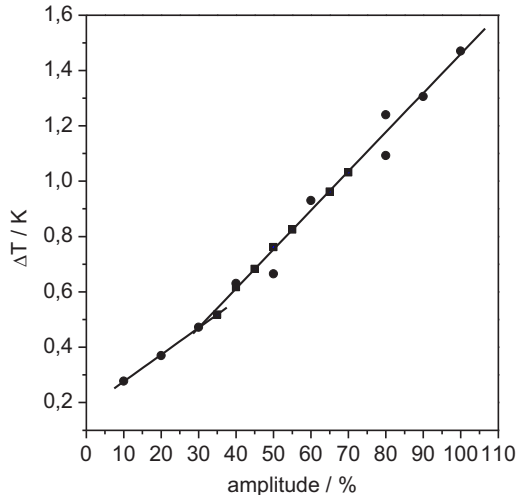

Figure 2.6 Power P_{direct} obtained from the temperature change of ultrasonic irradiation and corresponding heating experiment. Squares were measured first in a limited range and later another set of measurements (circles) at extended range of ultrasound amplitude was performed. The red lines represent linear regressions.

5. Power P_{inter} was determined from a linear regression of the ΔT vs amplitude curve and application of the heating power - ΔT regression.

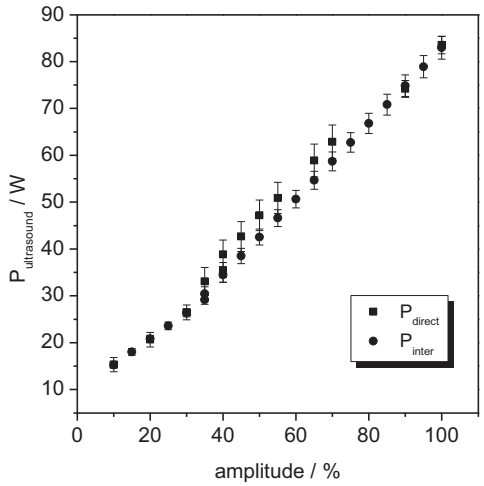

Figure 2.7 Ultrasonic power (P_{inter}) and heating power (P_{direct}) given in function of the amplitude.

A Table with ultrasonic powers obtained by the calibration is given in Annex 1.

2.5 Characterization methods

The morphology of the obtained Cu deposits was characterized by scanning electron microscopy (SEM) and the composition by energy dispersive X-ray spectroscopy (EDX) done on the CamScan instrument. For the co-deposits Ni/CeO_2 and Co/CeO_2 electron probe microanalysis (EPMA) was used as well and was done on a Cameca SX100 Electron Microprobe. The deposit thickness was determined by profilometry (Tencor Alpha-Step 500 Surface Profiler).

The Dynamic Light Scattering (DLS) technique was applied for the determination of the particle size and distribution of colloidal Cu, Ag and Au nanoparticles and was done on the Malvern Zetasizer Nano Instrumentation.

For the characterization of Mo-oxides X-ray diffraction technique was applied and done on the Siemens Diffractometer D5000. Transmission electron microscopy (TEM) of the colloidal samples of Mo oxide was carried out in a JEOL-2000 EX microscope operating at 200 kV.

Chapter 3-Fundamental study

EQCM in an ultrasound field

The quartz crystal resonator used in the EQCM technique is an acoustic wave based device and it is very sensitive to mechanical disturbances. Ultrasound, introduced in a liquid, is the source of acoustic cavitation and acoustic streaming, both possibly developed at and directed towards the electrode. The idea to combine EQCM and ultrasound was therefore not straightforward and it was necessary to prove that it is possible at all. With this aim an experimental study was at first carried out in distilled water. For the next step in the study, copper electrodeposition from a sulfate based electrolyte with a low Cu concentration was chosen, because of the well explored basic mechanisms involved. Further, the more complicated case of copper electrodeposition and –dissolution in a solution with excess chloride ions concentration is discussed.

3.1 Study in water

3.1.1 Resonance spectra of the quartz in an ultrasound field

With the setup shown in Figure 2.1, but without CE and RE, measurements of the quartz admittance with time were performed while the quartz to horn distance was varied between 8, 10 and 22 mm. A set of experiments was done for distances *d* of 22 and 10 mm with a variation of the ultrasound intensity and one experiment, with the highest ultrasound intensity was done for the 8 mm quartz-horn distance. It was shown in literature that the area below the ultrasonic horn, the so-called "near field" (less than 30 mm) is the most important zone for the sonoelectrochemical processes [214].

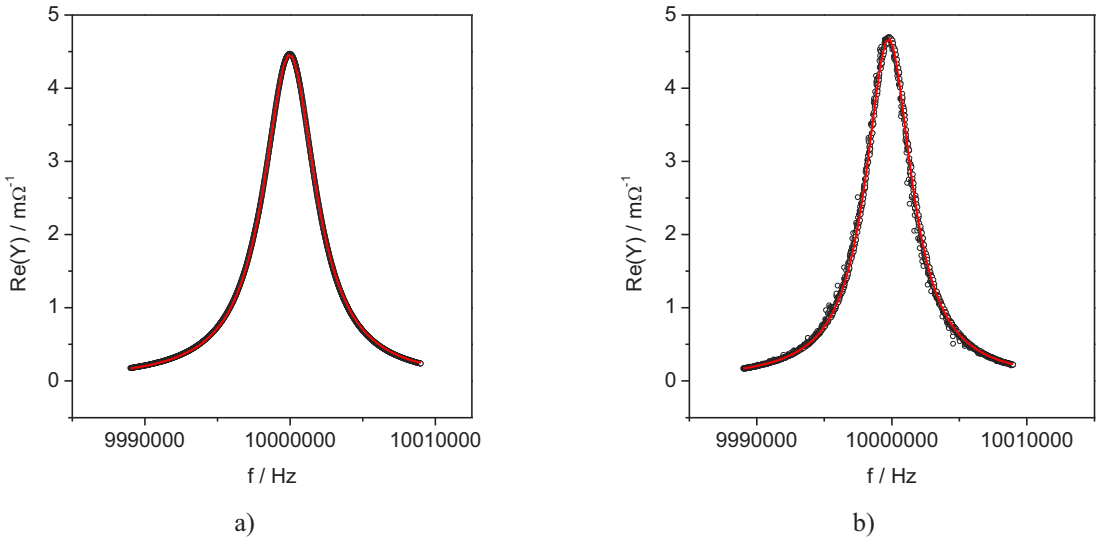

Figure 3.1 Real part of the quartz admittance measured in distilled water a) under silent conditions and b) at I_a = 76 Wcm^{-2} and d = 10 mm. Lorentz fits are represented as red lines.

For d = 10 mm the real part of the admittance of the quartz resonator under silent conditions and in the presence of ultrasound at I_a = 76 Wcm^{-2} are compared in Figure 3.1.

Under silent conditions the curve of the real part of the admittance matched almost perfectly the Lorentz fit. Under the influence of the ultrasound, the admittance curve remained the same in shape, but became noisier and the maximum slightly shifted to a lower frequency. Acoustic streaming, normally turbulent by nature, could be a possible explanation for the recorded noise. Still, there was no significant impact of the noise on the fitting of the admittance curve and it could be very well described with the Lorentz fit. Due to the relatively small distance between the quartz and the horn, the mechanical pressure developed on the electrode by the ultrasound energy (especially the acoustic streaming) can explain the small frequency shift.

3.1.2 The frequency and the damping change in an ultrasound field-Distance variation

After verifying that the quartz admittance could be measured and analyzed in the presence of ultrasound, the next step was to check how the resonance frequency and the damping behave and change with time in the presence of ultrasound. These changes are exemplarily presented in Figure 3.2.

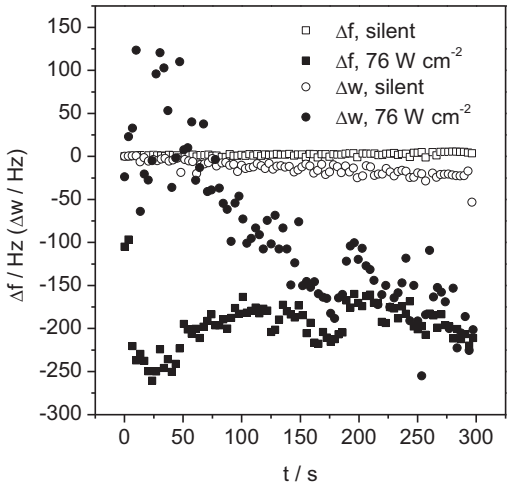

Figure 3.2 Resonance frequency (squares) and damping (circles) measured in distilled water under silent conditions (empty symbols) and at I_a = 76 W cm^{-2} and d = 10 mm (full symbols).

As one could expect, there was almost no frequency change and a negligible change in the damping under silent conditions. In the presence of the ultrasound the resonance frequency of the quartz resonator decreased (Δf calculated with respect to f_0 before turning on the ultrasound) and the change reached a maximal value of around -260 Hz. As mentioned above, the decrease in the resonance frequency was probably a result of the mechanical pressure of the streaming liquid towards the electrode and thus slower oscillations of the quartz resonator. This is similar to the behavior of quartz resonators under static pressure, where a similar decrease in the resonance frequency has been reported

in literature [215]. In the beginning of the experiment the resonance frequency rapidly decreased and then with some fluctuations the frequency changes leveled off at about -200 Hz. This was a hint to expect possible fluctuations in the beginning of the measurements. Therefore, one should, preventively, turn on the ultrasound before real measurements start and in this way avoid a very noisy signal and false results. Afterwards, when the frequency response is stable, the electrochemical experiment can start. For the damping, a similar situation under ultrasound influence is observed, an increase in the beginning and then a continuous decrease with time.

As a next step, Figure 3.3 shows the influence of the distance *d* between quartz and horn on frequency and damping of the quartz resonator with time, for d = 8, 10 and 22 mm at I_a = 76 W cm^{-2} in distilled water. For d = 22 mm, the frequency decreased upon turning on ultrasound by ~ 110 Hz. With time it was slightly increasing again and finally leveled off around -56 Hz. At d = 10 mm, as described above, Δf leveled off at -200 Hz. When *d* decreased to 8 mm, the frequency was constantly decreasing with time and started to stabilize at the end of the 5 minute measurement period, with a maximum Δf of around -430 Hz. At the distances of 22 and 10 mm, besides a slight difference in value (~100 Hz), the frequency changed in a similar way and became faster stable than at 8 mm distance. This clearly showed the enlarged influence of the ultrasound irradiation on the frequency with decreasing distance.

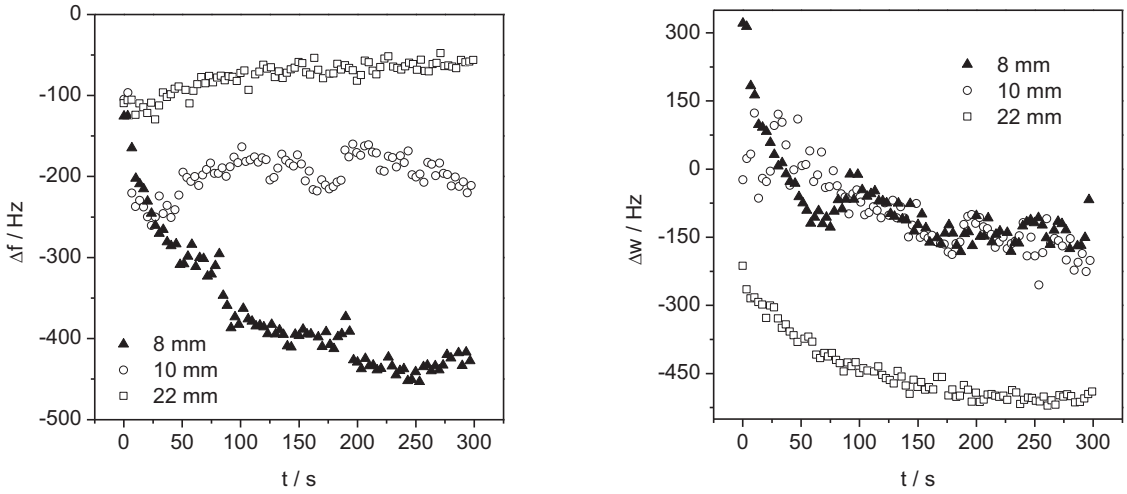

Figure 3.3 The resonance frequency a) and the damping b) of the quartz at 76 W cm^{-2} ultrasound intensity at various distances between horn and the quartz and with respect to the resonance frequency of the same quartz under silent conditions.

The damping for all horn-quartz distances was largest upon turning on the ultrasound and then decreased with time and stabilized. The shape of the admittance curve was not strongly influenced by the change in distance but there was a rather clear influence of the ultrasound irradiation on the frequency with decreasing distance.

3.1.3 The noise of the admittance curve under ultrasound influence

Further, the noise of the admittance curve, which could be determined from the standard deviation of the fits of the admittance spectra to the Lorentz function, was followed with respect to the ultrasound intensity and the horn-quartz distance. With an increase in the ultrasound intensity and a decrease in the horn-quartz distance the noise was increasing (Fig. 3.4).

At 22 mm distance, the noise increased more than 10 times and at 10 mm even 30 times with increasing ultrasonic intensity. The observed noise did not have a significant impact on the Lorentz fit of the admittance curve. Except extreme noise in resonance spectra in the beginning of some experiments upon turning on the ultrasound there was no big influence on the shape and quality of the resonance spectra of the quartz resonator. For the higher ultrasonic intensities and smaller horn-quartz distances, extreme noise appeared in the beginning but after a few moments the resonance frequency was normally stable.

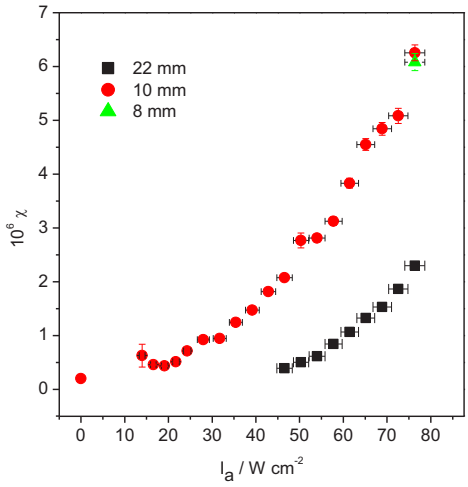

Figure 3.4 Standard deviation of Lorentz peak fit of quartz admittance spectra measured at different ultrasonic intensities and horn-quartz distances.

3.2 Studies in a copper sulfate - based electrolyte

Due to the well explored and discussed basic mechanism [201, 205] the copper sulfate system was chosen for further study. A low concentrated copper solution, 0.01 M $CuSO_4 \times 5H_2O$ and 0.1 M Na_2SO_4 (pH adjusted to ~1 by addition of an appropriate amount of concentrated H_2SO_4), was used. An initial study, done in a sulfate-based Cu electrolyte, was actually an extension and further development of the basic study in distilled water. Open circuit measurements, on the bare quartz as well as on deposited copper layers, with "pulsed" ultrasound (i.e. on/off cycles) were done in order to check if there is a change in the resonance frequency and the rest potential upon turning on ultrasound and how significant these changes are. Furthermore, the influence of the ultrasound intensity was studied as well.

3.2.1 Open circuit measurements with pulsed ultrasound on the bare quartz

In a first experiment, the open circuit potential of the bare quartz in the Cu electrolyte was measured for 10 min, and the behavior of the resonance frequency was followed during the measurement. Ultrasound with an intensity of 29 Wcm^{-2} was applied in the pulsed mode. The pulse length of the ultrasound was 30 s, as well as the time under silent conditions ($t_{on} = t_{off} = 30$ s). Figure 3.5a shows the change in the resonance frequency (with respect to $t = 0$ s) upon application of the ultrasound.

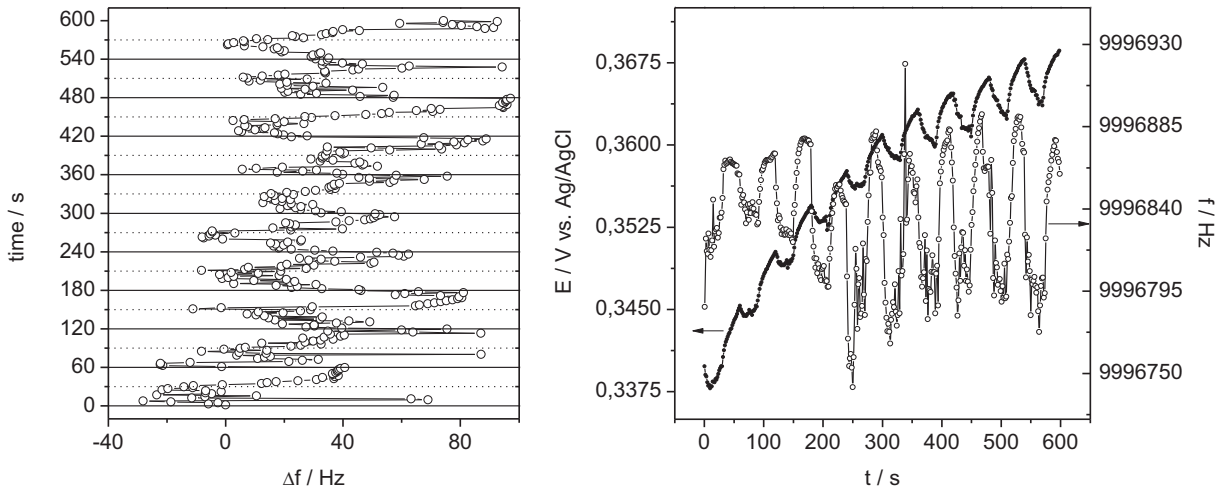

Figure 3.5 a) Frequency change during open circuit potential measurement of the bare Au electrode of a quartz resonator in 0.01 M $CuSO_4$, 0.1 M Na_2SO_4, pH ~ 1, the presence of air with pulsed ultrasound of I_a=29 W cm^{-2}, $t_{on} = t_{off}$ = 30 s, d = 22 mm (solid lines-ultrasound on, dotted lines-ultrasound off) b) corresponding potential changes.

The solid lines parallel to the abscissa indicate when ultrasound was turned on, and the dashed lines when it was turned off. As soon as the ultrasound was turned on, the resonance frequency shifted to

lower frequencies, and gradually increased again after turning the ultrasound off. In the ultrasound field, the frequency was approximately 64±20 Hz lower than under silent conditions.
In parallel to the frequency fluctuations, potential fluctuations in the range of 5 mV (Fig. 3.5 b) were also observed, superimposed to a potential drift of around 30 mV.

3.2.2 Open circuit measurements with pulsed ultrasound on the deposited Cu layer

A group of OCP measurements was performed on Cu layers, potentiostatically deposited for 2 min at a potential of −0.15 V and at different ultrasonic intensities. A set of such experiments with pulsed ultrasound with variation of the intensities was performed. Figure 3.6 shows a typical measurement at an ultrasonic intensity of 29 Wcm^{-2} under inert Ar atmosphere at d = 22 mm.

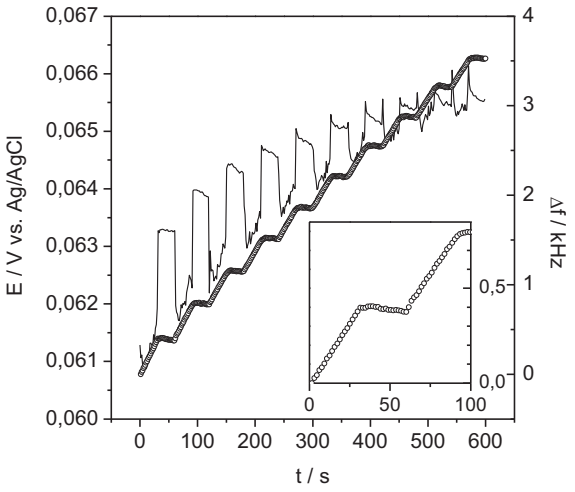

Figure 3.6 Measurement of open circuit potential (line) and frequency change (circles) of a quartz resonator after 2 min deposition of Cu at –0.15 V in Ar atmosphere with pulsed ultrasound of I_a=29 W cm^{-2}, $t_{on} = t_{off}$ = 30 s, d = 22 mm. The insert shows a part of the frequency curve enlarged.

The OCP decreased by 1–2 mV upon the application of ultrasound. While the ultrasound was on, the frequency was continuously increasing with the slope of ~ 13 Hz/s determined during the first 30 s of experiment (Δf=0.39 kHz, taken for the first 30 s from the graph in Fig. 3.6 and divided by the time of 30 s),. When the ultrasound was turned off, the frequency just slightly decreased. The irreversible increase in the resonance frequency in the presence of ultrasound indicates a mass decrease of the electrode and therefore the removal of Cu by erosion or corrosion caused by residual oxygen.
The rate of the frequency change slightly decreased during the experiment. When similar experiments were done in the presence of air, it was even larger, 24±1 Hz/s at 29 Wcm^{-2}, and 20 Hz/s at a low intensity of 11 Wcm^{-2}.

The role of erosion and corrosion

In order to explore the role of erosion (and thus cavitation) and of corrosion in more detail, a further study with a broader range of applied ultrasound intensities was done. A copper layer was deposited at -0.15 V at an ultrasound intensity of 80 Wcm^{-2} and with a 300 kHz frequency limitation (deposition was stopped after Δf caused by deposition exceeded – 300 kHz), in Ar, followed by an open circuit potential measurement with a variation of the ultrasonic intensities at d = 10 mm. Mass losses were observed during OCP with rates between 0.08 $\mu gcm^{-2}s^{-1}$ under silent conditions and ~0.15 $\mu gcm^{-2}s^{-1}$ at an ultrasonic intensity of 80 Wcm^{-2}, corresponding to the average corrosion currents of 0.24 and 0.45 $mAcm^{-2}$, respectively (Annex 2). The change in the resonance frequency with ultrasonic intensity during time is shown in Figure 3.7. The change in damping is also added to the graph.

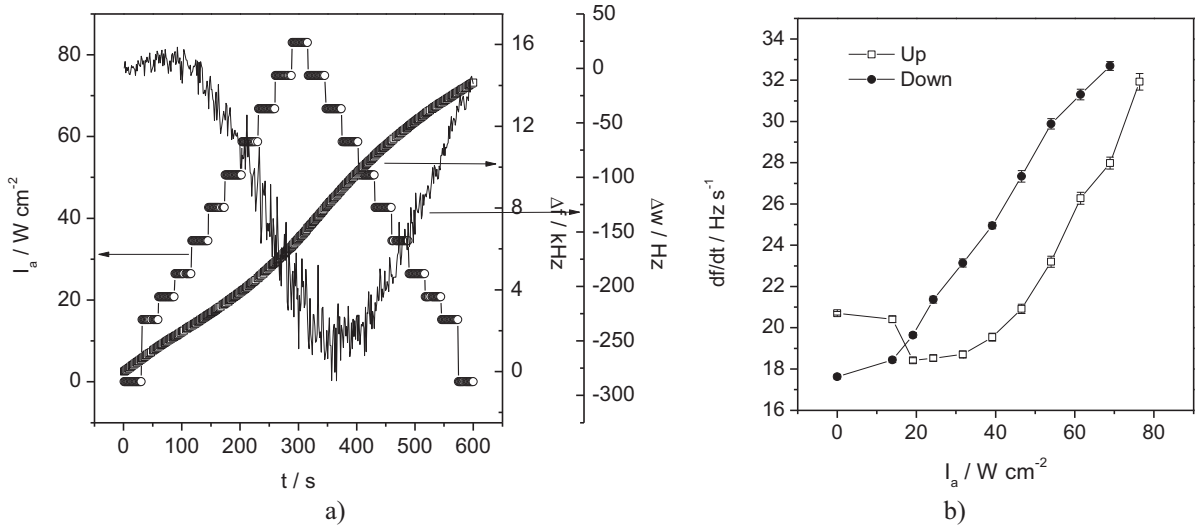

Figure 3.7 Open circuit measurements with a variation of ultrasonic intensity (upward and then backward) on a Cu layer (deposited at -0.15 V, 80 Wcm^{-2}, Δf=300 kHz, d=10 mm in Ar) a) frequency change (squares) and damping change (line) with time and I_a (circles) and b) rate of the frequency change with a stepwise increase followed by a stepwise decrease in I_a.

At lower ultrasonic intensities, up to ~ 20 Wcm^{-2}, the slope of the frequency change with time is small and there is almost no change in damping (Fig 3.7 a). At higher I_a, the rate of the frequency change becomes larger and then on the back sweep it decreases again. Damping was also increasing at higher ultrasonic intensities. Due to the larger frequency change observed under the influence of ultrasound and further with the increase in ultrasonic intensities, one can conclude that corrosion reactions were accelerated with enhanced transport of the oxygen towards the electrode. Further, in Figure 3.7 b, it is evident that the rate of the frequency change is finite under silent conditions indicating corrosion development due to the residual oxygen.

An erosion process, possibly developed through surface cavitation, could be another explanation for the frequency shift during OCP measurements. Although the finite rate of the frequency change observed in Figure 3.7 b did not prove the presence of surface cavitation, and especially the frequency

change under silent conditions cannot be explained by it, cavitation could be an additional explanation for the enhanced corrosion reactions in the presence of ultrasound via created oxidants like $OH^{\cdot}$ radicals and H_2O_2 in cavitation bubbles.

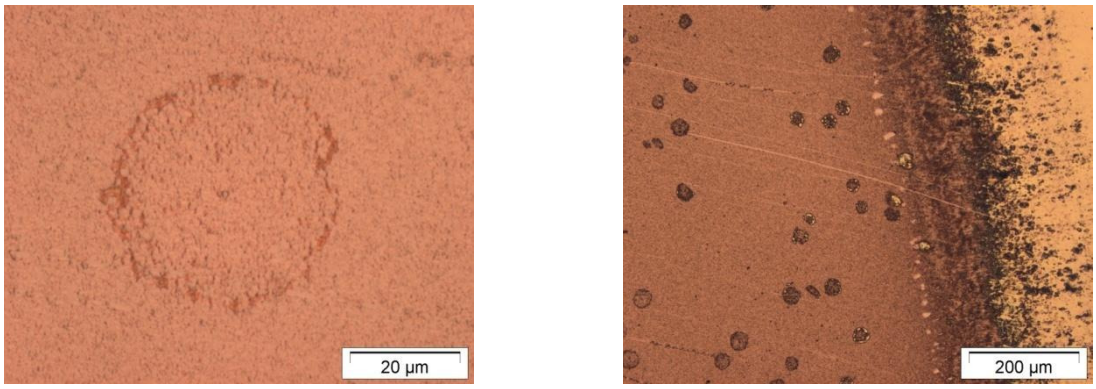

Figure 3.8 Optical microscopy pictures: round features observed on the surface of the deposited Cu layer

Round features shown in Figure 3.8 were observed by optical microscopy of a Cu film after deposition at -0.15 V, at 76 Wcm^{-2}, Δf = 300 kHz and d = 10 mm. They could be caused by cavitation bubbles at the electrode surface.

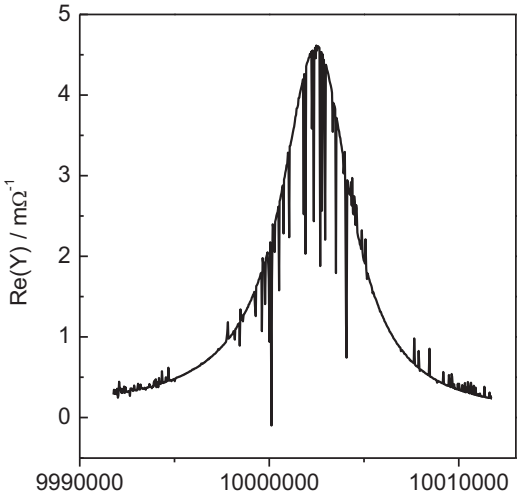

Figure 3.9 Admittance of quartz resonator at 24.6 Wcm^{-2} at the beginning of a deposition experiment

Another observation was that in the beginning of a deposition experiment, at an ultrasound intensity of 24.6 Wcm^{-2}, the resonance spectrum was very noisy (Fig. 3.9). One reason could be development of cavitation, bubble collapse near or at the electrode and micro jets creation. This happened very rarely in the experiments in sulphate based electrolytes discussed in this work. As long as there was a deposit on the electrode it was always possible to analyse the data.

3.2.3 Cyclic electrodeposition and dissolution of copper

A cyclovoltammetric study of the Cu electrodeposition on the Au electrode on the quartz was performed in a potential range between 0.45 V and -0.2 V vs. Ag/AgCl, with a 5mV/s scan rate, for two cycles under inert Ar atmosphere, first in silent conditions and afterwards in the presence of the ultrasound. A series of cyclovoltammetric measurements with a variation of the ultrasound intensity was performed. The potential sweep was started at a value where no deposition takes place and swept down to more negative values. In the sulfate system the deposition of copper takes place through a reduction of Cu^{2+} ions by a two consecutive one electron transfers [216-219].

$$Cu^{2+}+2e^{-}\rightarrow Cu\ (s) \qquad (3.2.1)$$

The standard electrode potential for this reaction is 0.34 V [159]. Neglecting activity coefficients, for the concentration of 0.01 mol/l, one calculates from the Nernst equation (Eq. 1.4.5) an equilibrium potential of 0.084 V vs Ag/AgCl (Annex 3).

Silent conditions

The cyclic voltammogram together with the simultaneously recorded change in the resonance frequency of the quartz resonator under silent conditions is shown in Figure 3.10. A slight change to more negative currents, indicating a cathodic process, was already observed at potentials just below 120 mV. Still, the first decrease in resonance frequency and consequently Cu electrodeposition was observed starting at the potential of 18 mV. Below this potential, a strong increase in the cathodic current as well as a decrease in the frequency was observed.

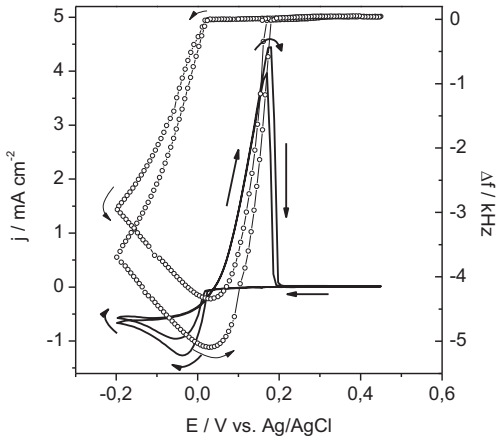

Figure 3.10 Current densities (lines) and associated frequency changes (circles) during cyclic deposition and dissolution of Cu from 0.01M $CuSO_4$, 0.1M Na_2SO_4, pH~1 at a scanrate of 5 mV/s under quiescent conditions in a cell under Ar atmosphere.

At lower potentials, a cathodic peak appeared due to the mass transport limitation typical for low concentration systems [220]. With time there was a depletion of Cu species near to the electrode and the current started to decrease. It is known from the literature that the cathodic peak disappears with a larger copper ion concentration [205, 221]. At the beginning of the back sweep, the frequency was further decreasing and the current remained negative, so deposition was still taking place. The damping *w* increased by around 300 Hz, but the resonance frequency decreased by almost 5 kHz. Sauerbrey equation could therefore be applied. Above a potential of ~ 45 mV the current became positive and the frequency started to increase, indicating dissolution. The equilibrium potential calculated from the Nernst equation was in a reasonable agreement with deposition and dissolution potentials. After the anodic peak was reached at a potential of 160 mV the current dropped to background values and the frequency returned to the starting value and remained constant, which was sign that all Cu deposited in the cathodic sweep was dissolved in the anodic one. In this study moderate overpotentials for deposition were applied, so that hydrogen evolution was limited and thus copper hydroxides precipitation was avoided. In literature [205] part of the deposited copper remained on the electrode after the dissolution peak but in that study lower (more negative) potentials had been applied. In the second cycle, the recorded currents for the anodic and the cathodic peak were larger than in the first cycle. More copper was also deposited. The concentration profile of Cu ions near the electrode after dissolution of Cu in the first cycle was in the beginning of the second cycle changed in comparison with the beginning of the first cycle. It must be assumed that the concentration of Cu ions in the vicinity of the electrode was increased prior to the second cycle as a consequence of the just finished Cu dissolution and not enough time for Cu ions to diffuse away from electrode. This could be a reason for the observed deviation between the first and the second cycle in cyclic voltammograms.

In an ultrasound field

Further, a set of cyclic voltammetry experiments with increasing ultrasound intensity was run, in order to explore the influence of the ultrasound on this system. The distance between the quartz and the horn was 10 mm. The presence of the ultrasound significantly changed the cyclic voltammogram of the Cu deposition from the sulfate based electrolyte.

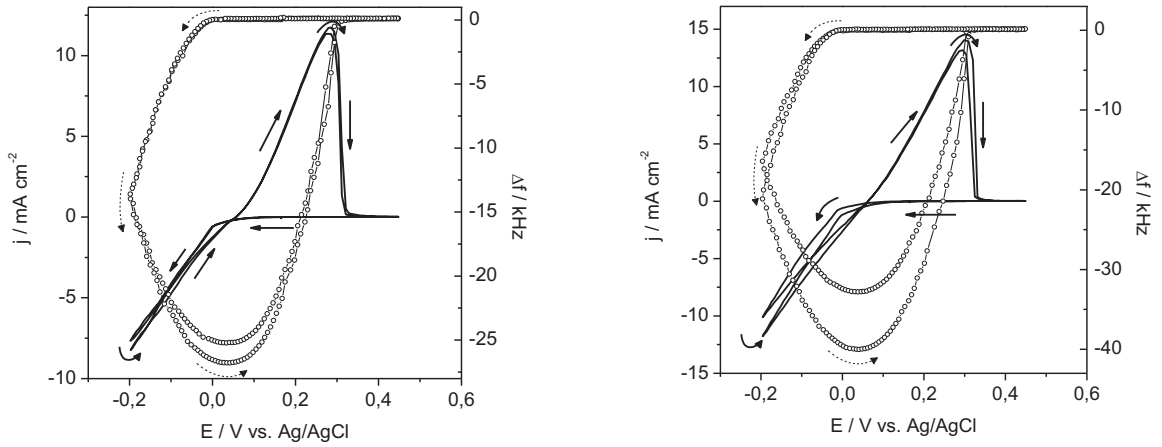

Figure 3.11 Current densities (lines) and associated frequency changes (circles) during cyclic deposition and dissolution of Cu from 0.01M $CuSO_4$, 0.1M Na_2SO_4, pH~1 at a scan-rate of 5 mV/s, d=10 mm under ultrasonic irradiation at an intensity of a) 14 W/cm^2 and b) 80 W/cm^2 under Ar atmosphere. Note: different scaling used because of the better visibility of the diagram showing different magnitudes of the recorded parameters.

Figure 3.11 shows the cyclic voltammograms for the deposition of Cu in presence of ultrasound with the lowest and the highest intensity used in the study, 14 Wcm^{-2} and 80 Wcm^{-2}, respectively.

At first, in an ultrasound field, there was no cathodic current peak, so mass transport control changed to charge transfer control. The presence of the ultrasound and the induced stirring effect led to a constant supplying of the electrode with the electroactive species. The current was continuously increasing while lowering the potential reaching values almost 7 (the lowest ultrasound intensity) and 10 (the highest ultrasound intensity) times higher than in silent conditions. The maximum frequency change increased from 5 kHz in silent conditions to around 26 and 40 kHz, for the lowest and the highest ultrasound intensity, respectively. The more Cu was deposited during the cathodic sweep, the larger and broader became the anodic peak. The anodic peak potential was also shifted to more positive values. Otherwise, there was no significant change in potentials upon the application of the ultrasound. This was an indication that ultrasound does not influence charge transfer kinetics or nucleation overpotentials, but enhances mass transport.

The influence of the ultrasound intensity on the electrochemical parameters was followed throughout this study. In Figure 3.12a, plots of the maximum cathodic current densities (at -0.15 V in the presence of ultrasound) and the anodic peak current densities versus the ultrasound intensity are shown. After a significant initial increase, values of these current densities were constantly, almost linearly, increasing with increasing ultrasound intensity. The maximum cathodic currents at the highest intensity reached values ten times larger than under silent conditions.

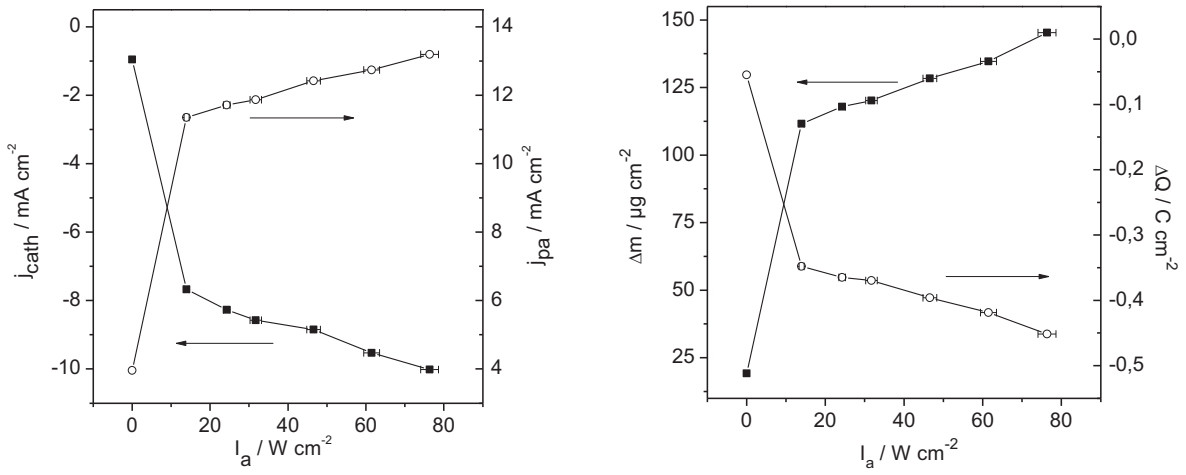

a) b)

Figure 3.12 Influence of the ultrasonic intensity on (a) maximum current densities in the cathodic sweep (full squares) and anodic peak current densities (empty circles) and (b) maximum areal mass densities deposited in a voltammetric cycle (squares-black) and the corresponding total cathodic charge fluxes (circles-blue). Data are taken from cyclic voltammetry in deaerated 0.01 M $CuSO_4$, 0.1M Na_2SO_4, pH~1 at a scan rate of 5 mV/s, d=10 mm.

Further, the maximum mass density of Cu deposited per cycle and the cathodic charge density obtained by integration of the current densities from the beginning of the Cu deposition in the forward sweep to the beginning of the Cu dissolution in the back sweep are given as a function of the ultrasound intensity in Figure 3.12 b. Under ultrasound influence, at an intensity of 80 Wcm^{-2}, the deposited mass was more than 7 times larger in comparison to silent conditions.

The increase in ultrasound intensity influences all parameters to change in a similar way. A strong increase in parameters is especially observed between experiments without any ultrasound and the low intensity ultrasound. With further increasing ultrasound intensity a less strong, almost linear increase is observed. In general, the parameters are mostly proportional to the square root of the ultrasound intensity.

Current efficiencies

In Figure 3.13, the change in the areal mass density versus the total electrical charge obtained from the cyclovoltammetric measurements with and without ultrasound is shown with dotted arrows indicating development of the process with time. In the beginning of the forward sweep (towards more negative potentials), there was a small cathodic current but it was not connected with any frequency change, thus no mass change, so no deposition started yet. For the cathodic deposition process the slope of the mass change versus charge curve was negative, as expected. In a small potential range, at the peak of the curve, where the change from the deposition to the dissolution process occurs, the slope was positive.

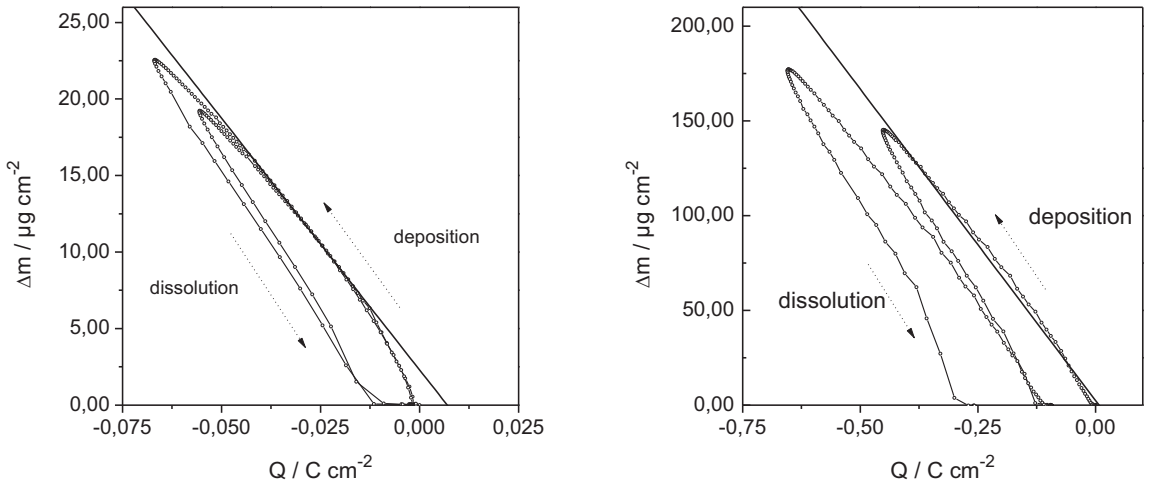

Figure 3.13 Mass changes *Δm(t)* as a function of the electrical charges *Q(t)* during deposition and dissolution of Cu in 0.01M $CuSO_4$, 0.1M Na_2SO_4, pH~1 (a) under quiescent conditions and (b) under ultrasonic irradiation at an intensity of 80 Wcm^{-2} measured in Ar atmosphere. Bold line: theoretical curves corresponding to 100% current efficiency. Arrows indicate deposition and dissolution and point in the direction of increasing time during the potential sweep. Note: different scaling used because of the better visibility of the diagram showing different magnitudes of the recorded parameters.

The deposition process takes place by reduction of Cu(II) ions through successive transfer of two electrons. When the slope of the mass-charge curve was compared to the calculated value for *dm/dQ* of $-3.29 \cdot 10^{-4}$ $g \cdot C^{-1}$, taking $z = 2$ and for a 100 % current efficiency (calculated in Annex 4 and according to Eq. 1.4.17), beside deviations in the beginning of the process (values larger than expected) and at the end of the deposition process (values smaller than expected) ideal behavior was approached. When *dQ* passes through 0 (current is zero) there is a mathematical discontinuity and thus a deviation from theoretical value. If *dQ* and *dm* do not pass through 0 in the same moment, it can influence the data. For the dissolution process the slope was most of the time larger than the theoretical one indicating that the dissolution process partly ends at Cu(I). In the presence of ultrasound, the mass-charge curve for Cu deposition was more linear and even more in agreement with theoretical values. This can be explained by a relatively smaller contribution of side reactions to the charge by selective enhancement of the Cu deposition rate. Under ultrasound also *dm/dQ* for Cu dissolution was more in agreement with theoretical values. Due to the thicker deposited layer in the presence of the ultrasound, dissolution takes place at higher currents and thus mostly Cu is dissolved via Cu(II), and no deviations from theoretically expected values for dm/dQ were observed as without ultrasound.

As *dm/dQ* was not constant during the deposition and dissolution (Fig. 3.13), time resolved apparent current efficiencies ε_{app} were calculated (shown in Annex 5 and according to Eq.1.4.19) and they are presented in Figure 3.14 a) for silent conditions and b) at an ultrasonic intensity of 80 Wcm^{-2}.

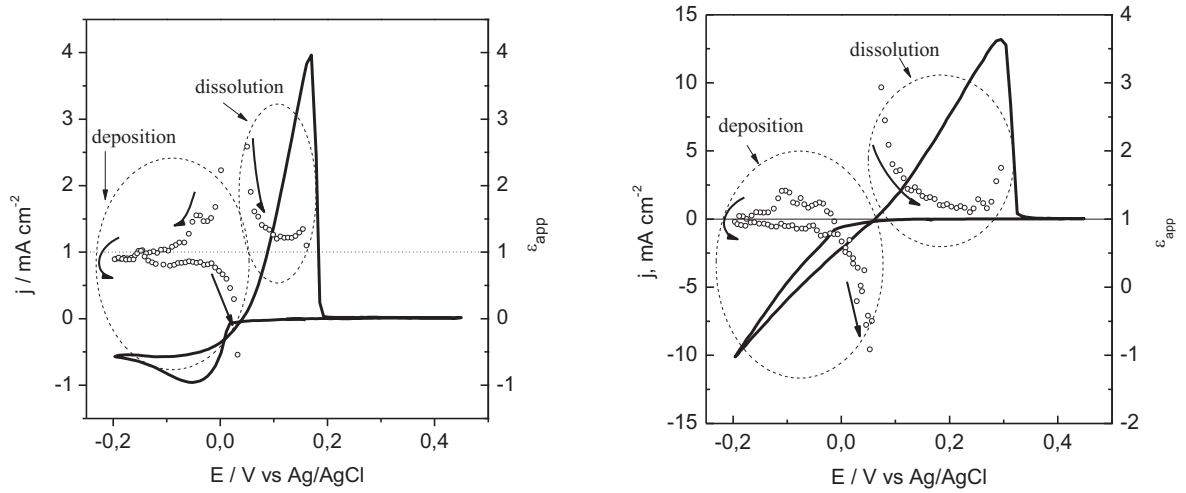

Figure 3.14 Cyclic voltammogram (lines) during deposition and dissolution of Cu from 0.01M $CuSO_4$, 0.1M Na_2SO_4, pH~1, *d*=10 mm and the calculated apparent current efficiencies (empty circles) (a) under quiescent conditions and (b) under ultrasonic irradiation at an intensity of 80 Wcm^{-2}. Arrows indicate scan direction. Note: different scaling used because of the better visibility of the diagram showing different magnitudes of the recorded parameters.

In the beginning of the deposition, when *dQ* crossed 0, in accordance with Eq.1.4.18, a mathematic discontinuity appeared and ε_{app}, calculated in Eq.1.4.19 had positive values toward $+\infty$ (Annex 4 and 5). Subsequently, positive values still larger than 1 were found for the current efficiency. In the literature [203], this is explained by reduction of Cu(I) accumulated at the surface of the electrode, not sensed by the quartz but with contribution to the enlarged values of current efficiency. This explanation is supported by the measured negative current in the beginning of the forward sweep (some reduction of Cu(II) to Cu(I) possibly took place) that was not connected with any frequency change. In addition, sulfate ions could be co-adsorbed from the electrolyte and stripped off later during dissolution. The nucleation process could also affect the discrepancy of the current efficiency through a possibly non-uniform mass distribution in the beginning of the deposition, introducing an error into the masses calculated by the Sauerbrey equation. At lower potentials, values for ε_{app} were approaching 1, corresponding to an ideal behavior. At the end of the deposition, in the back sweep there was again disagreement with the expected values. If residual oxygen leads to corrosion at low current densities *dm* is less than expected from the value for *dQ* and consequently ε_{app} decreased below 1. Furthermore, overall currents were still negative when *dm* crossed 0 and ε_{app} through 0 and became negative. When then the current approached 0 values of ε_{app} were increasing toward $-\infty$.

Once currents became positive, ε_{app} was toward $+\infty$ and with further increasing positive *dQ* and negative *dm* (dissolution process) the values for ε_{app} were normalizing being in the beginning larger than expected due to dissolution via Cu(I). This observation was explained by Bund et al. [201] with the assumption that part of Cu is dissolved via Cu(I) which diffuses away. In this way the charge needed for dissolution process was reduced and consequently the current efficiency had values larger than 1. In literature Cu dissolution is described as two-step mechanism [216]. At lower potentials in

acidic solutions the oxidation of Cu to Cu(I) is faster and larger values for ε_{app} are obtained. With increasing potential more Cu(I) was further oxidized to Cu(II) and the current efficiency decreased.
In the presence of ultrasound the dependence of ε_{app} on the potential was not significantly altered. As already explained for the *dm/dQ*-curves, values are in the presence of ultrasound closer to the theoretical ones due to the enhanced mass transport and deposition rate and thus less importance of side reactions. As more Cu is deposited, re-dissolution requires more time, and therefore a significant portion of the deposit dissolves at more positive potentials (same scanrate!) and higher current densities and thus dissolution via Cu(II) is more favored [222].

3.2.4 Potentiostatic electrodeposition of Cu

After the set of cyclovoltammetric measurements, potentiostatic depositions of Cu from the sulfate based electrolyte were carried out in order to study the influence of the presence and the intensity of the ultrasound on the quality and morphology of the obtained Cu films. All potentiostatic depositions were performed at -0.15 V, in air or in Ar atmosphere, with a variation of the ultrasonic intensity and the distance between the horn and the working electrode.
At first, potentiostatic deposition of copper was carried out under silent conditions for 1 h in air. Due to the growing of the diffusion layer and thus concentration depletion near to the electrode, the current was decreasing with time during the deposition process (Fig. 3.15). After an initial rapid current decrease, and a small peak recorded due to the nucleation process, it continued slowly to decrease with time. A current efficiency of 84 % (Annex 6) was calculated under silent conditions. A bright and glossy Cu film was obtained with the calculated mass of 0.58 mg cm^{-2} corresponding to 650 nm thickness.

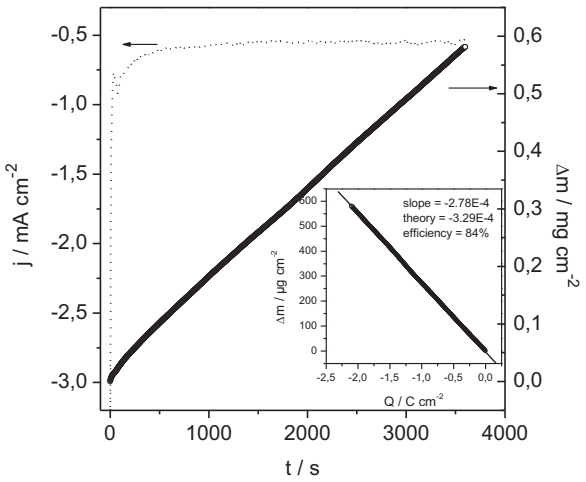

Figure 3.15 Current transient (dot line) measured in 0.01 M $CuSO_4$, 0.1 M Na_2SO_4, pH~1 during the potentiostatic electrodeposition of copper (mass curve-circles) at an applied potential of −0.15 V vs. Ag/AgCl without ultrasound and in a cell open to the air. Insert: linear behavior of mass vs. charge plots and the calculated current efficiency.

In the presence of ultrasound of 9 Wcm^{-2}, at a distance of 22 mm between horn and quartz, Cu deposition was carried out for 10 min. The current increased strongly in the beginning and then was slightly increasing until the end of the experiment, reaching values of about -4.7 $mAcm^{-2}$ (Fig 3.16). Opposite to the deposition in silent conditions under mass transport limitation, where the current was decreasing during the experiment, here the growing of the diffusion layer was eliminated and the deposition occurred under charge transfer control. With an apparent current efficiency of 104 %, the deposited mass was ~ 0.90 mg cm^{-2}, corresponding to a thickness of 1 μm as determined by profilometry measurements. Even with the lowest ultrasound intensity in 10 min much more deposit was obtained than in silent conditions in 1h.

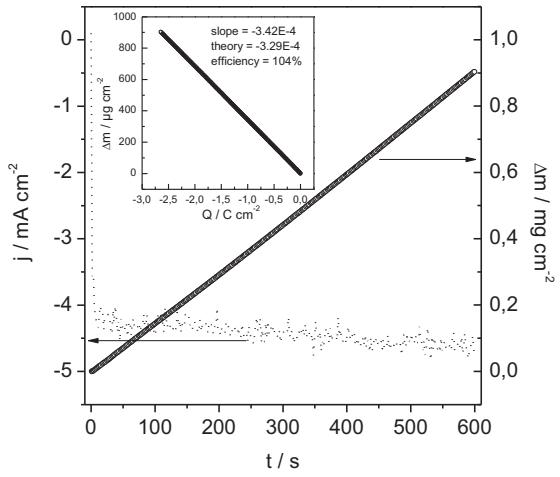

Figure 3.16 Current transient (dot line) measured in 0.01 M $CuSO_4$, 0.1 M Na_2SO_4, pH~1 during the potentiostatic electrodeposition of copper (mass curve-circles) at an applied potential of −0.15 V vs. Ag/AgCl under influence of 9 Wcm^{-2} ultrasonic intensity and 22 mm horn-quartz distance in a cell open to air. Insert: linear behavior of mass vs. charge plot and calculated current efficiency.

With an increase in the ultrasound intensity to 22 W cm^{-2} and otherwise the same conditions as in the previous experiment, the current transient was similar with a maximum value of -15.6 mA cm^{-2}. The deposited mass was ~ 2.3 mg cm^{-2}, corresponding to a layer thickness of about 2.5 μm. At an ultrasonic intensity of 22 W cm^{-2} the maximum cathodic current was more than 3 times higher and the deposited mass 2.5 times larger than at 9 Wcm^{-2}.

With a further increase in the ultrasound intensity to 29 W cm^{-2}, a frequency change limitation of 300 kHz was set up (i.e. the experiment was automatically stopped when the frequency decrease of the quartz resonator due to Cu deposition had accumulated to 300 kHz). Copper deposition was done under Ar atmosphere. Deposition lasted slightly longer than 13 min. With a maximum cathodic current of about -5.5 mA cm^{-2}, the obtained mass of the deposit was 1.36 mg cm^{-2}, corresponding to an average thickness of 1.5 μm.

With the highest applied intensity of 80 Wcm^{-2}, with the 300 kHz frequency change limitation, Cu deposition lasted less than 10 min. The distance between horn and the quartz was decreased to 10 mm. The deposition was done under Ar atmosphere. After an initial strong increase, the current continued to increase slowly with time due to the change in surface conditions and roughening reaching finally~-8.5 mA cm^{-2}. Based on the slope of the mass versus charge curve the current efficiency was calculated as 96 %. SEM images of the morphology of the obtained deposits are shown in Figure 3.17.

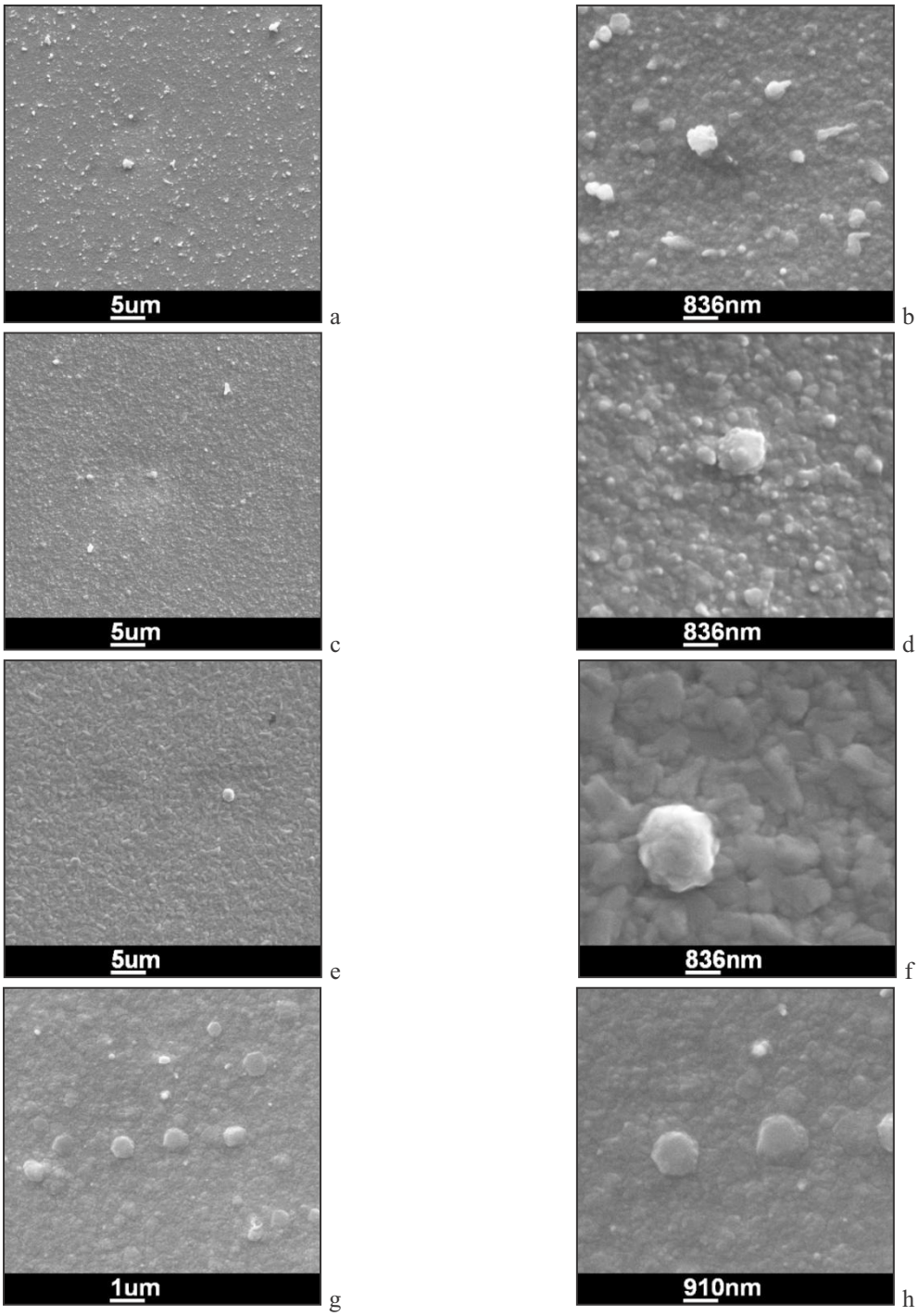

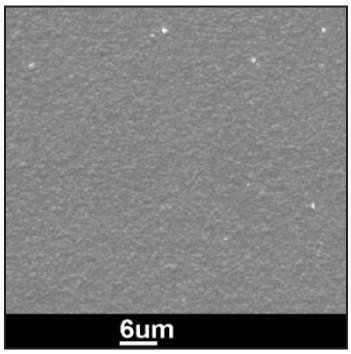

i

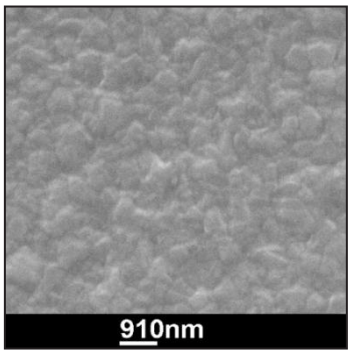

j

Figure 3.17 Scanning electron microscopy of Cu films deposited at -0.15 V, *d*=22 mm a,b) silent, 1 h, in air, c,d) at 9 Wcm^{-2}, 10 min, in air, e,f) 22 Wcm^{-2}, 10 min, in air, g,h) 29 Wcm^{-2}, Δf = 300 kHz, in Ar, i,j) 80 Wcm^{-2}, Δf = 300 kHz, in Ar, *d*=10 mm.

All potentiostatic depositions of Cu were done at the same potential of -0.15 V. Under silent conditions for one hour less deposit is obtained than in all other experiments, lasting at most 13 min in the presence of ultrasound. Without ultrasound the current was decreasing during potentiostatic deposition due to the depletion of the electroactive species and growing of the diffuse layer. Deposition under silent conditions was under mass transport limitation for the low concentration Cu electrolyte used in this study. In the presence of ultrasound the current was increasing during the potentiostatic deposition and the obtained mass of the deposit increased. The current efficiency was also increased upon application of ultrasound, due to the elimination of electroactive species depletion and less contribution of side reactions. In the presence of low intensity ultrasound (9 W cm^{-2}, cf. Fig 3.17 c, d) there was no significant change in morphology in comparison to Cu deposited under silent conditions (Fig 3.17 a, b). With an increase in the ultrasound intensity (22 Wcm^{-2}), the maximum current (-15.6 $mAcm^{-2}$) as well as deposited mass increased and larger and flatter grains were observed (Fig. 3.17 e, f). In further experiments, the limitation in frequency change of 300 kHz was set up and experiments were done under Ar inert gas atmosphere. In the presence of ultrasound with an intensity of 29 Wcm^{-2}, copper deposition lasted around 13 min with a maximum current of -5.5 mA cm^{-2} and a deposited mass of 1.36 mg cm^{-2}. The maximum values of the current and the deposited mass were less than at an ultrasound intensity of 22 Wcm^{-2}. The obtained deposit was more compact, the grains were in general slightly smaller but also some bigger particles were present (Fig 3.17 j, h). Depositions at 9, 22 and 29 W cm^{-2} ultrasound intensity were done at the same distance of 22 mm between horn and quartz. With the highest intensity of the ultrasound and the decreased distance between the horn and the quartz at 10 mm, with frequency limitation of 300 kHz, Cu deposition lasted less than 10 min. In this time the current was larger than at 29 Wcm^{-2} but still less than at an ultrasound intensity of 22 Wcm^{-2}. With an increase of the intensity, up to some intermediate values, the maximum currents as well as the deposited mass are increasing, whereas for further intensity increase they start to decrease in comparison with lower ultrasonic intensities. Whereas the morphology of the obtained deposits is similar without and with low intensity ultrasound, with increasing intensity it is severely changed. With ultrasound a less powdery deposit was obtained, more compact with slightly larger grains but

more uniform in size. As already reported in literature [233] when deposition is taking place under charge transfer control normally much better deposits are obtained than under mass transport control.

3.2.5 Experiments with the rotating disc electrode

Cyclo-voltammetric experiments with a platinum rotating disc electrode in the same type of solution were carried out in order to compare the ultrasound influence on the Cu electrodeposition from the sulfate based electrolyte to situations where purely effects of enhanced mass transport under well controlled conditions can occur. Cyclic voltammograms in the same potential range between 0.45 and -0.2 V vs. an Ag/AgCl reference electrode and using a PtTi wire as a counter electrode, with a rotation rate variation between 0 and 3000 rpm (in increments of 500 rpm) were recorded in air and are shown in Figure 3.18a. For the sake of comparison, recorded cyclic voltammogramms in the presence of ultrasound with intensities up to 28.2 Wcm^{-2} are shown in Figure 3.18b.

The behavior of the system with the RDE setup was similar as upon application of ultrasound. At first, in experiments with the rotating disc electrode the cathodic current peak disappeared as in experiments with ultrasound. Further, with increasing rotation rate, the cathodic currents were increasing and at the highest rotating rate the maximal cathodic current was 5 times larger than in quiescent conditions. In consequence of the increased cathodic currents more copper was deposited on the electrode, and the anodic peak became much larger with increasing rotation rate while the anodic peak potential was shifted to more positive values.

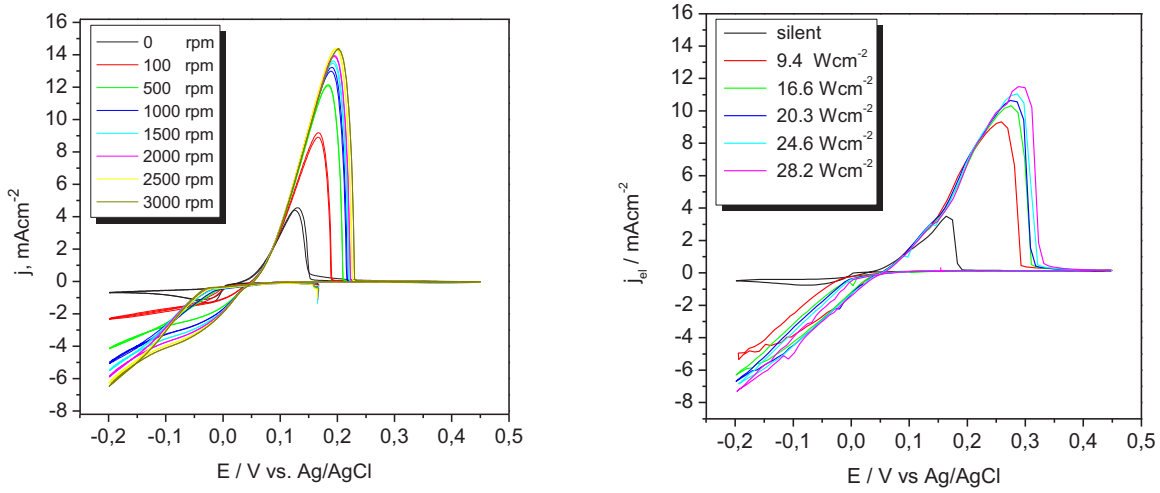

a) b)

Figure 3.18 Electrodeposition and -dissolution of Cu from 0.01M $CuSO_4$, 0.1M Na_2SO_4, pH~1 during cyclic voltammetry in a potential range of 0.45- (-0.2 V), at 5 mVs^{-1}, in air a) on Pt rotating disc electrode at 0-3000 rpm, b) under the influence of ultrasound, intensity variation 0-28.2 W cm^{-2}.

Maximum cathodic currents in the presence of ultrasound were in general slightly higher than in the rotation disc electrode setup. At an intensity of ~9.4 W cm^{-2} (the lowest intensity applied) the maximum cathodic current was equal to the one at 1000 rpm in the RDE setup. The maximum

cathodic current recorded at 3000 rpm corresponded to the one at 16.6 Wcm^{-2}. The increase in maximum currents with further intensity increase was less significant (in the range applied in the presented experiments).

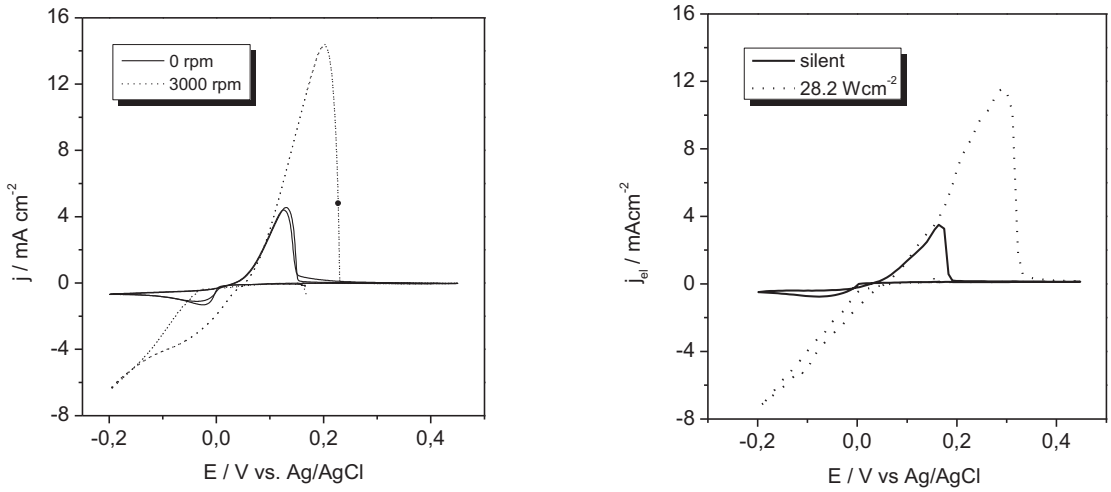

a) b)

Figure 3.19 Electrodeposition and -dissolution of Cu from 0.01M $CuSO_4$, 0.1M Na_2SO_4, pH~1 during cyclic voltammetry in a potential range of 0.45- (-0.2), 5 mVs^{-1}, in air a) on Pt rotating disc electrode at 0 and 3000 rpm, b) on Au electrode of quartz resonator under silent conditions and at an ultrasound intensity of 28.2 Wcm^{-2}.

In order to get a clearer overview, cyclic voltammograms in silent conditions are compared with the highest rotation rate (Fig. 3.19a) and the highest ultrasonic intensity (Fig. 3.19b). Although, recorded cyclic voltammograms are not completely the same the general tendency is clear. As in the case with the rotating disc electrode setup, in the presence of the ultrasound indications for a change from mass transport control (indicated by the cathodic peak observed in silent conditions) to charge transfer control (disappearance of the cathodic peak) were observed.

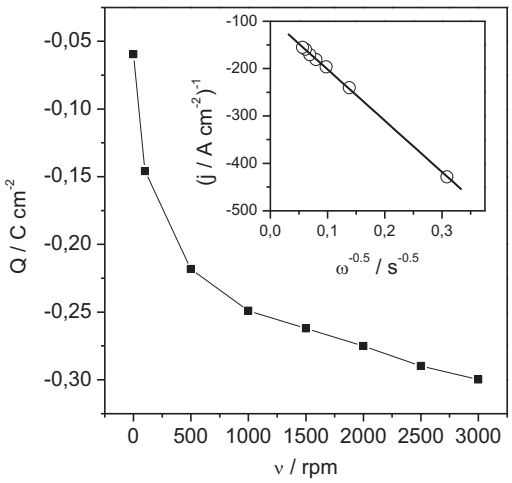

Figure 3.20 Dependance of maximum cathodic charge recorded during cyclic voltammetry in 0.01M $CuSO_4$, 0.1M Na_2SO_4, pH~1 on a Pt rotating disc electrode on rotation rate. Insert: Koutecky–Levich plot of inverse current densities at −0.2V as function of the inverse square root of the rotation rate.

In Figure 3.20, a plot of the cathodic charges versus the rotating rate is shown. Already at small rotation rates the cathodic charges are strongly increased. With a further rotation rate increase the cathodic charges continue to increase but less strongly. The Koutecky-Levich plot (according to Eq. 1.4.13 and given explanation) was linear in the entire range of applied rotation rates showing the gradual change from mass transport to charge transfer control. Cyclic voltammograms recorded on a rotating disc electrode were similar to those recorded under ultrasound influence. From the obtained similarity and the fact that ultrasound did not alter significantly potentials one could conclude that in the presented system the main influence of the ultrasound is enhanced mass transport. There is no evident impact on the charge transfer kinetics or nucleation overpotentials.

3.3 Studies in a copper chloride - based electrolyte

Opposite to the sulfate based electrolyte, a quite simple model system for metal electrodeposition, the chloride-based system with a high chloride concentration was more complicated. It has been postulated in the literature that in the presence of chloride ions, an anion-bridge activated complex of the Cu-Cl-Cu type is built for the Cu(II) reduction [223]. With different surface techniques it has been established that in the presence of the Cl^- ions, the copper surface is covered with an ordered layer of adsorbed Cl^- [224]. In an EQCM study of the electrodeposition and -dissolution of Cu from an electrolyte with a low chloride concentration, due to obtained *dm/dQ* data the accumulation of Cu(I) in the beginning of the cathodic scan and its adsorption on the surface was suggested [205]. The intermediate Cu(I) could form a porous film of CuCl [225, 226], which further in the excess of Cl^--ions dissolves forming $[CuCl_2]^-$, $[CuCl_3]^{2-}$ and $[CuCl_4]^{3-}$ complexes [227-229]. Due to the complex formation two well defined reduction (and oxidation) waves appear in cyclic and linear sweep voltammetry [230, 231]. The first reduction wave is due to the $Cu^{2+}/[CuCl_2]^-$ system with a standard potential of 0.53 V vs. NHE and thus 0.33 V vs. Ag/AgCl calculated the from standard potential for Cu^{2+}/Cu^+ (0.159V [159]) and the complex stability constant from [232] (Annex 7). The second reduction wave is due to the deposition of Cu from $[CuCl_2]^-$ with a standard potential of –0.05 V vs. Ag/AgCl (Annex 7). The electroplating of Cu from chloride electrolyte has been reported not to be favorable due to the high exchange currents reported in literature [233], resulting in powdery, low quality deposits. Furthermore, Cu is not stable in chloride solution in the presence of Cu(II) and according to T. Kekesi and M. Isshiki strong chemical corrosion of the Cu is due to the combined effect of the cupric and chloride ions [232]. Regarding the mechanism of Cu metal oxidation in hydrochloric acid solution, ireported and established in the literature is the formation of adsorbed CuCl species on the Cu surface at low current densities, further followed by the dissolution of $[CuCl_2]^-$ [234-237]. All above mentioned can lead to complex reaction dynamics [238].

The solution used in this study was 0.01 M $CuCl_2$ and 0.5 M NaCl with pH adjusted to ~1 by addition of an appropriate amount of concentrated HCl.

3.3.1 Cyclic electrodeposition and dissolution of copper

Cyclovoltammetric measurements were carried out in a potential range between 0.5 and -0.35 V vs. Ag/AgCl at a 5 mV/s scan rate. A series of cyclovoltammetric measurements, at first under silent conditions and then with variation of the ultrasound intensity, was performed. All measurements were performed under inert Ar atmosphere. As in the study in the sulfate system, the potential sweep was started at a value where no deposition takes place and swept down to more negative values.

Silent conditions

A typical cyclic voltammogram accompanied by the frequency response of the quartz under silent conditions is shown in Figure 3.21 a. In Figure 3.21 b plots of charge and mass change versus potential are presented, where regions with different electrochemical reactions can be distinguished.
Under silent conditions, two cathodic and two anodic peaks are observed, which is in agreement with literature data [205, 221, 239]. In the forward sweep the first cathodic peak appears at a potential of ~ 130 mV and then the second one at a potential of about -160 mV. On the back sweep the first peak is at a potential of about -10 mV and the second one at ~ 270 mV. A frequency change as an indication of a deposition and a dissolution process is recorded just for the cathodic and anodic peak pair at lower potentials, at -160 mV and -10 mV, respectively. Five ranges of potential can be distinguished, starting from the beginning of the forward sweep, where different reactions and processes take place (Fig. 3.21 b).

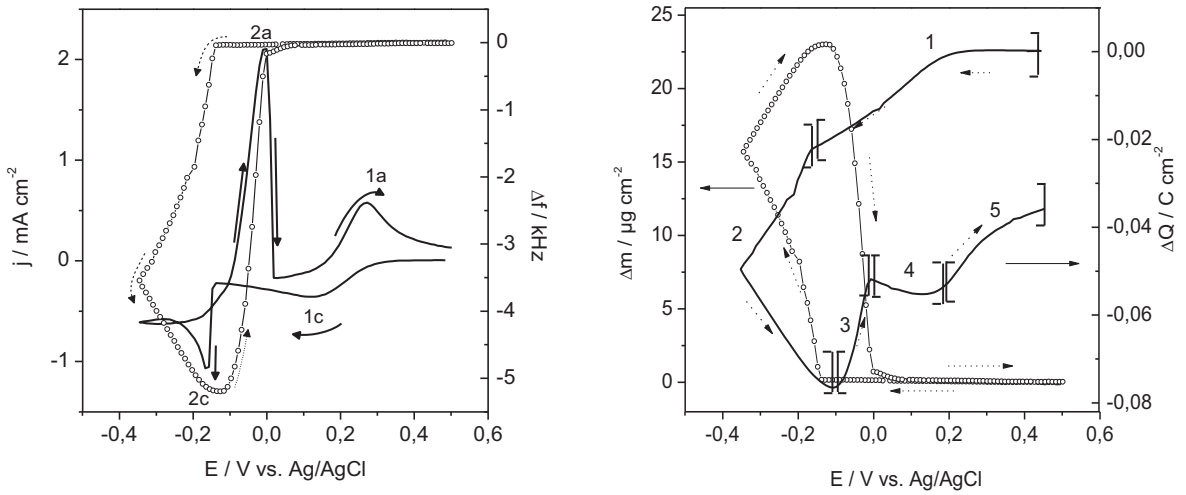

a) b)

Figure 3.21 Electrodeposition and -dissolution of Cu from 0.01 M $CuCl_2$, 0.5 M NaCl, pH~1 at a scan-rate of 5 m V/s under quiescent conditions in a cell under Ar atmosphere, a) current densities (lines-) and associated frequency changes (empty circles) with numbers showing cathodic (1c and 2c) and anodic (1a and 2a) peaks and b) charge density-potential curve (line) obtained from integration of current density and corresponding mass changes (circles) with numbers labeling regions where different combinations of electrochemical reactions are taking place.

1. 500-(-125) mV

In this region, the first cathodic peak appears, but no frequency change is recorded and thus no deposition takes place. The cathodic current in this potential range is due to Cu(II) to Cu(I) reduction according to the following reaction:

$$Cu^{2+}(aq) + 2Cl^{-}(aq) + e^{-} \leftrightarrow [CuCl_2]^{-}(aq) \qquad (3.3.1)$$

2. -125-(-350)-(-100) mV

The second cathodic peak appears in this region and is accompanied by a frequency decrease, so deposition takes place. The deposition of Cu is taking place partly by reduction of Cu(II) and partly by reduction of Cu(I) and this reaction is accompanied with continuing Cu(II) to Cu(I) reduction (at mass transport limited rate). The main reaction for this reduction process can be written as:

$$[CuCl_2]^- (aq) + e^- \leftrightarrow Cu(s) + 2Cl^- (aq) \quad (3.3.2)$$

3. -100-(~0) mV

The first anodic peak which appears at a lower potential and is connected with a frequency increase, is indicative of a dissolution process, with the main reaction being the dissolution of Cu to Cu(I). The efficiency obtained (for z=1) in this region is larger than 1 (Fig. 3.26), meaning that the actually measured anodic charge is less than the minimum charge for Cu dissolution as calculated from the frequency increase. This can be explained by the continued reduction of Cu(II) to Cu(I) taking place in parallel to Cu dissolution.

4. 0-200mV

This is the potential region after the dissolution peak in the anodic sweep. The currents are negative and determined by reduction of Cu(II).

5. 200-500mV

The second anodic peak appears in this region but it is not connected with any frequency change. The re-oxidation reaction of Cu(I) to Cu(II) takes place and determines the positive currents in this region.

In an ultrasound field – 15 mm horn-quartz distance

Cyclic voltammograms under ultrasonic irradiation were recorded at a distance of 15 mm between horn and quartz. In Figure 3.22 cyclic voltammograms and the corresponding frequency response of the quartz resonator at 14 Wcm^{-2} (the lowest applied) and at an ultrasound intensity of 76 Wcm^{-2} (the highest applied) are shown.

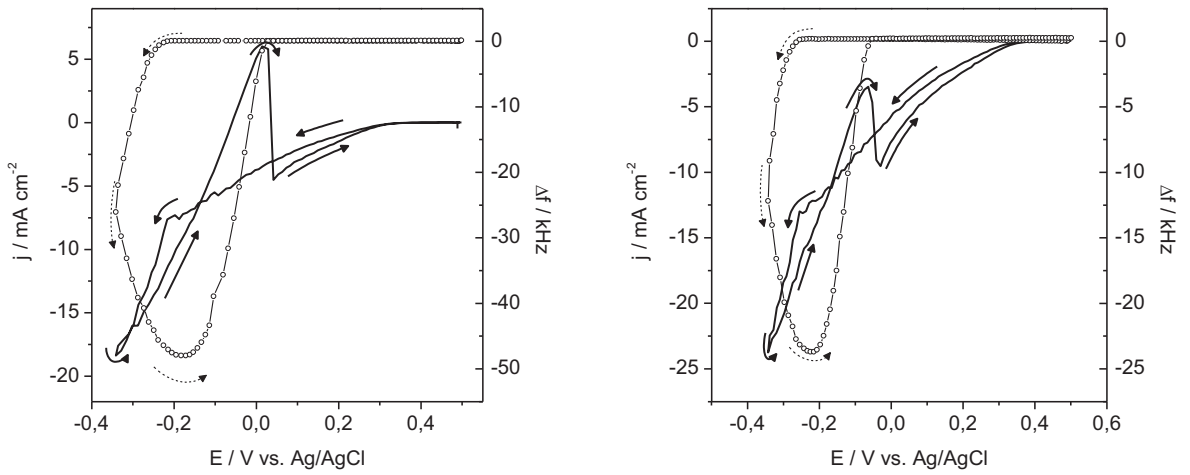

Figure 3.22 Electrodeposition and –dissolution of Cu, current densities (lines) and associated frequency changes (empty circles), from an electrolyte of 0.01 M $CuCl_2$ + 0.5 M NaCl, pH ~ 1 at d = 15 mm under an ultrasonic intensity of a) 14 Wcm^{-2} and b) 76W cm^{-2}. Arrows indicate the direction of potential sweeps, sweep rate 5 mV/s. Note: different scaling used because of the better visibility of the diagram showing different magnitudes of the recorded parameters.

Ultrasound, even with a low intensity, changed significantly the shape of the cyclic voltammogram. Both cathodic peaks as well as the anodic peak at higher potentials disappeared. The starting potential for Cu deposition, obtained from the initial change in frequency was shifted to a more negative value of -216 mV. Cathodic currents were constantly increasing until the deposition started. Maximum cathodic currents as well as the maximum frequency change were more than ten times larger than under silent conditions. The dissolution process started at a similar potential but the anodic peak was broader due to the dissolution of more deposited copper. After the dissolution peak, the current went back to negative values and just at the end of the back sweep became slightly positive, following the current trace from the forward scan.

With an increase in ultrasound intensity to 76 Wcm^{-2}, the entire cyclic voltammogram finally remained in the negative current range (Fig. 3.23b) and the potential where Cu deposition started became even more negative (-264 mV).

Figure 3.23a shows the shift of the potential where deposition started and of the anodic peak potential versus the ultrasound intensity. The potential of deposition shifted to more negative values upon application of ultrasound. Already at low intensity ultrasound there was a strong decrease in potential in comparison to silent conditions. With further increase in ultrasonic intensity the potential continued to shift slightly to more negative values up to ~ 30 Wcm^{-2} and then started to level off for higher intensities. In silent conditions, at a potential sufficiently below the standard potential for the redox couple Cu(II)/Cu(I), but still above the potential required for Cu deposition, all Cu(II) in the vicinity of electrode surface has been reduced to Cu(I). The concentration of Cu(I) close to the electrode surface therefore is equal to the bulk concentration of $CuCl_2$ before the onset of Cu deposition. Under these

circumstances Cu deposition is expected to take place entirely from Cu(I), and the electrode reaction given as reaction 3.3.3 and corresponding potential would be the Nernst potential for this reaction.

$$[CuCl_2^-] + e^- \rightleftarrows Cu + 2Cl^- \qquad (3.3.3)$$

With ultrasound and the intensive stirring provided, the concentration profile is changed, there is more Cu(II) and less Cu(I) in the vicinity of the electrode in comparison with silent conditions and therefore the potential where actual Cu deposition starts shifts to more negative values.

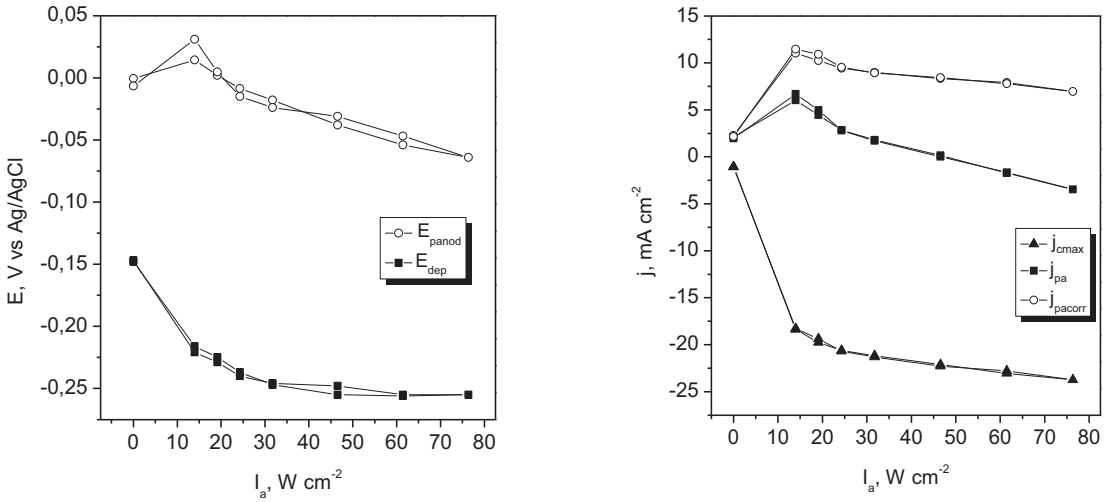

a) b)

Figure 3.23 Electrodeposition and –dissolution of Cu from an electrolyte of 0.01 M $CuCl_2$ + 0.5 M NaCl, pH ~ 1, (*E*: 0.5 V – (-0.35 V), 5 mV/s) at *d* = 15 mm. a) potential where deposition started (full squares) and potential of the anodic peak (empty circles) b) maximal cathodic currents (triangles), anodic peak currents (full squares) and corrected anodic peak currents (empty circles).

On the same graph, the change in the anodic peak potential (E_{pa}) under influence of ultrasound is also shown. At small ultrasonic intensities, E_{pa} shifts to more positive values as compared to silent conditions, but thereafter continuously shifts to more negative values with further increase in I_a. This shift of anodic peak potential is immediately connected with the total amount of Cu deposited beforehand (see Fig. 3.24a). With more Cu deposited E_{pa} moves to more positive values (analogous to the situation in sulfate-based electrolytes) and the anodic peak was also in the range of positive total currents. The negative shift in E_{pa} accordingly was caused by the deposition of less Cu at increasing I_a. At low ultrasound intensities the cathodic currents and the deposited mass were increased by a factor of nine or even more compared to silent conditions (Fig. 3.23b and Fig. 3.24a). The anodic peak currents shifted to larger more positive values while more Cu had to be dissolved. A further increase in the ultrasonic intensity still caused an increase in the maximum cathodic currents but the anodic peak currents decreased in magnitude, finally becoming negative above I_a~30 Wcm^{-2}. This behavior of the anodic peak currents was accompanied by a decrease in the deposited mass with ultrasonic intensity. In the forward scan, there was a significant cathodic current due to Cu(II) reduction at the same

potential where in the backward sweep the anodic peak was located. Due to the efficient stirring induced by the ultrasound, this current was not less in the backward sweep. Therefore the total anodic peak current actually is the sum of the dissolution current for Cu and the reduction current for Cu(II). After background corrections for the Cu(II)->Cu(I) reduction, the corrected anodic peak currents remained at positive values for all applied ultrasonic intensities, but still were decreasing in magnitude as a consequence of less deposited Cu.

From the total deposited mass and the total cathodic charge flux (Fig. 3.24a) an averaged (apparent) current efficiency ε_{app} (according to Eq. 1.4.19) for the deposition (assuming z = 2), and from the anodic peak charge (after background correction, assuming z = 1) for the dissolution was calculated (Fig. 3.24b). For the deposition process ε_{app} decreased from the value of 1 without ultrasound to 0.5 at the lowest ultrasonic intensity and decreased even further with increasing ultrasonic intensity. For the dissolution the ε_{app}-values were for all ultrasonic intensities larger than 1.

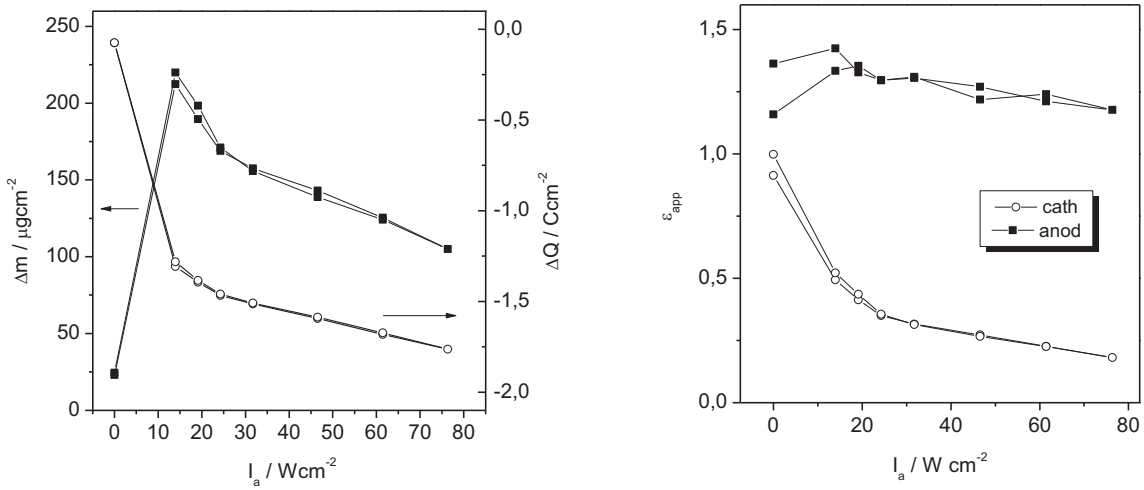

a) b)

Fig. 3.24 Electrodeposition and –dissolution of Cu from an electrolyte of 0.01 M $CuCl_2$ + 0.5 M NaCl, pH ~ 1 at d = 15 mm. a) maximum mass deposited and dissolved and maximum cathodic charge density in a single voltammetric cycle (E: 0.5 V – (-0.35 V), 5 mV/s) b) corresponding averaged cathodic and anodic apparent current efficiencies.

In an ultrasound field – 8 mm horn-quartz distance

In the next step of the study the distance between the horn and the quartz was decreased to 8 mm and a set of cyclovoltammetric experiments was performed under otherwise identical conditions.

The cyclic voltammograms at the lowest (14 Wcm^{-2}) and the highest (76 Wcm^{-2}) ultrasound intensity are shown in Figure 3.25. Both cyclic voltammograms were completely in the range of negative currents. At an intensity of 14 Wcm^{-2}, with exception of a small range in the very beginning of the forward sweep, the cathodic current was constantly increasing in magnitude and according to the first onset of a frequency change Cu deposition took place below -260 mV. The cathodic currents at the lower potential limit reached a maximum value of about -5.7 $mAcm^{-2}$. After the dissolution peak at

about -120 mV the currents were decreasing in magnitude and just at the very end of the back sweep became slightly positive. At an intensity of 76 Wcm^{-2} the deposition started at a slightly more negative potential of -270 mV, but the maximum cathodic currents were almost 4 times larger than at 14 Wcm^{-2} ultrasound intensity. The deposited mass was much less and consequently the anodic peak, measured with respect to the large background current, was smaller.

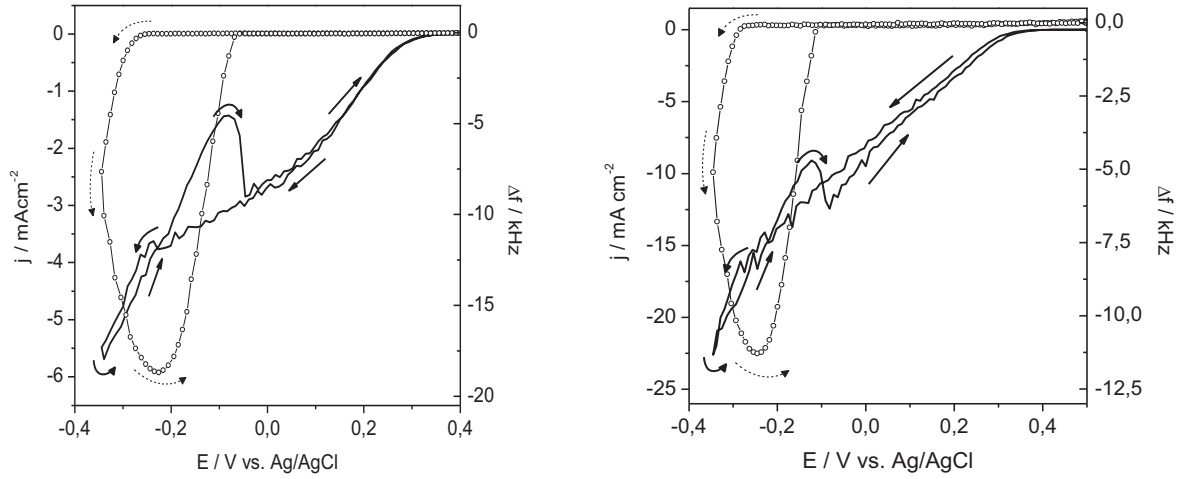

a) b)

Figure 3.25 Electrodeposition and –dissolution of Cu, current densities (lines) and associated frequency changes (empty circles), from an electrolyte of 0.01 M $CuCl_2$ + 0.5 M NaCl, pH ~ 1 at d = 8 mm under an ultrasonic intensity of a) 14 W cm^{-2} and b) 76 W cm^{-2}. Arrows indicate direction of potential sweeps, sweep rate 5 mV/s. Note: different scaling used because of the better visibility of the diagram showing different magnitudes of the recorded parameters.

The maximum mass deposited and the total cathodic charge density in a single voltammetric cycle as well as corresponding averaged cathodic and anodic apparent current efficiencies followed similar trends with increasing ultrasound intensity as in the case of 15 mm quartz-horn distance discussed above.

Similar to the situation discussed for the sulphate-based electrolyte, under silent conditions both reduction of Cu(II) to Cu(I) and Cu deposition are eventually under mass transport control, as seen by the two cathodic peaks. In the presence of ultrasound, the strong stirring effect connected with acoustic streaming, and possibly the collapse of cavitation bubbles and associated microjets led to a gradual change to charge transfer control, to the disappearance of both cathodic peaks and strongly enhanced cathodic currents.

Current efficiency

In silent conditions, small cathodic currents were recorded in the beginning of the forward sweep. In this region of potentials reduction of Cu(II) to Cu(I) occurred, as explained in literature [205, 220, 221, 225]. With increasing extent of reduction the concentration of Cu(II) close to the electrode decreased and the one of Cu(I) increased, and a cathodic peak appeared due to mass transport control. At a certain potential below the standard potential for the redox couple Cu(II)/Cu(I), Cu deposition started by reduction of the Cu(I) species enriched close to the electrode surface, while the parallel reduction of further Cu(II) to Cu(I) was already under mass transport limitation. This is a reason for ε_{app} (calculated for z = 1 in Eq. 1.4.19) to be around 1 in the beginning of the deposition (Fig. 3.26 a).

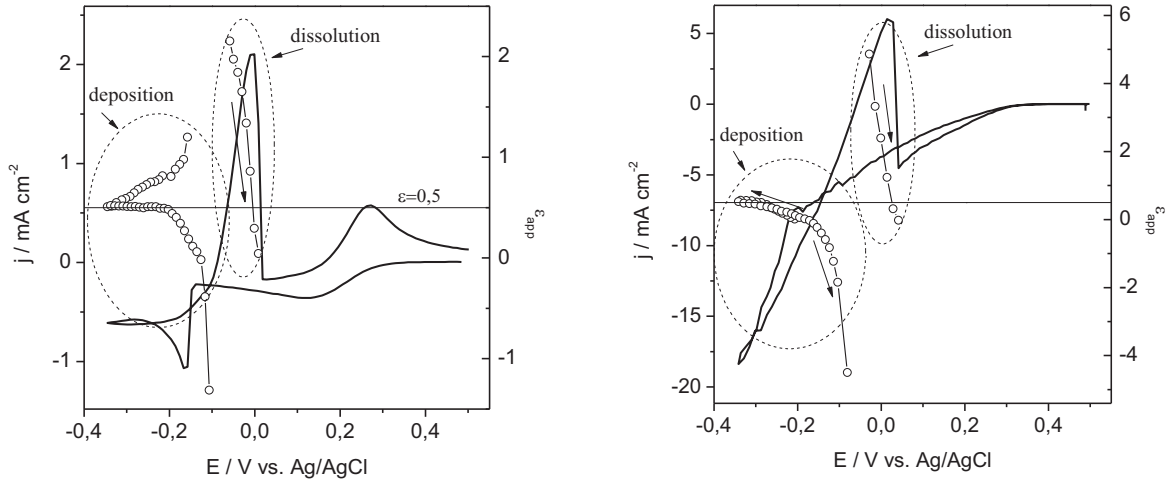

Figure 3.26 Currents (line) and potential-resolved apparent current efficiencies calculated for z=1 (empty circles and lines) during cyclic Cu deposition and dissolution from a $CuCl_2$-based electrolyte at 15 mm distance a) silent conditions b) at I_a=14 Wcm^{-2}. Note: different scaling used because of the better visibility of the diagram showing different magnitudes of the recorded parameters.

For values larger than one, it is possible that the short delay between the measurement of the current via the potentiostat and the change in frequency via the network analyzer is responsible. At even lower potentials most of the Cu(I) was consumed and the deposition was increasingly taking place by mass transport limited reduction of Cu(II), leading to a decrease in cathodic currents. Therefore ε_{app} was approaching 0.5. The values obtained for ε_{app} (calculated for z = 1) confirm therefore that at higher potentials the deposition occurs via Cu(I) and at lower potentials via Cu(II). In the beginning of the (anodic) back sweep, part of Cu(II) was reduced to Cu(I) and part to Cu, and ε_{app} decreased below 0.5. With further increasing the potential, an even smaller proportion of Cu(II) was reduced to Cu metal, further decreasing ε_{app}. Finally Cu dissolution to Cu(I) started while the total current was still negative due to the reduction of Cu(II) to Cu(I), and ε became negative. When the current became positive, ε_{app} had in the beginning values larger than 1. This is still due to the on-going negative current contribution

of Cu(II) to Cu(I) reduction, which is why the change in mass is larger than expected from the anodic charge.

Ultrasound enhanced mass transport and thus severely changed the situation. The current efficiency had a value of 0 in the beginning of the deposition, because the cathodic currents were already large due to the reduction of Cu(II) to Cu(I), but deposition just started (small Δm). At lower electrode potentials ε_{app} was approaching 0.5, so deposition from Cu(II) occurred. With accelerated mass transport there was little if any depletion of Cu(II) and no enrichment of Cu(I) and at lower potentials solely Cu(II) contributed to Cu deposition. Values of 0.5 were also found in the beginning of the back sweep but when dissolution started in the region of total negative current, ε_{app} became negative. With currents becoming positive ε_{app} became positive and had larger values than 1. In this potential range there was also Cu(II) reduction taking place, as explained above for silent conditions. With increasing rate of Cu dissolution ε_{app} was decreasing, and became finally negative.

The reduction process in the copper chloride system is a two-step process and this mainly determines the behavior of parameters also under the influence of ultrasound. Ultrasound leads to enhanced mass transport and the depletion of Cu(II) near the electrode, as in the case without ultrasound, is eliminated. From one side this encourages Cu(I) formation but from another side Cu can be easier corroded with Cu(II). With enhanced mass transport not just Cu(II) ions are faster brought to the electrode but also Cu(I) can be faster removed from the electrode, being then no longer available for further reduction to Cu metal. Cu deposition is therefore maximal at intermediate ultrasonic intensities and then it decreases, leading to a decreasing of current efficiency. This is in part caused by the large cathodic currents due to the reduction of Cu(II) to Cu(I). When less mass is deposited with increasing I_a, the anodic peak currents are decreasing as well and the anodic peak potential shifts to lower potentials. With a further increase of the ultrasound intensity, although cathodic currents were further slightly increasing, deposited mass was decreasing and current efficiencies strongly decreased.

3.3.2 Potentiostatic deposition of Cu

The potentiostatic deposition of Cu layers was performed at different potentials and at different ultrasonic intensities at a same horn-quartz distance (d=22 mm) and the morphology of the obtained deposits was examined by scanning electron microscopy.

At the potential of -0.3 V and at an ultrasound intensity of 30 Wcm^{-2}, with the given limiting frequency change of 300 kHz of the quartz resonator in less than 5 minutes Cu deposition was finished. After an initial increase in the current, it was noisy, leveled off and slightly decreased toward the end of the deposition (Fig. 3.27). The mass was continuously (almost linearly) increasing and reached a value of 1.34 mg cm^{-2} (predetermined by the limitation of Δf) corresponding to a thickness of 1.5 μm. For these conditions, potentiostatic deposition occurred with a 76 % current efficiency, calculated from the slope of the mass versus charge curve.

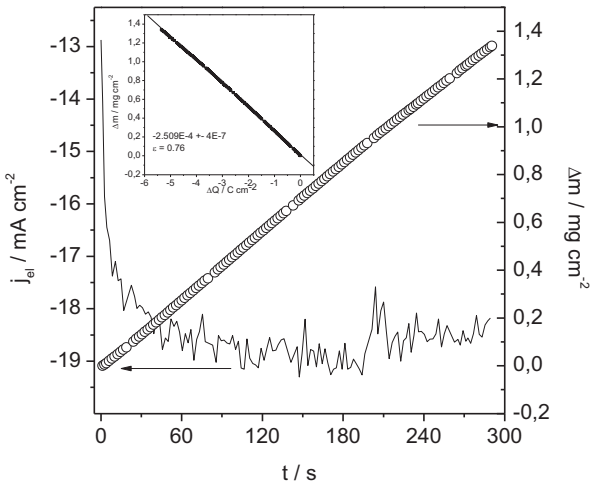

Figure 3.27 Current transient (line) recorded at –0.3 V and I_a = 30 W cm^{-2} in 0.01 M $CuCl_2$, 0.5 M NaCl, pH ~ 1, and mass change of the resonator (empty circles). Insert: Corresponding mass versus charge plot with given current efficiency calculated from the slope.

The deposited layer was not uniform and one could also observe small holes or cracks (Fig 3.28a). On the top of the layer, consisting of grains similar in size merged together (Fig. 3.28b), were bigger grains different in size and shape.

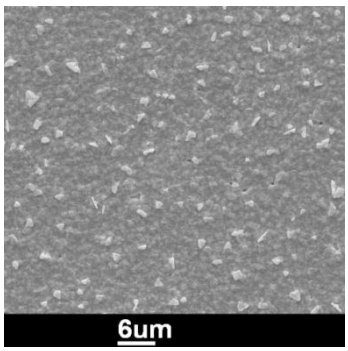

a)

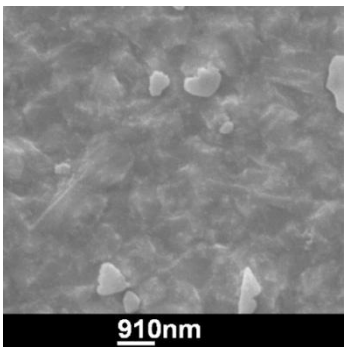

b)

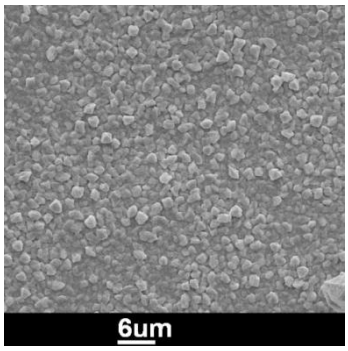

c)

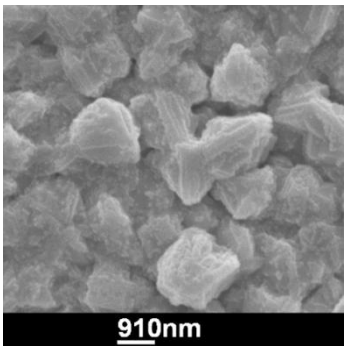

d)

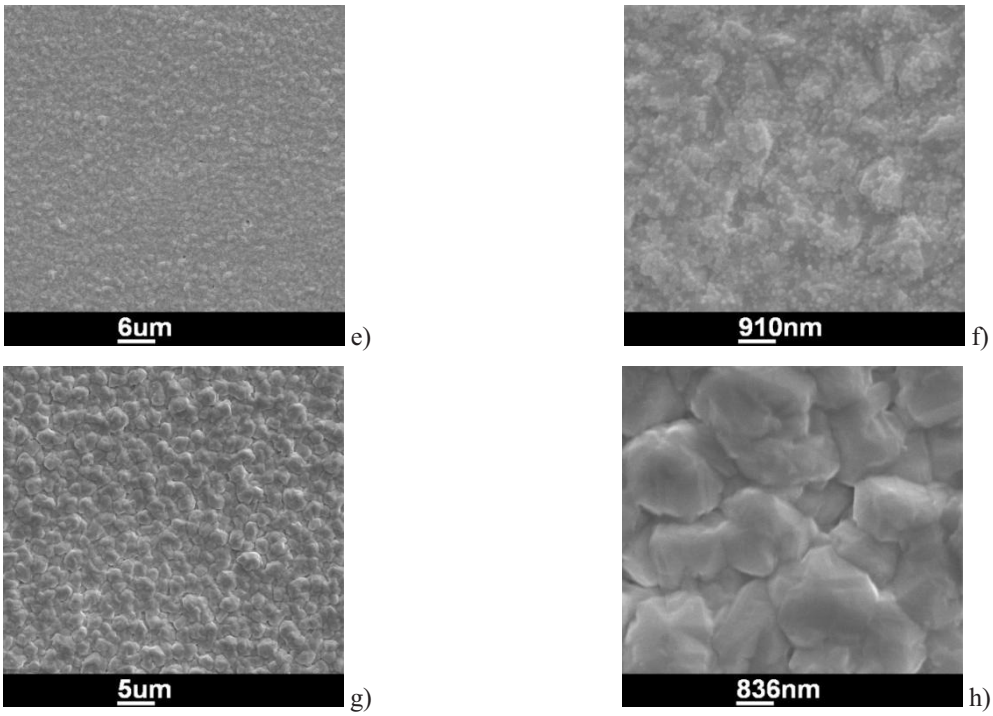

Figure 3.28 Cu films deposited from an electrolyte of 0.01 M $CuCl_2$ + 0.5 M NaCl, pH ~ 1, sweep rate 5mV/s, d=22mm at I_a = 30Wcm^{-2} and E = - 0.3 V, $|\Delta f| \geq 300$ kHz (a and b), at I_a = 11Wcm^{-2} and E = - 0.3 V, $|\Delta f| \geq 300$ kHz (c and d), I_a = 29Wcm^{-2} and E = - 0.33 V, 10 min (e and f), I_a = 27.5Wcm^{-2} and E = - 0.25V, $|\Delta f| \geq 300$ kHz (g and h).

At the same potential of -0.3 V and a lower ultrasound intensity of 11 Wcm^{-2} deposition of copper lasted less than 7 min. Grains, bigger but more uniform in size, without merging together formed a powdery, rough layer, shown in Figure 3.28 (c, d).

At a lower potential of -0.33 V at an ultrasound intensity of 29 Wcm^{-2}, deposition took place with a current efficiency of 91% in less than 5 min, and a layer with a uniform size of particles was obtained (Fig. 3.28e). At a higher magnification smaller particles with a similar shape and size merged together with a flat compact layer underneath were visible (Fig. 3.28f).

When the applied overpotential was lower (E= -0.25 V vs Ag/AgCl), with an ultrasound intensity of 27.5 Wcm^{-2}, the copper layer was deposited with a current efficiency of 100 % in the beginning and 90 % towards the end of experiment, which lasted 10 min. The grains were large and flat forming a rather rough layer (Fig. 3.28g, h).

When lowering the ultrasonic intensity from 30 to 11 Wcm^{-2} under otherwise identical conditions, a potential of -0.3 V and a frequency change limitation of 300 KHz, the deposition lasted 2 min longer and a more powdery and rougher layer was obtained with a bigger grain size. At an ultrasonic intensity of 29 Wcm^{-2}, the same frequency limitation, but a higher overpotential (E = -0.33 V) smaller grains and a more compact, less rough layer was obtained in the same time (less than 5 min). At an intensity of 27.5 Wcm^{-2} in 10 min but at a rather low overpotential of -0.25 V, the largest size of the flat grains was observed forming a rough layer.

With a higher ultrasound intensity in the range of applied intensities in these experiments grains smaller and more uniform in size and more compact layers were obtained. A similar effect was observed for a more negative potential (corresponding to a higher overpotential). With the lowest overpotential, the largest grains were observed and with the lowest ultrasound intensity the roughest and most powdery layer was deposited.

3.3.3 Potentiostatic depositions at different overpotentials and ultrasound intensities

With the aim to investigate in more details the influence of the potential and the ultrasonic intensity on the current efficiency of the potentiostatic deposition of copper from chloride electrolyte, a set of the potentiostatic depositions with a potential and an ultrasonic intensity variation at a distance of 22 mm between horn and electrode, was done. A potential range between -0.25 and -0.35 V was chosen because in that potential range Cu deposition was obtained in the cyclovoltammetric study (cf. Fig. 3.26). At the potential of -0.2 V there was no deposition taking place. For each value of the applied potential ultrasound intensity was varied between 10.6 and 30 Wcm^{-2}. In Figure 3.29, the rate of the deposition and the current efficiency are presented with potential and intensity variation.

The deposition rate strongly increased upon turning on the ultrasound for all applied potentials (Fig. 3.29a). With increasing ultrasound intensity and at more negative potentials the deposition rate gradually increased. When increasing the ultrasonic intensities beyond ~ 13 Wcm^{-2}, for lower overpotentials the deposition rate was slightly decreasing, for intermediate potentials it leveled off and for higher potentials it was slightly increasing.

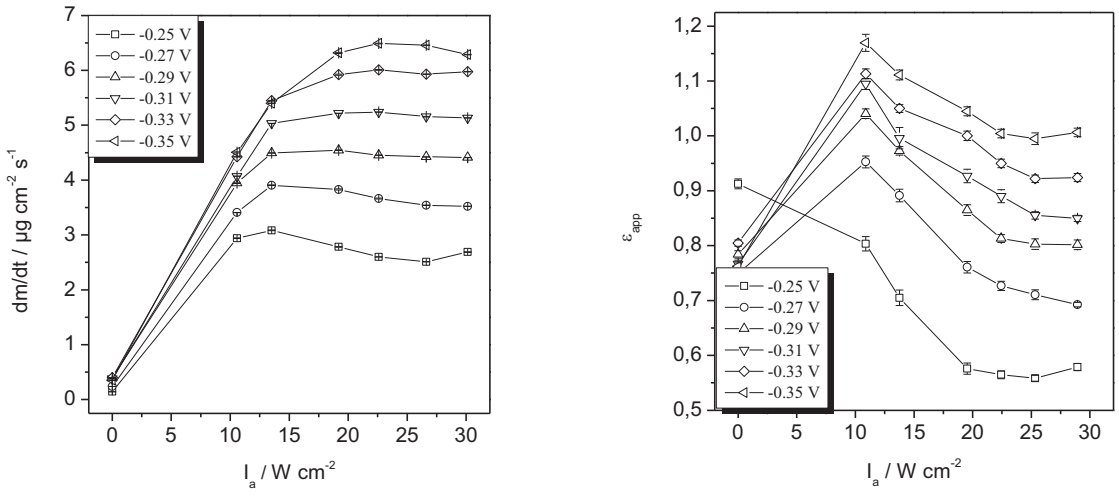

a) b)

Figure 3.29 Potentiostatic deposition from an electrolyte of 0.01 M $CuCl_2$ + 0.5 M NaCl, pH ~ 1, sweep rate 5 mV/s, *d*=22 mm. Change in a) deposition rate and b) apparent current efficiency with ultrasonic intensity at potentials between -0.25 and -0.35 V.

The apparent current efficiency strongly decreased at a potential of -0.25 V with increasing ultrasonic intensity, although the deposition rate was increasing at the lower ultrasonic intensities. At all other

potentials the current efficiency at first strongly increased upon turning on the ultrasound whereas with further intensity increase it decreased (Fig. 3.29b). For the higher overpotentials the decrease in efficiency was less significant.

The current densities j_{el} measured in these experiments (Fig. 3.30a) were much larger upon application of ultrasound. At the lowest intensity of 10.6 Wcm^{-2} the electrical current for the lowest applied potential was about 6 times larger than under silent conditions. Up to 22.6 Wcm^{-2} the current was significantly increasing with increasing I_a for all potentials. With a further increase in ultrasound intensity currents became only slightly larger. Increasing of the currents with larger ultrasonic intensity was more significant at lower potentials (larger overpotentials).

A similar tendency was found for the currents j_M, (by Eq. 1.4.20 as in Annex 2) expected from the deposited mass and calculated for z = 2 (Fig 3.30b). At lower ultrasonic intensities and for all potentials, there was a strong increase in these currents, but with a further intensity increase, over 19 Wcm^{-2} the effect was much less, almost negligible.

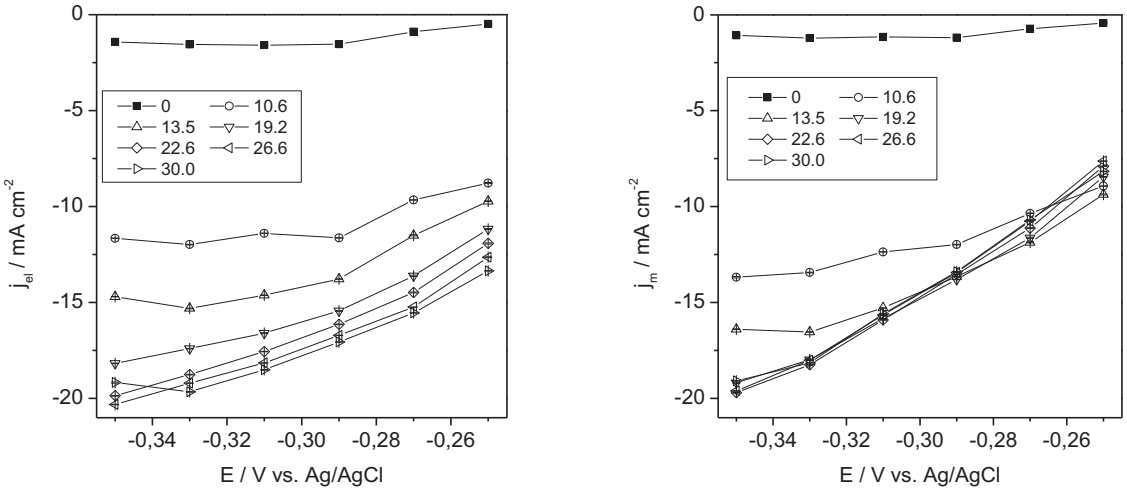

a) b)

Figure 3.30 Potentiostatic deposition from an electrolyte of 0.01 M $CuCl_2$ + 0.5 M NaCl, pH ~ 1, sweep rate 5mV/s, variation of ultrasonic intensity up to 30 Wcm^{-2}, a) measured current and b) calculated current from the mass for 100 % current efficiency for z=2, versus potential.

The two step nature of the redox process in chloride electrolyte is mostly responsible for the behavior of the parameters in these experiments. The presence of the ultrasound leads to enhanced mass transport, and thus an enlarged Cu (II) concentration near to the electrode. More Cu(II) provokes more Cu (I) formation, which is beneficial for electrodeposition. However, mass transport is not enhanced just in one way and the formed Cu(I) is also very effectively removed from the electrode. Reverse effects caused by ultrasound explain maximum deposited mass at intermediate intensities and mass decrease with further intensity increase. Cavitation at the electrode also might contribute to the mass decrease, that in turn leads to a decrease in current efficiency. In order to further improve the understanding of the kinetics of the Cu chloride system in the presence of ultrasound, rotating disc electrode studies were carried out for comparison.

3.3.4 Rotating disc electrode experiments

In the experimental setup with a rotating disc electrode the mass transport was enhanced as well. For the sake of comparison and further clarifying the nature of the ultrasound influence, cyclic voltammograms on the Pt rotating disc electrode with a rotation rate between 500 and 3000 rpm were recorded in the same potential range as the sonovoltammograms (Fig. 3.31a). Next to the recorded cyclic voltammograms, for comparison, cyclic sonovoltammograms at ultrasonic intensities up to 29 Wcm^{-2} are presented as well (Fig. 3.31b). A stirring effect is present in RDE as in experiments with ultrasound, thus mass transport is enhanced and currents are larger due to the decreased diffusion layer thickness. All these effects are further enhanced with increasing rotating rate of the RDE. The peak couple at higher potentials also disappeared as with ultrasound. With increasing the rotation rate there was a slight shift in the potential where the deposition started but not as significant as with ultrasound. Anodic peak currents also increased with the rotation rate, as a consequence of increased deposited mass, but part of the peak still remained at negative currents.

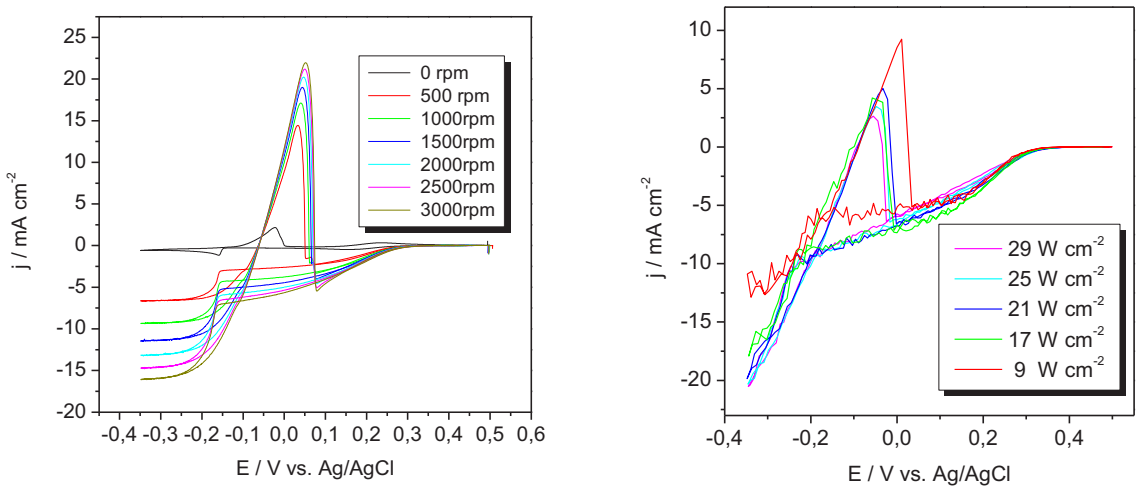

a) b)

Figure 3.31 Electrodeposition and –dissolution of Cu from an electrolyte of 0.01 M $CuCl_2$ + 0.5 M NaCl, pH ~ 1 a) on a rotating Pt disc electrode at rotation rates of 0, 500, 1000, 1500, 2000, 2500, and 3000 rpm and b) at different ultrasonic intensities on Au as given in the legend. Sweep rate: 5 mV/s. Experiments were performed under Ar. Note: different scaling used because of the better visibility of the diagram showing different magnitudes of the recorded parameters.

Maximum cathodic currents from RDE experiments and from experiments with ultrasound intensity up to 29 Wcm^{-2} are shown on the Figure 3.32. The maximum cathodic currents at 1500 rpm are similar in magnitude as maximum currents at an intensity of 9 Wcm^{-2}. The maximum cathodic currents for the highest rotation rate (3000 rpm) are less than at an intensity of 17 Wcm^{-2}. Under the influence of the ultrasound, even with the lowest intensity, currents were much noisier than in RDE measurements, Cu deposition under ultrasound started always at more negative potentials and the anodic peak current was smaller.

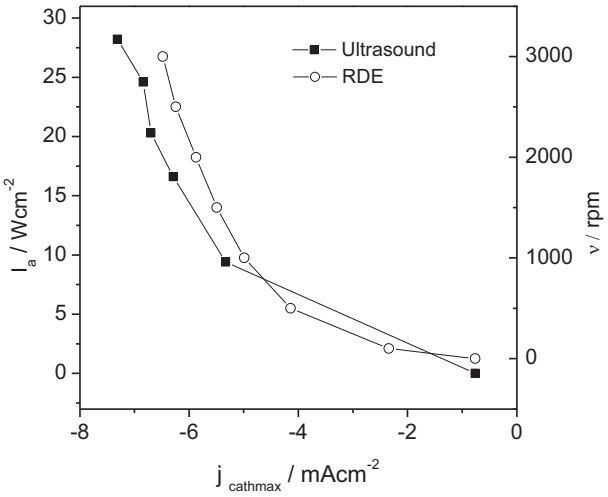

Figure 3.32 Maximum cathodic currents (full squares-in ultrasound field and empty circles in RDE experiments) recorded during electrodeposition and –dissolution of Cu from an electrolyte of 0.01 M $CuCl_2$ + 0.5 M NaCl, pH ~ 1 a) on a rotating Pt disc electrode at rotation rates of 0, 100, 500, 1000, 1500, 2000, 2500, and 3000 rpm and b) at different ultrasonic intensities on Au as given in the legend. Sweep rate: 5 mV/s. Experiments were performed under Ar.

In RDE experiments, for both reduction processes, the reduction of Cu(II) to Cu(I) and Cu deposition, limiting current conditions were reached. The limiting currents for Cu(II) reduction to metallic Cu were slightly larger than twice the limiting current of Cu(I) formation (Fig. 3.33). The reason for this small deviation could be the increased surface area due to the deposition of a rough Cu layer. On the other hand with ultrasound, only at the lowest ultrasonic intensity limiting behavior is observed.

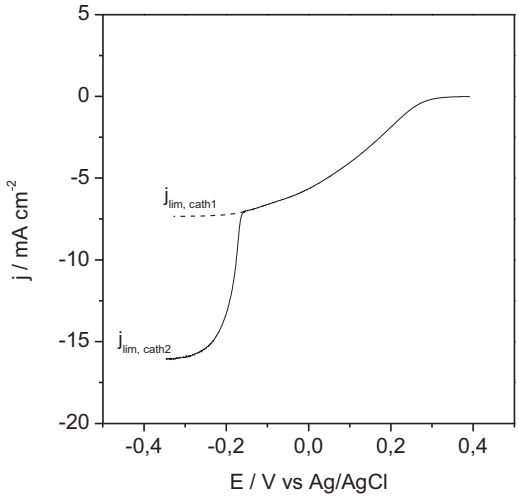

Figure 3.33 Limiting currents for Cu(I) ($j_{lim,\ cath1}$) and Cu metal formation ($j_{lim,\ cath2}$) during electrodeposition of Cu from an electrolyte of 0.01 M $CuCl_2$ + 0.5 M NaCl, pH ~ 1 on a rotating Pt disc electrode at rotation rate of 3000 rpm, sweep rate 5mVs^{-1}, under Ar atmosphere.

From the recorded cyclic voltammograms diffusion coefficients and the diffusion layer thicknesses can be obtained [159].

Equation 1.4.11 could be applied for both redox processes (both showed limiting behavior for all rotation rates) and one could expect a straight line for the plot j_{lim} versus $\omega^{0.5}$, the Levich plot (Fig. 3.34a). From the slope and for ν = 0.0103 cm^2 s^{-1} (literature data for 0.5 M NaCl [240]), z = 1 for Cu(I)

formation and $z = 2$ for Cu formation under limiting conditions diffusion coefficients of 5.6 10^{-6} and 6.7 10^{-6} cm^2 s^{-1} (Annex 8) were obtained and they were in a good agreement with values of D = 5-8·10^{-6} cm^2s^{-1}obtained in literature [232, 239]. From Equation 1.4.12, diffusion layer thicknesses of 11 μm at 1500 rpm and 7.9 μm at 3000 rpm can be calculated (Annex 9).

A Levich plot was also made for currents at an intermediate potential of -0.17 V (taken from CV data), where Cu deposition is already taking place, but not yet under diffusion control (Fig. 3.34b). In this region two parallel reactions are taking place, reduction of Cu(II) to Cu(I) occurs under diffusion control and Cu(I) to Cu under mixed control. In addition nucleation processes are taking place as well. Thus the Levich plot is not linear in this region.

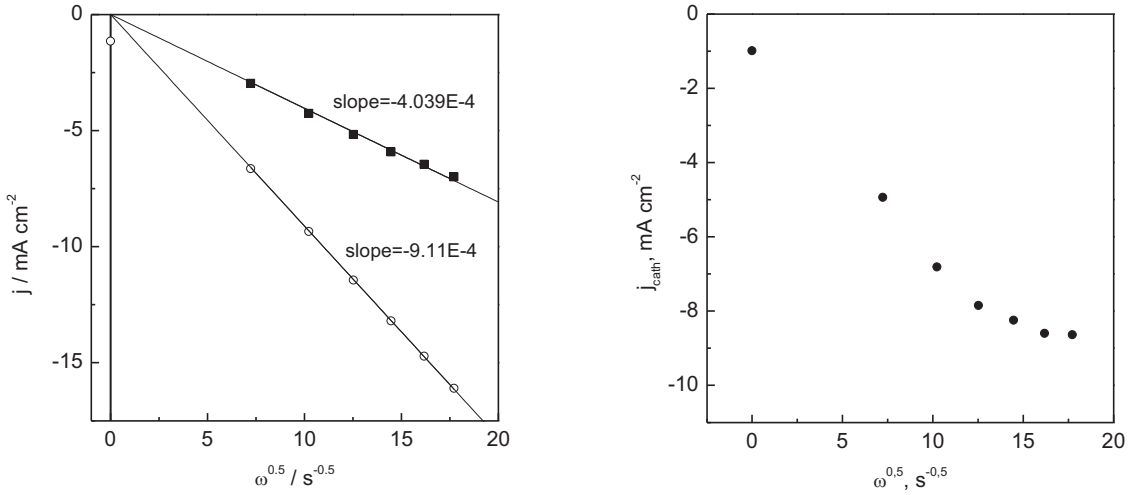

Figure 3.34 a) Dependence of limiting currents for the electrochemical formation of Cu(I) (squares) and Cu(0) (circles) on the electrode rotation rate. Lines: linear fits through the origin, neglecting the current measured without rotation b) Dependence of cathodic currents on rotation rate at an intermediate potential of -0.17 V where deposition takes place but before reaching limiting conditions.

According to Eq. 1.4.14 and from the set of potentiostatic depositions with a potential variation between -0.25 and -0.35 V and a variation of ultrasonic intensities for each potential (Fig. 3.30a), by plotting reciprocal of measured current $1/j$ versus $1/I_a^{0.5}$ one obtains the analogue of a Koutecký-Levich plot for the ultrasonic data (Fig. 3.35).

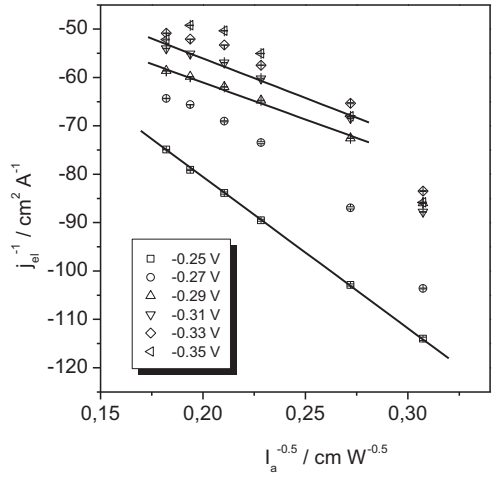

Figure 3.35 Mass transport plots analogous to Koutecký-Levich plots for the currents j_{el} measured during potentiostatic Cu deposition at different applied potentials (legend) and ultrasonic intensities I_a. Lines: Linear fits.

Only at a potential of -0.25 V the plot was linear. At this potential most of the electric current was due to Cu(II) reduction to Cu(I), and only little Cu deposition occurred. The slope of the linear fit gave a value for $K = 1.21 \cdot 10^6\ \Omega^{-0.5}\ cm^{1/6}\ mol^{-1}\ s^{2/3}$, and from the intercept an activation-controlled current density of 56 mA cm^{-2} was calculated (Annex 10). The obtained values were close to the values found in literature [241]. A dependency $j_{lim} = -3.17 \cdot 10^{-3}\ I_a^{0.5}$ (Eq. 1.4.14) was obtained and currents of j_{lim} = -9.5 mA cm^{-2} at 9 W cm^{-2} and j_{lim} = -17 mA cm^{-2} at 30 W cm^{-2} were calculated. The obtained limiting currents were larger than the currents observed in cyclic voltammograms at -0.25 V under ultrasound influence. Therefore the limiting behaviour for Cu(II) to Cu(I) reduction could not be reached.

Linear fits, despite a small deviation from linearity, were also done for -0.29 and -0.31 V. Slopes of the fits were smaller than for -0.25 V. Since the slope (and thus K) is proportional to the number of electron transferred (in analogy to the RDE Eq. 1.4.13) it indicates that for lower potentials z has higher values. This is in agreement with the consideration that at lower potentials more deposition of Cu occurs via Cu(II).When the potential range in cyclic voltammetry was extended to -0.7 V (Fig. 3.36) still no limiting current behaviour in experiments with higher intensity ultrasound at small distance was seen. This in part could be due to hydrogen evolution that will take place at such low potential in a pH 1 electrolyte. However, at a lower potential limit, still much larger amounts of Cu (Δf was almost 25 times larger) were deposited and the anodic peak appeared at positive currents. Because also the current efficiency did not decrease at the lower potentials, as one would expect if Cu deposition was under diffusion control and the increasing current due to hydrogen, the continuous increase in current must be due to cavitation disruption of the Nernst diffusion layer preventing depletion even at large deposition rates – even though one would then expect the occurrence of erosion. Since there was no residual deposit after the dissolution process was finished (Δf=0), there was no precipitation of Cu hydroxide as a possible consequence of the hydrogen evolution.

In all experiments with ultrasound, except for the lowest ultrasonic intensity at 22 mm distance between horn and quartz, no limiting behaviour was observed. Still, when the ultrasonic intensity increased above a certain value and especially for lower overpotentials the deposited mass started to decrease. Moreover, as a consequence of the decreased mass and enhanced removal of Cu(I), current efficiency also decreased.

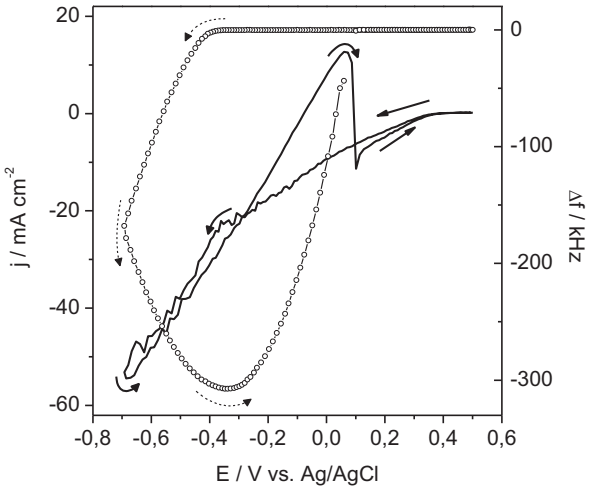

Figure 3.36 Electrodeposition and –dissolution of Cu, current densities (lines) and associated frequency changes (empty circles), from an electrolyte of 0.01 M $CuCl_2$ + 0.5 M NaCl, pH ~ 1 at d = 8 mm under an ultrasonic intensity of 76 W cm^{-2}, under Ar atmosphere. Arrows indicate direction of potential sweeps, sweep rate 5 mV/s.

3.3.5 Influence of ultrasonic intensity on Cu leaching

With the intention to resolve remaining unclarities and to understand more in depth how the presence of the ultrasound influences this specific electrochemical system, the development of copper corrosion in $CuCl_2$ was also studied.

At first, open circuit measurements with variation of the ultrasound intensity between 10 and 30 Wcm^{-2} were performed. A Cu layer was deposited for 3 minutes, at a potential of -0.33 V and at an ultrasonic intensity of 30 Wcm^{-2}. After the deposition was finished, an open circuit potential measurement was made, the first minute under silent conditions and then 9 minutes with different ultrasound intensities. The recorded open circuit potential and the concurrent change in mass during the measurement at 25 Wcm^{-2} is shown in Figure 3.37a. The OCP increased slightly, with a rate of 0.02 mVs^{-1}, under silent conditions and more significantly, with 0.2 mV s^{-1}, at an ultrasonic intensity of 25 Wcm^{-2}, as long as some Cu still remained on the electrode. After all Cu was dissolved, the potential steeply increased to a value of 350 mV. The mass decrease was about 0.20 $\mu gcm^{-2}s^{-1}$ under silent conditions, and at an ultrasonic intensity of 25 Wcm^{-2} increased to 6.4 $\mu gcm^{-2}s^{-1}$. Corrosion currents, calculated from the mass change were 0.3 $mAcm^{-2}$ and 9.8 $mAcm^{-2}$ (calculated according to Eq.1.4.20-Annex 11), for silent conditions and with ultrasound, respectively.

In Figure 3.37b, corrosion currents are presented for intensities up to 30 Wcm^{-2}, calculated from the mass change during open circuit measurements of Cu films, and cathodic currents recorded at same

potential (during cyclic voltammetry) as the corrosion potential in OCP measurements (-0.055 V) but in the absence of a Cu film on the electrode. Except for the lowest applied ultrasonic intensity, the absolute values of cathodic currents were smaller than the corrosion currents. Further, the corrosion currents were smaller than the limiting currents for Cu(II) reduction, calculated from the dependency $j_{lim} = -3.17 \cdot 10^{-3} I_a^{0.5}$ for all intensities (j_{lim} = -9.5 mA cm^{-2} at 9 W cm^{-2}, given in previous Chapter).

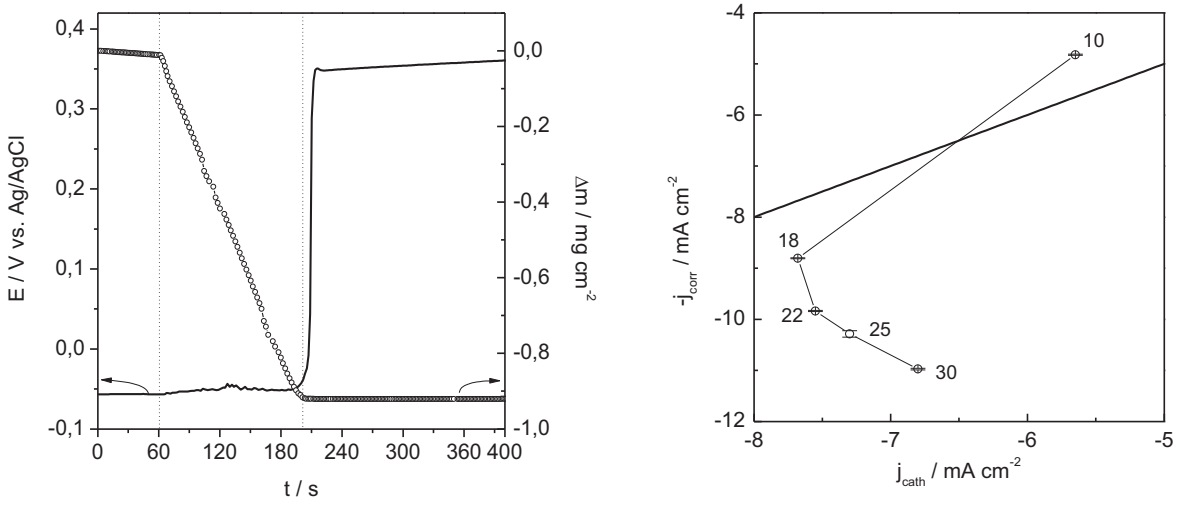

a) b)

Figure 3.37 a) Corrosion of Cu in $CuCl_2$ solution in open circuit potential measurements, under silent conditions (first 60 s) and at I_a = 25 W cm^{-2}, OCP potential (line) and mass change (empty circles) b) Corrosion currents calculated from mass changes in function of the currents measured at an applied potential of -0.055 V in the absence of a Cu layer. Numbers: I_a / W cm^{-2}. Straight line: $-j_{corr} = j_{cath}$.

In addition, 30 minutes of an open circuit measurement, for the first 60 seconds in silent conditions and the remaining time at an ultrasonic intensity of 76 Wcm^{-2}, was made on a Cu layer, deposited in 3 minutes at a potential of -0.3 V and at I_a = 19 Wcm^{-2}. The potential and the mass change recorded during the measurement are shown in Figure 3.38.

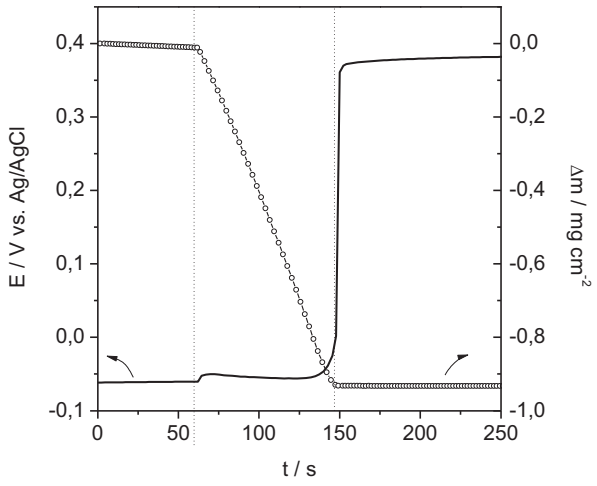

Figure 3.38 Corrosion of Cu in $CuCl_2$ solution during an open circuit potential measurement, under silent conditions (first 60 s) and at I_a = 76 W cm^{-2}, a) OCP potential (line) and mass change (empty circles).

The open circuit potential increased in silent conditions by about 0.02 mVs^{-1} and 0.8 mVs^{-1} at an intensity of 76 Wcm^{-2}. Under silent conditions, the mass decrease rate was about 0.2 $\mu gcm^{-2}s^{-1}$. When ultrasound with I_a= 76 Wcm^{-2} was applied, the mass loss rate increased to a value of 9.8 $\mu gcm^{-2}s^{-1}$. These mass decreases were corresponding to corrosion currents of 0.3 and 14.8 $mAcm^{-2}$ (calculated according to Eq.1.4.20 in a way as in Annex 10). After the entire deposit was dissolved the open circuit potential jumped by several hundred mV to a value of 380 mV. The potential, measured during corrosion in silent conditions was around -0.060 V. At this potential under silent conditions and without a Cu layer the measured cathodic current was about -0.32 $mAcm^{-2}$ (taken from the CV under silent conditions-Fig. 3.21a). At an intensity of 76 Wcm^{-2} the measured potential was about -0.055 V and the corresponding cathodic current was about -7.4 $mAcm^{-2}$ and about -10.8 $mAcm^{-2}$, at 15 mm and 8 mm horn-quartz distance respectively.

At the highest applied ultrasonic intensity, similar behavior was observed as at intermediate intensities up to 30 Wcm^{-2}. The cathodic current recorded at the corrosion potential was much smaller than the corrosion current, which in turn was smaller than the limiting cathodic current for I_a = 76 Wcm^{-2}.

As explained above and seen in many experiments, the deposited copper layer is not stable in Cu(II) solution in the presence of Cl^- ions (for characterization of the morphology it was always necessary to remove the samples very fast from the solution after deposition).

As for all applied intensities corrosion currents were smaller than calculated limiting currents for Cu(II) reduction, the decrease in mass during open circuit measurements on the previously deposited Cu layer (Fig. 3.37a and 3.38) can be described by the corrosion process:

$$Cu + Cu^{2+} + 4\ Cl^- \rightarrow 2\ [CuCl_2]^- \qquad (3.3.4)$$

At higher ultrasonic intensities, at the corrosion potential, cathodic currents were smaller than limiting currents but also by absolute value smaller than the corrosion currents. Therefore, the measured cathodic currents and thus corrosion could not completely explain the mass loss at larger I_a. There are two possibilities for the discrepancy between cathodic currents and (corrosion) currents calculated from mass loss: On the one hand the exchange current density for Cu(II)/Cu(I) might be larger on Cu than on Au, and on the other hand erosion might contribute to the mass change. The latter aspect will be discussed in the following section.

3.3.6 Influence of cavitation

In a chloride based electrolyte there were a few indications for the presence of the surface cavitation. At first, noisy currents were generally observed during cyclovoltammetric and potentiostatic measurements. At a potential of -0.33 V, with a 300 kHz frequency limitation, at an ultrasonic intensity of 76 Wcm^{-2} and at a horn-quartz distance of 8 mm a potentiostatic deposition experiment was intended to be done. The recorded resonance spectrum (Fig. 3.39a) at the beginning of the experiment was extremely noisy and there was almost no deposition occurring at the electrode. These are strong indications for the occurrence of caviation at or in the proximity of the electrode surface. After lowering the ultrasound intensity to 47 Wcm^{-2}, deposition started, indicated by the increase in the current efficiency from 0.6 to 49 % (Fig. 3.39b). Furthermore, the noise, quantitatively determined from the standard deviation χ of Lorentzian peak fit of the quartz admittance spectra, decreased by two orders of magnitude (Fig. 3.39b).

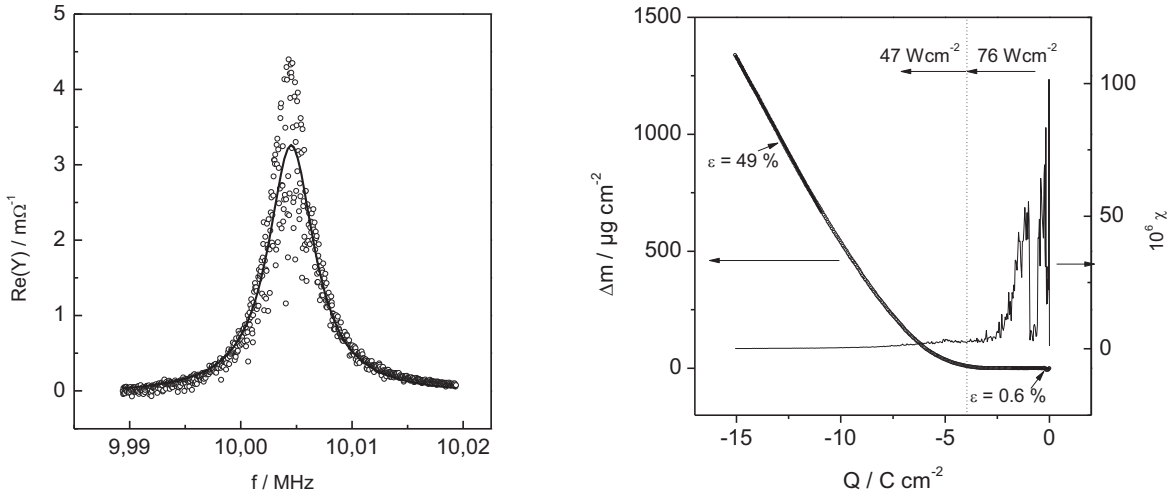

Figure 3.39 a) Characteristic resonance spectrum in the presence of cavitation at quartz surface at I_a = 76 W cm^{-2} and b) potentiostatic deposition of Cu from 0.01 M $CuCl_2$ + 0.5 M NaCl, pH ~ 1, at E = -0.33 V vs. Ag/AgCl, at a range of ultrasonic intensities (76 W cm^{-2} – 47 W cm^{-2}, see text): Total mass change Δm as function of total charge Q (ε determined from slope, I_a given on top of figure) and the corresponding standard deviation χ of Lorentzian peak fit of the quartz admittance spectra.

The resonance frequency of the bare quartz was followed during a set of cyclovoltammetric experiments where the intensity of the ultrasound was first stepwise increased and then stepwise decreased. It was observed that in the course of the experiment, after all deposited Cu was dissolved, the resonance frequency of the bare quartz increased (Fig. 3.40). This was a clear indication of gold electrode erosion. Also, after a set of the potentiostatic depositions and dissolutions performed at different ultrasonic intensities, one could see that the surface of the gold electrode was much rougher in the center, where it was exposed to the ultrasound, than at the edge (Fig. 3.41).

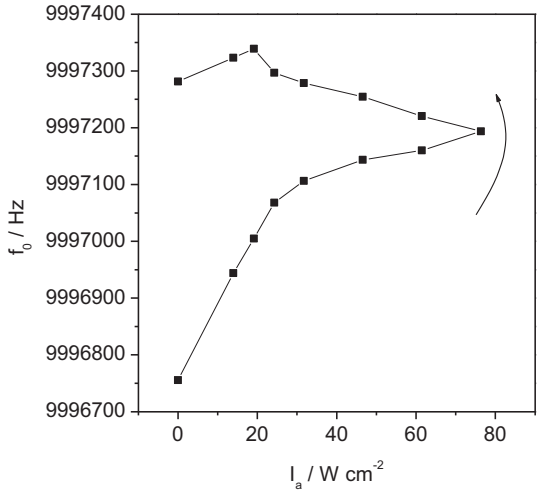

Figure 3.40 Resonance frequency measured before Cu deposition during cyclovoltammetric experiments with stepwise increasing and stepwise decreasing of I_a in a Cl^- based electrolyte. Arrow shows the order of experiments.

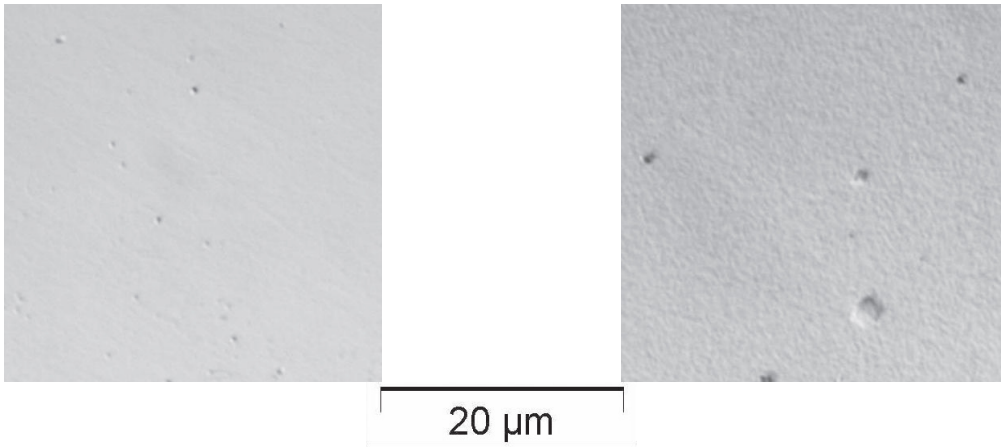

a) b)

Figure 3.41 Au surface of a quartz resonator after a series of sonoelectrochemical experiments in 0.01 M $CuCl_2$ + 0.5 M NaCl, pH ~ 1 at d = 8 mm a) outside the sealing O-ring where the Au was not in contact with the electrolyte b) in the center of the electrode exposed to solution and ultrasound.

Several observations made during the study in the chloride system could not be explained only by the enhanced mass transfer influenced by the ultrasound. In experiments with higher ultrasonic intensities, with increasing I_a, total Cu mass deposited was decreasing. Due to the decreased deposited mass the anodic peak currents decreased. In some potential ranges, with increasing I_a a decrease in cathodic currents was also observed. Beside cyclic voltammograms recorded at 22 mm horn-quartz distance, no limiting behavior was observed in experiments with ultrasound even for the extended range of potentials, and the cathodic currents were (except at 9 Wcm^{-2}) always higher than in RDE experiments for all applied rotation rates. A possible explanation for these discrepancies could be the presence of surface cavitation generated by the ultrasound. Erosion, as a consequence of the surface cavitation could lead to the removing of the deposited copper metal and therefore could explain the dependence of anodic peak currents on intensity as well as the large values for corrosion currents.

Chapter 4 - Synthesis of composites

4.1 Background

By combining two or more materials, having quite different properties, composites can be formed. Two different materials can build up a composite with unique properties. In the composite it is still possible to distinguish the individual materials. Most composites are made up of just two materials. One material (the matrix or binder) surrounds and binds together a cluster of fibers or fragments of a much stronger material (the reinforcement) [242].The biggest advantage of composite materials is their strength and stiffness combined with lightness [243]. With appropriately chosen combination of reinforcement and matrix material, as well as the manufacturing processes, it is possible to tailor properties that exactly fit the requirements for a particular structure for a particular purpose [244]. In general, composite materials are very durable. The flaw of composites is usually the cost. For the sake of synthesizing new materials and lowering the costs many studies have been conducted [245].

The electrochemical codeposition of metals and ceramic particles has been widely studied in literature in order to modify the metals properties like hardness, corrosion resistance, and high temperature oxidation resistance [246-251]. Fine particles are suspended in the electrolyte and embedded in the growing metal layer during electrocodeposition. Recently, intense research has been done on electrocodeposition of nanostructured composites due to enhanced mechanical properties, including wear and corrosion resistance [252]. It has been reported that by the incorporation of oxide particles such as Al_2O_3 and TiO_2 hardening of metals could be achieved [253-255]. Further, the corrosion rate was significantly decreased by $A1_2O_3$, $BaSO_4$, Si_3N_4, V_2O_5 and Cr_2O_3 embedded in a metal matrix [253-258]. N. S. Qu et al. reported higher microhardness, better wear resistance, enhanced corrosion resistance and improved high temperature oxidation resistance of Ni/CeO_2 composite in comparison to pure nickel both prepared by electrocodeposition [259].

As mentioned above, the experimental parameters play a significant role in the structure of the produced composite material and thus its properties. In this manner many studies were carried out in order to optimize the experimental conditions, rise the percentage of the incorporated particles and obtain desired improved material properties. It was found that the volume percentage of Al_2O_3 particles in a nickel matrix increases with increasing particle concentration in the bath [260]. Moreover, the nature of the particles has its own influence. Greco et al. reported that in a Ni matrix, three times as much TiO_2 was incorporated than Al_2O_3 for the same plating conditions [255]. Furthermore, an increase in the particles size increased the percentage of Al_2O_3 in Ni [261], but lowered the deposition rate [262]. Temperature was shown to have an influence on some systems. For $Ni-V_2O_5$ a maximum particle content at 50 °C was reported [258], but for $Ni-A1_2O_3$ no effect of temperature on the percentage of embedded particles was found [260, 263]. The use of codeposition for electrocatalysis was reported [264, 265]. Electrodes are made by codeposition of particles of an

electroactive material with a metallic matrix. The behavior of these electrodes was found to be controlled by the embedded material.

Nickel electroplating is one of the few surface finishing processes that can satisfy the requirements of decorative and functional applications. Ultrasound irradiation was found to enhance electrodeposition of Ni from a modified Watts electrolyte via increased mass transport of the electroactive species to the cathode caused by acoustic streaming [266]. It is reported that many plating characteristics, such as coating structure and morphology could be modified by the presence of ultrasound [267]. Parameters like internal stress and hardness distribution were found to be very sensitive on the ultrasound presence [268]. Application of the ultrasound irradiation showed many advantages in electrodeposition of pure metals and alloys, mostly higher current efficiencies [269], but also harder, more compact and better adherent deposits [270-272] corresponding to improved wear resistance, smoothness and brightness [172, 271].

Although many advantages of electrocodeposition of nanoparticles in thin metal films are reported, problem of nanoparticles agglomeration was frequently present [273]. In order to reduce agglomeration of particles, several strategies were developed such as variation of pH [274] and dilution of electrolyte [275]. O. V. Abramov reported ultrasound irradiation to be very helpful in dispersion of the agglomerated nanoparticles in the electrolyte as well as on the surface of the deposited film [269]. Moreover, when ultrasound was applied before and during electrodeposition, more uniform dispersion and less agglomeration of particles was observed [275, 276] in comparison without ultrasound.

Composites of Ni/CeO_2 and Co/CeO_2 [248, 259] have large significance because of the possible application in high temperature fuel cells. Nickel oxide is frequently used as cathode material in molten carbonate fuel cells. Under the extreme conditions, the cathode material undergoes dissolution. Addition of $LiCoO_2$ on the surface of the cathode is known to reduce the precipitation of Ni in the bath [265]. It is also reported that cerium oxide layers and Co-oxide ceria layers reduce nickel oxide dissolution and catalyze the Li incorporation into the nickel oxide cathode [277, 278] and therefore there is an increased interest in the electrodeposition of Co/CeO_2 composites for protection of cathodes in fuel cells.

Due to the strong interest in the electrocodeposition of Ni/CeO_2 and Co/CeO_2 composites and benefits ultrasound irradiation could provide sonoelectrochemical deposition of these composites applying the EQCM technique was studied.

The electrocodeposition of Ni and Co with dispersed nano-sized ceria particles was studied by the incorporation of oxide (ceria) dispersed in the electrolyte during electroplating of Ni or Co metal. For composite deposition, commercial nanocrystalline gadolinia doped ceria powder - GDC (Fuel Cell Materials, 5-10 nm crystallite size, softly agglomerated, particle size < 149 μm) was added to the metal electrolyte. Prior to the deposition, the electrolyte was ultrasonically treated before transfer to the cell. Ultrasound also was applied a few seconds before and for the entire duration of the deposition

ensuring bath agitation and break up of particle agglomerates. All experiments were done without deaeration. Ceria content in solution and the applied ultrasonic intensity I_a were varied. Layers of the co-deposits were made by potentiostatic and galvanostatic co-deposition, with the aim to find optimal conditions for the deposition of good composites.

4.2 Ni/CeO_2 system

For the electrodeposition of Ni/CeO_2 composite, two different electrolyte compositions were used: The Watts electrolyte (30 g/l $NiCl_2$+234 g/l $NiSO_4$×6 H_2O+30 g/l H_3BO_3+3 mg/l sodium dodecylsulfate (SDS) [207]) and a sulfamate bath (100 ml/l of a 50 wt% solution of $Ni(NH_2SO_3)_2$+10 g/l $NiCl_2$×6H_2O+40 g/l H_3BO_3 [208]) at 50 °C. For both electrolytes, always first experiments with cyclic voltammetry in pure electrolyte were carried out, without addition of ceria, to obtain basic information about the electrochemical behavior of Ni in the corresponding electrolyte.

4.2.1 Watts electrolyte

Cyclic voltammetry under silent conditions

A preliminary cyclovoltammetric study was done in a Ni-Watts electrolyte without presence of the ceramic ceria particles. Three cycles in a potential range between 0.3 and -0.8 V, at a 5 mVs^{-1} scan rate, were recorded. The cyclic voltammograms under quiescent conditions are shown in Figure 4.1.

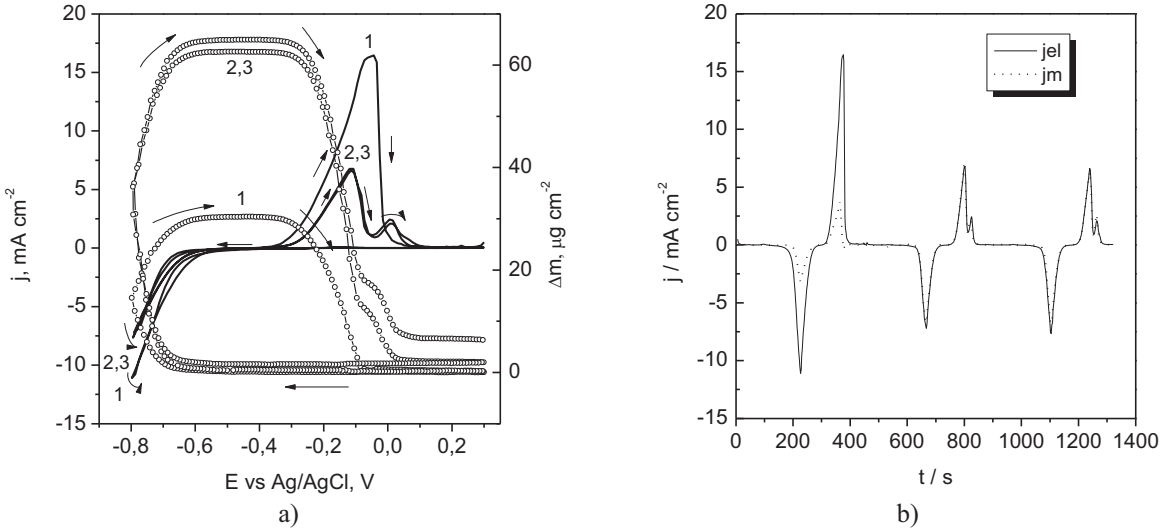

Figure 4.1 Electrodeposition and dissolution of Ni from Watts electrolyte at 5 mVs^{-1} at 50 ºC under silent conditions, a) measured electrical current and deposited mass versus potential and b) measured (dotted line) and calculated current (from the deposited mass for 100 % current efficiency-Eq. 1.4.19) versus time.

There was no cathodic peak observed in any of the three recorded cycles due to the high concentration of Ni in the electrolyte, thus deposition was not under mass control. There was a big discrepancy in the measured currents as well as in the frequency changes between the first and the second/the third cycle.

In the first cycle deposition started at potential below -0.6 V, which was accompanied by a decrease in the resonance frequency of the quartz resonator. The maximum cathodic current density was about -11 $mAcm^{-2}$ and the frequency change was 7 kHz, corresponding to ~ 30 μgcm^{-2}. In the beginning of the back sweep currents were decreasing, but still negative, and deposition was still taking place. At a potential of around -0.35 V the dissolution of the deposited Ni started. After the anodic peak, all deposit was dissolved and the current dropped to a background value. The traces of the second and the third cycles were severely different from the trace of the first cycle. The deposition started at a slightly lower value and the maximum cathodic currents were lower, up to about -7.6 $mAcm^{-2}$. The maximal change in the resonance frequency was up to 14 kHz, corresponding to the deposited mass of ~62.6 μgcm^{-2}, in the second and slightly larger in the third cycle. In the back sweep two anodic peaks were recorded. The second anodic peak was the smaller one (and more like a shoulder of the first anodic peak), overlapped the first one. After the second peak the dissolution process was complete. In the curve of the mass change a shoulder corresponding to the second anodic peak in the current trace was observed. When measured j_{el} and calculated j_M (from the mass change, determined by EQCM via frequency change, for 100 % current efficiency-Eq. 1.4.17) current densities were plotted versus time one could see a big discrepancy in the first cycle and very good matching for the second and the third cycle. In the first cycle maximum cathodic currents were higher but less deposit was obtained opposite to the second and third cycle where less current but more deposit was observed. The strong deviation between the measured and the calculated currents was detected when the change in damping was observed, and that could be the possible source (Fig. 4.2).

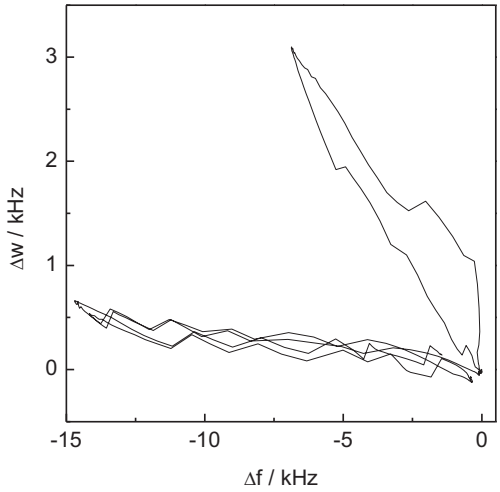

Figure 4.2 The change in the damping vs change in the frequency during electrodeposition and dissolution of Ni from Watts electrolyte at 5 mVs^{-1}, at 50 ºC, in a potential range of 0.3-(-0.8) V.

In the first cycle the damping change was ~ 3 kHz and the frequency change less than 7 kHz, thus the condition for the Sauerbrey equation (the frequency change to be at least 10 times larger than the change in damping) to be applied was not satisfied [128]. The calculated mass and thus the calculated current did not have realistic values. Normally, during the deposition of a rough, inhomogeneous

layer, the damping is increasing. When a rough layer is deposited, the surface area is also larger. The situation was clearly different in the second and the third cycle. The frequency change of almost 15 kHz was more than ten times bigger than the damping change (less than 1). Moreover, the mass on the quartz, after the dissolution cycle was finished, was increasing from cycle to cycle indicating incomplete dissolution in these conditions and probably due to $Ni(OH)_2$ incorporation into the deposit.

Cyclic voltammetry in an ultrasound field

At an ultrasound intensity of 26 Wcm^{-2} cyclic voltammograms in two cycles were recorded (Fig. 4.3).

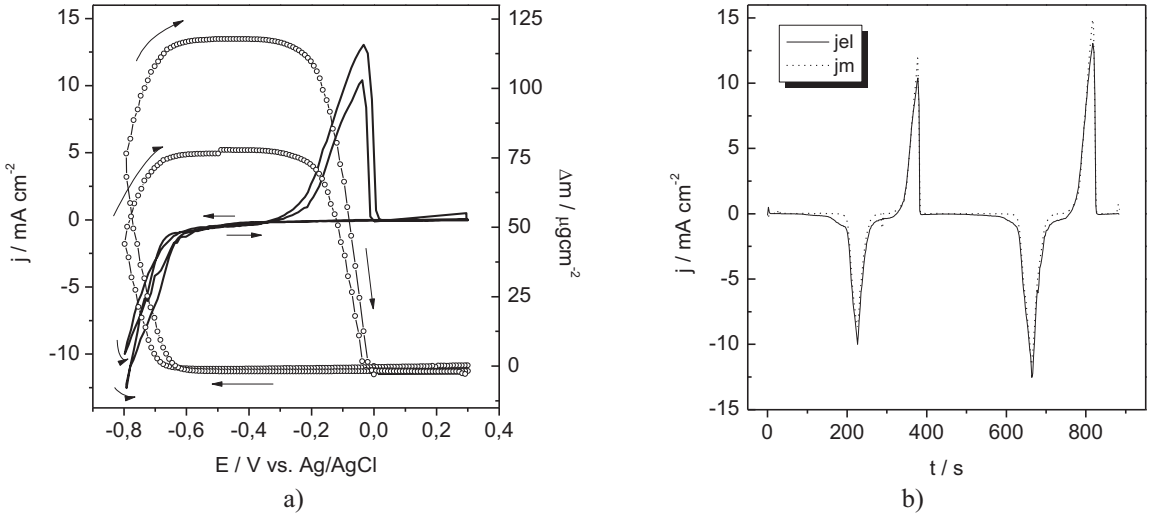

Figure 4.3 Electrodeposition and -dissolution of Ni from Watts electrolyte at 5 mVs^{-1} at 50 ºC, at 26 Wcm^{-2}, a) measured electrical current and deposited mass versus potential and b) measured and calculated current (from the deposited mass for 100 % current efficiency - Eq. 1.4.20) versus time.

The shape of the recorded cyclic voltammograms in the first and the second cycle was similar, with enlarged maximum current densities and deposited mass in the second cycle. The ultrasound did not influence the potentials where deposition and dissolution took place. The dissolution peak did not have a shoulder as without ultrasound. The highest damping increase recorded was ~1 kHz and was less than ten times of the frequency change, thus Sauerbrey equation could be applied. The currents calculated from the mass j_M for 100 % efficiency (Eq. 1.4.20) were in a very good agreement with the measured values.

The dependency of the recorded parameters on the ultrasonic intensity is shown in Figure 4.4. All observed parameters, the maximum cathodic current density, the deposited mass, and consequently the current of the anodic peak as well as the cathodic charge followed a similar trend with the ultrasonic intensity. In the presence of ultrasound and at lower intensities, an initial increase was observed. With a further increase in the ultrasound intensity, a decrease in these parameters was observed and again an increase with the highest ultrasound intensity applied (26 Wcm^{-2}).

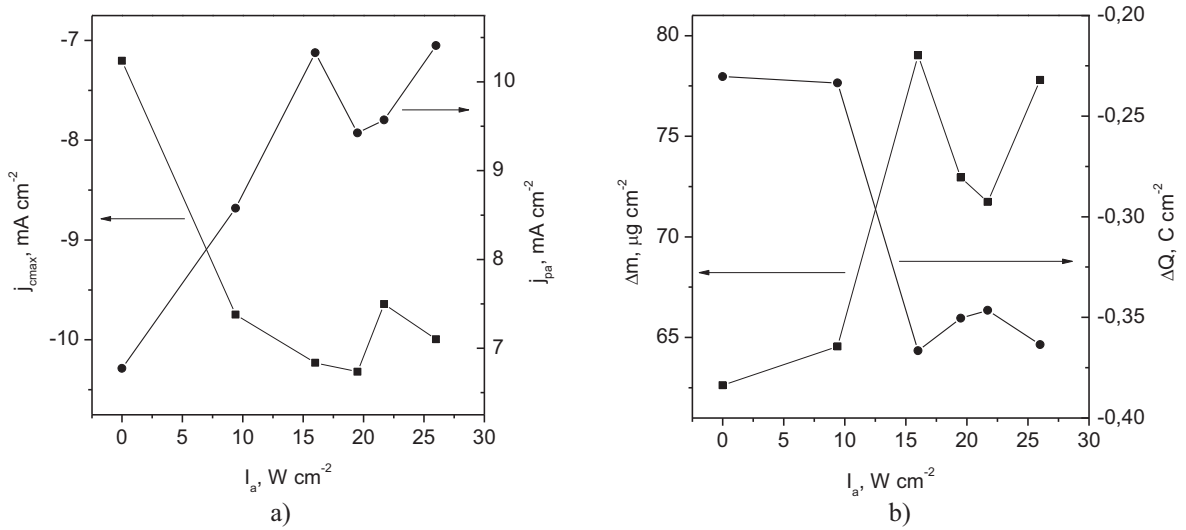

Figure 4.4 Recorded parameters during electrodeposition and –dissolution of Ni from Watts electrolyte in a single voltammetric cycle between 0.3 – (-0.8), 5 mVs^{-1}, a) maximum cathodic current (squares) and anodic peak current (circles) densities and b) maximum deposited mass and total cathodic charge densities.

After addition of 5 g/l GDC to the Watts electrolyte and at an ultrasound intensity of 26 Wcm^{-2}, cyclic voltammetry was carried out. The shape of the first and the second cycle were similar, without cathodic peaks and with one anodic peak in each cycle (Fig. 4.5). Still, there was a big difference in values of measured parameters between the cycles. In the first cycle, the maximum cathodic current (about -7.5 mAcm^{-2}) and the deposited mass (~53 µgcm^{-2}) were almost half the ones in the second cycle (about -13.2 mAcm^{-2} and ~102 µgcm^{-2}, respectively). In the beginning of the first cycle, there were some drifts in the mass change curve. At the end of the first cycle not all deposited mass was dissolved during the back sweep.

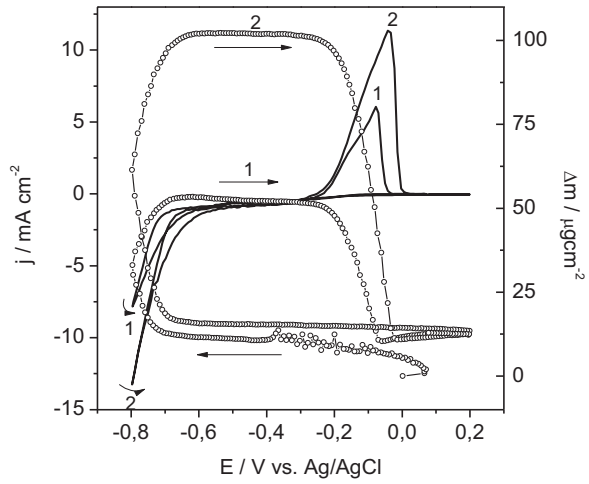

Figure 4.5 Measured electrical current (line) and the deposited mass (empty circles) during electrodeposition and -dissolution of Ni from Watts electrolyte in potential range of 0.2-(-0.8), at 5 mVs^{-1} and 50 ºC, at an ultrasonic intensity of 26 Wcm^{-2}.

Potentiostatic deposition

Potentiostatic deposition of Ni from Watts electrolyte was done at a potential of -0.8 V for 10 min and at an ultrasound intensity of 28 Wcm^{-2}, without and with addition of 5 g/l ceria. Current transients recorded during deposition are shown in Figure 4.6. Under the same conditions as for pure nickel, Ni-ceria composite deposition was performed in order to study the influence of the ceria addition on the morphology of the deposits and to determine the amount of the embedded ceria.

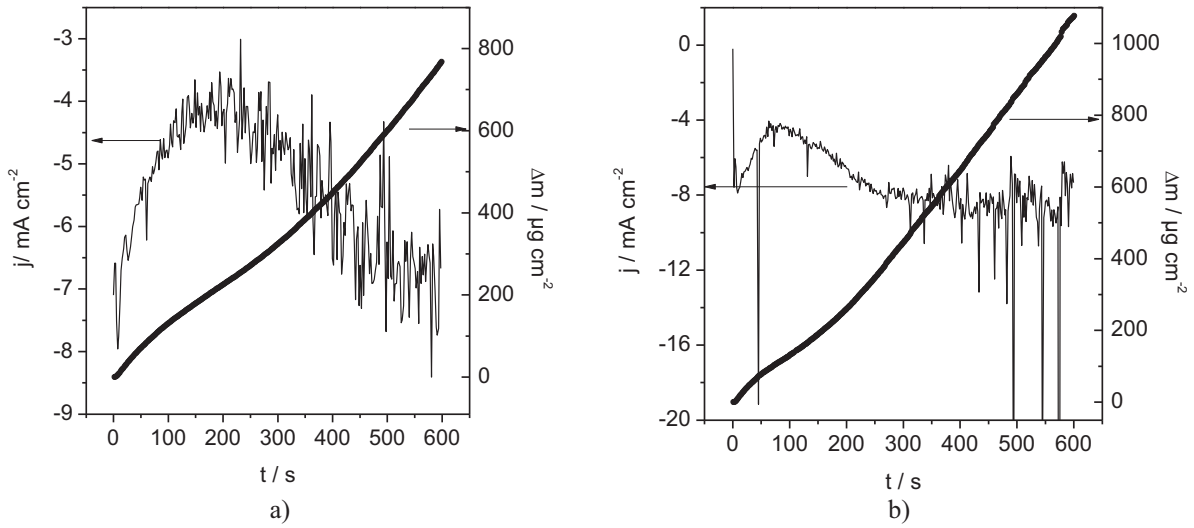

Figure 4.6 Current transients (line) recorded during 10 min of potentiostatic deposition from Watts electrolyte at -0.8 V and at 28 Wcm^{-2}, together with deposited mass (circles) a) without ceria and b) with 5 g/l ceria. Note: different scaling used because of the better visibility of the diagram showing different magnitudes of the recorded parameters.

At a 78 % current efficiency, about 770 μgcm^{-2} of nickel was deposited. At the same current efficiency ~ 1.1 $mgcm^{-2}$ of composite was deposited, with an average maximum current density of – 7.6 $mAcm^{-2}$. The current was already noisy during deposition of pure nickel (Fig. 4.6a), but with ceria additional jumps in the current values were observed (Fig. 4.6b). Observed spikes in the current transients are explained in literature as the consequence of the developed cavitation when the ultrasound intensity is above the threshold for a certain system [170, 178, 182]. Cavitation leads to a combined effect of material ablation from the surface and fast random changes in the surface concentration.

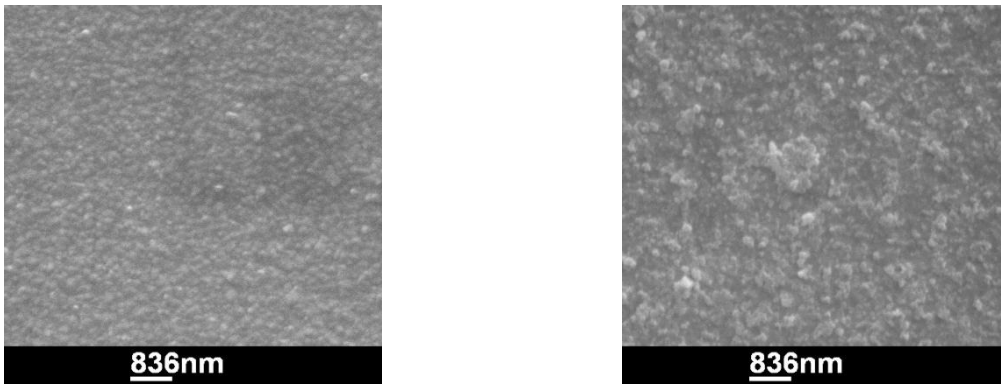

a) b)

Figure 4.7 Morphology of potentiostatically deposited layers for 10 min at E = -0.8 W at 28 W cm^{-2} from Watts electrolyte a) without and b) with ceria addition.

The amount of ceria embedded was found by EDX to be 1.8 wt% (applying a correction factor of 1.15 based on EPMA measurements). An EDX measurement at a specific location (point analysis) gave a much larger ceria content of 12%. It was supposed that at this position a larger CeO_2 particle was embedded. For this electrolyte, where features of embedded ceria were visible, the morphology of the deposits was clearly altered by the presence of ceria (Fig. 4.7). Similar observations have been made in literature [246].

4.2.2 Sulfamate bath

Electrodeposition and dissolution of Ni and Ni/CeO_2 in an ultrasound field

Ultrasound caused significant changes in cyclovoltammograms in nickel sulfamate bath (Fig. 4.8a). At an ultrasonic intensity of 22 Wcm^{-2}, in the potential range of 0.3 to (-0.73) V and at 5 mVs^{-1} scan rate, cyclovoltammetric electrodeposition and -dissolution of nickel was carried out. Whereas the curve of the deposited mass looked similar as under silent conditions, the current trace was totally different. The currents during the forward sweep at more negative potentials were smaller than during the back sweep. Besides a small potential range in the beginning of the forward sweep and at the end of the back sweep, the current was negative, even in the range where Ni dissolution was recorded in the EQCM signal. On the back sweep there was a positive peak superimposed to the current trace. When the current, calculated from the mass change during the deposition and the dissolution by Faraday's law (for 100 % current efficiency), was plotted versus the potential and compared with the recorded cyclic voltammogram at 22 Wcm^{-2}, one could see that the superimposed peak was matching with the dissolution peak (Fig. 4.8b). The obtained curve was also very similar to the corresponding curve under silent conditions.

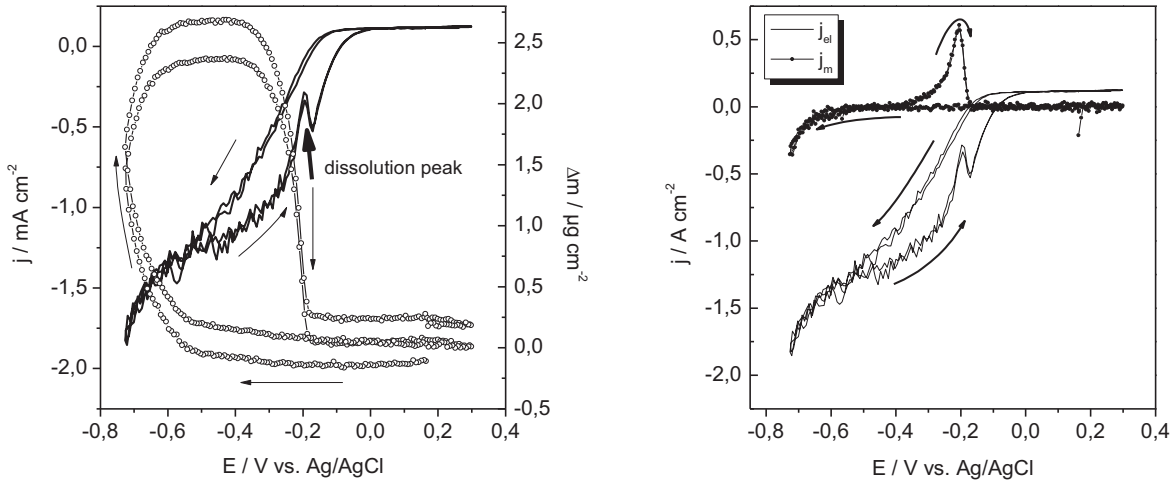

a) b)

Figure 4.8 Measured electrical current density (black) during electrodeposition and -dissolution of Ni from sulfamate bad, (0.3-(-0.73) V), 5 mVs^{-1}, 50 ºC and 22 Wcm^{-2} (bold arrow shows the position of the dissolution peak) and a) deposited/dissolved mass (empty circles), b) current density (circles) calculated from the mass deposited assuming 100 % current efficiency. Note: different scaling used because of the better visibility of the diagram showing different magnitudes of the recorded parameters.

From the comparison of cyclic voltammograms it was concluded that the ultrasound did not alter Ni deposition itself a lot, but that it rather strongly accelerated side reactions. The main difference to the Watts electrolyte was the presence of the sulfamate ions. These ions could be the reason for the recorded discrepancy.

Addition of 5 g/l ceria to the sulfamate bath did not change significantly the shape of the cyclic voltammogram. The maximum cathodic currents were slightly larger and the deposited mass increased as well. The mass change curve, calculated from the frequency change, was also noisier in the presence of ceria (Fig. 4.9).

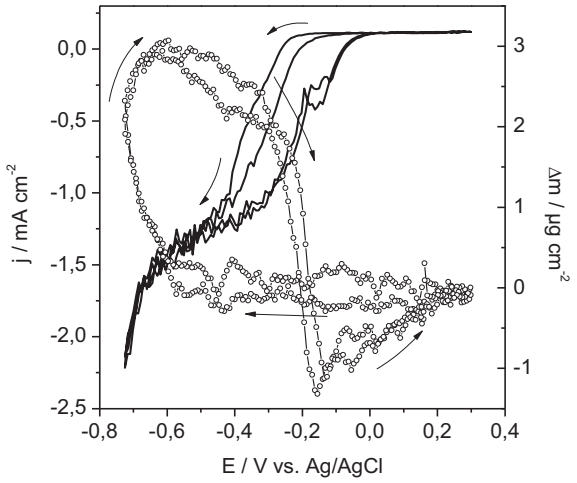

Figure 4.9 Measured electrical current density (line) and deposited/dissolved mass (empty circles), during electrodeposition and -dissolution of Ni from sulfamate bath, (0.3-(-0.73) V), 5 mVs^{-1}, 50 ºC and 22 Wcm^{-2}, 5 g/l ceria.

Potentiostatic and galvanostatic depositions

A series of potentiostatic and galvanostatic depositions of the Ni/ceria composite from the sulfamate bath was performed in order to study the morphology of the obtained deposits and to determine the embedded ceria content and finally to find optimal parameters for a good quality composite to be obtained.

The potentiostatic deposition of nickel from the Ni-sulfamate bath without addition of ceria was carried out at a potential of -0.73 V, for 30 min, under quiescent conditions. The change in the current and mass with time are shown in Figure 4.10. After an initial increase in the current, it decreased and then continued slightly to increase till the end of the deposition. The deposited mass of the nickel layer was ~0.9 mgcm^{-2}. An apparent current efficiency of 103 % indicated a slight role of side reactions and a possible deposition of $Ni(OH)_2$.

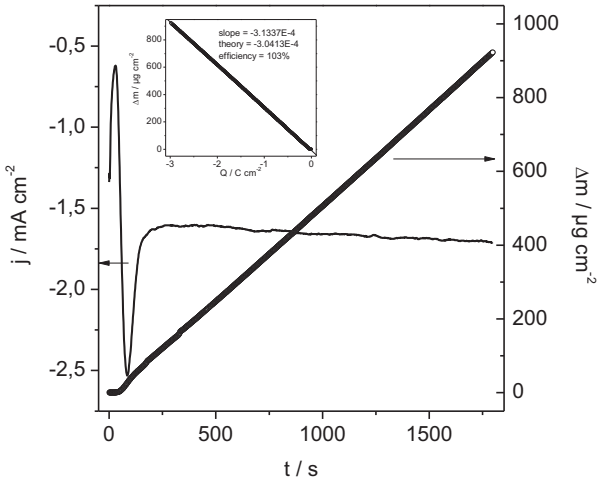

Figure 4.10 Current transient (line) recorded during 30 min of potentiostatic deposition of Ni from a sulfamate bath at -0.73 V, together with the deposited mass (circles).

The morphology of the obtained Ni layer is shown in Figure 4.11.

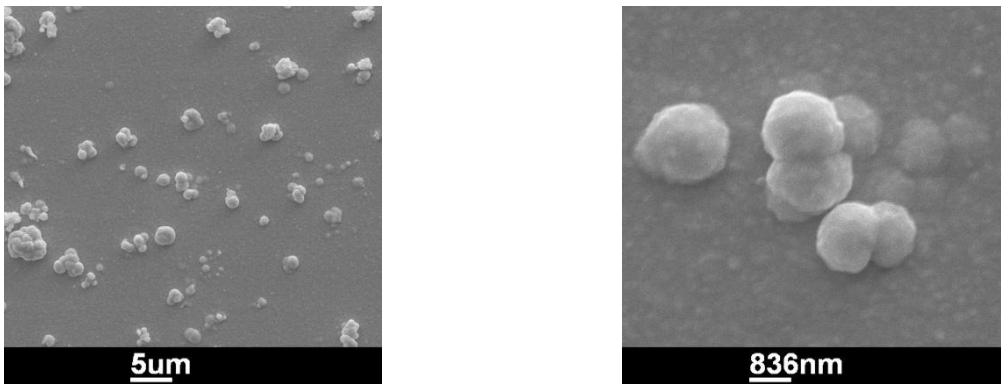

Figure 4.11 Morphology of the potentiostatically deposited Ni layer from sulfamate bath without ceria addition, 30 min, -0.73 V.

With deposition time extended to one hour, at an ultrasonic intensity of 28 Wcm^{-2}, deposition of a nickel/ceria composite was carried out at a potential of -0.73 V. Co-deposition was performed from the Ni-sulfamate bath with addition of 5 g/l of ceria. The currents increased in comparison with deposition without ceria addition and became also noisier (Fig. 4.12a). The current efficiency decreased to 30 % and the deposition rate was smaller. During one hour slightly more deposit was obtained, ~ 1 $mgcm^{-2}$. Figure 4.13a shows the morphology of the obtained deposit. With the normalization to a total content of 100 % an average 1.2 ±0.03 wt% of ceria content was obtained by EPMA analysis.

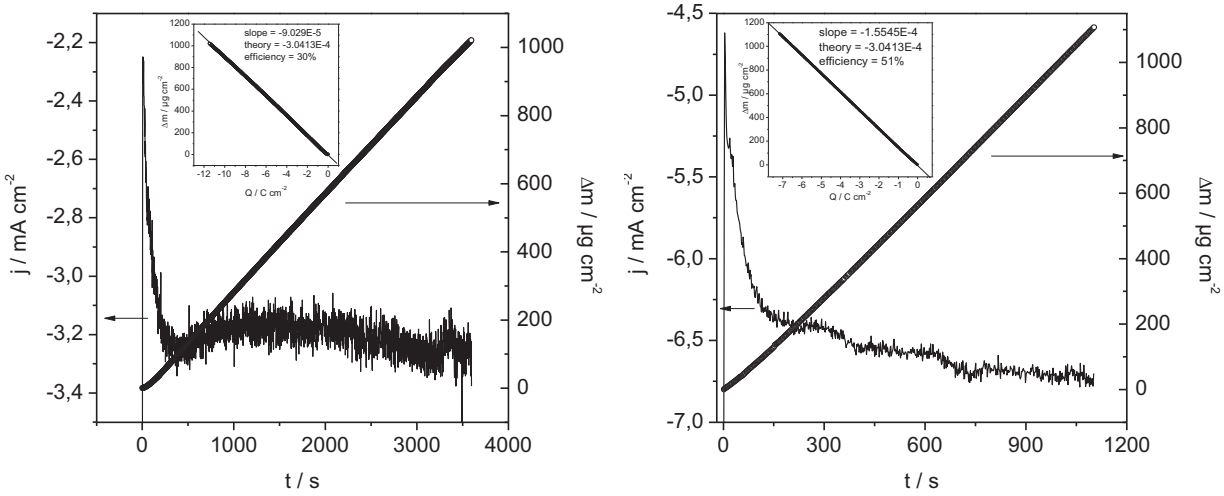

a) b)

Figure 4.12 Current transients (line) together with deposited mass (circles) recorded during potentiostatic deposition of a Ni/ceria co-deposit from a sulfamate bath at 28 Wcm^{-2} with addition of 5 g/l ceria a) at -0.73 V, 1 h and b) at -0.8 V, $\Delta f \leq 250$ kHz. Inserts: mass vs. charge plots for the determination of apparent current efficiencies. Note: different scaling used because of the better visibility of the diagram showing different magnitudes of the recorded parameters.

At a lower potential, -0.8 V, with a 250 kHz frequency limitation and under otherwise the same conditions co-deposition of Ni-ceria was also performed. At this larger overpotential, the deposition rate as well as the current efficiency (51 %) increased and a ceria content of 1.55 ± 0.02 wt% in the deposit was found. Besides slightly larger ceria content at -0.8 V in comparison to -0.73 V there was no significant difference in the morphology (Fig. 4.13).

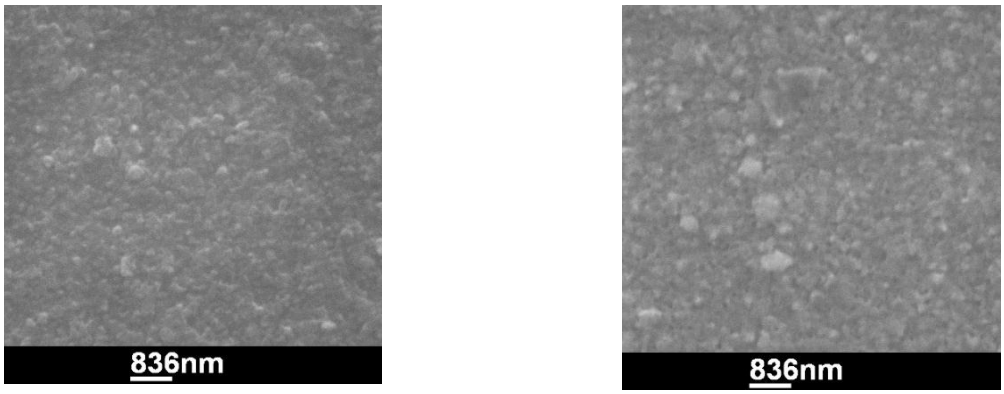

a) b)

Figure 4.13 Morphology of the potentiostatically deposited (28 Wcm^{-2}) Ni/ceria layer from sulfamate bath with 5 g/l ceria addition a) at -0.73 V, 1 h and b) at -0.8 V, $\Delta f \leq 250$ kHz.

From the sulfamate bath with addition of 5 g/l ceria, at an ultrasonic intensity of 28 Wcm^{-2} galvanostatic deposition of Ni-ceria composite was performed as well. For the first galvanostatic co-deposition the applied current density was -15 mA/cm^2. The change in potential and the deposited mass with time are shown in Figure 4.14a. With 70 % current efficiency, 1.9 $mgcm^{-2}$ of composite was deposited and an average of 2.08 wt% embedded ceria was found. The morphology of the obtained deposit is shown in Figure 4.15a.

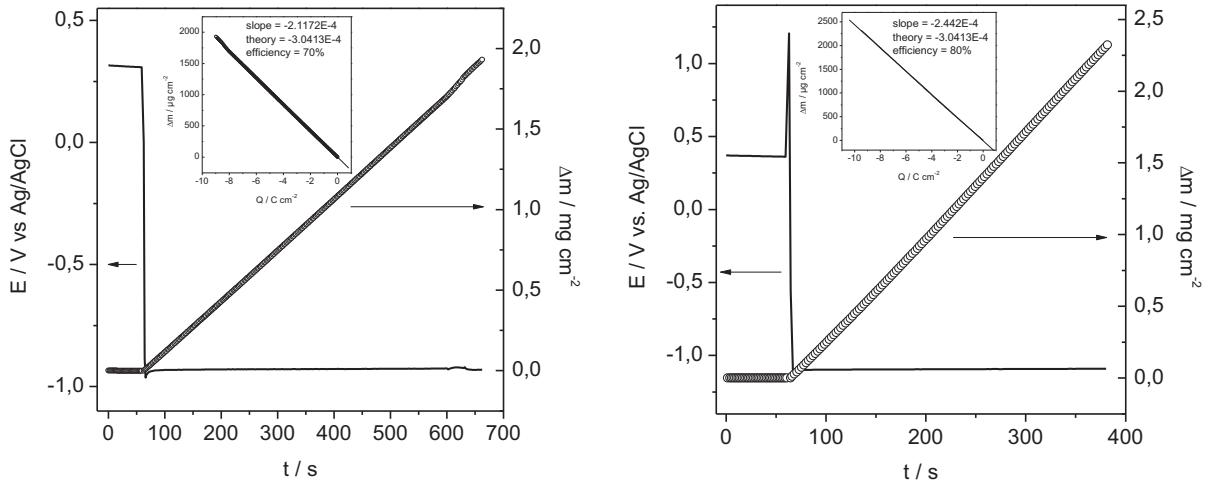

a) b)

Figure 4.14 Potential and mass change during galvanostatic deposition of a Ni/ceria composite from Ni sulfamate bath with addition of 5 g/l ceria in electrolyte at I_a=28 $Wcm^{-2}$and a current density of a) 15 and b) 30 $mAcm^{-2}$. Note: different scaling used because of the better visibility of the diagram showing different magnitudes of the recorded parameters.

For the following deposition, the current density was increased to -30 mA/cm^2 and otherwise the conditions remained the same. With an increased current efficiency of 80 %, 2.3 $mgcm^{-2}$ of composite was deposited corresponding to 2.4 wt% embedded ceria.

The morphology of the galvanostatically obtained deposits from sulfamate bath with added 5 g/l ceria is presented in Figure 4.15.

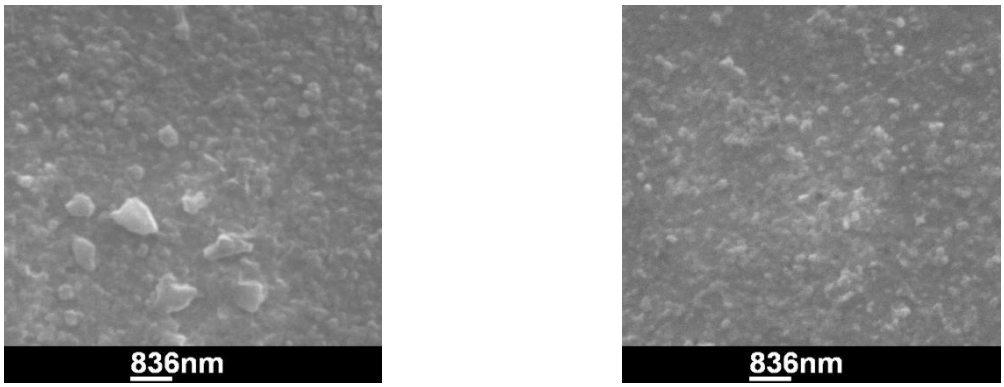

a) b)

Figure 4.15 Morphology of the galvanostatically deposited Ni/ceria composite from Ni sulfamate bath with addition of 5 g/l ceria in electrolyte at I_a=28 Wcm^{-2}and a current density of a) 15 and b) 30 mAcm^{-2}.

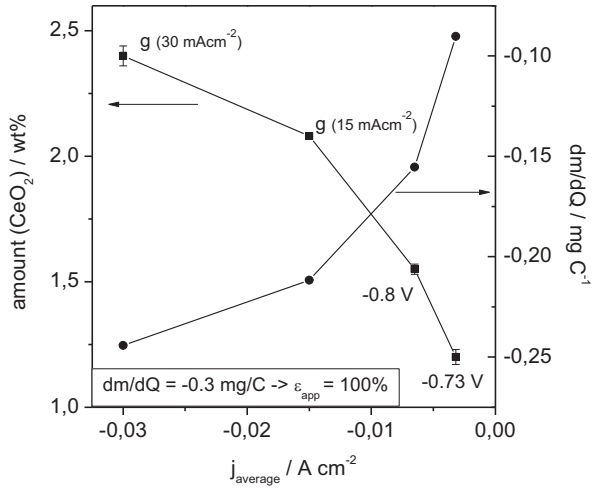

Figure 4.16 Amount of CeO_2 embedded in Ni (squares- g is for galvanostatic experiments with given current density in brackets and given potentials for potentiostatic experiments) and the average mass/charge ratio *dm/dQ* (circles) for electrodeposition of Ni/CeO_2 composites in function of the average current density.

In Figure 4.16, an overview of the results obtained for potentiostatic and galvanostatic depositions is presented. All depositions were carried out at an ultrasonic intensity of 28 Wcm^{-2}. With increasing current density, more ceria was embedded. The current efficiency increased as well. Still 2.4 wt% was the largest amount of ceria incorporated in the nickel layer. In these experiments rather low contents, 5 g/l ceria in the starting electrolyte, were used. In the literature [248], more ceria, between 5 and 20 vol% were found but for ceria concentrations of 50 g/l in the starting electrolyte.

Under the influence of the ultrasound, deposition and dissolution of nickel from Watts electrolyte and sulfamate bath are found to be very different. EQCM measurements gave the possibility to reveal the presence of side reactions and to conclude that these differences are not directly connected with the deposition of Ni films. The Ni concentrations in both electrolytes were high and deposition was not under mass control, so there was just a slight influence of the ultrasound on the deposition enhancement. In general, more negative currents led to an increase in current efficiency and an increase in the amount of the embedded ceria. The morphology of the deposits with ceria embedded

was altered but not so significant due to the small percentage of ceria content. There was no big difference in morphology of the films with ceria from two different electrolytes. Due to the quite enhanced side reactions, the current efficiency was far less than theoretically expected so that less ceria was embedded and it was not possible to determine the amount of ceria in the deposited films from EQCM data. Contrary to the relatively smooth pure Ni layer deposited, especially from Watts electrolyte, addition of ceria caused layer roughness. On the other hand the formation of very rough layers is actually, due to enhanced surface, a very good property for the application in fuel cells or as support for catalytic reactions.

4.3 Co/CeO_2 system

For the co-deposition in the Co system, a solution of 0.1 M $CoSO_4$ + 0.1 M Na_2SO_4 with pH adjusted to 4 [209] was used. All measurements were performed at 25 ºC with the electrochemical cell open to air.

4.3.1 Electrodeposition and dissolution of Co and Co/CeO_2

A cyclovoltammetric study of the Co system was performed in a potential range between 0.5 and -0.85 V at 5 mVs^{-1} scan rate. At first, the Co electrolyte without ceria addition was studied with a variation of the ultrasound intensities.

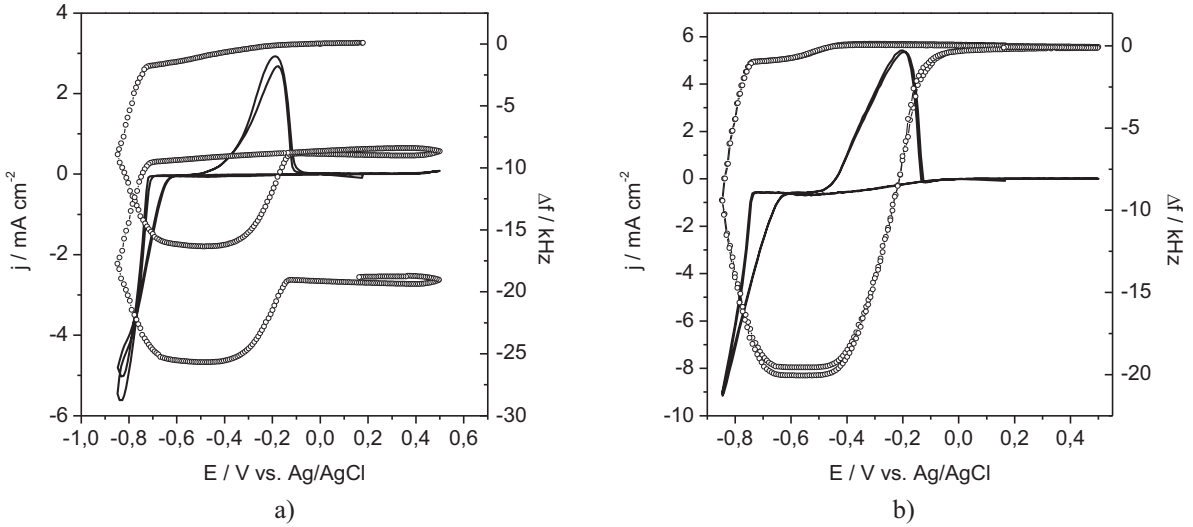

Figure 4.17 Current density (line) and deposited mass (circles) during electrodeposition and –dissolution of Co in a potential range of 0.5-(-0.85) V, at 5 mVs^{-1} in a function of potential in a) silent conditions and at b) 29 Wcm^{-2} ultrasonic intensity. Note: different scaling used because of the better visibility of the diagram showing different magnitudes of the recorded parameters.

Cyclic voltammograms under silent conditions and at an ultrasonic intensity of 29 Wcm^{-2} are shown in Fiure 4.17. Cobalt deposition under silent conditions started below –0.7 V (Fig. 4.17a). There was no cathodic peak observed, so deposition was not under mass transport control. Dissolution started around –0.5 V, and an anodic peak was located around –0.18 V. The frequency change curve followed

the deposition and dissolution process as expected, but not all deposited material during the cathodic sweep was dissolved during the anodic one. Almost half of the material remained on the electrode at the end of the first cycle. As already reported in literature [209], $Co(OH)_2$ was probably incorporated in the deposit, especially significant at lower potentials. This situation is more noticeable in the Co than in the Ni system because Co is less noble, standard potentials for the redox couples are for Ni/Ni^{2+} -0.25 V and for Co/Co^{2+} -0.29 V. Hydrogen evolution takes place already during the deposition process. Therefore the pH value near to the electrode is increased causing $Co(OH)_2$ precipitation. The remaining deposit was removed from the electrode by polarization to 0.65 V for several minutes.

There was no significant change in the shape of the voltammogram under ultrasonic irradiation. At an ultrasonic intensity of 29 Wcm^{-2} the currents and the mass deposited were slightly increased (Fig. 4.17b), but by a factor of less than two. Still, in the presence of ultrasound deposition was completely reversible. The enhanced mass transport under ultrasonic irradiation reduces the pH increase at the electrode and therefore the tendency for $Co(OH)_2$ precipitation.

Figure 4.18 shows cyclic voltammograms in the presence of 3 (a) and 5 g/l CeO_2 (b) at an ultrasonic intensity of 29 W cm^{-2}.

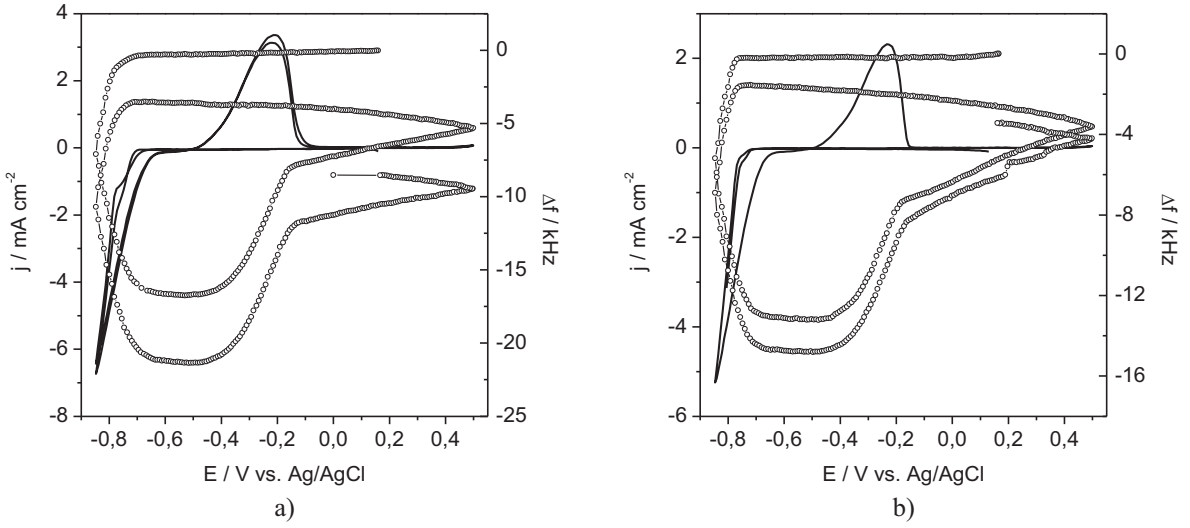

Figure 4.18 Current density (line) and frequency change (circles) during electrodeposition and –dissolution of Co in a potential range of 0.5-(-0.85) V, at 5 mVs^{-1} at 29 Wcm^{-2} with addition of a) 3 g/l and b) 5 g/l ceria. Note: different scaling used because of the better visibility of the diagram showing different magnitudes of the recorded parameters.

There was no significant change in the shape of the cyclic voltammograms. With the addition of ceria the damping was so high that the conditions for the Sauerbrey equation were not fulfilled anymore and it was not possible to calculate the deposited mass from EQCM. The addition of CeO_2 caused a decrease in the currents which further caused less frequency change due to the less deposited Co. And this was even more evident with increased amount of ceria added.

After the addition of ceria, even in the presence of ultrasound deposition was not totally reversible. There were always remaining deposits on the electrode after the end of the dissolution peak. Addition

of ceria particles increases the solution pH and thus favors the precipitation of hydroxides. According to highly increased damping, it can be concluded that a very inhomogeneous layer was deposited.

4.3.2 Potentiostatic deposition

Potentiostatic depositions at a potential of -0.85 V with a 250 kHz frequency change limitation and at an ultrasonic intensity of 28 Wcm^{-2} were carried out in Co electrolyte without and with 3 and 5 g/l ceria addition.

A comparative overview for potentiostatic depositions is given in Figure 4.19. After a strong initial increase, currents continued increasing till the end of the depositions. Still, the maximum cathodic currents were decreasing with the addition and a further increase of the ceria content. The frequency change was fastest for 3 g/l CeO_2. In the presence of ceria a strong increase in the damping was observed after a few minutes of deposition, indicating roughening of the electrode. The damping increased from less than 5 kHz in the electrolyte without ceria to more than 20 kHz (3 g/l ceria) and almost 120 kHz (5 g/l ceria) with ceria addition.

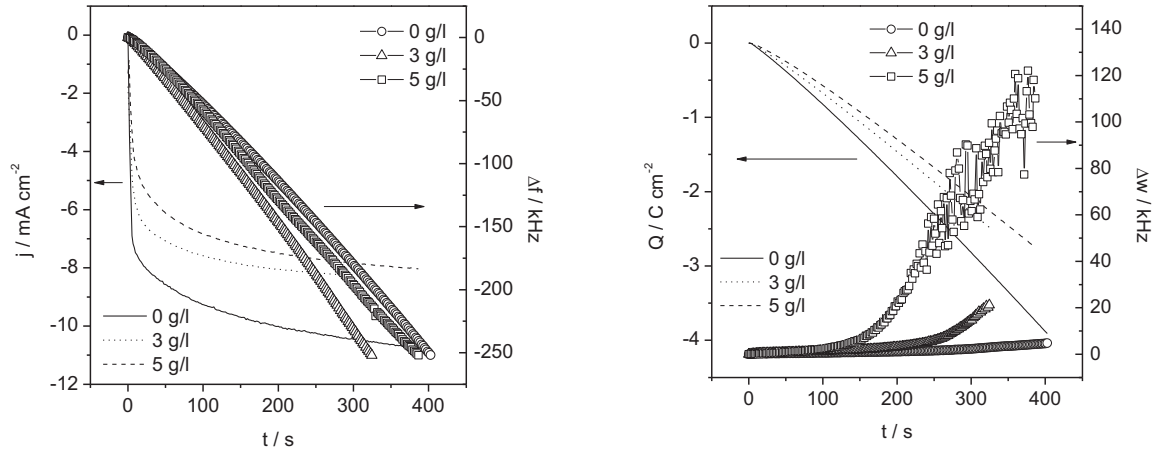

Figure 4.19 Potentiostatic deposition of Co and Co-ceria co-deposits at -0.85 V, 28 Wcm^{-2}, 250 kHz frequency limitation, without and with addition of 3 g/l and 5 g/l ceria. a) current transients and change in the frequency b) charge density and damping change.

For 3 g/l ceria the damping was still in the range where Sauerbrey equation can be applied, for 5 g/l ceria this was not any more the case.

Without ceria, with an apparent current efficiency ε_{app} of 93%, 1.1 $mgcm^{-2}$ deposit was obtained with an average thickness of about 2.3 μm, as determined from profilometry measurements. With the addition of 3g/l of ceria with an apparent current efficiency of 146 %, for the same frequency change, the average thickness was about 5.8 μm. The weight percentage of the embedded ceria was about 6.2% (from EPMA measurements). With the increased content of 5 g/l of ceria in the starting solution, the weight percentage of the embedded ceria was around 7.75 % and the average thickness was about 8.8 μm.

The morphology of the obtained deposits is shown in Figure 4.20.

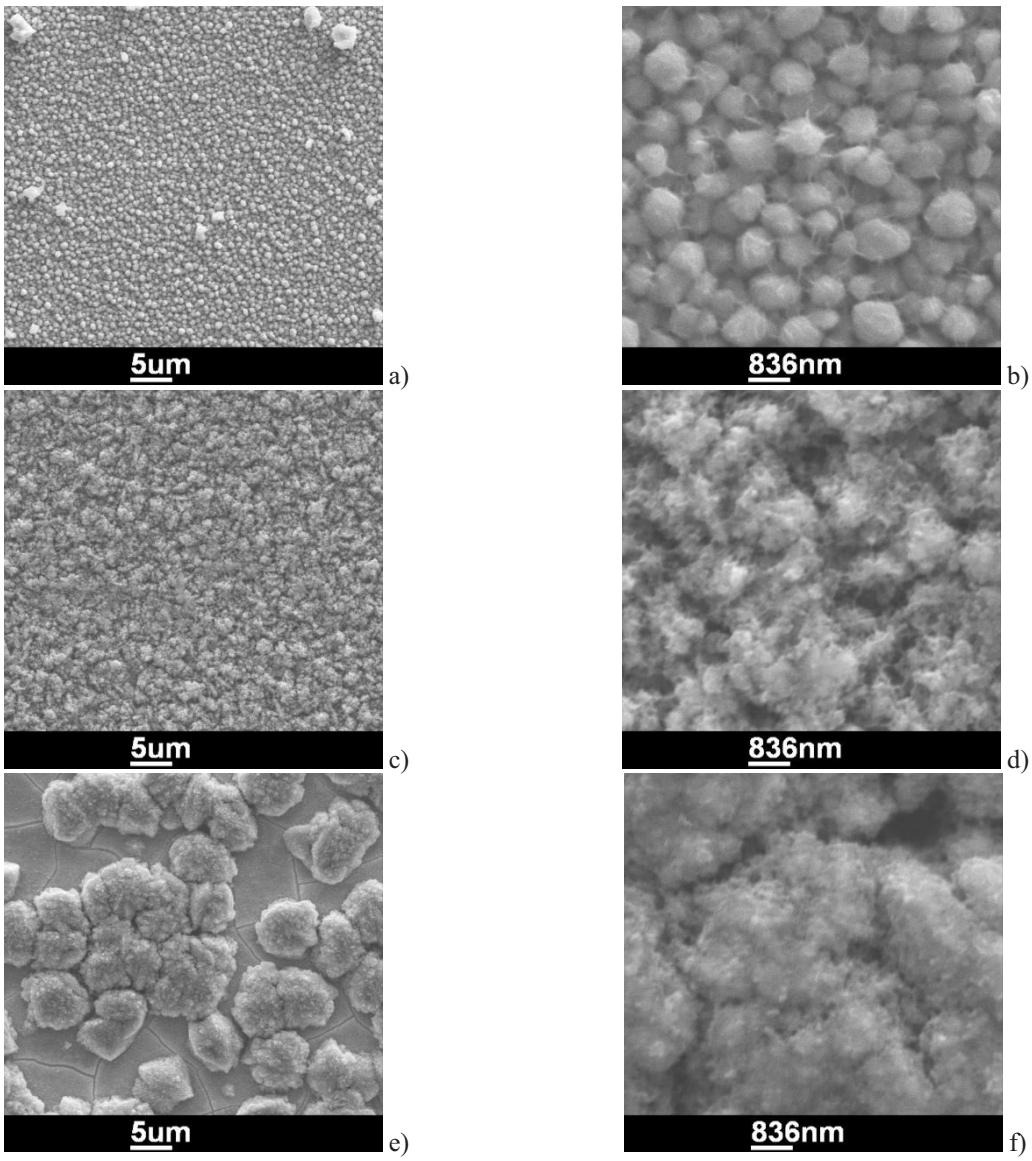

Figure 4.20 Morphology of the obtained deposits from potentiostatic deposition of Co and Co-ceria co-deposits at -0.85 V, 28 Wcm^{-2}, 250 kHz frequency limitation a) and b) without ceria, c) and d) with 3 g/l and e) and f) with 5 g/l ceria added.

The significant difference in the morphology of the deposits upon ceria addition is obvious from SEM pictures (Fig. 4.20). Deposits were less uniform, especially at the edges of the electrode where the layer thickness was also higher. With the ceria addition inhomogeneous and rough layers were deposited which caused also the damping to increase. For the same frequency change limitation, the thickness of the pure Co film was 2.35 μm, with 3 g/l 5.83 μm and with 5 g/l 8.86 μm indicating the porous nature of the deposits. Large numbers for the apparent current efficiencies, 146 % for 3 g/l ceria and 144 % for 5 g/l ceria (still calculated for obtaining a relative value despite the fact that Sauerbrey equation was not valid), can be caused by precipitation of $Co(OH)_2$, as already discussed, by a contribution of the damping, and by the mass of the co-deposited ceria. According to EPMA the

ceria contents in the deposits were 6.2 wt% for 3 g/l and 7.8 wt% for 5 g/l solution concentration. These numbers are quite large for the low solution concentrations. Cârâc et al. found – using a 1.2 M Co electrolyte and 50 g/l µm-sized CeO_2 particles– values of 22 wt% [248].

Chapter 5 - Sonoelectrochemical synthesis of stable colloidal nanoparticles

5.1 Background

Metallic nanoparticles are quite attractive because of their physicochemical characteristics such as catalytic activity, optical properties, electronic properties, and magnetic properties [279]. In the field of catalysis, the size and shape of the nanoparticles are extremely important since they greatly influence the catalytic reactivity [280-282]. Due to the high surface energy nanoparticles possess, they tend to agglomerate and one of the challenges in research work is to find possible ways to prevent this process and avoid loss of the surface area. The synthesis of stable colloidal particles with controlled size and shape is very important. By reduction of appropriate metal salts in the presence of a suitable surfactant, stable metal colloids can be obtained [283].

The sonoelectrochemical method and more recently pulsed sonoelectrochemistry have been shown to be very useful methods in the production of a number of metal and semiconductors nanoparticles [284, 285]. A narrow size distribution of the synthesized nanomaterials has been reported [286, 287].

The sonoelectrochemical synthesis of a stable colloid of copper dendrites in the presence of polyvinyl alcohol (PVA) [288] and polyvinyl pyrrolidone (PVP) [289] has been reported. A stable solution of Au nanoparticles with a particle size between 5 and 35 nm was prepared by means of sonoelectrochemistry in the presence of several stabilization agents [290]. Monodisperse silver nanoparticles with spherical shape were reported to be synthesized from the saturated solution of silver citrate in the presence of PVP by sonoelectrodeposition [291]. Later on, from an aqueous solution of $AgNO_3$ in the presence of ethylenediaminetetraacetic acid disodium salt (EDTA) and PVP silver nanoparticles in a shape of spheres, wires and dendrites were synthesized [292].

The pulsed sonoelectrochemical method comprises successive electrochemical and ultrasonic pulses for the production of nanopowders. A planar circular area on the bottom of the ultrasonic horn serves both as the cathode (sonotrode) and as an ultrasound emitter. The rest of the ultrasonic horn is electrically insulated in order to prevent permanent metal plating on it. At first, during an electrochemical pulse a high density of metal nuclei is formed on the cathode and the horn acts just like an electrode. After the electric pulse is over, it is followed by an ultrasound pulse which bursts the formed nuclei into the liquid, cleans the electrode and supplies the electrode with a new portion of cations by the acoustic streaming caused [293]. After the ultrasonic pulse there is a rest time before the next electric pulse which is important for obtaining conditions in the cell, especially in the vicinity of the sonotrode, similar to the starting ones [294]. With an optimization of the electrochemical parameters, such as current density and time of electric pulse duration and ultrasonic parameters such

as ultrasonic intensity and time of the sonic pulse, one can obtain materials with desired shape and particle size as well as with a narrow size distribution. If there is an appropriate surfactant in an appropriate amount in the liquid, the particles could be stabilized and agglomeration and thus loosing of active surface area could be prevented.

Stable colloids of noble metal nanoparticles have a special significance as catalyst materials. It has been reported in literature that decoration of Ni based materials with metal nanoparticles such as Cu, Ag and Au leads to advanced stability towards the process of anode material degradation in SOFC caused by C and S [295, 296]. Due to their particular importance, in this work, for the preliminary study on the pulsed sonoelectrochemical synthesis of stable nanoparticles, exactly these materials Cu, Ag and Au were chosen. PVP was chosen for the stabilization of particles since the usage was already reported [289, 291, 292] in these systems.

PVP has the structure of a polyvinyl skeleton with polar groups. Nitrogen and oxygen atoms form the polar groups [289] and they serve as donators of ion-pair electrons. The number of metal ions can be attached to a PVP molecule forming a complex compound M_m^{m+}-PVP, where m is the number of attached metal ions. Yin B et al. [297] proposed that the electrochemical deposition process develops through four steps. In the first step a M_m^{m+}-PVP complex compound is formed. In the second step reduction of the complex on the electrode/electrolyte interface occurs and PVP protected metal adatoms M_m^0-PVP with chemical bonds are formed. As polar groups of PVP contribute more to the electronic density of metal atom orbitals than H_2O thus metal ions in M_m^{m+}-PVP complex can possibly obtain easier electrons from cathode than hydrous metal ions. Therefore the M_m^{m+}-PVP complexes rather than single ions are reduced and in the third step a number of PVP protected nuclei are formed. In the fourth step PVP contributes to nucleation but also inhibits growth and agglomeration of the formed nuclei.

5.2. EQCM study

In a Cu electrolyte with the composition of 0.1 M $CuSO_4 \times 5H_2O$, 2 wt% PVP and pH~0 (adjusted with H_2SO_4)according to [289], EQCM measurements were performed in order to obtain information about electrochemical deposition and dissolution of Cu in the presence of the surfactant. The main differences to the solution used previously were that the solution was more concentrated (0.1 M instead 0.01 M in the fundamental study) and that the surfactant PVP was present. As in the fundamental study, a cyclic voltammogram in Cu electrolyte was at first recorded in silent conditions in a potential range between 0.5 V and -0.3 V vs. Ag/AgCl, with a 5mV/s scan rate in inert Ar atmosphere. The recorded current density and the frequency change upon potential change are shown in Figure 5.1a.

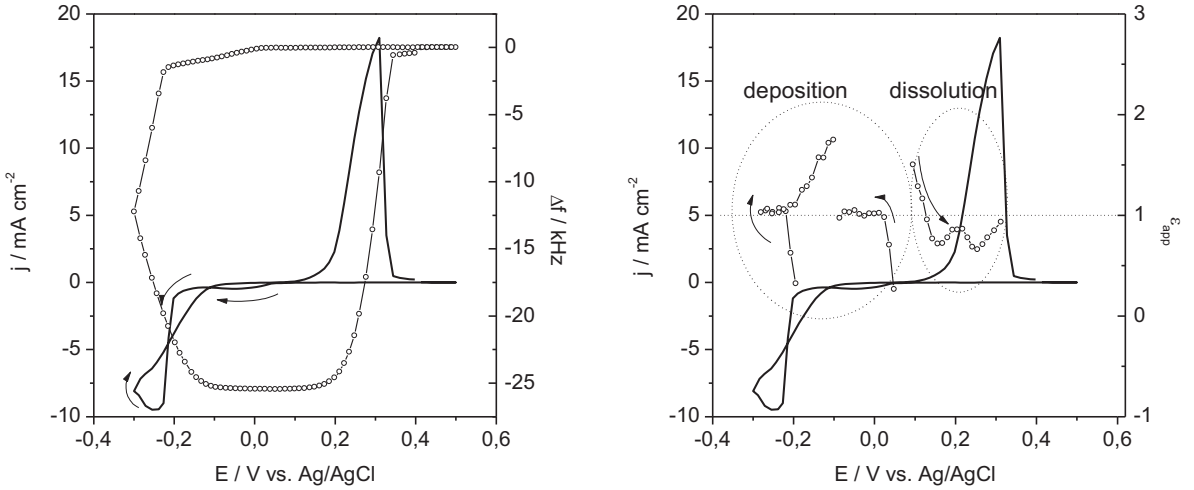

Figure 5.1 Electrodeposition and -dissolution of Cu from 0.1 M $CuSO_4 \times 5H_2O$, 2 wt% PVP and pH~0 (adjusted with H_2SO_4), measured current density (line) and a) frequency change (circles) and b) apparent current efficiency (circles) in a potential range of 0.5 V to -0.3 V vs Ag/AgCl, at 5 mVs^{-1} scan rate under silent conditions, in Ar.

In the presence of PVP two cathodic waves are visible in the cyclic voltammogram. Below a potential of about 28 mV the cathodic current slightly increased and a frequency change (about 2 kHz) was observed as well, so Cu deposition was taking place. After reaching the peak the current slightly decreased and then remained constant. At a potential of about -220 mV, the current started to increase significantly reaching values of almost -10 $mAcm^{-2}$, whereas the frequency change was around 25 KHz. After a cathodic peak was reached, the cathodic current started to decrease till the end of the forward scan. In the beginning of the back scan deposition was still taking place. Above -85 mV the cathodic currents and the mass increase were very small, leading to the appearance of a wide plateau in the frequency curve. This is very different from the fundamental study, where a more or less immediate change from deposition to dissolution was observed (cf. Fig. 3.11). At a potential of around 170 mV anodic currents started to increase and the frequency was decreasing, so Cu dissolution was taking place till no deposit was left on the electrode, when the current dropped to starting values.

The behavior of the apparent current efficiency (calculated for z=2) during the deposition and dissolution process is shown in Figure 5.1b. During the first cathodic step, ε_{app} had the theoretically expected values with exception of a small deviation in the very beginning indicating that already then reduction of Cu^{2+} to Cu occured. For the second cathodic wave, besides deviations in the beginning of the process (values smaller than expected) and at the end of the deposition process (values larger than expected) ideal behavior was approached. For the dissolution process, from the values larger than 1 in the beginning of the process values of efficiencies were fluctuating between 1 and 0.5.

Cyclovoltammetric deposition and dissolution of Ag in the presence of PVP was studied by Yin B. et al [297]. In their study no additional peaks were observed but the anodic peak was smaller in the presence of PVP, whereas the cathodic peak remained the same. They concluded that the cathodic current in the presence of PVP was from reduction of silver ions deposited on the electrode and from

reduction of silver ions to silver nanoparticles stabilized with PVP. Since during the dissolution process just part of the silver which was deposited on the electrode was dissolved, the anodic peak appeared to be smaller than in the case without PVP. However, the results on Cu in this work could not be explained by a similar theory, since the performed EQCM measurements demonstrated that cathodic currents in both cathodic waves were connected with a frequency change and thus deposition of Cu on the electrode. This effect of the PVP presence on the behavior of Cu deposition should be further studied.

Further, cyclic voltammograms in the presence of ultrasound at different ultrasonic intensities were recorded, and an example with an intensity of 76 Wcm^{-2} is shown in Figure 5.2. The horn-quartz distance was 15 mm and the experiment was done in Ar inert atmosphere.

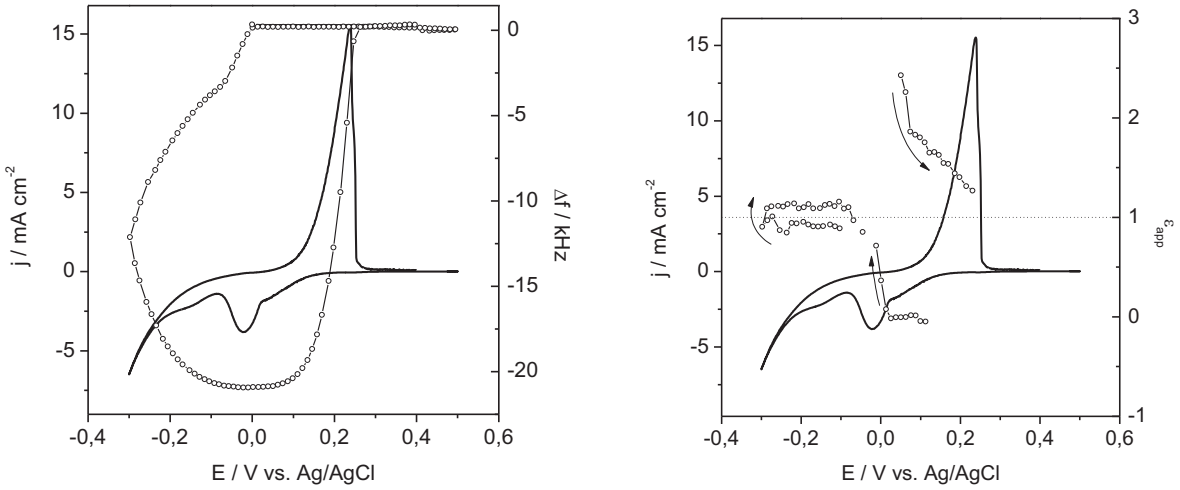

Figure 5.2 Electrodeposition and -dissolution of Cu from 0.1 M $CuSO_4 \times 5H_2O$, 2 wt% PVP and pH~0 (adjusted with H_2SO_4), measured current density (line) and a)frequency change (circles) and b) apparent current efficiency (circles) in a potential range of 0.5 to -0.3 V, at 5 mVs^{-1} scan rate at an 76 Wcm^{-2} ultrasonic intensity, d=15 mm, in Ar.

In comparison with silent conditions the cathodic currents during the first cathodic wave were larger but the frequency change just slightly larger influencing the current efficiency (Fig. 5.4b) to have values less than expected. This was in part due to a side reaction at more positive potentials that was not associated with any frequency change. During the second cathodic wave, the maximum cathodic currents were smaller than under silent conditions and less mass was deposited. Current efficiencies had values smaller than 1 during the forward scan and larger than 1 during back scan. After the dissolution peak was reached the currents went back to the starting values as well as the frequency indicating that all deposited mass was removed from the electrode. Current efficiencies were decreasing from positive values during dissolution but remained all the time larger than 1.

5.3. Pulsed sonoelectrochemical deposition

5.3.1 General setup

After the EQCM study of the electrodeposition and -dissolution of the copper system in the presence of the surfactant PVP in silence and in an ultrasound field, the Cu system was the first one under study for the pulsed sonoelectrochemistry. The solution used was the same as in the EQCM measurements. With the aim to use the horn tip as an electrode, the sides of the horn had to be electrically insulated in order to prevent permanent metal plating on them. The insulation of the horn was done by the use of shrinkage tube, appropriately mounted and adjusted.

The general synchronization of the times of the galvanostatic deposition, the ultrasound emission and the rest time, controlled by the computer, is presented in Figure 5.3. At first, during an electric pulse with duration t_{el} nuclei of metal are formed on the electrode and grown to nanoparticles. Afterwards during the time t_{us} these nanoparticles are burst from the electrode by the action of the ultrasound. At the end of one cycle there is a rest time t_r for restoring initial conditions in the cell.

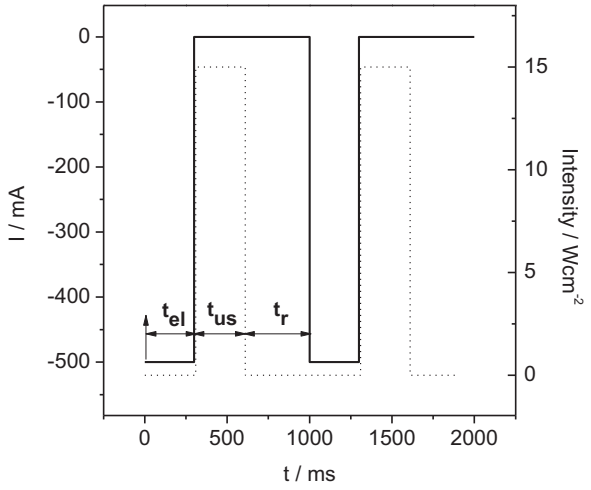

Figure 5.3 Synchronisation of the times of the particular steps during the pulsed sonoelectrochemical synthesis of colloidal Cu nanoparticles from 0.1 M $CuSO_4 \times 5H_2O$, 2 wt% PVP and pH~0 (adjusted with H_2SO_4) solution, t_{el} is the time of the electrical pulse, t_{us} of the ultrasonic pulse and t_r is the rest time.

In all experiments performed for the pulsed sonoelectrochemical synthesis of nanoparticles each cycle, containing the time of the electric pulse, the time of the ultrasonic pulse and the rest time lasted 1s. Each experiment lasted 30 min or 1800 cycles. Currents, the time of current pulses and the time of sonic pulses varied through experiments. The ultrasonic intensity was fixed to 15 Wcm^{-2} throughout the study. Since the product was in all cases a stable colloidal suspension, the particle size distribution was determined by the Dynamic Light Scattering (DLS) technique.

The potential change during the periodical action of electric and ultrasonic pulses is shown in Figure 5.4. During the electric pulse, the potential is from the OCP value moved to more negative potentials (reduction overpotential) needed for supplying the given current between WE and CE electrode, and thus for deposition of the metal. When the electric pulse is over and the ultrasound pulse is on, the potential returns to a more positive value, but does not reach the OCP value during action of the ultrasound (shift of the OCP under action of ultrasound as explained in chapter 3.2.1). This is shown in the enlarged part of the graph on the Figure 5.4. After turning off the ultrasound the OCP value is finally reached and it stays unchanged until a new cycle starts.

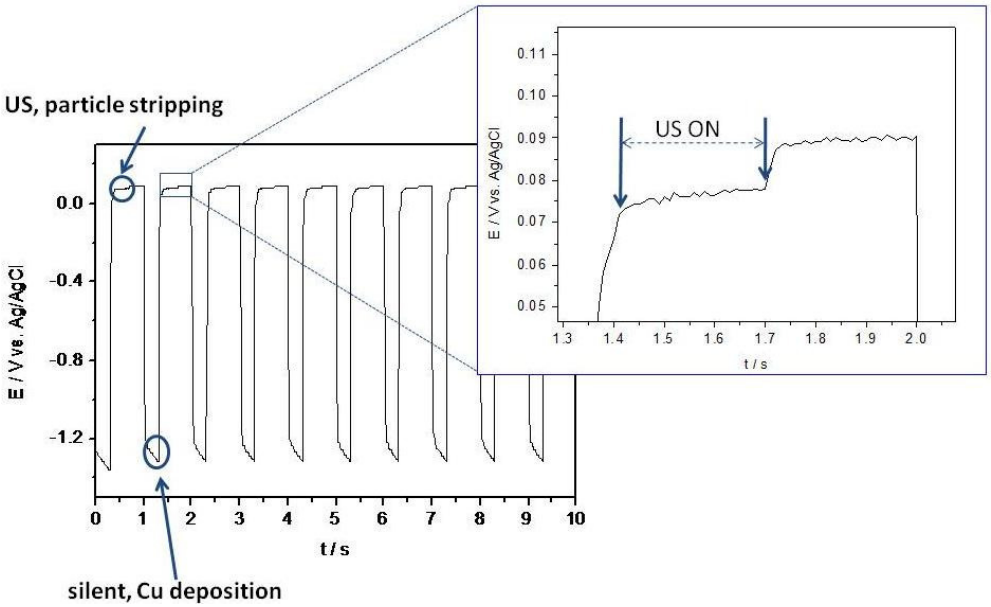

Figure 5.4 Potential changes during galvanostatically depositing Cu metal nanoparticles from 0.1 M $CuSO_4 \times 5H_2O$, 2 wt% PVP and pH~0 (adjusted with H_2SO_4) solution, their removal from the electrode by ultrasound and the rest phase. The enlarged part shows the potential during the time when the ultrasound is on and during the rest time.

5.3.2 Synthesis of colloidal Cu nanoparticles

In the Cu electrolyte with the composition of 0.1 M $CuSO_4 \times 5H_2O$, 2 wt% PVP and pH~0 (adjusted with H_2SO_4) two experiments were done and the conditions used are shown in Table 5.1.

Table 5.1 Conditions for pulsed sonoelectrochemical synthesis of Cu colloidal nanoparticles from 0.1 M $CuSO_4 \times 5H_2O$, 2 wt% PVP and pH~0 (adjusted with H_2SO_4) solutions, lasting 30 min at 15 Wcm^{-2} ultrasonic intensity, under Ar.

Sample	Current (I, mA)	Time of current pulse (t_I, ms)	Time of ultrasound pulse (t_{US}, ms)
Cu(1)	-500	300	300
Cu(2)	-500	50	100

The particle size distribution of the obtained stable colloids of Cu nanoparticles is shown in Figure 5.5. The main difference between the two experiments was the duration of the current pulse. The duration of ultrasound was also different but one can assume that the major role of ultrasound is mechanical thus removing the formed particles and that this difference did not have a significant influence on the size and the size distribution of the formed colloidal nanoparticles.

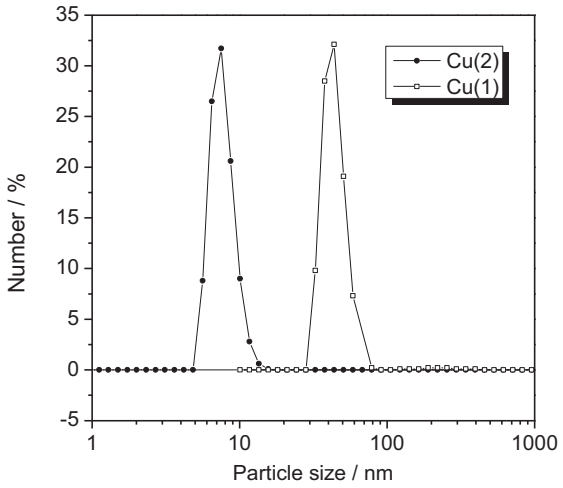

Figure 5.5 Particle size distribution of Cu colloidal nanoparticles produced during pulsed sonoelectrochemical deposition from an electrolyte of 0.1 M $CuSO_4 \times 5H_2O$, 2 wt% PVP and pH~0 (adjusted with H_2SO_4) solution, lasting 30 min at 15 Wcm^{-2} ultrasonic intensity. Cu(1): I=-500 mA, t_I=300 ms, t_{US}=300 ms, Cu(2): I=-500 mA, t_I=50 ms, t_{US}=100 ms.

When the electric pulse in the experiment lasted 300 ms the mean diameter of the obtained nanoparticles was around 40 nm. With shortening the time to 50 ms nanoparticles with a mean diameter of less than 10 nm were obtained. The application of very short pulses therefore is crucial for the preparation of small nanoparticles.

5.3.3 Synthesis of colloidal Ag nanoparticles

Synthesis of the colloidal Ag nanoparticles was done in four experiments from a solution with the composition of 1 mM $AgNO_3$, 0.1 M $NaNO_3$ and 20 g/l PVP in Ar inert atmosphere (according to [297]). Conditions for particular experiments are given in Table 5.2.

Table 5.2 Conditions for the pulsed sonoelectrochemical synthesis of Ag colloidal nanoparticles from 1 mM $AgNO_3$, 0.1 M $NaNO_3$ and 20 g/l PVP solution, lasting 30 min, at 15 Wcm^{-2} ultrasonic intensity, under Ar.

Sample	Current (I, mA)	Time of current pulse (t_I, ms)	Time of ultrasound pulse (t_{US}, ms)
Ag(1)	-50	300	300
Ag(2)	-100	50	100
Ag(3)	-100	100	100
Ag(4)	-100	200	200

The particle size distribution for all obtained colloidal samples is shown in Figure 5.6. The first sample Ag(1) was obtained with the lowest applied current of - 50 mA and the largest time of electric pulse and showed a mean particle size of about 30 nm. The other three samples were obtained with the same applied current of – 100 mA and the electric pulse length was varied. Sample Ag(2) with the shortest electric pulse of 50 ms showed the largest mean particle size of about 60 nm, even larger than particles in sample Ag(1). With increasing electric pulse time smaller nanoparticles were detected and accordingly the smallest particle size was recorded for the sample where the longest electric pulse of 200 ms was applied. The origin of this behavior and its reproducibility should be the focus of further studies. Ag solutions are in general light sensitive and a purely sonochemical formation or growth of nanoparticles just by acoustic cavitation might contribute to the observed trends for particle size distribution.

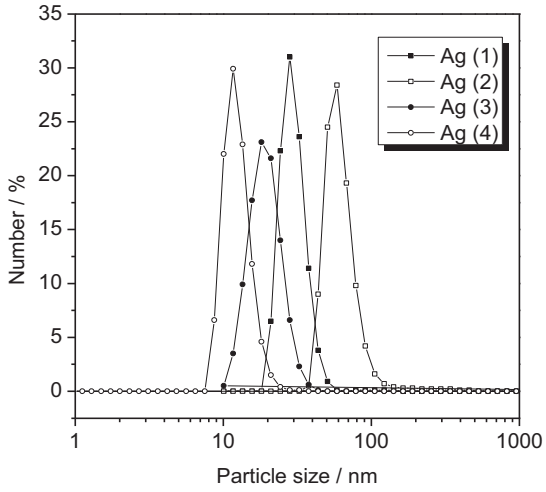

Figure 5.6 Particle size distribution of Ag colloidal nanoparticles formed during pulsed sonoelectrochemical deposition from a 1 mM $AgNO_3$, 0.1 M $NaNO_3$ and 20 g/l PVP solution, lasting 30 min, at 15 Wcm^{-2} ultrasonic intensity, Ag(1): I=-50 mA, t_I=300 ms, t_{US}=300 ms, Ag(2): I=-100 mA, t_I=50 ms, t_{US}=100 ms, Ag(3): I=-100 mA, t_I=100 ms, t_{US}=100 ms, Ag(4): I=-100 mA, t_I=200 ms, t_{US}=200 ms.

5.3.4 Synthesis of colloidal Au nanoparticles

The composition of the electrolyte for synthesis of Au colloidal nanoparticles (according to [290])was $2.8 \cdot 10^{-4}$ M $HAuCl_4 \cdot 3H_2O$, 20 g/l PVP, pH ~1 (adjusted with HCl). Two experiments were done and the conditions are given in Table 3.

Table 5.3 Conditions for pulsed sonoelectrochemical synthesis of Au colloidal nanoparticles from $2.8 \cdot 10^{-4}$ M $HAuCl_4 \cdot 3H_2O$, 20 g/l PVP, pH ~1 (adjusted with HCl), lasting 30 min, at 15 Wcm^{-2} ultrasonic intensity in Ar.

Sample	Current (I, mA)	Time of current pulse (t_I, ms)	Time of ultrasound pulse (t_{US}, ms)
Au(1)	-100	50	100
Au(2)	-60	50	100

The only difference between the two syntheses of colloidal Au particles was the applied current which was in the first experiment Au(1) -100 mA and in the second one Au(2) -60 mA. A decrease in current led, as it can be seen in Figure 5.7, to a decrease in the mean particle size.

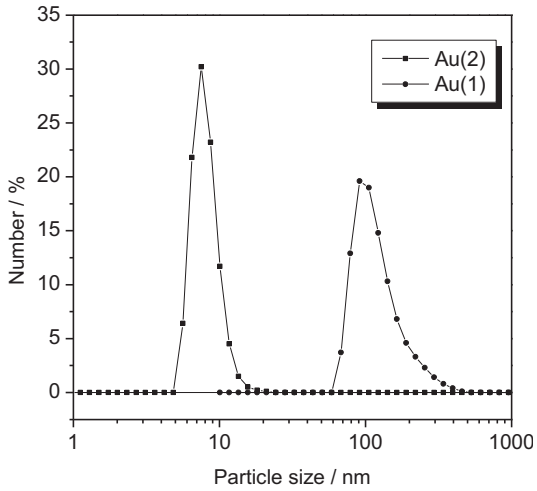

Figure 5.7 Particle size distribution of Au colloidal nanoparticles obtained by pulsed sonoelectrochemical synthesis from $2.8 \cdot 10^{-4}$ M $HAuCl_4 \cdot 3H_2O$, 20 g/l PVP, pH ~1 (adjusted with HCl), lasting 30 min, at 15 Wcm^{-2} ultrasonic intensity, Au(1): I=-100 mA, t_I=50 ms, t_{US}=100 ms, Au(2): I=-60 mA, t_I=50 ms, t_{US}=100 ms.

5.3.5 Summary of nanoparticles synthesis

Colloidal Cu, Ag and Au nanoparticles were prepared by the means of pulsed sonoelectrochemical deposition. The mean particle size of prepared particles was in the range between 10 and 100 nm and the stabilization of colloids with addition of appropriate amount of PVP as the stabilizer was successfully done. Particle size was determined by DLS and would have to be further proven by TEM studies. It is shown that the variation of parameters such as the electric current and the duration of the electric pulse influence the particle size. One of the most important findings this preliminary study

provided is that by optimization of the experimental conditions the size of the obtained particles can be tailored. In order to learn more about nucleation and growth process and to understand better how surfactant as well as other experimental parameters influence them, a study of the deposition of Cu, Ag and Au on the Ti alloy (the ultrasonic horn is made of this alloy) would be needed. This study would contain variation of applied currents, potentials, concentrations of stabilizers and metal precursors as the crucial parameters influencing size and particle size distribution.

Chapter 6 - Synthesis of molybdenum oxide

6.1 Background

Nano-sized transition metals as well as their compounds with their exceptional chemical and physical properties have drawn a lot of attention in recent years. Molybdenum oxide materials are particularly attractive due to their photochromic, thermochromic, electrochromic as well as gas sensing and catalytic properties.

Several synthetic routes for molybdenum oxide materials have been already established. The synthesis of molybdenum oxide nanoparticles via a citrate sol-gel process has been reported [298]. It was shown that the obtained MoO_3 (10-100 nm in size) possesses enhanced gas sensing capabilities. Sun Jiebing et al. [299] synthesized molybdenum oxide thin films by preparing a molybdenum acetylacetonate sol from which MoO_3 films on fused silica, Si and Al_2O_3 substrates were obtained. Besides sol-gel routes [300-303] atomic layer deposition was used for the synthesis of nanodispersed molybdenum oxide on mesoporous silica [304]. Hydrothermal synthesis [7, 305, 306] and oxidation of molybdenum coil [307, 308] have been reported as well. With the above mentioned preparation routes a variety of particle shapes was obtained, including nanorods, nanofibers, nanospheres, nanobelts and lamellas, all of which depended on particular synthetic route and parameters. Also, different types of molybdenum oxides were reported, such as molybdenum oxide in its different oxidation and hydration states (most frequently stable orthorhombic α-MoO_3 and somewhat rarely metastable monoclinic β-MoO_3) [309-311]. MoO_2 nanospheres were prepared by the redox etching method [312] by facile solution-phase approach [313] and by the solvothermal method [314].

It has been proven over the years that the sonochemical decomposition of volatile transition-metal carbonyls is a successful method for obtaining nano-sized particles of transition metals alloys and metal oxides (see Chapter 1.3). Decomposition of metal-carbonyl bonds takes place upon the extreme conditions that arise from the acoustic cavitation, driven by sonication of liquids. Since many parameters influence the final structure and size of the obtained nanoparticles, it is necessary to make a proper choice of precursor, solvent and experimental conditions. Several papers have been published on the synthesis of molybdenum oxide by means of sonochemical decomposition of $Mo(CO)_6$, mainly followed by in-situ coating on different types of supports. N. Arul Dhas and A. Gedanken reported preparation of pentavalent molybdenum oxide ($Mo_2O_5 \times H_2O$) and molybdenum carbide (Mo_2C) nanoparticles coated on silica spheres [112, 315]. As it was shown, sonication of $Mo(CO)_6$ under argon atmosphere yielded molybdenum carbide, while sonication under air resulted in production of molybdenum oxide with an average size of the nanoparticles in the range of 5-10 nm. Sonochemically prepared unsupported nanostructured pentavalent molybdenum oxide resulted in particles of an

average size of ~20 nm. Similar preparation and coating of molybdenum oxide on alumina submicrospheres was performed [316].
In those studies, sonication was typically carried out for about 3h and the obtained molybdenum oxide particles were either coated on supports or recovered from slurry followed by further treatments and analysis. In all cases obtained powder showed the presence of agglomerates.

6.2 Sonochemical synthesis

Molybdenum oxide colloid suspensions were prepared by sonochemical decomposition of molybdenum hexacarbonyl in n-hexadecane and n-decane as solvents as well as with oleic acid as a stabilizing agent. The usage of oleic acid in similar systems has been already reported [101, 317]. It was shown that the stabilization can be achieved by coating the particles with long-chain surfactants, such as oleic acid with its double bond which inhibits the neighboring chains from bundling together. N-decane and n-hexadecane were used as a solvents due to their low vapor pressure thus preventing the increase in vapor content of the cavity, since it has been shown that high vapor pressure of the solvent cushions the implosion of the cavity and lowers the temperature of implosion (Chapter 1.2.3).

6.2.1 System with n-hexadecane as a solvent

According to the previously reported synthesis of cobalt nanoparticles, a proportional amount of molybdenum carbonyl and oleic acid and 3h of sonication time were chosen. A reaction vessel with cooling jacket was filled with 140 ml of n-hexadecane, 7 ml (150.9mM) of oleic acid and 1.4 g (36.1mM) of $Mo(CO)_6$. The intensity of ultrasound irradiation was 76 Wcm^{-2}. The first color change, from transparent to light blue, was registered after 3 minutes of sonication and the color gradually became darker with time, so that after 30 minutes it appeared to be almost black. According to N. Arul Dhas et al. the blue color is believed to be due to generation of pentavalent molybdenum oxide [112]. The obtained liquid appeared to be a stable colloid suspension even after 2.5 months.
Figure 6.1a and 6.1b show the TEM images of the sample taken after 10 min of sonication. Agglomerates with an average size between 200 and 300 nm consist of small spherical particles with a diameter of 3-10 nm. Next to the each agglomerate, a single spherical particle with a size proportional to the corresponding agglomerate could be observed and varied from 50 to 100 nm in diameter. Electron diffraction pattern (Fig. 6.1c) showed the narrow diffraction rings with diffraction spots indicating the presence of polycrystalline material. On the other hand, diffraction spots can appear due to crystallization of the amorphous sample under the electron beam in the TEM chamber during the analysis.

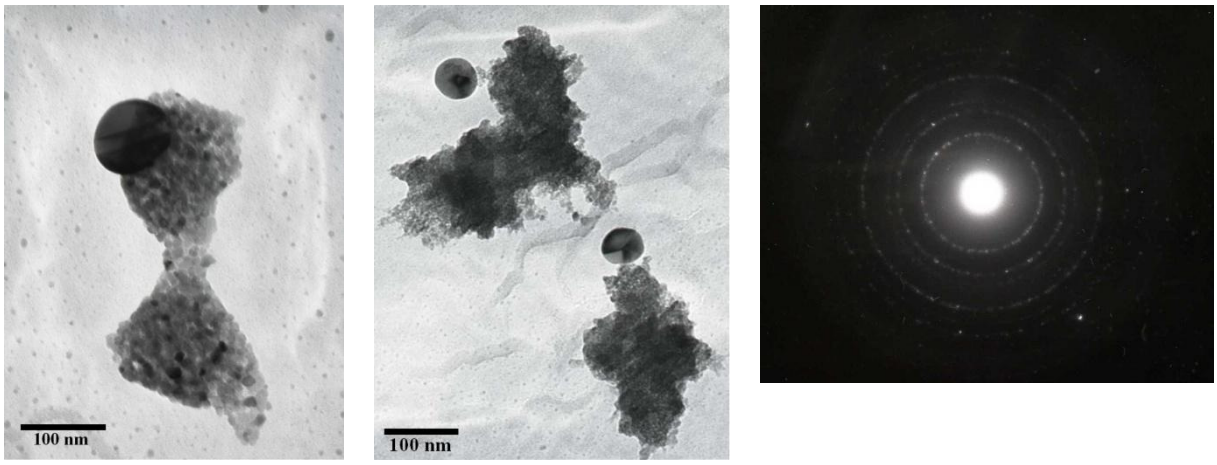

a) b) c)

Figure 6.1 a) and b) TEM images and c) electron diffraction pattern of the sample after 10 min of sonication of 140 ml of n-hexadecane, 7 ml (150.9 mM) of oleic acid and 1.4 g (36.1 mM) of $Mo(CO)_6$ at I_a=76 Wcm^{-2}.

In comparison with the sample taken after 10 min, the sample taken after 3 h of sonication (Fig. 6.2a) had slightly different particle size and morphology. The agglomerates of the spherical particles became smaller and less coherent with a prolonged time and more diffuse rings were present on the diffraction pattern (Fig. 6.2b).

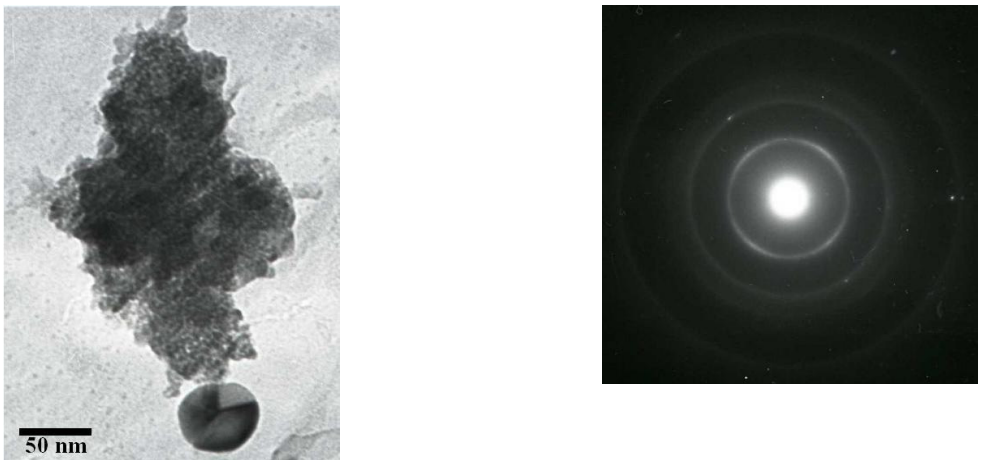

a) b)

Figure 6.2 a) TEM image, b) electron diffraction pattern of the sample after 3h of sonication of 140 ml of n-hexadecane, 7 ml (150.9 mM) of oleic acid and 1.4 g (36.1 mM) of $Mo(CO)_6$, at I_a=76 Wcm^{-2}.

The obtained diffractogram of the powder recovered by the centrifugation and dried at 110 °C (Fig. 6.3) did not show any peaks proving that the sample was amorphous.

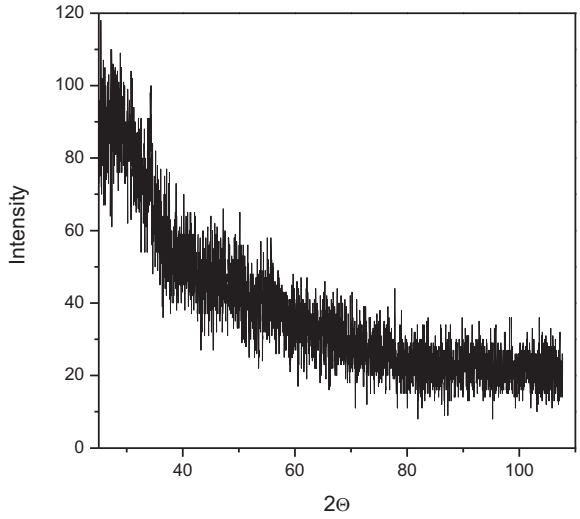

Figure 6.3 XRD of the sample of the sample after 3h of the sonication of 140 ml of n-hexadecane, 7 ml (150.9 mM) of oleic acid and 1.4 g (36.1 mM) of $Mo(CO)_6$, at I_a=76 Wcm^{-2}.

Without any peaks in the XRD patterns, the identity of the obtained material could not be determined and EDX analysis was done (Tab. 6.1). The presence of molybdenum and oxygen peaks was obvious and the quantitative analysis gave a higher percentage of oxygen, even in comparison with the one expected for MoO_3 where molybdenum is in the highest oxidation state. Either the higher oxygen was from still adherent oleic acid or an indication for the formation of hydrates with moisture from the ambient air since the samples were kept in air.

Table 6.1 Results of the EDX analysis done for the samples after 3h of the sonication of 140 ml of n-hexadecane, 7 ml (150.9 mM) of oleic acid and 1.4 g (36.1 mM) of $Mo(CO)_6$, at I_a=76 Wcm^{-2}.

	Point 1, %	Point 2, %
Mo	25.94	21.23
O	74.06	78.77

Due to the first changes in color of the suspension observed after 3 min it was assumed that decomposition of the carbonyl takes place in the first minutes of sonication in a system with low precursor concentration. Therefore, sonication time for the subsequent experiments was lowered to 6 min. Consequently, the chosen precursor concentration and volume of the solution were set to a lower value and the following experiments were done in a 100 ml cylindrical reaction vessel in order to provide the proper immersion of the ultrasonic horn into the small volume of the solution.

In order to dissolve 0.1 g (7.58 mM) $Mo(CO)_6$ in 50 ml of hexadecane stirring on a magnetic stirrer for 30 min was applied followed by addition of 631 μl (0.04 M) of oleic acid. Mixing was continued for additional 15 min. The obtained mixture was transferred to the cylindrical vessel open to air and sonication lasted 6 min. First change in color was observed after 2 min of sonication when the

transparent solution turned to a light blue and then at the end of the third minute to an almost black colored solution. The obtained colloid was stable even after 45 days.

The change in the experimental parameters in comparison with the first experiment led to a completely different morphology of the synthesized material. The TEM image of the sample taken after 6 min of sonication showed the presence of porous aggregates of poorly ordered nanotubes (Fig. 6.4a). Tubes with a diameter of around 20 nm were observed on the magnified image of one of the nanotubes aggregates (Fig. 6.4b). Due to the broad variation it was not easy to determine the length of the tubes.

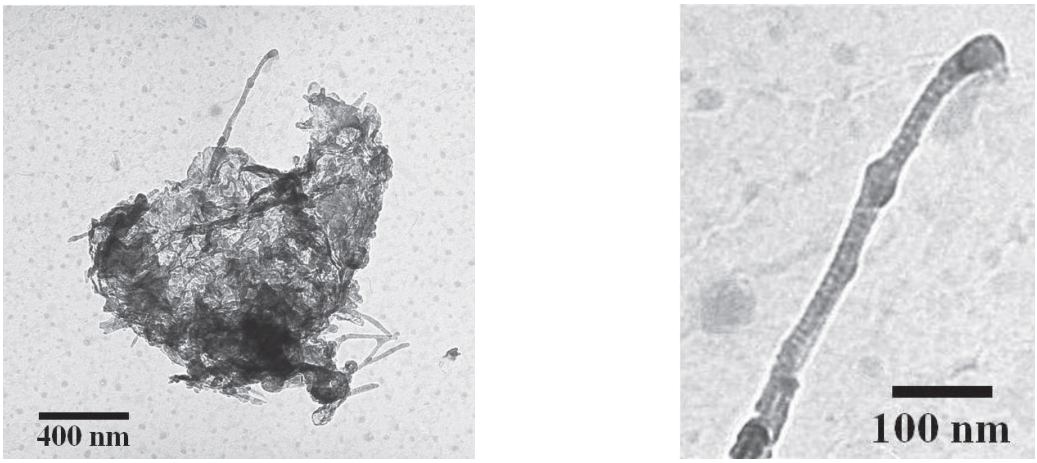

a) b)

Figure 6.4 TEM images of the sample obtained by 6 min of sonication of 0.1 g (7.58 mM) $Mo(CO)_6$ and 631 μl (0.04 M) of oleic acid in 50 ml of hexadecane, at I_a=76 Wcm^{-2}.

Samples were in the same way as in the previous experiment prepared and XRD and EDX analysis was done showing very similar results.

The dramatic change in morphology of the obtained sample, in comparison to samples from the previous experiment, was assumed to be primarily a consequence of the change in temperature and time of sonication. Since the adsorption is by its nature exothermic process, lower temperature facilitates surfactant adsorption on the surface of formed particles. Therefore, upon temperature regulation (~20°C) a particle easily becomes coated with surfactant and keeps its prior spherical shape. In systems without this regulation where temperature increases during sonication, it is more probable that molecules of surfactant will group in a formation, so called micelles, which varies in shape depending on the type of used solvent and surfactant. Concerning the investigated system, where unpolar solvent was used, it was assumed that inverse micelles were obtained forming a tubular structure, which presents the template for the shaping of the synthesized material. In this manner, oxide particles can be adsorbed on the polar heads of the surfactant molecules at the outer wall of the formed inverse micelle. Further on, with a shorter time of sonication it is easier to keep the formed tubular structure.

6.2.2 System with n-decane as a solvent

In order to dissolve 0.1 g (7.58 mM) of $Mo(CO)_6$ in 50 ml of n-decane, 20 min stirring on a magnetic stirrer was performed, followed by addition of 631 μl (0.04 mM) of oleic acid. Stirring was continued for the next 10 min. Ultrasound was applied for 9 min at an intensity of 80 Wcm^{-2} without temperature regulation and the samples for TEM analysis were taken after 6, 8 and 9 min (at the end of the experiment). During sonication the first color change was observed after 4 min, when the solution changed color from transparent to light brown. Even after 2 months of ageing, the obtained colloidal suspension appeared to be stable. For the better overview and possibility to compare obtained samples, TEM images together with particular diffraction patterns are presented together in the Figure 6.5.

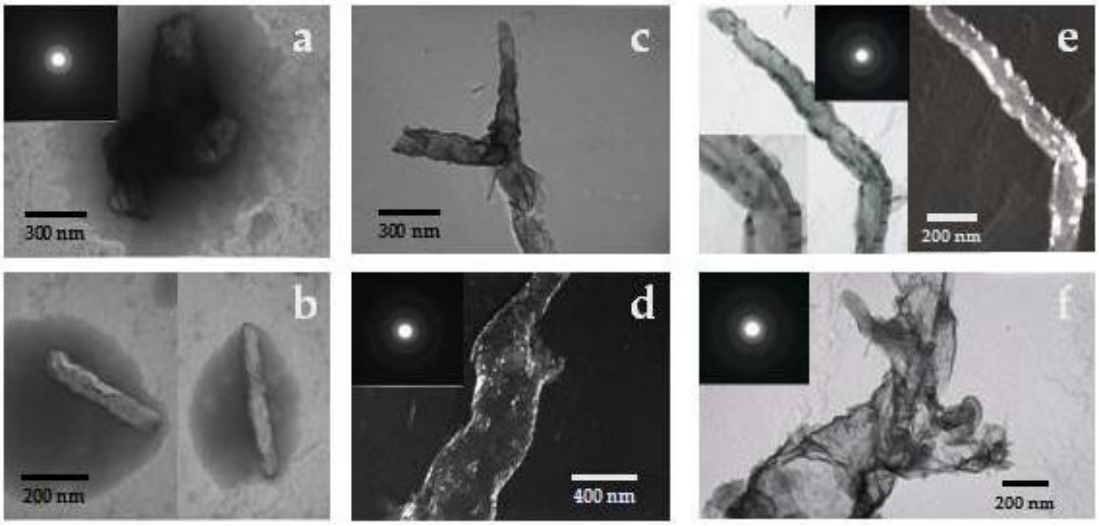

Figure 6.5 TEM images together with diffraction patterns of the samples prepared from 0.1 g (7.58 mM) of $Mo(CO)_6$ and 631 μl (0.04 mM) of oleic acid in 50 ml of n-decane at I_a=80 Wcm^{-2} after 6 min a) and b), 8 min c) and d) and 9 min of sonication e) and f).

Particles with not well defined shape, several hundred nanometers wide and around 1 μm long were detected in the sample within the shortest time of sonication (Fig. 6.5 a-b). Beside this type of particles tubular shaped particles with a diameter of 60-70 nm and a length of 300-500 nm were found in the same sample. Diffraction patterns of these particles showed dispersed diffraction rings which indicated an amorphous structure. In the sample taken after 8 min (Fig. 6.5 c-d) of sonication more complex tubular structures were detected. On the dark field image, the presence of hollow tubes whose walls are formed by a network built from small (primary) particles was clearly noticable. TEM analysis done on the sample taken at the end of sonication, after 9 min (Fig. 6.5 e-f), indicated again a hollow tube structure with small particles on the walls. The diameter of these tubes was around 130 nm and their length around 1 μm. In this sample, also some very complex structures, porous and irregular in the shape, were located. The tubes with bigger diameter and the walls were made from the network of small 20 nm wide rods. This experiment showed once more that with longer time of sonication there is a tendency for particle growth as well as for forming of a not so compact structure. The diffraction

patterns with dispersed rings gained from all samples obtained in this experiment indicated the amorphous structure.

Due to the high stability of the colloid suspension, centrifugation appeared to be inefficient for recovering the powder. Therefore, the layer of powder was isolated by filtration, dried at 110°C in the oven and taken for EDX analysis. EDX analysis (Tab. 6.2) showed even higher percentage of oxygen in comparison with the sample obtained in hexadecane as the solvent.

Table 6.2 Results of the EDX analysis done for the sample of 0.1 g (7.58 mM) of $Mo(CO)_6$ and 631 µl (0.04 mM) of oleic acid in 50 ml of n-decane after 9 min of sonication at I_a=80 Wcm^{-2}.

	Point 1, %	Point 2, %
Mo	16.92	16.79
O	83.08	83.21

In order to get information about the influence of precursor concentration an experiment with half of the carbonyl concentration (0.05 g, 3.79 mM) and 8 min of sonication was performed. The first color change from transparent to light blue occurred at the end of the 3rd min and by the end of the 4th minute color changed to light brown. In comparison to the previous experiment, the obtained colloidal suspension was lighter. It appeared to be stable even after 2 months of ageing.

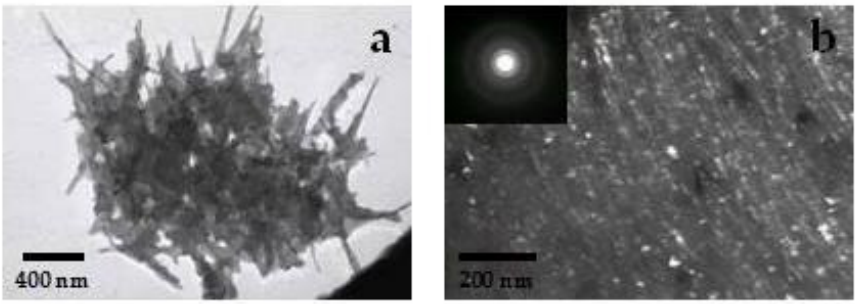

Figure 6.6 TEM images together with diffraction patterns of the samples prepared from 0.05 g (3.79 mM) of $Mo(CO)_6$ and 631 µl (0.04 mM) of oleic acid in 50 ml of n-decane after 8 min of sonication at I_a=80 Wcm^{-2}.

On the TEM picture (Fig. 6.6 a) a 2µm wide porous agglomerate was observed. This agglomerate was formed by a great number of 20 nm wide nanorods. Very small (3-15 nm) particles were observed in this agglomerate on the dark field TEM image (Fig. 6.6 b). In comparison with the previous experiment there was a clear difference in the shape as well as in the particle size. A more ordered and dense structure was observed in the sample obtained from the experiment with the lower concentration of the precursor in comparison with the irregular and less compact nanorods network in the sample formed in the experiment with higher precursor concentration. Diffraction pattern showed amorphous structure as in the previous experiment.

Chapter 7 - Conclusions

In the present study the EQCM technique was used in an ultrasound field for the study of sonoelectrochemical reactions. As acoustic wave based technique EQCM is very sensitive on mechanical disturbances. Since ultrasound is a source of phenomena such as acoustic cavitation and acoustic streaming, both origins of extreme mechanical agitation and disturbances, the imagined concept to combine ultrasound and EQCM technique was very challenging and in the beginning not for sure a realizable one.

EQCM data in addition to electrochemical data give opportunity to obtain informations about mass changes on the electrode and current efficiencies and thus facilitate the study of mechanism of sonoelectrochemical reactions and distinguishing the nature of reactions taking place at the electrode. In addition quantification of current-less processes such as corrosion and erosion is much easier to be done.

The study was performed in two steps. In the first step of the study done in water and in a sulfate and chloride-based Cu electrolyte, the applicability of the EQCM technique in an ultrasound field was proven and the influence of ultrasound on the electrochemical parameters was studied. In the second step materials with a possible practical usage were synthesized.

In experiments done in water the resonance frequency, the damping and the noise of the quartz response signal (quartz admittance) were recorded and their behavior was followed, as function of time and with a variation of the ultrasonic intensity and the quartz-horn distance. The major trend was that with an increase in the ultrasonic intensity and a decrease in the distance, the admittance signal became noisier and there was a larger shift in the resonance frequency. A problem usually occurred in the beginning of the measurements, especially at higher intensities and smaller distances, where a certain time was needed to obtain a stable signal and where fluctuations in the frequency and damping were bigger. When the horn-quartz distance was 8 mm and the ultrasonic intensity 76 Wcm^{-2}, the drift in the frequency was significant and it took more than 4 minutes for the signal to become stable. However, even the highest recorded noise was not large enough to destroy the signal and make it useless. Frequency changes observed during these measurements were also much smaller than Δf caused by actual mass changes normally obtained during EQCM measurements. Nevertheless, when analyzing the deposition/dissolution of very small amounts of material in the presence of ultrasound, as for deposition of (sub)monolayers or for underpotential deposition studies, ultrasound induced effects on Δf might become important.

The basic study done in water was further performed in a sulfate-based Cu electrolyte due to the well explored basic mechanism. Ultrasound irradiation, in a pulsed mode and with different intensities, was applied in the Cu electrolyte. The open circuit measurements on the bare quartz and on the previously deposited Cu layers were done in order to check the influence of ultrasound on the frequency change

and the rest potential. The observed shifts in followed parameters, more pronounced at elevated ultrasonic intensities, indicated a significant role of the corrosion and also the surface erosion developed due to the acoustic cavitation.

The electrodeposition of Cu from the sulfate based electrolyte was further studied and the influence of the ultrasound on the electrochemical parameters was investigated. It was found that all parameters are influenced in a similar manner, mostly proportional to the square root of the ultrasound intensity. Enhanced mass transfer, due to acoustic streaming and phenomena such as microjets formed due to asymmetric collapse of the cavitational bubble, was mainly responsible for the enhanced cathodic currents and mass changes during deposition of Cu. EQCM data gave the possibility to determine current efficiencies in function of the applied potential or the time. Their deviation from theoretical values was explained as a consequence of a few phenomena such as dissolution and partial deposition of Cu via Cu(I), co-adsorption of sulfate ions and developed acoustic cavitation. These deviations were less significant in an ultrasound field due to the enhanced mass transport and less influence of the side reactions. One further indication that the main influence of the ultrasound is enhanced mass transport is the similarity of the obtained cyclic voltammograms under ultrasound irradiation with those ones obtained in RDE experiments in a similar potential range. The morphology of the obtained deposits was influenced as well. In solutions with a low concentration of the electroactive species, electrodeposition generally occurs under mass transfer control. With the presence of ultrasound and eliminated depletion of electroactive species, a gradual change from mass to charge transfer control occurs and in principal better quality deposits can be obtained. In the present experiments, under ultrasound radiation, less powdery and more compact layers were observed with larger grains but a more uniform size distribution.

The two step nature of the Cu electrodeposition was more pronounced in a chloride based solution, due to the complex formation and the stabilization of Cu(I) in the presence of Cl^- ions, and was mainly responsible for the behavior of the electrochemical parameters also in an ultrasound field. Enhanced mass transport and eliminated depletion of electroactive species leads to enhanced formation of Cu(I), beneficial to the electrodeposition but also to corrosion of Cu. This dual effect of the ultrasound is visible in its effect on cathodic currents and deposited mass as well as in the current efficiencies. With an increase in ultrasound intensity till intermediate values an increase in deposited mass was observed, but with further ultrasound intensity increase the deposited mass started to decrease. Despite a further slight increase in the cathodic currents, the current efficiency decreased. From the data obtained in RDE experiments it was possible to calculate limiting currents as a function of ultrasound intensity and it was shown that they were higher than the cathodic currents actually observed during cyclic voltammetry. Beside the enhanced mass transfer due to the acoustic streaming, accompanying processes like corrosion and erosion were observed as well. The latter is due to the occurrence of acoustic cavitation, and was more evident in the chloride electrolyte. Cathodic currents were found to be smaller than corrosion currents obtained from the OCP measurements on the deposited layer in an

ultrasound field. Several indications pointed out a significant role of the erosion which in turn explained the decrease in deposited mass and high values for corrosion currents.

The synthesis of materials with practical usage such as Ni/CeO_2 and Co/CeO_2 composites was also done. Since the electrolytes used for both systems were quite concentrated there was no need for ultrasound to enhance mass transport, but rather to supply a stirring effect to distribute ceria homogeneously in the electrolyte as well as to break up soft agglomerates and to direct them towards the electrode. On the other hand, in some systems, ultrasound enhanced significantly side reactions and changed the electrochemical behaviour. In these cases EQCM permitted distinguishing them from the actual metal deposition and via a change in damping indicated the roughening of deposited layers. Still, it was not possible to determine the amount of the incorporated ceria from the EQCM data, due to greatly enhanced side reactions. Whereas in synthesized Ni/ceria composites a rather small amount of ceria was embedded (up to 2.4 wt% for the 5 g/l ceria addition), the content of the ceria in the Co/ceria composite was up to almost 8 wt% (for the 5 g/l ceria addition). With an enhanced amount of the ceria embedded in the Co film, the damping also increased and more inhomogeneous and rougher layers were obtained. These results are promising for the purpose of a possible application of such materials in fuel cells where rather rough and porous than smooth and dense high quality layers are needed.

The sonochemical synthesis of colloidal solutions of Mo-oxide particles with amorphous structures was performed as well. The prepared colloids were successfully stabilized and remained stable for months. With the regulation of the temperature during sonication, agglomerates with mostly spherical particles were produced due to enhanced adsorption of surfactants on the particle surface. With increased temperatures the process of micelles formation was enhanced and more tubular structures were formed.

In some experiments the influence of the sonication time was also examined. In general with longer sonication times more complex structures were produced. In the case of tubular structures, growing of tubes and rods with the time was observed. The agglomerates of the spherical particles became smaller and less coherent with a prolonged time. These contradictory observations can be explained with the dual influence of ultrasound, on one side collision and on the other side fragmentation of particles. In the system with decane as a solvent, higher concentrations of molybdenum precursor led to the production of less ordered agglomerates of bigger nanorods in comparison to the case with lower precursor concentration.

In addition, a preliminary study on the pulsed sonoelectrochemical electrodeposition of Cu, Ag and Au colloidal nanoparticles was carried out. Stable colloidal nanoparticles in the nanometer range were obtained and it was shown that particle size strongly depends on the experimental conditions. This finding was very important since with further optimisation of crucial parameters influencing size of the particles it can be tailored and the desired size can be achieved.

Annexes

Annex 1-Table with ultrasonic powers obtained from calibration of Bandelin Sonopuls HD 3200

amplitude	P_{direct}	dP_{direct}	P_{inter}	DP_{inter}
100	83.5	1.9	83.0	2.5
95	-	-	78.9	2.4
90	74.2	1.8	74.9	2.3
85	-	-	70.8	2.2
80	-	-	66.8	2.2
75	-	-	62.8	2.1
70	62.9	3.6	58.7	2.0
65	58.9	3.5	54.7	1.9
60	-	-	50.6	1.9
55	50.9	3.3	46.6	1.8
50	47.2	3.3	42.6	1.7
45	42.7	3.2	38.5	1.6
40	38.8	3.1	34.5	1.6
35	33.1	3.0	29.1	0.9
30	26.5	1.6	26.4	0.9
25	-	-	23.6	0.8
20	20.6	1.5	20.8	0.8
15	-	-	18.0	0.7
10	15.3	1.5	15.2	0.7

Annex 2-Calculation of rates of mass changes and corrosion currents

From Sauerbrey equation (Eq.1.4.16):

$$\Delta f = -\frac{2f_0^2}{Z_Q}\Delta m \Rightarrow \Delta m = -\frac{\Delta f Z_Q}{2f_0^2}$$

$$\frac{\Delta f}{\Delta t} = -\frac{2f_0^2}{Z_Q}\frac{\Delta m}{\Delta t} \Rightarrow \frac{\Delta m}{\Delta t} = -\frac{\Delta f}{\Delta t}\frac{Z_Q}{2f_0^2}$$

Z_Q=8.849·10^5 gcm^{-2}s^{-1}

f_0 (for the quartz used in the experiment in Figure 3.7b) = 9.6958739560·10^6 Hz

for silent conditions:

$\Delta f/\Delta t$ (taken from the Figure 3.7 b upward case) = 17.62 Hzs^{-1}

$$\frac{\Delta m}{\Delta t} = -17.62\frac{8.849 \cdot 10^5}{2 \cdot (9.6958739560 \cdot 10^6\ )^2} = -8.2 \cdot 10^{-8}\ \text{gcm}^{-2}\text{s}^{-1} \approx -0.08\ \mu\text{gcm}^{-2}\text{s}^{-1}$$

From the equation 1.4.17 with an integral value for Δm/Δt one can calculate the expected current from mass, corresponding to the corrosion currents under open circuit conditions, as follows:

$$j_M = j_{corr} = -\frac{zF}{M}\frac{\Delta m}{\Delta t}$$

where:

F=96485 Cmol^{-1}

and for Cu z=2 and M=63.59 gmol^{-1}

$$j_{corr} = -\frac{2 \cdot 96485}{63.59}(-0.08 \cdot 10^{-6}) \approx 0.24 \text{ mAcm}^{-2}$$

In the same way one calculates $\Delta m/\Delta t$ and j_{corr} for 80 Wcm^{-2}

$\Delta f/\Delta t$ (taken from the graph 3.7 b upward case)=32.69 Hzs^{-1}

$$\frac{\Delta m}{\Delta t} = -32.69\frac{8.849 \cdot 10^5}{2 \cdot (9.6958739560 \cdot 10^6)^2} = -1.5 \cdot 10^{-7} \text{ gcm}^{-2}\text{s}^{-1} \approx -0.15 \text{ µgcm}^{-2}\text{s}^{-1}$$

$$j_{corr} = -\frac{2 \cdot 96485}{63.59}(-0.15 \cdot 10^{-6}) \approx 0.45 \text{ mAcm}^{-2}$$

Annex 3-Calculation of the equilibrium potential for Cu^{2+} reduction in $CuSO_4$ system

For $Cu^{2+}+2e^- \rightarrow Cu$ (s)

Nernst equation (Eq. 1.4.5) can be written as follows:

$$E = E^0 + \frac{RT}{zF} ln\, c(Cu^{2+})$$

For:

E^0=0.34 V vs. NHE (normal hydrogen electrode)

In our experiments Ag/AgCl (0.197 V vs NHE) was used and thus E^0=0.143 vs Ag/AgCl

R=8.315 Jmol^{-1}K^{-1}

T=298.15 K (25 °C room temperature)

z=2

F=96485 Cmol^{-1}

$c(Cu^{2+})$=0.01 moldm^{-3}

$$E = 0.143 + \frac{8.315 \cdot 298.15}{2 \cdot 96485} ln\, 0.01 = 0.143 + 0.01284 \cdot (-4.605) = 0.084 \text{ V}$$

Annex 4-Calculation of $\frac{dm}{dQ}$ function for Cu

From the equation 1.4.18:

$$\frac{dm}{dQ} = \frac{1}{i}\frac{dm}{dt} = -\frac{M}{zF}$$

and for *z*=2 one calculates:

$$\frac{dm}{dQ} = -\frac{M}{zF} = -\frac{63.59}{2 \cdot 96485} = -3.29 \cdot 10^{-4}\ \mathrm{gC}^{-1}$$

When dQ in this equation is 0 a mathematical discontinuity appears because dividing with 0 is not defined.

Annex 5-Calculation of apparent current efficiency

Calculation is done in Origin for experimentally obtain data in the following steps:

From the equation 1.4.19:

$$\varepsilon = \frac{(dm/dQ)_{exp}}{(dm/dQ)_{th}} \rightleftharpoons \varepsilon = -\frac{zF}{M}\left(\frac{dm}{dQ}\right)_{exp}$$

one calculates a set of data:

$$\varepsilon_{app} = -3.03 \cdot 10^{3}\left(\frac{dm}{dQ}\right)_{exp}$$

For each value of *dm* (calculated from Sauerbrey equation similar as in Annex 1) and differentiated by *t* one obtains:

$$(\frac{dm}{dQ})_{exp} = \frac{dm/dt}{j_{el}}$$

j_{el} is the measured current divided per electrically active area (in this experiment 0.2917 cm^2).

Annex 6-Calculation of the current efficiency

In Origin *dm* (calculated from Sauerbrey equation similar as in Annex 1) is plotted versus *Q* (obtained as one of electrochemical data and then divided per electrically active area) and one obtains the slope of this plot. The value of this slope is divided by $\left(\frac{dm}{dQ}\right)_{th} = -3.29 \cdot 10^{-4}\ \mathrm{gC}^{-1}$ and by multiplying it with 100% the current efficiency is obtained.

Annex 7-Calculation of the standard electrode potentials for the electron transfer reactions in the $CuCl_2$ system

Solution composition: 0.01 M $CuCl_2$ and 0.5 M NaCl (pH=1 addition of HCl)

$c(Cu^{2+})=0.01$ moldm^{-3}

$c(Cl^-)=c(Cl^-$ from $CuCl_2)+ c(Cl^-$ from NaCl)$+c(Cl^-$ from HCl)

$c\ (Cl^-$ from $CuCl_2)=0.01$ moldm^{-3}

$c\ (Cl^-$ from NaCl)$=0.5$ moldm^{-3}

pH=-log$c(H_3O^+)$=> $c(H_3O^+)= c(Cl^-)=0.1$ moldm^{-3}

$c(Cl^-)=0.62$ moldm^{-3}

$Cu^{2+} + e^- \leftrightarrow Cu^+$ $\qquad E^0_{Cu^{2+}/Cu^+} = 0.159$

$Cu^+ + e^- \leftrightarrow Cu(s)$ $\qquad E^0_{Cu^+/Cu(s)} = 0.52\ V$

a)

For reaction 1. $Cu^{2+} + e^- \leftrightarrow Cu^+$

Nernst equation (Eq. 1.4.5) can be written as:

$$E = E^0_{Cu^{2+}/Cu^+} + \frac{RT}{F} ln \frac{c(Cu^{2+})}{c(Cu^+)}$$

For the reaction: Cu^+ (aq) + $2Cl^-$(aq) $\leftrightarrow [CuCl_2]^-$ (aq)

$K_{\beta 2}$ (complex stability constant) = $1.995 \cdot 10^6$

and can be written as:

$$K_{\beta 2} = \frac{c([CuCl_2]^-)}{c(Cu^+)c(Cl^-)^2} \Rightarrow c(Cu^+) = \frac{c([CuCl_2]^-)}{K_{\beta 2} c(Cl^-)^2}$$

$$E = E^0_{Cu^{2+}/Cu^+} + \frac{RT}{F} ln \frac{c(Cu^{2+})}{c(Cu^+)} = E^0_{Cu^{2+}/Cu^+} + \frac{RT}{F} ln \frac{c(Cu^{2+})}{\frac{c([CuCl_2]^-)}{K_{\beta 2} c(Cl^-)^2}}$$

$$E = E^0_{Cu^{2+}/Cu^+} + \frac{RT}{F} ln \frac{c(Cu^{2+}) K_{\beta 2} c(Cl^-)^2}{c([CuCl_2]^-)}$$

For reaction: 2. Cu^{2+} (aq) + $2Cl^-$(aq) + e^- $\leftrightarrow [CuCl_2]^-$ (aq)

Nernst equation (Eq. 1.3.5) can be written as:

$$E = E^0_{[CuCl_2]^-/_{Cu^{2+}}} + \frac{RT}{F} ln \frac{c(Cu^{2+})\mathrm{c}(\mathrm{Cl}^-)^2}{c([CuCl_2]^-)}$$

E(for reaction 1)=E(for reaction 2)

$$E^0_{Cu^{2+}/_{Cu^+}} + \frac{RT}{F} ln \frac{c(Cu^{2+})\mathrm{K}_{\beta 2} c(Cl^-)^2}{c([CuCl_2]^-)} = E^0_{[CuCl_2]^-/_{Cu^{2+}}} + \frac{RT}{F} ln \frac{c(Cu^{2+})\mathrm{c}(\mathrm{Cl}^-)^2}{c([CuCl_2]^-)}$$

$$E^0_{Cu^{2+}/_{Cu^+}} + \frac{RT}{F} ln\mathrm{K}_{\beta 2} = E^0_{[CuCl_2]^+/_{Cu^{2+}}}$$

$$E^0_{[CuCl_2]^-/_{Cu^{2+}}} = 0.159\ V + \frac{8.315\, JK^{-1}\mathrm{mol}^{-1} \cdot 298.15\mathrm{K}}{96485 J\mathrm{mol}^{-1}} \cdot 14.5 = 0.372$$

$E^0_{[CuCl_2]^-/_{Cu^{2+}}}$ =0.53V vs NHE = 0.33 V vs Ag/AgCl

b)

For reaction 3: $[CuCl_2]^-$ (aq) + e^-↔ Cu(s) + $2Cl^-$ (aq)

Nernst equation (Eq. 1.4.5) can be written as:

$$E = E^0_{Cu(s)/_{[CuCl_2]^-}} + \frac{RT}{F} \ln \frac{c([CuCl_2]^-)}{\mathrm{c}(\mathrm{Cl}^-)^2}$$

where: $c([CuCl_2]^-) = \mathrm{K}_{\beta 2} c(Cl^-)^2 c(Cu^+)$

$$E = E^0_{Cu(s)/_{[CuCl_2]^-}} + \frac{RT}{F} ln \frac{\cancel{c(Cl^-)^2}\mathrm{K}_{\beta 2} c(Cu^+)}{\cancel{c(Cl^-)^2}}$$

For reaction 4: $Cu^+ + e^- \leftrightarrow Cu(s)$

Nernst equation (Eq. 1.4.5) can be written as:

$$E = E^0_{Cu(s)/_{Cu^+}} + \frac{RT}{F} lnc(Cu^+)$$

E(for reaction 3)=E(for reaction 4)

$$E^0_{Cu(s)/_{[CuCl_2]^-}} + \frac{RT}{F} ln\ \mathrm{K}_{\beta 2} c(Cu^+) = E^0_{Cu(s)/_{Cu^+}} + \frac{RT}{F} lnc(Cu^+)$$

$$E^0_{Cu(s)/_{[CuCl_2]^-}} = E^0_{Cu(s)/_{Cu^+}} - \frac{RT}{F} ln\ \mathrm{K}_{\beta 2}$$

$$E^0_{Cu(s)/_{[CuCl_2]^-}} = 0.52 - \frac{8.315\, JK^{-1}\mathrm{mol}^{-1} \cdot 298.15\mathrm{K}}{96485 J\mathrm{mol}^{-1}} \cdot 14.5 = 0.147 \text{ V vs NHE} = -0.05 \text{ V vs Ag/AgCl}$$

Annex 8-Calculation of the diffusion coefficients

From experimental data and according to the Levich equation (Eq. 1.4.11):

$j_l = 0.62zFD^{2/3}\nu^{-1/6}\omega^{1/2}c_0$

the plot j_l vs $\omega^{1/2}$ for both reactions was made (Fig. 3.33 a) and slopes are given

For the first electron transfer, first reduction reaction:

Slope $4.039 \cdot 10^{-4} = 0.62zFD^{2/3}\nu^{-1/6}c_0$

for z=1, ν = 0.0103 cm^2 s^{-1} ($\nu^{-1/6} = \frac{1}{\nu^{1/6}} = \frac{1}{\sqrt[6]{\nu}} = 2.143$)

c_0=0.01 moldm^{-3}=0.01 10^{-3}molm^{-3}

$4.039 \cdot 10^{-4} = 0.62 \cdot 96485 \cdot 0.01 \cdot 10^{-3} \cdot 2.143 \ D^{2/3}$

$4.039 \cdot 10^{-4} = 1.282 \ D^{2/3}$

$3.149 \cdot 10^{-4} = \ D^{2/3}$

$D = \sqrt{(3.149 \cdot 10^{-4})^3} = \ 5.6 \cdot 10^{-6} cm^2 s^{-1}$

In the same way for the second reduction reaction: slope $9.11 \cdot 10^{-4}$ and z=2

$9.11 \cdot 10^{-4} = 2.564 \ D^{2/3}$

$3.55 \cdot 10^{-4} = D^{2/3}$

$D = \sqrt{(3.55 \cdot 10^{-4})^3} = \ 6.7 \cdot 10^{-6} cm^2 s^{-1}$

Annex 9- Calculation of the diffusion layer thickness

When D is known one can calculate the diffusion layer thickness from (Eq. 1.4.12):

$\delta_N = 1.61\omega^{-1/2}\nu^{1/6}D^{1/3}$

1) f=1500rpm=1500/60=25rps=>ω=2πf=2·3.14·25=157 ms^{-1}

$\delta_N = 1.61\frac{1}{\omega^{1/2}}\nu^{1/6}D^{1/3} = 1.61\frac{1}{\sqrt{157}}\sqrt[6]{0.0103 \cdot 10^{-4}}\sqrt[3]{6.7 \cdot 10^{-10}}$

$\delta_N = 1.61 \cdot 0.0798 \cdot 0.1 \cdot 8.75 \cdot 10^{-4} = 1.1 \cdot 10^{-5} m = 11 \ \mu m$

2) f=3000rpm=3000/60=50rps=>ω=2πf=2·3.14·50=314 ms^{-1}

$\delta_N = 1.61 \cdot 0.0564 \cdot 0.1 \cdot 8.75 \cdot 10^{-4} = 7.9 \cdot 10^{-6} m = 7.9 \ \mu m$

Annex 10 -Calculation of K from the analogue of a Koutecký-Levich plot for the ultrasonic data

$$\frac{1}{j_l} = \frac{j}{j_k} + \frac{1}{Kd^{-1/2}A^{1/2}D^{2/3}cI_a^{1/2}}$$

where:

d (distance between tip and electrode)=2.2 cm=> $d^{-1/2}$=0.674 $cm^{-1/2}$

A (tip area) = 1.2 cm^2=>$A^{1/2}$=1.095 cm

D=$6.7\cdot10^{-6}$ cm^2s^{-1}=>$D^{2/3}$=$3.55\cdot10^{-4}$ $cm^{4/3}s^{-2/3}$

c=0.01 $moldm^{-3}$=$1\cdot10^{-5}$ $molcm^{-3}$

$j_l^{-\frac{1}{2}}$ was plotted versus $I_a^{-\frac{1}{2}}$ and and fitted linearly and from the obtained slope=313.19 $cm\Omega^{0.5}$ K was calculated as follows

$d^{-1/2}A^{1/2}D^{2/3}c = 2.62\cdot10^{-9}$ $molcm^{-7/6}s^{2/3}$=>$1/d^{-1/2}A^{1/2}D^{2/3}c$=$3.8\cdot10^{8}$ $mol^{-1}cm^{7/6}s^{-2/3}$

313.19 $cm\Omega^{0.5}$=$3.8\cdot10^{8}$ $mol^{-1}cm^{7/6}s^{-2/3}\cdot K^{-1}$

K=$1.21\cdot10^{6}$ $mol^{-1}cm^{1/6}s^{-2/3}$ $\Omega^{-0.5}$

From the intercept of the linear fit = 17.9 cm^2A^{-1}, one can calculate activation controlled current as reciprocal value:

I_k=1/17.9 cm^2A^{-1}=56 $mAcm^2$

Annex 11-Calculation of the corrosion currents

From the mass changes rates, 0.20 $\mu gcm^{-2}s^{-1}$ under silent conditions and 6.4 μgcm^{-2} s^{-1} (obtained by linear regression of the plots in a certain range) under ultrasound corrosion currents were calculated according to Eq. 1.4.20

$$j_M = j_{corr} = -\frac{zF}{M}\frac{\Delta m}{\Delta t}$$

$j_{corr} = -\frac{96485}{63.59}\cdot(-0.20\cdot10^{-3}\ \mathrm{mgcm^{-2}s^{-1}}) = 3\ \mathrm{mAcm^2}$ for silent conditions, and

$$j_{corr} = -\frac{96485}{63.59}\cdot(-6.4\cdot10^{-3}\ \mathrm{mgcm^{-2}s^{-1}}) = 9.8\ \mathrm{mAcm^2}$$

References:

1. C. P. Poole Jr., F. J. Owens, Introduction to Nanotechnology, Wiley & Sons, Inc., Hoboken, New Jersey, 2003
2. C. M. Lieber, MRS Bulletin 28 (2003) 486
3. A. Gedanken, Ultrasonics Sonochemistry 11 (2004) 47
4. Nanomaterials handbook, ed by Yuri Gogotsi, CRC Press, Taylor&Francis Group, 2006, NW
5. D. Mahajan, C.L. Marshal, N. Castagnola, J.C. Hanson, Applied Catalysis A: General 258 (2004) 83
6. A.M. Taurino, A. Forleo, L. Francioso, P. Siciliano, Appl. Phys. Lett. 88 (2006) 152111
7. A. Michailovski, G.R. Patzke, Chem. Eur. J. 12 (2006) 9122
8. A. Bala, T. Nautiyal, S. Auluck, J. App, Phys. 104 (2008) 014302
9. H. Kronmüller, M. Bachmann, Physica B: Condensed Matter 306 (2001) 96
10. L. Jianzhong, T. Tao, X. Zhang, L. Shiyun, L. Min, Mat. Lett. 61 (2007) 4351
11. Y. Wang, Q. Su, C. H. Chen, M. L. Yu, G J Han, G Q Wang, K Xin, W Lan, X Q Liu, J. Phys. D: Appl. Phys. 43 (2010) 185102
12. C.N. He, N.Q. Zhao C.S. Shi, S.Z. Song, Journal of Alloys and Compounds, 484 (2009) 6-11
13. J. D. Mackenzie, E. P. Bescher Acc. Chem. Res. 40 (2007) 810
14. P.Knauth, Science&Technology, 8 (2004) 23O.
15. R.R. Piticescu, C. Monty, D. Taloi, A. Motoc, S. Axinte, Journal of the European Ceramic Society, 21 (2001) 2057
16. N. Koprinarov, M. Konstantinova, M. Marinov, Solid State Phenomena, 159 (2010) 105
17. I. J. Plante, T. W. Zeid, P. Yang, T. Mokari, J. Mater. Chem. 20 (2010) 6612
18. Z. G. Bai, D. P. Yu, J. J. Wang, Y. H. Zou, W. Qian, J. S. Fu, S. Q. Feng, J. Xu, L. P. You, Mater. Sci. Eng. B 72 (2000) 117
19. S. C. Singh, R. K. Swarnkar, R. Gopal, J. Nanosci. Nanotechnol. 9 (2009) 5367
20. S.T. Lee, N. Wang, C.S. Lee, Mater. Sci. Eng. A 286 (2000) 16
21. T.J. Mason, Ultrasonics Sonochemistry 10 (2003) 175
22. A. Gedanken, Ultrasonics Sonochemistry 14 (2007) 418
23. S. Ramesh, Yu. Koltypin, R. Prozorov, A. Gedanken, Chem. Mater. 9 (1997) 546,
24. V.G. Pol, R. Reisfeld, A. Gedanken, Chem. Mater. 14 (2002) 3920
25. S. Avivi, A. Gedanken, Biochemical Journal 366 (2002) 705,
26. S. Avivi, Y. Nitzan, R. Dror, A. Gedanken, J. Am. Chem. Soc. 125 (2003) 15712
27. S. Avivi, A. Gedanken, Ultrasonics Sonochemistry 12 (2005) 405
28. A. Calusaru, Electrodeposition of Metal Powders, Materials Science Monographs, vol. 3, Elsevier, Amsterdam, 1979

29. J.-L. Delplancke, in: Baraton (Ed.), Synthesis, Functionalization and Surface Treatment of Nanoparticles, American Scientific Publishers, Stevenson Ranchi, CA, 2003, pp. 17–29
30. J. Reisse, H. Francois, J. Vandercammen, O. Fabre, A. Kirsch-de Mesmaeker, C. Maerschalk, J.L. Delplancke, Electrochim. Acta 39 (1994) 37
31. A.J. Martin, A.M. Chaparro, L. Daza, Journal of Power Sources 169 (2007) 65–70
32. D.A. Buttry, M.D.Ward, Chem. Rev. 92 (1992) 1355
33. V. Tsionsky, L. Daikhin, M. Urbakh, E. Gileadi, in: A.J. Bard, I. Rubinstein (Eds.), Electroanalytical Chemistry: A Series of Advances, vol. 22, 2004, p. 1
34. A. Bund, G. Schwitzgebel, Electrochim. Acta 45 (2000) 3703.
35. D. Gimenez-Romero, C. Gabrielli, J.J. Garcıa-Jareno, H. Perrot, F. Vicente, J. Electrochem. Soc. 153 (2006) J32
36. M. Zhou, N. Myung, X. Chen, K. Rajeshwar, J. Electroanal. Chem. 398 (1995) 5
37. O. Schneider, S. Martens, Chr. Argirusis, ECS Transactions 25 (2010) 69
38. O. Schneider, S. Matić, Chr. Argirusis, Electrochim. Acta 53 (2008) 5485
39. Chr. Argirusis, S. Matić, O. Schneider, phys. stat. sol. (a) 205 (2008) 2400
40. O. Schneider, S. Martens, Chr. Argirusis, ECS Transactions, 16 (2009) 107
41. M. Hyde, R. Compton, J. Electroanal. Chem. 549 (2003) 1
42. H. F. Mark, D. F. Othmer, C.G. Overberger, G. T. Seaborg, Ultrasonics. In Kirk-Othmer Encyclopedia of Chemical Technology, 3rd ed. Wiley: New York, 23 (1983) 462
43. D. Ensminger, Ultrasonic: The Low and High-Intensity- Applications; Marcel Dekker: New York 1973
44. K. Suslick from The Yearbook of Science & the Future (1994), Encyclopedia Britannica: Chicago, (1994) 138
45. T. J. Mason, J. P. Lorimer, “Applied Sonochemistry”, Wiley-VCH Verlag GmbH, Weinheim 2002
46. E. L. Carstensen, Flynn, H. G. Ultrasound Med. Biol. 8 (1982) 1720
47. F. W. Kremkau, Clinics Obstet. Gyn. 10 (1983) 395
48. T. J. Mason, Chemistry with Ultrasound, Elsevier, Oxford (1990)
49. Y. G. Adewui, Ind. Eng. Chem. Res. 40 (2001) 4681
50. L. Boeve, In Petroleum Contaminated Soils; E. J. Calabrese, P. T. Kostecki, Eds.; Lewis Publishers: Boca Raton, FL, (1989) p 279.
51. G.J. Price, "Current Trends in Sonochemistry" Royal society of Chemistry, Cambridge, (1992)
52. K.S. Suslick, G. J. Price, Ann. Rev. Mater. Sci. 29 (1999) 295
53. A. Gedanken, CURRENT SCIENCE, 85 (2003) 25
54. M. Ashokkumar, J. Lee, S. Kentish, F. Grieser, Ultrason. Sonochem. 14 (2007) 470
55. M. Ashokkumar, J. Lee, Y. Iida, K. Yasui, T. Kozuka, T. Tuziuti, A. Towata, Phys. Chem. Chem. Phys. 11 (2009) 10118

56. L.A. Crum, Ultrasonics 22 (1984) 215
57. J. Lee, S.E. Kentish, M. Ashokkumar, J. Phys. Chem. B 109 (2005) 14595
58. M. Ashokkumar, Phys. Chem. Chem. Phys. 9 (2007)5631
59. K. Yasui, J. Acoust. Soc. Am. 112 (2002) 1405
60. M. Ashokkumar, F. Grieser, Rev. Chem. Eng. 15 (1999) 41
61. M. Ashokkumar, F. Grieser, in: A. Hubbard (Ed.), Encyclopedia of Surface and Colloid Science, Marcel Dekker, New York, 2002, p. 4760
62. K. Suslick, Y. Didenko, M. M. Fang, T. Hyeon, K. J. Kolbeck, W. B. McNamara III, M. M. Mdleleni, M. Wong Phil. Trans. R. Soc. Lond. A 357 (1999) 335
63. E. B. Flint, K. S. Suslick, Science 253 (1991)1397
64. M. A. Margulis, Ultrasonics 30 (1992) 152
65. K. S. Suslick, Science 247 (1990) 1439
66. P. Riesz, T. Kondo, C.Murali Krishna, Ultrasonics 28 (1990) 295
67. R. Hiller, S. J. Putterman, B.P. Barber, Phys. Rev. Lett. 69 (1992) 1182
68. B.P. Barber, S. J. Putterman, Nature, 352 (1991) 414
69. K.S. Suslick, D. A. Hammerton and R. E. Cline, J. Am. Chem. Soc. 108 (1986) 5641
70. A. Henglein -Ultrasonics Sonochemistry 2 (1995) S115
71. K. Okada, E. Tschuikow-Roux, P. J. Evans, J. Phys. Chem. 84 (1980) 467
72. S. Fujikawa, T. Akamatsu, Journal of Fluid Mechanics 97 (1980) 481
73. H. X. Xu, K. S. Suslick, Phys. Rev. Lett. 104 (2010) 244301
74. D. J. Flannigan, K. S. Suslick, Nature Physics 6 (2010) 598
75. M. H. Entezari, M. H. Kruus, Ultrason. Sonochem. 1 (1994) S75
76. A. Franconi, C. Petrier, Ultrason. Sonochem. 3 (1996) S77
77. M.H. Entezari, Ultrason. Sonochem. 4 (1997) 49
78. K. Suslick, J. Am. Chem. Soc. 105 (1983) 5781
79. M. Gutierrez, A. Henglein, J. Phys. Chem. 94 (1990) 3625
80. M. Contamine, F. Faid, A.M. Wilhelm, J. Berlan, H. Delmas, Chem. Eng. Sci. 49 (1994) 5865
81. G.O.H. Whillock, B. F. Harvey, Ultrason. Sonochem. 4 (1997) 33
82. J. P. Lorimer, T. J. Mason, Chem. Soc. Rev. 16 (1987) 239
83. J. L. Luche, Ultrasonics 25 (1987) 40
84. S. V. Ley, C. M. R. Low, Ultrasound in Synthesis, Springer-Verlag: Berlin, 1989
85. J. Berlan, F. Trabelsi, H. Delmas, A.M. Wilhelm, J.F. Petrignani, Ultrason. Sonochem. 1 (1994) S97
86. W. Bonrath, Ultrason. Sonochem. 12 (2005) 103
87. X. Cao, Yu. Koltypin, G. Kataby, A. Gedanken, J. Mater. Res. 10 (1995) 2952
88. X. Cao, Yu. Koltypin, R. Prozorov, G. Kataby, A. Gedanken, J. Mater. Chem. 7 (1997) 2447
89. S. Avivi, M. Mastai, G. Hodes, A. Gedanken, J. Amer. Chem. Soc. 121 (1999) 4196

90. R. A. Roy, Ultrason. Sonochem. 1 (1994) S5
91. D. Lohse, Nature 418 (2002) 381
92. K. S. Suslick, S. B. Choe, A. A. Cichoulus, M. W. Grinstaff. Nature 353 (1991) 414
93. L. A. Crum, T. J. Mason, J. Reisse, K. S. Suslick, Sonochemistry and Sonoluminescence, eds. Kluwer Publishers: Dordrecht, Netherlands, 1999, pp. 291
94. V. Kesavan, D. Dhar, Y. Koltypin, N. Perkas, O. Palchik, A. Gedanken, S. Chandrasekara, J. Indian Inst. Sci.82 (2002) 113
95. V. Kesavan, D. Dhar, Y. Koltypin, N. Perkas, O. Palchik, A. Gedanken, S. Chandrasekara, Pure Appl. Chem. 73 (2001) 85
96. J. Livage, J. Phys. 42 (1981) 981,
97. M. Sugimoto, J. Magn. Mater. 133 (1994) 460
98. K. S. Suslick, T. Hyeon, M. Fang Chem. Mater. 8 (1996) 2173
99. Y. Koltypin, G. Katabi, X. Cao, R. Prozorov, A. Gedanken, Journal of non-crystalline solids 201 (1996) 159
100. D. Mahajan, E. T. Papish, K. Pandya, Ultrason. Sonochem. 11 (2004) 385
101. K. V. P. M. Shafi, A. Gedanken, R. Prozorov, J. Balogh, Adv. Mater. 10 (1998) 590
102. W. J. Erasmus, E. van Steen, Ultrason. Sonochem. 14 (2007) 732
103. L. Qiu, V. G. Pol, J. Calderon-Moreno, A. Gedanken, Ultrason. Sonochem. 12 (2005) 243
104. M. Winter, J.O. Besenhard, Electrochim. Acta 45 (1999) 31
105. R. Bellissent, G. Galli, T. Hyeon, P. Migliardo, G. Parette, K.S. Suslick, Journal of Non-Crystalline Solids 205-207 (1996) 656
106. K.V.P.M. Shafi, A. Gedanken, R.B. Goldfarb, I. Felner. J. Appl. Phys. 81 (1997) 6901
107. V. Kesavan, P. S. Sivanand, S. Chandrasekaran, Y. Koltypin, A. Gedanken, Angew. Chem. Int. Ed. 38 (1999) 3521
108. X. Cao, R. Prozorov, Y. Koltypin, G. Kataby and A. Gedanken. J. Mater. Research 12 (1997) 40
109. M. Sivakumar, A. Gedanken, Ultrason. Sonochem. 11 (2004) 373
110. K. V. P. M. Shafi, A. Gedanken, R. Prozorov, J. Balogh, Chem. Mater. 10 (1998) 3445
111. Y. Koltypin, S. I. Nikitenko, A. Gedanken, J. Mater. Chem, 12 (2002) 1107
112. N. A. Dhas and A. Gedanke, Chem. Mater. 9 (1997) 3159
113. D. N. Srivastava, N. Perkas, A. Zaban, A. Gedanken, Pure Appl. Chem. 74 (2002) 1509
114. X. Tang, S. Liu, Y. Wang, W. Huang, Y. Koltypin, A. Gedanken. Chem. Commun. (2000) 2119
115. Y. Wang, X. Tang, L. Yin, W. Huang, A. Gedanken. Adv. Mater. 12 (2000)1137
116. Y. Wang, A. Gedanken, Adv. Mater. 12 (2000) 1183
117. Y. Q. Wang, L. X. Yin, O. Palchik, Y. R. Hacohen, Y. Koltypin, A. Gedanken, Langmuir 17 (2001) 4131

118. D. N. Srivastava, N. Perkas, A. Gedanken, I. Felner. J. Phys. Chem. B 106 (2002) 1878
119. D. N. Srivastava, S. Chappel, O. Palchik, A. Zaban, A. Gedanken, Langmuir 18 (2002) 4160
120. D. N. Srivastava, N. Perkas, G.A. Seisenbaeva, Y. Koltypin, V.G. Kessler, A. Gedanken, Ultrason.. Sonochem. 10 (2003) 1
121. D. N. Srivastava, V.G. Pol, O. Palchik, L. Zhang, J. C. Yu, A. Gedanken, Ultrason. Sonochem. 12 (2005) 205
122. A. Gedanken, X. Tang, Y. Wang, N. Perkas, Y. Koltypin, M. V. Landau, L. Vradman, M. Herskowitz, Chem. Eur. J. 7 (2001) 21
123. M. V. Landau, L. Vradman, M. Herskowitz, Y. Koltypin, A. Gedanken, J. Catal.,201 (2001) 22
124. N. Perkas, Y. Wang, Y. Koltypin, A. Gedanken, S. Chandrasekaran, Chem. Commun. 11 (2001) 988
125. L. Vradman, M. V. Landau,M. Herskowitz, V. Ezersky, M. Talianker, S. Nikitenko, Y. Koltypin, A. Gedanken, J. Catal. 213 (2003) 163
126. L. Vradman, M. V. Landau, M. Herskowitz, V. Ezersky, M. Talianker, S. Nikitenko, Y. Koltypin, A. Gedanken, Stud. Surf. Sci. Catal., 146 (2003) 721
127. I. Grigoriants, L. Sominski, H. Li, I. Ifargan, D. Aurbach, A. Gedanken, Chem. Commun. (2005) 921
128. G. Schmid, Ed. Colloids and Clusters; VHC Press: New York, 1995
129. K. Aika, L. L. Ban, I. Okura, S. Namba, J. Turkevich, J. Res. Inst. Catal., Hokkaido Univ. 24 (1976) 54
130. A. Henglein, E. G. Ershov, M. Malow, J. Phys. Chem. 99 (1995) 14129
131. K. Okitsu, Y. Mizukoshi, H. Bandow, Y. Maeda, T. Yamamoto, Y. Nagata, Ultrason. Sonochem. 3 (1996) S249
132. Y. Nagata, Y. Mizukoshi, K. Okitsu, Y. Maeda, Radiation Research 146 (1996) 333
133. Y. Mizukoshi, R. Oshima, Y. Maeda, Y. Nagata, Langmuir 15 (1999) 2733
134. Y. Mizukoshi, E. Takagi, H. Okuno, R. Oshima, Y. Maeda, Y. Nagata, Ultrason. Sonochem. 8 (2001) 1
135. R.A. Salkar, P. Jeevanandam, S. T. Aruna, Y. Koltypin, A. Gedanken, J. Mater. Chem. 9 (1999) 1333
136. J. Park, M. Atobe, T. Fuchigami, Ultrason. Sonochem. 13 (2006) 237
137. C. Kan, W. Cai, C. Li, L. Zhang, H Hofmeister, J. Phys. D: Appl. Phys. 36 (2003) 1609
138. H. Takatani, H. Kago, M. Nakanishi, N. Kobayashi, F. Hori, R. Oshima, Rev. Adv. Mater. Sci. 5 (2003) 232
139. M. Bowker, L. Millard, J. Greaves, D. James, J. Soares, Gold Bull. 37 (2004) 170
140. M. Bowker, D. James, P. Stone, R. Bennett, N. Perkins, L. Millard, J. Greaves, A. Dickson, J. Catal. 217 (2003) 427

141. Y. Mizukoshi, S. Seino, K. Okitsu, T. Kinoshita, Y. Otome, T. Nakagawa, T.A. Yamamoto, Ultrason. Sonochem. 12 (2005) 191
142. Y. Mizukoshi, S. Seino, T. Kinoshita, T. Nakagawa, T. A. Yamamoto, S. Tanabe, Scripta Materialia 54 (2006) 609
143. K. Okitsu, S. Nagaoka, S. Tanabe, H. Matsumoto, Y. Mizukoshi, Y. Nagata, Chemistry Letters (1999) 271
144. Y. Mizukoshi, Y. Makise, T. Shuto, J. Hu, A. Tominaga, S. Shironita, S. Tanabe, Ultrason. Sonochem. 14 (2007) 387
145. V. G Pol, D. N. Srivastava, O. Palchik, V. Palchik, M. A. Slifkin, A. M. Weiss, A. Gedanken, Langmuir 18 (2002) 3352
146. V. G. Pol, A. Gedanken, J. Calderon-Moreno, Chem. Mater. 15 (2003) 1111
147. Z. Y. Zhong, Y. Mastai, Y. Koltypin, Y. M. Zhao, A. Gedanken, Chem. Mater. 11 (1999) 2350
148. V. G. Pol, M. Motiei, A. Gedanken, J. Calderon-Moreno, Y Mastai, Chem. Mater. 15 (2003) 1378
149. V.G. Pol, H. Grisaru, A. Gedanken, Langmuir 21 (2005) 3635
150. N. Perkas, H. Rotter, L. Vradman, M. V. Landau, A. Gedanken, Langmuir 22 (2006) 7072
151. G.S. Ranhotra, G.W. Haddix, A.T. Bell, J.A. Reimer, J. Catal. 108 (1987) 40
152. J.S Lee, S.T. Oyama, M. Boudart, J. Catal. 125 (1990) 157
153. M.J. Ledoux, C. Pham-Huu, J. Guille, H. Dunlop, J. Catal. 134 (1992) 383
154. B.C. Gates, Catalytic Chemistry; John Wiley & Sons, New York (1992) pp. 387
155. M.M. Mdleleni, T. Hyeon, K.S. Suslick, J. Am. Chem. Soc. 120 (1998) 6189
156. S. I. Nikitenko, Y. Koltypin, Y. Mastai, M. Koltypin, A. Gedanken, J.Mater.Chem.12 (2002) 1450
157. J. Lu, Y. Xie, X. Jiang, W. He, G. Du, J. Mater. Chem., 11 (2001) 3281
158. S. Djordjevic, V. Drazic, Physical Chemistry, Facultat for Technology and Metallurgy, Belgrade, 2002
159. A. J. Bard , L. R. Faulkner, Electrochemical Methods: Fundamentals and Applications, 2nd edition, John Wiley & Sons, New York (2001)
160. J. Lighthill, Waves in Fluids, Cambridge University Press, Cambridge 1978, p337
161. A. Henglein, Ultrasonics 25 (1987) 6
162. R. G. Compton, J. C. Eklund, F. Marken, Electroanalysis 9 (1997) 509
163. R. Walker, Chem. Britain. 26 (1990) 251
164. B. Brown, J. E. Goodman, High Intensity Ultrasonics: Industrial Applications Iliffe Books, London and Princeton, N.J (1965)
165. U. Akbulut, L. Toppare, K. Yurrtas, Polymer 27 (1986) 803
166. S. Oswana, M. Ito, K. Tanaka, J. Kuwano, Synthetic Metals 18 (1987) 145

167.T. J. Mason, J. P. Lorimer, D. J. Walton, Ultrasonics 28 (1990) 333
168.A. Chyla, J. P. Lorimer, G. Smith, D. J. Walton, J. Chem. Soc.,Chem. Commun. 603 (1989)
169.S. Floate, M. Hyde, R. G. Compton, J. Electroanal. Chem., 523 (2002).49
170.C. E. Banks, R. G. Compton, A. C. Fisher, I. E. Henley, Phys. Chem. Chem.Phys. 6 (2004) 3147
171.T. Lampke, B. Wielage, D. Dietrich, A. Leopold, Appl. Surf. Sci. 253 (2006) 2399
172.R. Walker, C. T. Walker, Ultrasonics 13 (1975) 79
173.R. G. Compton, J. C. Eklund, F. Marken, Electroanalysis 9 (1997) 509
174.J. Klima, C. Bernard and C. Degrand, J. Electroanal. Chem. 367 (1994) 297
175.H. Huck, Ber. Bunsenges. Phys. Chem. 91 (1987) 648
176.J. Ecklund, F. Marken, D. N. Waller, R. G. Compton, Electrochim. Acta, 41 (1996) 1541
177.B. G. Pollet, J.-Y. Hihn, M.-L. Doche, J.P. Lorimer, A. Mandroyan, T. J. Mason, J. Electrochem. Soc. 154 (2007) E131
178.I.E. Henley, A.C. Fisher, R.G. Compton, C.E. Banks, J. Phys. Chem. B 109 (2005) 7843
179.J. A. D. Jensen, P. Pocwiardowski, P. O.A.A. Persson, L. Hultman, P. Moeller, Chemical Physics Letters 368 (2003) 732
180.A. Kumar, P. R. Gogate, A. B. Pandit Ind. Eng. Chem. Res. 46 (2007) 4368
181.C. E. Banks, R. G. Compton, Electroanalysis 15 (2003) 329
182.M. E. Hyde, R. G. Compton, J. Electroanal. Chem. 531 (2002) 19
183.I. Haas, A. Gedanken, Chem. Mater. 18 (2006) 1184
184.F. Marken, J. C. Eklund, R. G. Compton, J. Electroanal. Chem. 395 (1995) 335
185.J. Reisse, H. Francois, J. Vandercammen, A. Fabre, A. K. Mesmaeker, C. Maerschalk, J. L. Delplancke, Electrochim. Acta 39 (1994) 37
186.R. Compton, J. C. Eklund, F. Marken, D. N. Waller, Electrochimica Acta, 41 (1996) 315
187.A. Aqil, H. Serwas, J. L. Delplancke, R. Jérôme, C. Jérôme, L. Canet, Ultrason. Sonochem. 15 (2008) 1055
188.S. Liu, W. Huang, S. Chen, S. Avivi, A. Gedanken, J. Non-Crystalline Solids 283 (2001) 231
189.L. M. Webber, J. Hlavay, G. G. Guilbauk. Mikrochim. Acta 1 (1978) 351
190.G. G. Guilbault, Analyt. Proc. 19 (1982) 68
191.M. R. Deakin, H. Byrd. Anal. Chem. 67 (1989) 290
192.M. Thompson, C. L Arthur, G. K. Dhaiiwai, Anal. Chem. 58 (1966) 1206
193.P. L. Konash; O. Bastlaans, J. Anal. Chem. 52 (1960) 1929
194.C. Lu, O. Lewis, J. Appl. Phys. 43 (1972) 4385
195.P. Curie, J. Curie, C.R. Acad. Sci. 91 (1880) 294
196.A. Grigas, S. Kaskel, Beilstein J. Nanotechnol. 2 (2011) 28
197.H. She, H. L. Tuller, H. Fritze, Sensors and Actuators B 93 (2003) 169

198. P. Hofmann, K. Jacobs, H. Federmann, M. Schulz, H. Fritze, H.L. Tuller, Solid State Ionics 177 (2006) 3175
199. S. J. Martin, V. E. Granstaff, G. C. Frye, Analytical Chemistry, 63 (1991) 2273
200. G. Sauerbrey, Zeitschrift für Physik 155 (1959) 206
201. A.Bund, G. Schwitzgebel, Electrochim. Acta 45 (2000) 3703
202. L. Daikhin, E. Gileadi, G. Katz, V. Tsionsky, M. Urbakh, D. Zagidulin, Anal. Chem. 74 (2002) 554
203. R. Lucklum, C. Behling, P. Hauptmann, Sensors and Actuators B 65 (2000) 277
204. D. Johannsmann, K. Mathauer, G. Wegner , W. Knoll, Physical Review B 65 (1992) 7808
205. D. Giménez-Romero, C. Gabrielli, J.J. García-Jareño, H. Perrot, F. Vicente, J. Electrochem. Soc. 153 (2006) J32
206. S. Bruckenstein, M. Shay, Electrochim. Acta 30 (1985) 1295
207. T. Lampke, B. Wielage, D. Dietrich and A. Leopold, Appl. Surf. Sci., 253, 2399 (2006)
208. J-F. Castagnet, Ph.D. Thesis, TU Clausthal, Germany (2004)
209. J. T. Matsushima, F. Trivinho-Strixino, E. C. Pereira, Electrochim. Acta 51 (2006) 1960
210. M.A. Margulis, I.M. Margulis, Ultrason. Sonochem. 10 (2003) 343
211. www.sonics.com
212. M.A. Margulis, Sonochemical Reactions and Sonoluminescenc, in: M. Chimia (Ed.), (1986) pp. 286
213. M.A. Margulis, I.M. Margulis, Acoustical Physics 51 (2005) 695
214. B.G. Pollet, J. Y. Hihn, M. L. Doche, J.P. Lorimer, A. Mandroyan, T. J. Mason, J. Electrochem. Soc. 154 (2007) E131
215. A. Grzegorzewski, K. E. Heusler, J. Electroanal. Chem. 228 (1987) 455 Lorentz
216. E. Mattson, J. O'M. Bockris, Trans. Faraday Soc., 55 (1959) 1586
217. J. O'M. Bockris, M. Enyo, Trans. Faraday Soc. 58 (1962) 1187
218. O. R. Brown, H. R. Thirsk, Electrochim. Acta, 10 (1965) 383
219. F. Chao and M. Costa, Bull. Soc. Chim. Fr. 10 (1968) 4015
220. A.L. Kipling, M. Thompson, Anal. Chem. 62 (1990) 1514
221. M. Zhou, N. Myung, X. Chen, K. Rajeshwar, J. Electroanal. Chem. 398 (1995) 5
222. A. Jardy, A. Legal Lasalle-Molin, M. Keddam, H. Takenouti, Electrochim. Acta 37 (1992) 2195
223. Z. Nagy, J. P. Blaudeau, N. C. Hung, L. A. Curtiss, and D. J. Zurawski, J. Electrochem. Soc. 142 (1995) L87
224. D. W. Suggs, A. J. Bard, J. Phys. Chem. 99 (1995) 8349
225. C. Gabrielli, P. Moçotéguy, H. Perrot, and R. Wiart, J. Electroanal. Chem. 572 (2004) 367
226. D. M. Soares, S. Wasle, K. G. Weil, and K. Doblhofer, J. Electroanal. Chem. 532 (2002) 353
227. A. Moreau, J. P. Frayret, F. Del Rey, R. Pointeau, Electrochim. Acta, 27 (1982) 1281

228. M. Itagaki, M. Tagaki, K. Watanabe, Corros. Sci. 38 (1996) 1109
229. H. P. Lee, K. Nobe, A. J. Pearlstein, J. Electrochem. Soc. 132 (1985) 1031
230. S. N. Ovchinnikova, T. P. Aleksandrova, A. A. Vais, Russian Journal of Electrochemistry 40 (2004) 755
231. C. Nila, I. González, Journal of Electroanalytical Chemistry 401 (1996) 171
232. T. Kekesi, M. Isshiki, J. Appl. Electrochem. 27 (1997) 982
233. R. Winand, Electrochimica Acta 39 (1994) 1091
234. F. K. Crunkwell, Electrochim. Acta, 15 (1992) 2707
235. O. E. Barcia, O. R. Marros, N. Pebere, B. Tribollet, J. Electrochem. Soc. 140 (1993) 2825
236. M. R. Vogt, A. Lachenwitzer, O. M. Magnussen, R. J. Behn, Surf. Sci. 399 (1998) 49
237. H. P. Lee, K. Nobe, J. Electrochem. Soc. 133 (1986) 2035
238. H. P. Lee, K. Nobe, A. J. Pearlstein, J. Electrochem. Soc. 132 (1985) 1031
239. B.G. Pollet, J.-Y. Hihn, T.J. Mason, Electrochim. Acta 53 (2008) 4248
240. CRC Handbook of Chemistry and Physics, 83rd edn., edited by D. R. Linde, CRC Press, Boca Raton, London, New York, Washington, 2002
241. T. Lampke, B. Wielage, D. Dietrich, A. Leopold, Appl. Surf. Sci. 253 (2006) 2399
242. www.science.org.au
243. D.Hull, T.W.Clyne, An introduction to composite materials, Cambridge University Press 1981, 1996
244. E. J. Barbero, Introduction to composite materials design, Taylor & Francis, Philadelphia, Pa.; 1999
245. V. O. Nwoko, L. L. Shreir, Journal of Applied Electrochemistry 3 (1973) 137
246. N. S. Qu, D. Zhu, K. C. Chan, Scr. Mater. 54 (2006) 1421
247. D. Lee, Y. X. Gan, X. Chen, J. W. Kysar, Mater. Sci. Eng. A 447 (2007) 209
248. G. Cârâc, L. Benea, C. Iticescu, T. Lampke, S. Steinhäuser, B. Wielage, Surf. Eng. 20 (2004) 353
249. A. Bund, D. Thiemig, Surf. Coat. Technol. 201 (2007) 7092
250. H. Ferkel, B. Müller, W. Riehemann, Mater. Sci. Eng. A 234–236 (1997) 474
251. J.R. Roos, J. P. Celis, J. Fransaer, C. Buelens, J. Metals 42 (1990) 60
252. L..Z. Du, B. S. Xu, S.Y. Xu, H. Dong, H. Yang, W. Y. Tu, Wear 257 (2004) 1058
253. C. Buelens, J. Fransaer, J. P. Celis, J. R. Roos, Bull. Electrochem. 8 (1992) 371
254. V.P. Greco, W. Baldauf, Plating 55 (1968) 250
255. N. Periene, A. Cesuniene, L. Taicas, Plat. Surf. Finish. 80 (1993) 73
256. T.W. Tomaszewski, R. J. Clauss, H. Brown, Proc. Am. Electroplaters Soc. 50 (1963) 169.
257. G.N.K. Ramesh Bapu, M. Mohammed Yusuf, Mat. Chem. Phys. 36 (1993) 134
258. F.K. Sautter, J. Electrochem. Soc. 110 (1963) 557
259. N.S. Qu, D. Zhu, K.C. Chan, Scripta Materialia 54 (2006) 1421
260. E.A. Brandes, D. Goldthorpe, Metallurgia 76 (1967) 195

261. H. Hayashi, S. Izumi, I. Tari, J. Electrochem. Soc. 140 (1993) 362
262. M. Verelst, J. P. Bonino, A. Rousset, Mat. Sci. Eng. A 135 (1991) 51
263. M. Keddam, S. Senyarich, H. Takenouti, P. Bernard, J. Appl. Electrochem. 24 (1994) 1037
264. A. Anani, Z. Mao, S. Srinivasan and A. J. Appleby, ibid. 21 (1991) 683
265. T. Brenscheidt, F. Nitschke, O. Söllner, H. Wendt, Electrochim. Acta 46 (2001) 783
266. J.A.D. Jensen, P. Pocwiardowski, P.O.A. Persson, L. Hultman, P. Möller, Chemical Physics Letters 368 (2003) 732
267. F. Touyeras, J.Y. Hihn, X. Bourgoin, B. Jacques, L. Hallez, V. Branger, Ultrason. Sonochem. 12 (2005) 13
268. D.J. Walton, S.S. Phull, in: T.J. Mason (Ed.) Advances in Sonochemistry, vol. 4, JAI Press, London, 1996, p. 205
269. O.V. Abramov, Ultrasound in Liquid and Solid Metals, CRC Press, 1994,p. 354 and 398
270. L. Martins, J.I. Martins, A.S. Romeira, M.E. Costa, J. Costa, M. Bazzaoui, Mater. Sci. Forum 455–456 (2004) 84
271. P. Kristof, M. Pritzker, Plat. Surf. Finish. 85(1998) 237
272. P.B.S.N.V. Prasad, R. Vasudevan, S.K. Seshadri, S. Ahila, Bull. Electrochem.9 (1993) 468
273. D. Lee, Y. X. Gana, X. Chena, J. W. Kysar, Materials Science and Engineering A 447 (2007) 209
274. G. Vidrich, J.F. Castagnet, H. Ferkel, J. Electrochem. Soc. 152 (2005) C294
275. S.L. Kuo, Y.C. Chen, M.D. Ger,W.H. Hwu, Mater. Chem. Phys. 86 (2004) 5
276. N.S. Qu, K.C. Chan, D. Zhu, Scripta Mater. 50 (2004) 1131
277. J. Hoffmann, C.-Y. Yuh, A. Godula Jopek, in: Handbook of Fuels Cells, Fundamentals and applications, Vol. 4, edited by W. Vielstich, H. A. Gasteiger, Arnold Lamm, John Wiley & Sons, (2003), p. 921
278. M. H. Kim, M. Z. Hong, Y.-S. Kim, E. Park, H. Lee, H.-W.Ha, K. Kim, Electrochim. Acta 51 (2006) 6145
279. Schmid, G., Ed. Colloids and Clusters; VHC Press: New York, 1995
280. R. Xu, D. Wang, J. Zhang, Y. Li, Chem. Asian J. 1 (2006) 888
281. K. H. Park, K. Jang, H. J. Kim, S. U. Son, Angew. Chem. 119 (2007) 1170
282. N. N. Mallikarjuna, R. S. Varma, Cryst. Growth Des. 7 (2007) 686
283. H. Bonnemann, R. M. Richards, Eur. J. Inorg. Chem. (2001) 2455
284. X.F. Qiu, J.Z. Xu, J.M. Zhu, J.J. Zhu, S. Xu, H.Y. Chen,J. Mater. Res. 18 (2003) 1399
285. Y. Mastai, R. Polsky, Y. Koltypin, A. Gedanken, G. Hodes, J. Am. Chem. Soc. 121 (1999) 10047
286. A. Durant, J.-L. Delplancke, R. Winand, J. Reisse, Tetrahedron Lett. 36 (24)(1995) 4257
287. V. Mancier, A.-L. Daltin, D. Leclercq, Ultrason. Sonochem. 15 (2008) 157
288. I. Haas, S. Shanmugam, A. Gedanken, Chem. Eur. J. 14 (2008) 4696
289. I. Haas, S. Shanmugam, A. Gedanken, J. Phys. Chem. B 110 (2006) 16947

290. A. Aqil, H. Serwas, J.L. Delplancke, R. Jérôme, C. Jérôme, L. Canet, Ultrason. Sonochem. 15 (2008) 1055
291. L-P. Jiang, A-N. Wang, Y. Zhao, J-R. Zhang, J-J. Zhu, Inorganic Chemistry Communications 7 (2004) 506
292. C. Jingquan and Y. Suwei, RARE METALS 24 (2005) 376
293. J. Zhu, S. Liu, O. Palchik, Y. Koltypin, A. Gedanken, Langmuir 16 (2000) 6396
294. V. Sáez, T. J. Mason, Molecules, 14 (2009) 4284
295. S. D. Park, J. M. Vohs, R. J. Gorte, Nature 404 (2000) 265
296. R. J. Gorte, H. Kim, J. M. Vohs, J. Power Sources 106 (2002) 10
297. B. Yin, H. Ma, S. Wang, S. Chen, J. Phys.Chem. 107 (2003) 8898
298. R.G. Ganguly, Bull. Mater. Sci. 30 (2) (2007) 183
299. S. Jiebing, X. Rui, W. Shimin, T. Wufeng, T. Hua, S. Jing, Journal of Sol-Gel Science and Technology 27 (2003) 315
300. W. Dong, B. Dunn, Journal of Non-Crystalline Solids 225 (1998) 135–140
301. J. Mendez-Vivar, A. Campero, J. Livage, C. Sanchez, J. Non-Cryst. Solids 121 (1990) 26
302. J.A. Hollingshead, M.T. Tyszkiewicz, R.E. McCarley, Chem. Mater. 5 (1993) 1600
303. M.I. Yanovskaya, I.E. Obvintseva, V.G. Kessler, B.Sh. Galyamov, S.I. Kucheiko, R.R. Shifrina, N.Y. Turova, J.Non-Cryst. Solids 124 (1990) 155
304. J. E. Herrera, J.H. Kwak, J.Z. Hu, Y. Wang, C.H.F. Peden, Topics in Catalysis 39 (2006) 245
305. S. Wang, Y. Zhang, X. Ma, W. Wang, X. Li, Z. Zhang, Y. Qian, Solid State Communications 136 (2005) 283
306. T. Xia, Q. Li, X. Liu, J. Meng, X. Cao, J. Phys. Chem. B 110 (2006) 2006
307. Y. Zhao, J. Liu, Z. Zhengjun, Y. Xu, H. Naramoto, S. Yamamoto, J. Phys.: Condens. Matter 15 (2003) L547
308. Q.P. Ding, H.B. Huang, J.H. Duan, J.F. Gong, S.G. Yang, X.N. Zhao, Y.W. Du, Journal of Crystal Growth 294 (2006) 304
309. L. Seguin, M. Figlarz, R. Cavagnat, J.-C. Lassegues, Spectrochimi. Acta, Part A 51 (1995) 1323
310. X.W. Lou, H.C. Zeng, J. Am. Chem. Soc. 125 (2003) 2697
311. J. Zhou, N.S. Xu, S.Z. Deng, J. Chen, J.C. She, Z.L. Wang, Adv. Mater. 15 (2003) 1835
312. S. Wang, Y. Zhang, W. Wang, G. Li, X. Ma, X. Li, Z. Zhang, Y. Qian, Journal of Crystal Growth 290 (2006) 96
313. X. Chen, Z. Zhang, X. Li, C. Shi, X. Li, Chem. Phys. Lett. 418 (2006) 105
314. G. Demazeau, J.M. Millet, C. Cros, A. Largeteau, Journal of Alloys and Compounds 262-263 (1997) 271
315. N. Arul Dhas, A. Gedanken, J. Phys. Chem. B 101 (1997) 9495
316. Z.Y. Zhong, Y. Mastai, R.A. Salkar, Y. Koltypin, A. Gedanken, J. Mater. Res. 15 (2000) 393
317. K.S. Suslick, M. Fang, T. Hyeon, J. Am. Chem. Soc. 118 (1996) 11960

Publications in the Framework of the Thesis

1. S. Matić, O. Schneider, C. Argirusis, An in-situ EQCM study of sonoelectrochemical deposition of metallic materials, Proceedings of 19th International Congress on Acoustics, Madrid, 02.-07. 09. 2007

2. O. Schneider, S. Matić, Chr. Argirusis, Application of the electrochemical quartz crystal microbalance technique to copper sonoelectrochemistry Part 1. Sulfate-based electrolytes, Electrochim. Acta 53 (2008) 5485

3. Chr. Argirusis, S. Matić, O. Schneider, An EQCM study of ultrasonically assisted electrodeposition of Co/CeO2 and Ni/CeO2 composites for fuel cell applications, phys. stat. sol. (a) 205 (2008) 2400

4. O. Schneider, S. Martens, Chr. Argirusis, Sonoelectrochemical Deposition of Functional Composite Layers, ECS Transactions, 16 (2009) 107

5. J. Große-Brauckmann, S. Matić, O. Schneider, Chr. Argirusis, Deposition of sonochemically derived nano particles, Key Engineering Materials 412 (2009) 65

6. O. Schneider, S. Martens, Chr. Argirusis, The Electrochemical Quartz Crystal Microbalance Technique in Sonoelectrochemistry, ECS Transactions 25 (2010) 69